Innovative Butler Matrix Concepts

Based on Novel Components For 2-D Beamforming

Kejia Ding

A Thesis
In the Department
of
Electrical and Computer Engineering

Presented in Partial Fulfillment of the Requirements
For the Degree of
Doctor of Philosophy (Electrical and Computer Engineering) at
Concordia University
Montreal, Quebec, Canada

October 2019

CONCORDIA UNIVERSITY

SCHOOL OF GRADUATE STUDIES

This is to certify that the thesis prepared

By: Kejia Ding

Entitled: Innovative Butler Matrix Concepts based on Novel Components For 2-D Beamforming

and submitted in partial fulfillment of the requirements for the degree of

Doctor of Philosophy (Electrical and Computer Engineering)

complies with the regulations of this University and meets the accepted standards with respect to originality and quality.

Signed by the Final Examining Committee:

	Chair
Dr. Akif A. Bulgak	
	External Examiner
Dr. Zhongxiang Shen	
	Examiner
Dr. Tayeb Dinidni	
	Examiner
Dr. Robert Paknys	
	Examiner
Dr. Abdel Sebak	
	Examiner
Dr. Ali Dolatabadi	
	Supervisor
Dr. Ahmed. A. Kishk	

Approved by _____
Dr. Rastko Selmic, Graduate Program Director

December 3, 2019

_____
Dr. Amir Asif, Dean
Gina Cody School of Engineering & Computer Science

Abstract

Innovative Butler Matrix Concepts based on Novel Components for 2-D Beamforming

Kejia Ding, Ph. D.

Concordia University 2019

Several innovative concepts and schemes to enrich the features of Butler matrices (BMs) to enhance their suitability over the conventional schemes are discussed, demonstrated, and analyzed. Mobile communication and radar systems require compact and versatile multibeam-forming networks (MBFNs). Therefore, the study is aimed to provide feasible and practical solutions with more flexible beam numbers of BMs, more concise configurations of the two-dimensional (2-D) beamforming, and broadband characteristics while maintaining the intrinsic merits of conventional BMs (such as theoretically lossless, spatially orthogonal beams, and relatively simple structure). In addition, the study implements some of the concepts to millimeter-wave (mm-wave) frequencies applications.

Concretely, the effects of some components, such as T-junctions and crossovers, on the bandwidth of parallel-feeding networks and MBFNs, are investigated and analyzed. The corresponding solutions to broaden the bandwidth are suggested and verified by the measurements. Further, for the 2-D beamforming based on BMs, a generalized scheme to build 2-D MBFN with any 2^{M+N} beams based on traditional $2^{M}\times 2^{M}$- and $2^{N}\times 2^{N}$ BMs is elaborated and experimentally verified. Especially as the key component of 2-D BMs, an innovative eight-port coupler with a very compact structure is proposed. The applications of the coupler for 2-D monopulse arrays, dual-polarized monopulse arrays, and mm-wave 2-D beamforming are also demonstrated. Besides, two solutions

to extend the numbers of beams of BMs from traditional $2^N \times 2^N$ to almost arbitrary number, such as $2^M \times 3^N$ or $M \times 2^N$, are introduced by using a three-way coupler and electrically switchable coupler, respectively (M and N are arbitrary integers greater than 0).

Though the majority of ideas and examples presented is exemplified by planar circuits and transverse-electro-magnetic (TEM) transmission lines, they can also be transferred to and applied on other circuit forms, such as ridge-gap waveguide (RGW), printed RGW (PRGW), substrate-integrated waveguide (SIW), and packaged microstrip line (PMSL) for mm-wave applications.

Keywords: Butler matrices, two-dimensional Butler matrices, directional couplers, reconfigurable couplers, phase shifters, crossovers, eight-port couplers, packaged microstrip line.

Acknowledgement

I would like to express my deep gratitude to my supervisor, Dr. Ahmed A. Kishk, for his guidance, patience and invaluable comments.

Thanks are also due to Dr. Zhongxiang Shen, Dr. Tayeb Dinidni, Dr. Robert Paknys, Dr. Abdel Sebak, and Dr. Ali Dolatabadi for their valuable comments and serving in my examining committee.

I would also like to thank Concordia University technical staff, Mr. Jeffery Landry, Mr. Vincent Mooney-Chopin, for their assistance in building and measuring the presented prototypes in this work.

Lastly, I offer my love, regards and blessings to my wife, my mother, and my father, for their unlimited support during the compilation of this work.

Table of Content

List of Figures

List of Tables

List of Acronyms

AMC	Artificial Magnetic Conductor
BM	Butler matrix
CPW	Co-planar Waveguide
5G	Fifth Generation
MBFN	Multibeam forming network
mm-Wave	Millineter-Wave
1-D	One-Dimensional
PEC	Perfect Electric Conductor
PMC	Perfect Magnetic Conductor
PMSL	Packaged Microstrip line
PRGW	Printed Ridge Gap Waveguide
RGW	Ridge Gap Waveguide
SIW	Substrate-Integrated Waveguide
2-D	Two-Dimensional

Chapter 1

Introduction

In this chapter, a short and general introduction to the thesis is presented, which includes a brief background of Butler matrices with their advantages and limitations from a conventional point of view, the intention to overcome some restrictions for more versatile and flexible performances over the conventional schemes, and the anticipated accomplishments based on some proposed innovative concepts. And then, the framework of this thesis is briefly introduced with the significant contribution and research achievements in each chapter.

1.1 Background About Butler Matrices

A Butler matrix (BM) is one of the most important multiple-beam-forming networks (MBFN) [1], [2], which has been intensively studied and extensively applied in communication systems to increase the channel capacity and reduce the spatial interference among users, due to their unique properties [3], [4]. A classical $2^N \times 2^N$ BM connecting a 2^N antenna elements in a linear array produces 2^N independent beams with spatial orthogonal directions from the same array. Perfect matching, isolation, and equal power division can be achieved at the same time (N is an integer larger than 1). Compared with other MBFNs, such as the Blass matrix [5], Nolen matrix [6], and Rotman lens [7], BM has some attractive features [8] as the realizable bandwidth, structural simplicity, and theoretically lossless transition.

In terms of the composition, a conventional BM is composed of couplers, phase shifters, and crossovers, as the example of the functional blocks of an 8 × 8 BM configuration shown in Figure 1-1. Here, the rectangular frames with two wider and two narrower lines represent 3-dB 90° hybrid couplers; the folded transmission lines with a half-circular bent denote the phase shifters and the number alongside it is the value of phase delay; the cross surrounded by an ellipse indicates a crossover.

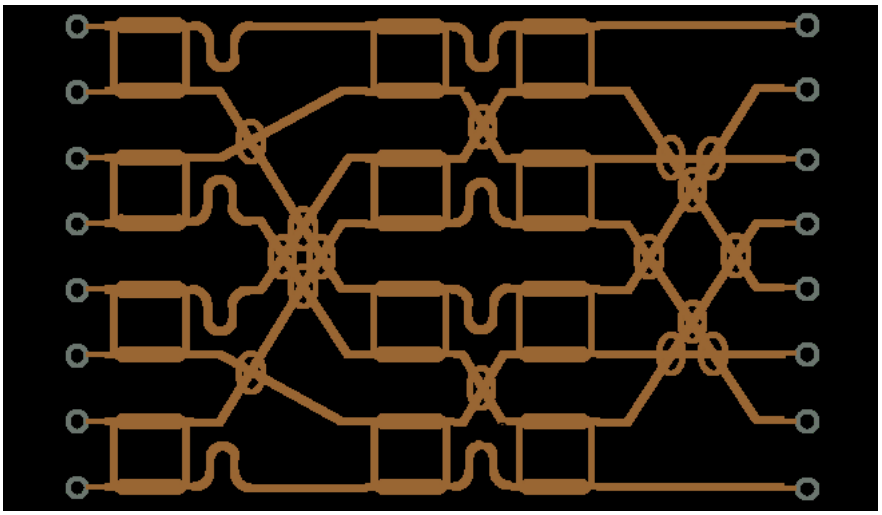

Figure 1-1. Example of a functional block view of 8 × 8 BM configuration.

The components and the BMs can be implemented by variety of the forms of transmission line, such as microstrip line [9], multi-layer microstrip line [10], co-planar waveguide (CPW) [11], substrate-integrated waveguide (SIW) [12], rectangular waveguide [13], ridge gap waveguide (RGW), substrate-integrated ridge gap waveguide, (RGW, or printed ridge gap waveguide, PRGW) [15], groove waveguide [16], and packaged microstrip line (PMSL) [17] et. al, according to the limitations of dimension, power capacity, weight, and volume, as well as the frequencies that BMs will work for. Two of the examples have been shown in Figure 1-2, which are the BMs built based on the double-layer microstrip line and CPW.

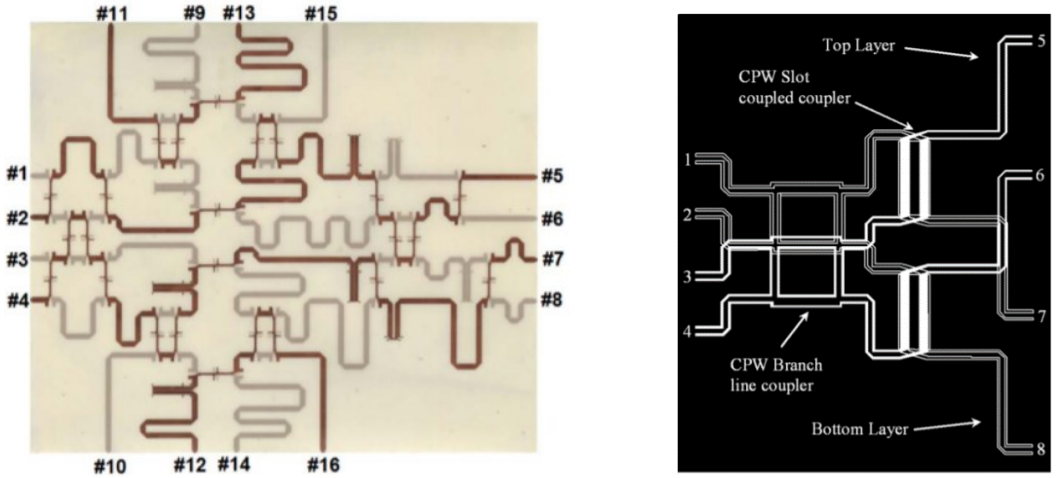

(a) Wideband 8 × 8 BM based on double-layer microstrip line [10] (b) Wideband 4 × 4 BM based CPW [11]

Figure 1-2. Examples of BMs based on different forms of transmission lines from reported work.

In terms of the interfaces to the external devices, to obtain the typical features of a BM, the ports can be sorted into two types: antenna-ports and beam-ports. All antenna-ports of a conventional BM will be connected to the elements of a linear array sequentially; while, each of the beam-ports will be corresponding to a progressive phase difference between adjacent antenna-ports. An example of a conventional 4 × 4 BM is shown in Figure 1-3 to illustrate the connections between BM and antenna array, as well as the correspondence between beam-ports and the beams.

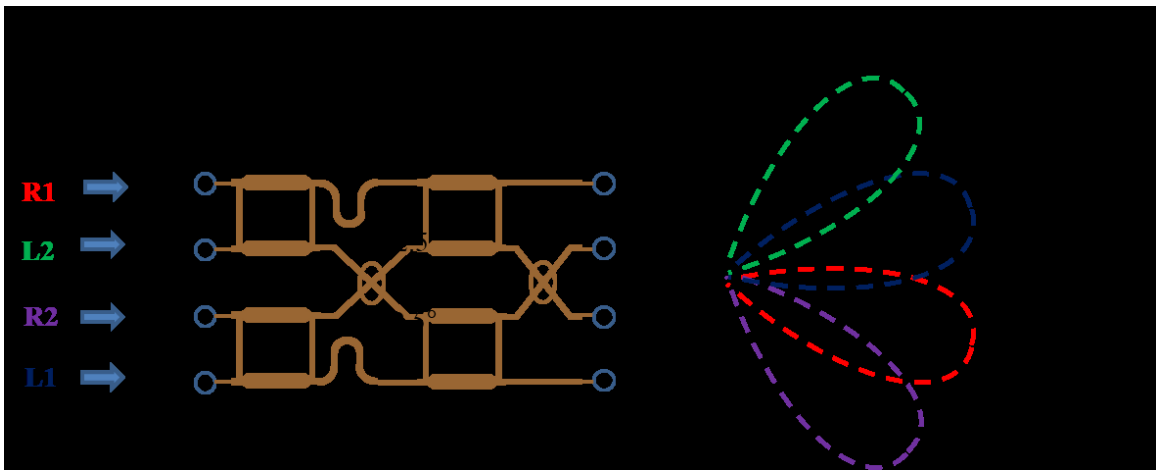

Figure 1-3. Demonstration a 4 × 4 BM to the antenna array for four-beamforming.

Here, A-ports represent antenna-ports, and B-ports indicate beam-ports, respectively, as the ports A1- A4 and B1 - B4 demonstrated in Figure 1-3. The values of progressive phase differences for each beam are listed alongside the beam. Besides, the correspondence between a specific beam and the B-port is demonstrated by the same color. For example, the beam with a 45° progressive phase difference is denoted by a red dotted line, which is referred to as beam R1 and indicated by red color. The R1 is placed next to Port B1. Therefore, Port B1 is corresponding to beam R1.

Some examples from [18], [19] are exhibited in Figure 1-4 to demonstrate BMs integrated with an antenna array.

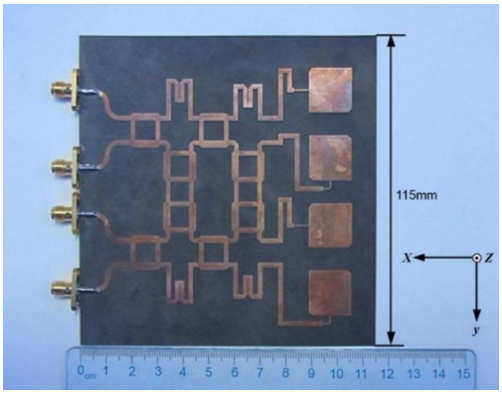

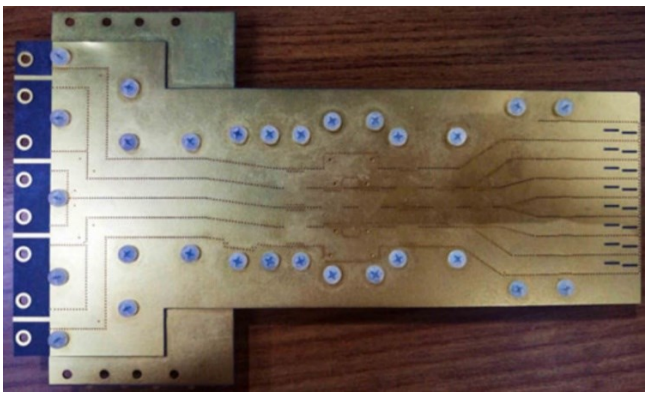

(a) 4 × 4 microstrip BM with a 1 × 4 patch array [18] (b)) 8 × 8 double-layer SIW BM with 1 × 8 array [19]

Figure 1-4. Examples from reported work for the demonstration of BM integrated with an antenna array.

In summary, a conventional BM has 2^N antenna-ports, and 2^N beam-ports (also referred to as a $2^N \times 2^N$ BM) generates 2^N independent beams by the connected linear array of 2^N elements. Ideal matching, perfect isolation, and equal power division can be achieved if the couplers, crossovers, and phase shifters inside the BM are theoretically perfect. Besides, no loads or absorbers are required in BMs; in other words, BMs are theoretically lossless networks. The progressive phase differences between adjacent antenna-ports are $\pm \pi/2^N$, $\pm 3\pi/2^N$, … $\pm (2^N\text{-}1)\ \pi/2^N$. Each one of the beam-ports is corresponding to a progressive phase difference, or, a beam. In terms of the spatial distribution of the beams, the 2^N beams will be spatially orthogonal to each other. In any direction

where one beam reaches its peak gain, all other beams must have nulls regardless of the space between the elements.

1.2 Motivation

Though many advantages of BMs have been introduced in Section 1.1, there is still room for further enhancements to meet the demands of many applications, which require simpler structures, more flexible adaptabilities, and more comprehensive features. For example, the number of beams generated by traditional BMs must be identical to the number of antenna array elements. This limitation is only due to the intrinsic property of BMs, but it will restrict adopting BMs on many demands which require beam numbers different from the number of antenna elements or the number of input ports. Even if both numbers are identical to each other, they may not be an integer power of two. Therefore, such demand cannot be met by conventional BMs. Clearly, a solution to diversify the beam and element numbers is needed.

Besides, classical BMs are intended to one-dimension (1-D) beamforming application by connecting to linear arrays. For the requirements of utilizing BMs with planar arrays to achieve two-dimension (2-D) beamforming, a generalized solution is required to design the BMs and arrange the array to planar array.

Furthermore, to develop the potential of 2-D BMs for more widespread and comprehensive applications, it would be better to increase the beam number than what is commonly used in conventional BMs, far beyond 4 × 4, for example. In other words, higher-order 2-D BMs are demanded. However, the complexity of BMs will considerably increase with the growth of the

beam numbers, in terms of the numbers of components and the route of traces. Therefore, a novel idea to simplify the BM structure is desired for compact and concise 2-D BMs.

In addition to the motives for improvement based on the ports outside BMs, the effects from components inside BMs also need to be observed and analyzed. For example, to expand the operation bandwidth of BMs, besides the effects of each component itself, the interactions among components are required to be investigated and explained.

Finally, the approach of employing and transferring the techniques related to BMs from lower frequencies to millimeter-wave (mm-wave) frequencies are required for the demands to operate at mm-wave bands, such as fifth-generation new radio (5G NR), automotive radars, and microwave imaging. According to the demands related to BMs for some background applications discussed above, the intentions of this study can be determined and clarified.

1.3 Objectives

First, the investigations of the interactions and effects among the components, such as T-junctions and crossovers, on the feed networks and BMs will be conducted. This research will reveal some sources to impact the bandwidth performance of feed networks and BMs, which are beyond the features of the individual components, and usually, are neglected.

Secondly, a generalized scheme to construct 2-D BMs with the required numbers of beams in 2-D is expected. The scheme is supposed to be simple, clear, and feasible to be implemented by planar circuits. Besides, the intrinsic features of conventional BMs are expected to be inherited to the 2-D BMs.

Further, a novel directional coupler with more multiple ports and compact sizes to simplify the structural complexity of BMs is expected, such as an eight-port coupler. The aimed coupler will just take an area similar to the usual quadrature couplers but can achieve the directional coupling from four ports to another four ports with ideal matching, isolation, and fixed phase difference. Rather than accumulating and stacking more conventional four-port couplers (such as 3-dB 90^{o} quadrature coupler) for higher-order BMs or 2-D BMs, using an eight-port coupler can effectively reduce the number of components needed to construct BMs.

Moreover, some methods to diversify the structural topology of BMs to different configurations from the conventional one for more flexible numbers of beams and elements are introduced. For example, the beam number can be different than the element number, and they are not necessarily 2^N. The approaches could involve some novel couplers to replace the traditional 3-dB 90^{o} couplers, such as three-way couplers or reconfigurable couplers.

Finally, a 2-D beam steerable array with feed work based on the eight-port coupler and packaged microstrip line will be implemented for mm-wave frequencies applications. By using the artificial magnetic conductor (AMC) packaging circuit, the ideas proposed above, such as 2-D BMs and eight-port coupler, can be transferred from lower-frequency to mm-wave circuits without many significant changes.

1.4 Outline of the Thesis

The subsequent chapters in this thesis will be briefly arranged into the sequence coinciding with the objectives introduced in Section 1.3, but a literature review will be presented first, as well as a conclusion and future work will be summarized at the end.

Chapter 2 is the literature review, which includes several sections. Each section is corresponding to an individual objective related to one of the following chapters. The reported work in the related field is introduced and analyzed.

In Chapter 3, the impacts of some inner-components on the features of feeding networks are introduced. Two studies are considered, respectively. The effects of crossover on BMs and the influence of the T-junctions on a parallel feeding network are presented. A scheme to design parallel feeding networks with multi-octave fractional bandwidth is proposed and experimentally verified.

In Chapter 4, a method to design 2-D BMs with $2^{(N+M)}$ spatially distributed beams based on the conventional BMs is introduced. In addition, another novel component, the phase-shifter group, is introduced to provide wideband phase shifter. A 16 × 16 2-D BM for 4 × 4 beams is implemented by a planar circuit.

In Chapter 5, a compact eight-port coupler with a very concise configuration is presented with the principle, and analytical expressions of its features are presented with simulated and measured results. Based on this novel coupler, different applications are demonstrated, such as a four-beam 2-D beamforming network, a 2-D monopulse array, and a dual-polarized monopulse array.

In Chapter 6, two schemes are introduced to build BMs beams not equal to 2^N for elements not equal to 2^N, which based on three-way directional couplers and electrically switchable couplers, respectively. A quasi-6 × 6 BM, a real 6 × 6 BM, and an electrically switchable 12 × 4 BM will be demonstrated.

In Chapter 7, a compact 2-D beamforming network based on the eight-port coupler and AMC packaging for mm-wave frequencies is proposed. The antenna array with compact 4 × 4 MBFN is

based on a back-to-back double-layer microstrip line structure covered by two AMC layers on the top and bottom surfaces to prevent surface-wave and leakage and ensure the quasi-TEM propagation.

Finally, a conclusion is described in Chapter 8 with the main contributions and the future work of the research. It is also a summary, a review, and an outlook of the entire thesis, in terms of the contributions on both innovation and application.

Chapter 2

Literature Review

In this chapter, some reported works in the relevant research fields for similar objectives are summarized, compared, and analyzed in terms of their features, merits, limitations, and the inspiration to this thesis.

Structurally, there are four sections in this chapter, and each section is corresponding to an individual research objective, which is described in an independent chapter. The literature review is concentrated on the essential contributions and the latest progress regarding the innovative concepts of BMs, rather than implementation based on different forms of microwave circuits. Concretely, the approaches of beam number extension for BMs, the methods for 2-D beamforming based on BMs, the novel components to simplify BMs, and the effects of some components on BMs are focused on.

2.1 Wideband Feed Networks

2.1.1 Wideband Parallel Feed Networks

The feeding network is a necessary part of most antenna arrays to transfer and distribute the energy from the feed port to every element with the required power division and phase distribution. Compared with the series-feeding configurations [20] - [22], the parallel-feeding network [23] - [25], or, corporate-feeding network [26] has several intrinsic advantages, such as in-phase

transmission on each path, smaller mutual interaction between elements, and better performances with wideband properties. As a fundamental functional component, T-junctions are usually utilized in parallel-feeding networks for energy separation/combination.

To enhance the matching bandwidth of parallel-feeding networks, some studies have been reported for the bandwidth improvement of T-junction. In [27], by introducing and tuning several metal walls inside a rectangular waveguide nearby the junctions, expected bandwidth of matching and phase compensation could be achieved at Ka-band covering more than 10% fractional bandwidth. The scheme is demonstrated in Figure 2-1.

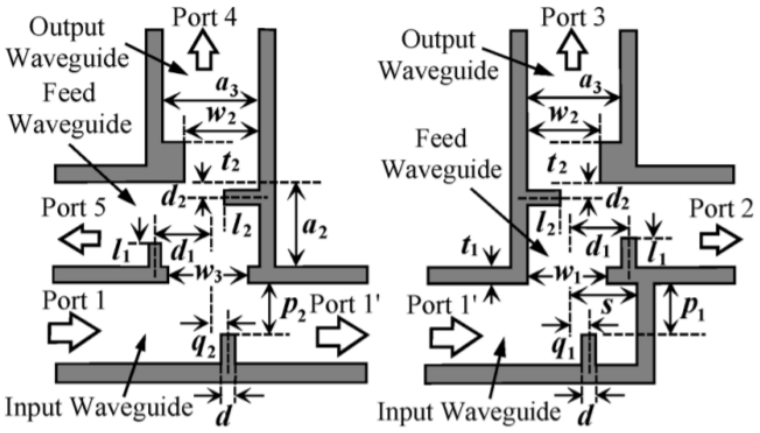

Figure 2-1. Demonstration of the method to enhance the bandwidth of T-junction proposed in [27]

In [28] and [29], corporate-feed hollow-waveguide circuits were introduced as a 64-way divider for a 60 GHz band usage, and a more than 8.3% fractional bandwidth can be observed with reflection lower than -22.3 dB.

Another corporate-feed network-based hollow rectangular coaxial line was introduced in [30], and the modified T-junctions with shorted stub were employed for bandwidth broadening. A fractional bandwidth of 8.3% can be realized with the VSWR less than 1.5 for the T-junction. The parallel-feed network-based T-junctions can also be implemented by other quasi-transverse

electromagnetic transmission lines, such as ridge gap waveguide [31]. In particular, part of the ridge with a gradually tapered width was used in the middle of the four-way power divider to replace the conventional λ/4 transformer section for a wider bandwidth, and about 27% fractional bandwidth can be obtained at Ku-band. The scheme is illustrated in Figure 2-2.

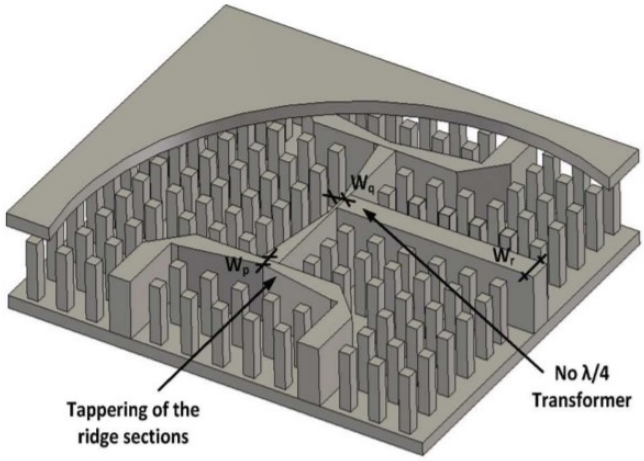

Figure 2-2. Four-way power divider with tapered width for bandwidth enhancement proposed in [31].

For the same operating frequency band, another full-corporate waveguide feeding network was proposed in [32], [33]. In [32], the four-way dividers can cover 12.5 - 14.5 GHz with reflection coefficients lower than -8 dB. The enlarged view for the four-way power divider and the entire layout are shown in Figure 2-3. The cut-corners for bandwidth improvement can be found in the layout.

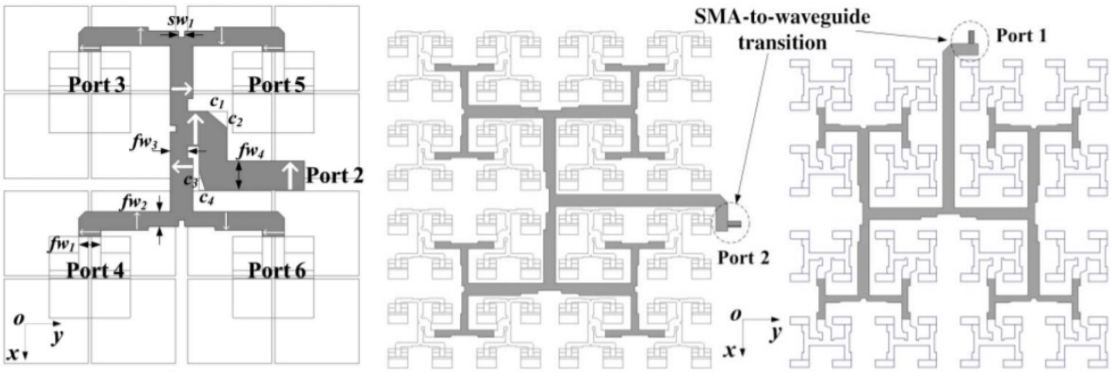

Figure 2-3. Enlarged view for the four-way power divider and the entire layout proposed in [32].

In addition, it has been found that the spacing distances between T-junctions in a parallel-feeding network can result in a significant impact on the matching bandwidth [34]. Moreover, some useful improvements have been demonstrated to increase the matching bandwidth by adjusting the intervals between the T-junctions. It revealed the potential feasibility to extend the matching bandwidth by treating the network as a whole rather than part by part. The configuration of the feeding network, circuit model, and calculated results shown in Figure 2-4.

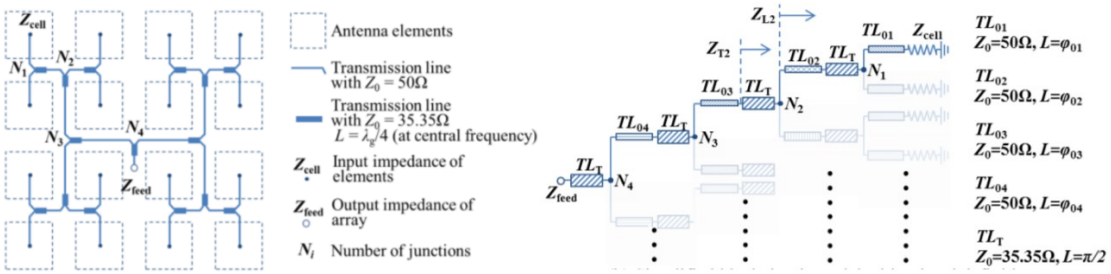

(a) Configuration of the feeding network (b) Circuit model

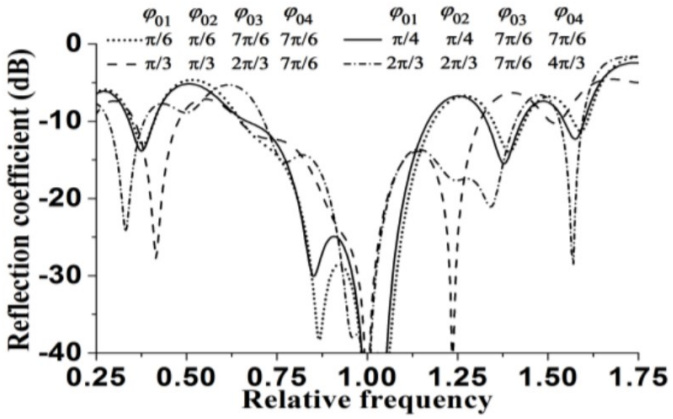

(c) Calculated results

Figure 2-4. Effects of distances between T-junctions on matching bandwidth proposed in [34]

2.1.2 Effects of Imperfect Isolation of Crossovers on Bandwidth of Butler Matrices

From the perspective of microwave networks, the merits of BMs entirely correspond to the major transmission characters, such as consecutively progressive phase differences, equal power division among output ports, and isolation between input ports. More clearly, the transmission characters

are utterly dependent on the performances of all components, which are couplers, phase shifters, and crossovers.

Generally, and intuitionally, the property of equal power distribution is supposed to be related to the couplers; meanwhile, the phase response looks more dependent on phase shifters. In contrast, crossovers are usually considered as structural devices rather than functional devices to serve the needs of topologic arrangement. Concretely, the perfect crossovers are expected to behave as two ideal transmission lines with an exchange of routes between the input and output ends.

In some reported research, various novel crossovers have been introduced [35] - [39] and applied to build BMs [38] - [42]. These crossovers have satisfying features at matching, isolation, and efficiency. Both return loss and isolation were better than 15dB covering a specific bandwidth, for example. Generally, they were qualified and quite competent, as independent components.

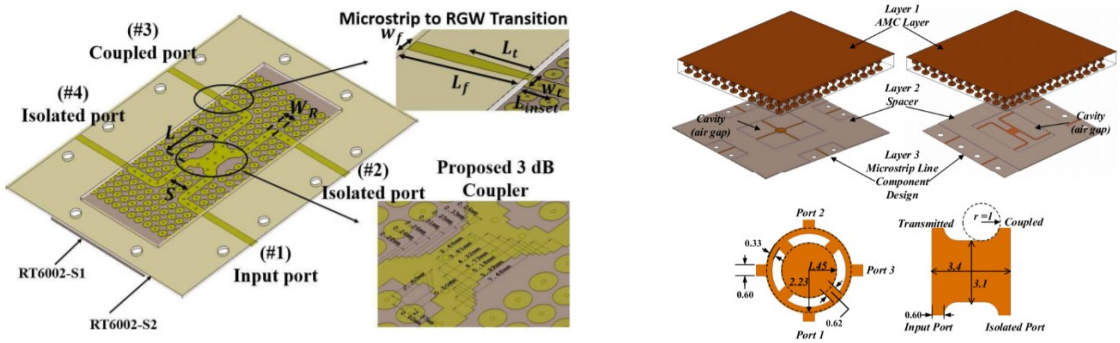

(a) Example proposed in [36] (b) Example proposed in [37]

Figure 2-5. Two examples of crossovers proposed in [36] and [37] for the application in BMs.

However, the imbalance of power division and the derivation of progressive phase differences can be found in almost all the designs of BMs, regardless of how excellent performances the couplers and phase shifters can achieve. On the other hand, the design and assessment of these crossovers were independent of the requirements and performance of the BMs, particularly without the

systematic consideration of their effects on BMs. For example, a quantitative evaluation of the relationship of the crossovers to BMs has not been derived.

Besides, it can be found from some work [10], [11], [19], [43] - [45] that the BMs with wideband characteristics and/or higher order than 4 × 4 are more likely to adopt multilayer structure to reduce or avoid the usage of crossovers. The reason is that when the number of crossovers in a BM notably increases, the overall performances of BMs will deteriorate unexpectedly because of crossovers, as well as the bandwidth will be obviously limited, even though wideband couplers and phase shifters have already been utilized.

The facts above imply that there is still some critical influence beyond hybrid couplers and phase shifters on BMs. In other word, crossovers might play a more critical role in BMs than just the structural components, and it has not been discussed and analyzed thoroughly.

2.2 Two-Dimensional Butler Matrices and Phase Shifters

2.2.1 Two-Dimensional Beamforming Networks

Though the conventional BMs are supposed to be applied on 1-D beam steering, there are many researchers who have presented the contributions of employing BMs for 2-D beam steering. Obviously, by involving BMs for 2D beam manipulation, the arrays could have more flexible functions and various versatilities, such as covering an area with a distinct shape or differentiating signals from different directions. Generally, the reported work of 2-D beamforming network-based BMs can be sorted into three types.

The most commonly reported method is adopting 4 × 4 BMs as the beamforming network to feed 2 × 2 planar arrays to produce four beams on the perpendicular two dimensions [46], [47]. For

example, a 4 × 4 BMs built based on substrate integrated waveguide (SIW) is constructed for a 2 × 2 magneto-electric (ME) dipole array to implement four-beam 2-D beam steering [46], as shown in Figure 2-6 (a) and (b).

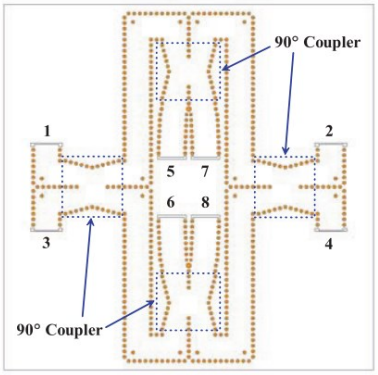

(a) Top view of BM in [46] for dual-polarized applications

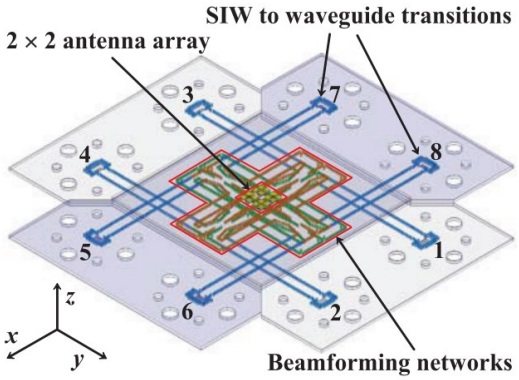

(b) 3-D view of BM in [46]

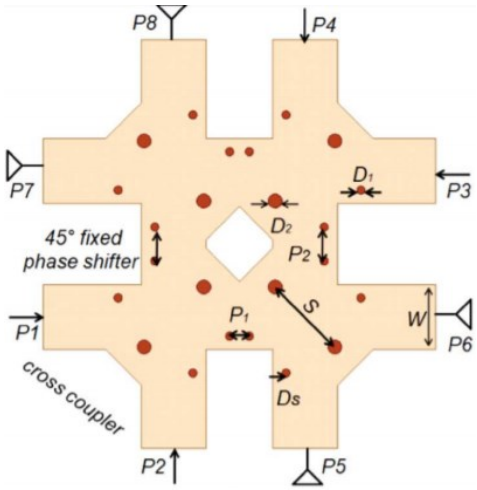

(c) Top view of BM in [47] driven by integrated phase shifter

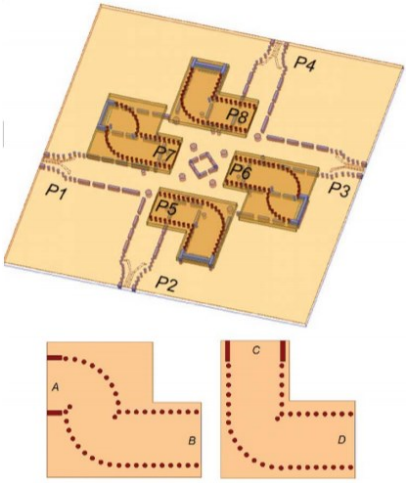

(d) 3-D view of BM in [47]

Figure 2-6. Examples of 2-D beamforming networks based on 4 × 4 BMs.

The most outstanding merit of this method is the structural simplicity due to no needs of crossovers. Consequently, the circuits can be very compact and concise and adopted on mm-wave applications. However, for sure, the insufficient beam number will also limit the potential of this scheme. To meet some demands that require more beams, the second method has been widely employed.

The second type solution to build higher-order 2-D beamforming networks is cascading two sets of stacked planar BMs as sub-beamforming networks into two perpendicular directions and connecting them successively. The schematic framework is demonstrated in Figure 2-7 and exemplified by a 16 × 16 2-D beamforming network composed of two sets of stacked 4 × 4 BMs. Some reported studies [48] - [50] are demonstrated in Figure 2-8.

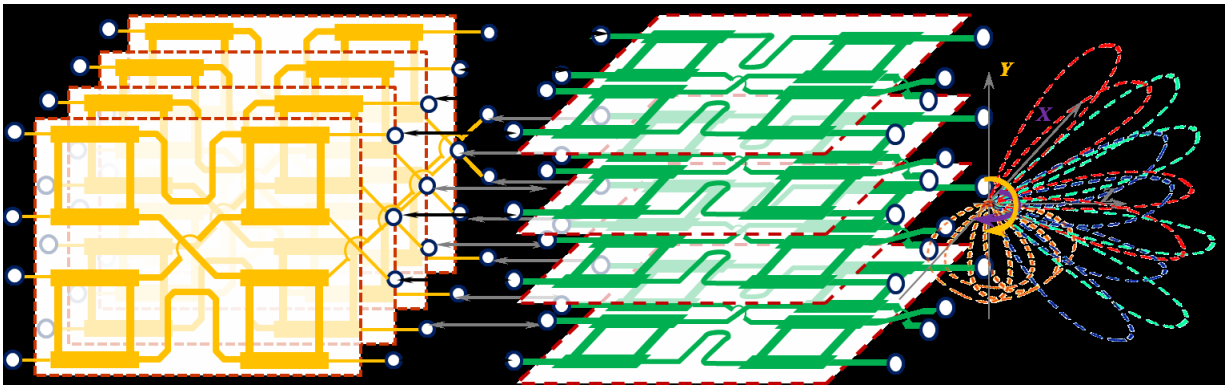

Figure 2-7. Schematic framework to build 2-D BM by two sets of conventional BMs with perpendicular configurations.

Two examples of 2-D beamforming network based on the second type method are [48], [49] are shown in Figure 2-8. Here, the circuit shown in Figure 2-8 (a) is based on grounded CPW; another one shown in Figure 2-8 (b) is based on multi-layer substrate-integrated waveguide (SIW). It can be found that the principle of this method is lucid and clear to understand. However, the structure is complex and complicated to design, assemble, connect, and adjust.

Besides the two methods mentioned above, which entirely based on the conventional BMs, there are a few schemes that made modifications to the designs for more flexible configurations, such as [51] - [53]. Some of them have been shown in Figure 2-9 and Figure 2-10.

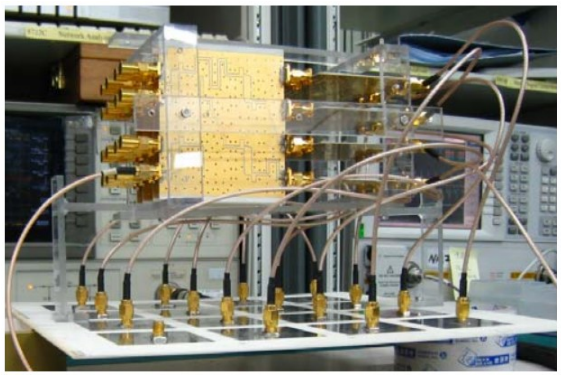

(a) Example prposed in [48]

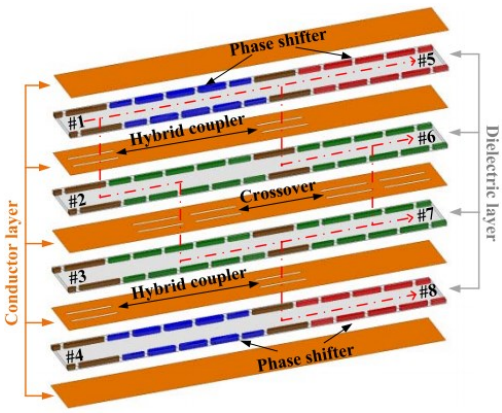

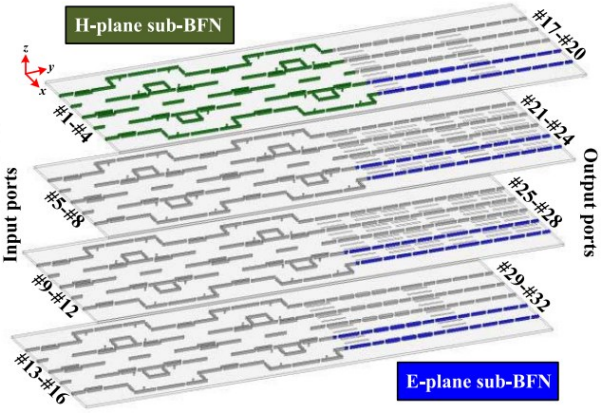

(b) Example prposed in [49] for the vertical coupling structure (c) Overall view of BM in [49]

Figure 2-8. Examples of 2-D beamforming network based on the second type method.

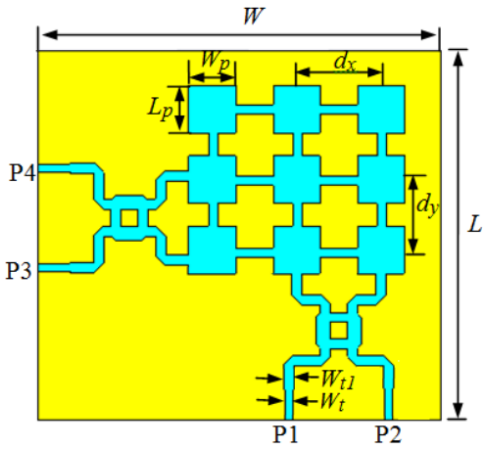

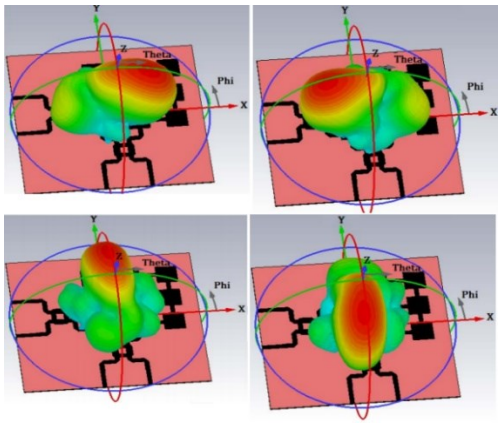

(a) Circuit layout (b) Radiation patterns

Figure 2-9. Scheme proposed by [50] to feed a 3×3 planar array for 2 × 2 beamforming.

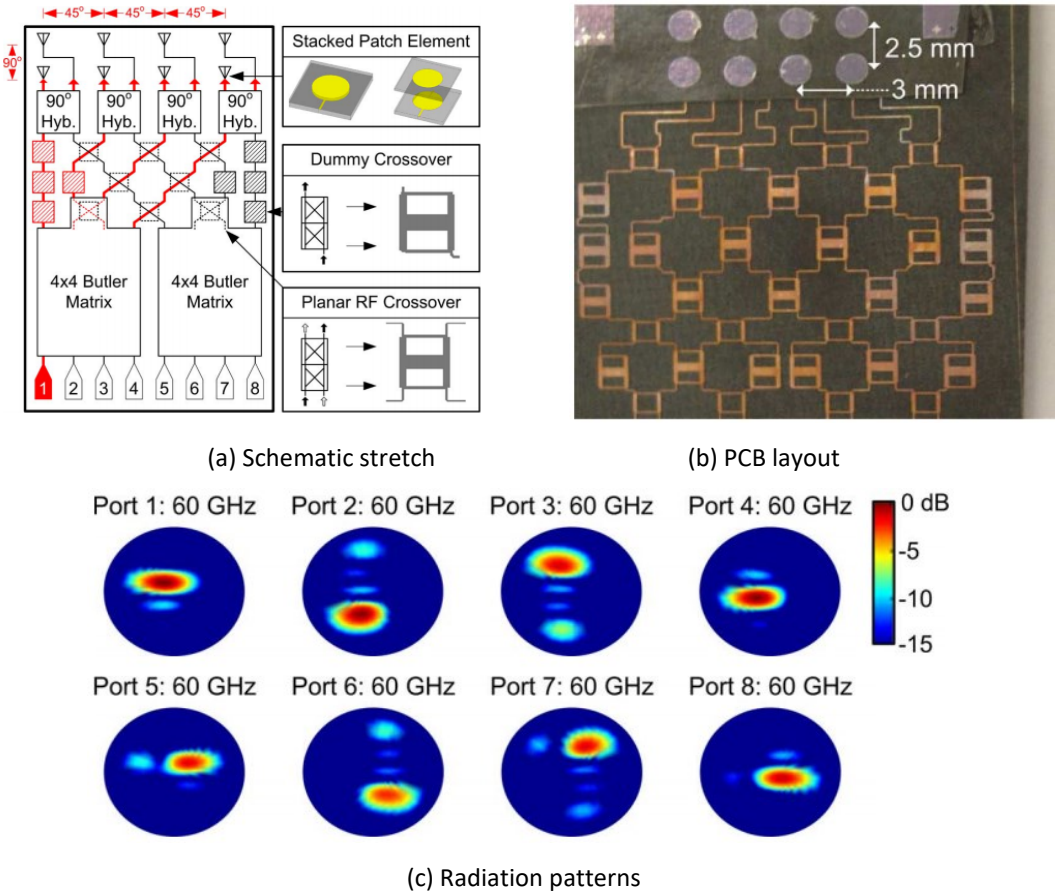

Figure 2-10. Scheme proposed by [51] to achieve 2 × 4 beam steering based on modified BM.

This method could be a balanced combination of beam number and circuit complexity. However, it can only be applied to some individual cases and not easily generalized to ordinary cases.

In summary, it can be found that most of the work of 2-D beam operations is based on the same principle and design method of the traditional BMs. Therefore, it has a limited number of input ports and output ports, such as 4 × 4 or 8 × 8, due to the structural complexity of BMs. The insufficient number of beams separated into two dimensions would lead to low resolutions on each dimension. Though there are some works with 16 × 16 configurations, the spatial framework and interconnections are required, or four-layer circuits are needed, which would cause complicated assembly and costly fabrications. Furthermore, the freedom of arranging the positions of all output

ports to fit the array elements is restricted because the plane of arrays is vertical to the plane of the BM circuits.

2.2.2 Phase Shifters

As demonstrated in Figure 2-20, with the increase of the beam number of BMs, the number of the required phase shifters with various phase shift values will drastically grow up. Therefore, the performance of the phase shifters will make an apparent impact on the BMs, especially for 2-D BMs or wideband BMs, which usually have relatively higher-order and require satisfying broadband features.

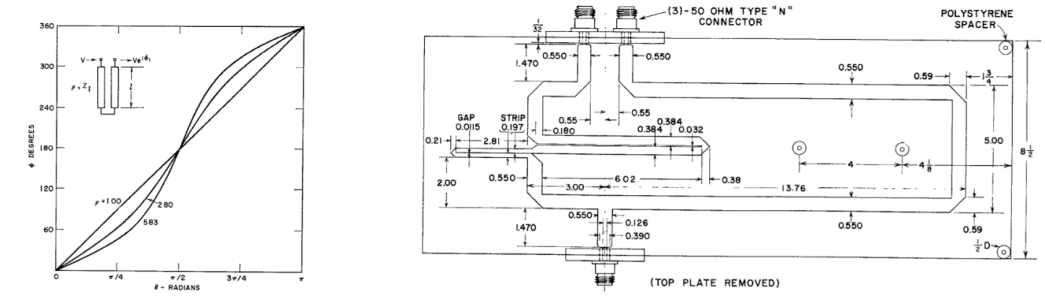

(a) Schiffman phase shifter [54]

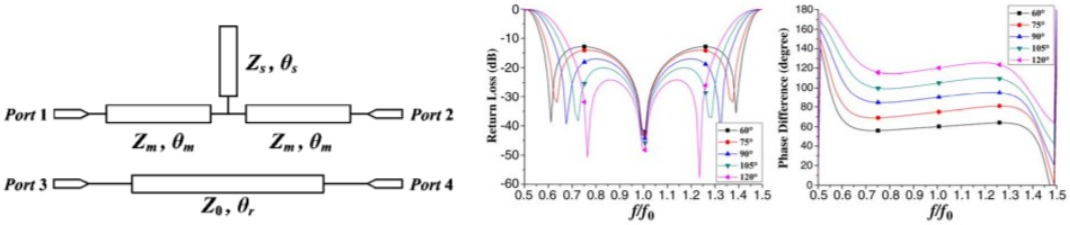

(b) Open-transmission line-loaded phase shifter [55]

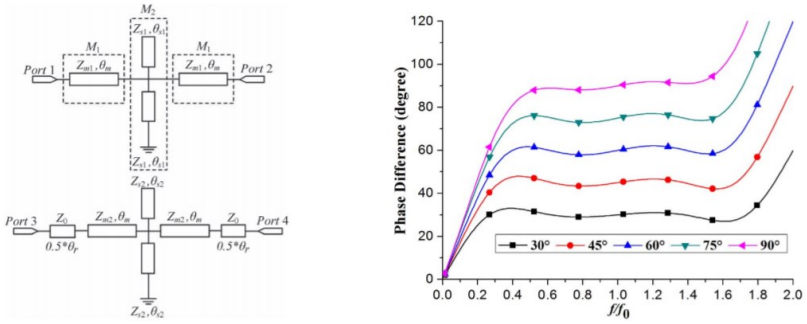

(c) A wideband phase shifter proposed in [56]

Figure 2-11. Commonly used phase shifter structures with circuits or typical performances.

The commonly used wideband phase shifters include Schiffman phase shifter [54], loaded transmission line phase shifter [55], and some others [56], as illustrated in Figure 2-11. All the wideband are the differential phase shifter, which needs a reference line with specific parameters working as a standard for the given value of phase shifting.

When two or more distinct phase differences are required on three or more paths, it could be challenging to implement because no reference line can work for two or more phase-shift values simultaneously.

2.3 Eight-Port Couplers and Applications

2.3.1 Eight-Port Couplers

Directional couplers are the necessary components in many microwave systems to implement the power distribution from certain input ports to some specific output ports while keeping the isolation between the input ports. Besides, the most commonly utilized four-port couplers, which have two input and two output ports, eight-port couplers are the crucial part to some microwave circuits, such as comparators, tracking radar systems and multi-beam forming networks, especially to the recently proposed two-dimensional Butler matrices [57], [58].

Therefore, the eight-port couplers have continuously been studied and improved in terms of performance, configuration, and the type of transmission lines used. In [59] and [60], the eight-port couplers with a ring-style structure and compact size are introduced with a satisfying performance of matching, isolation, the balance of power transmission, and bandwidth, as shown in Figure 2-12. However, four ports are confined in an isolated circular area by the closed circle composed of strips and slots in the designs.

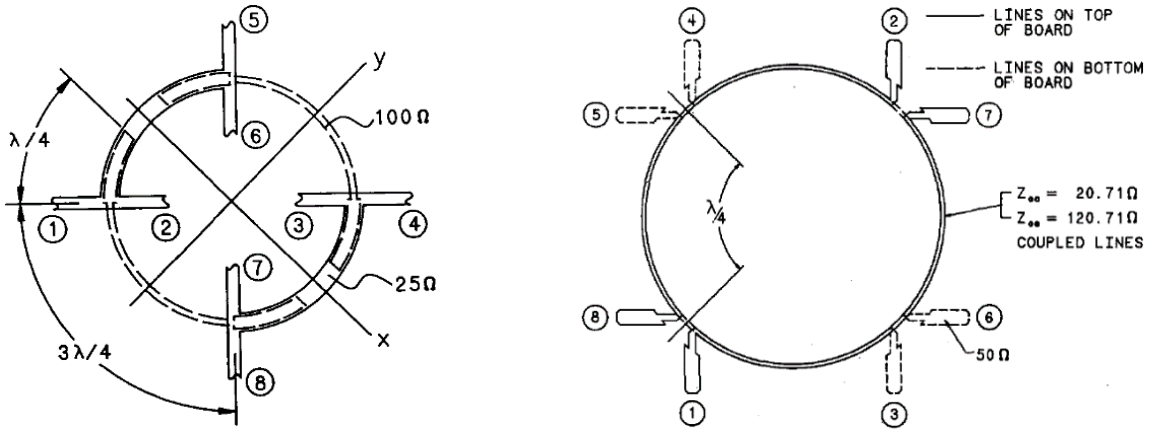

(a)Scheme proposed in [59] (b) Scheme proposed in [60]

Figure 2-12. Two schemes of eight-port couplers proposed.

Besides, in [61], a conventional eight-port coupler composed of four quadrature couplers based on microstrip line is proposed with the modification for bandwidth expansion. It has also been applied in [57] and [58] as the key components. This design has a satisfying performance, but the size is a little bit large when employed in a two-dimensional Butler matrix. Another design, [62], has similar properties, as well as the same deficiency. Both designs are illustrated in Figure 2-13.

In addition, two innovative eight-port forward-wave couplers with periodically patterned ground have been presented [63] and [64], which have the arbitrary coupling level and the wideband characters of matching and phase differences respectively, based on the four-mode method, as shown in Figure 2-14. They have f remarkable performance in terms of functionality, but the structural complexity (some junctions, coupling slots, and metalized vias), relatively large length (more the three guided wavelengths for 6-dB coupler case) and some high impedance lines (128 Ω) can be found. Consequently, they lack potential as a component of the greater scale network, especially for higher frequency usage.

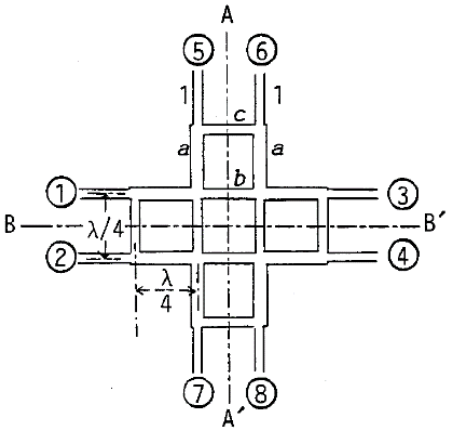

(a) Branch-line eight-port coupler proposed in [51]

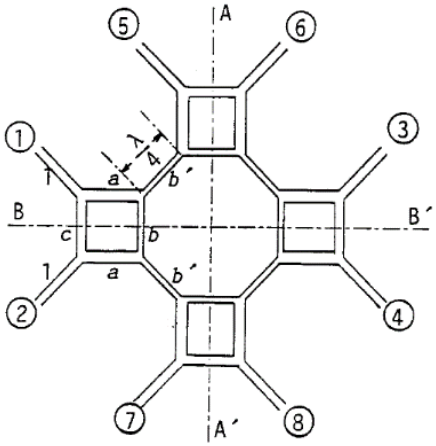

(b) Bandwidth enhancement method proposed in [51]

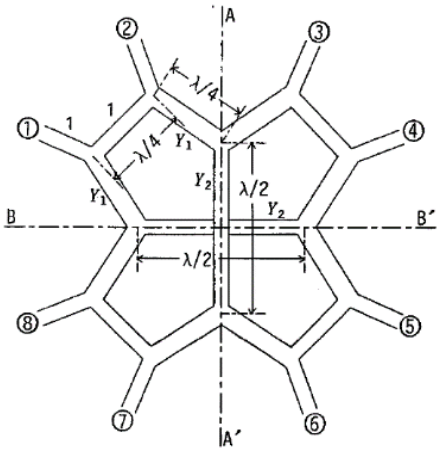

(c) Another form eight-port coupler proposed [62]

Figure 2-13. Branch-line type eight-port couplers.

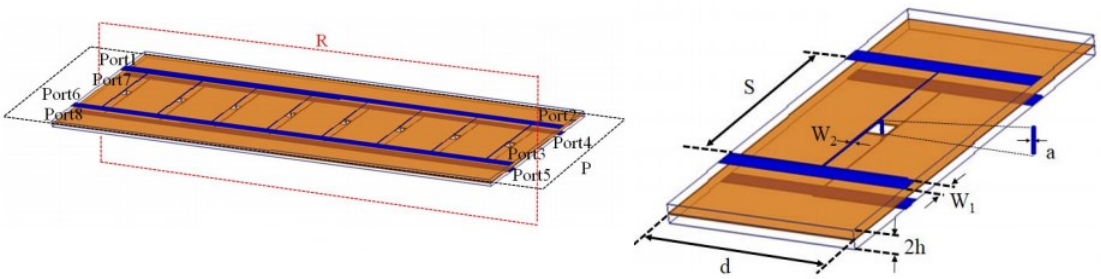

(a) Overall structure (b) View of unit cell

Figure 2-14. Broadband eight-port coupler with 6-dB coupling proposed by [63].

2.3.2 Comparators for Monopulse Array Based on Directional Couplers

The monopulse technique is an effective mechanism to detect the direction of arrival of a target and has been extensively studied and applied on tracking radars, satellite communications, automotive radars, etc. [65], [66]. As the crucial component in a feeding network of monopulse antenna array, the comparator can combine the signals from both sides of the array and rearrange them into the sum- and difference channels, which is also the fundamental difference from other conventional arrays.

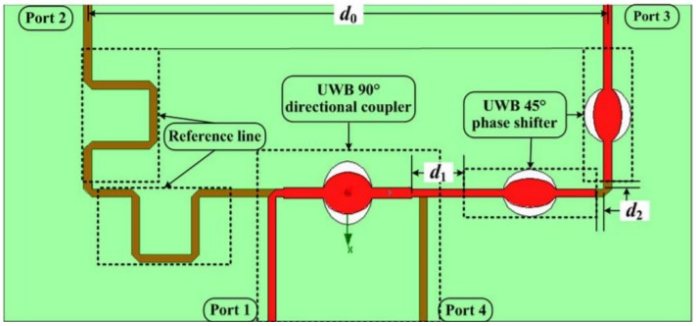

(a) Comparators based on magic-T [67]

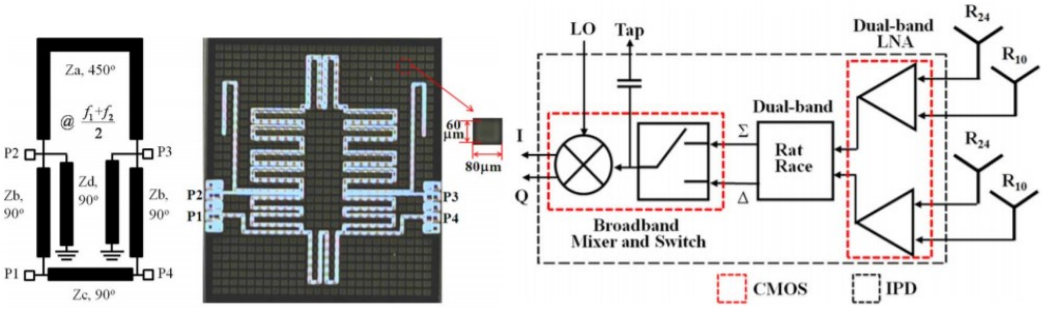

(b) Comparators based on rat-race coupler [68]

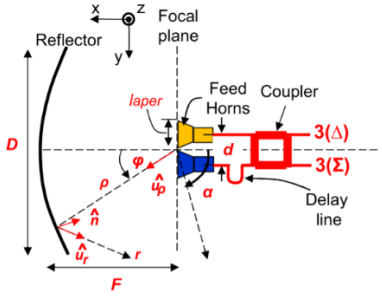

(c) Comparators based on quadrature coupler [69]

Figure 2-15. Examples of comparators based on different couplers for monopulse arrays.

Usually, a classical comparator for one-dimension and the single-polarized array can be achieved by a magic-tee [67], rat-race coupler [68], or quadrature coupler [69] which have relatively simple and compact structures, as demonstrated in Figure 2-15. It can be found that most of the comparators can be implemented by planar circuits.

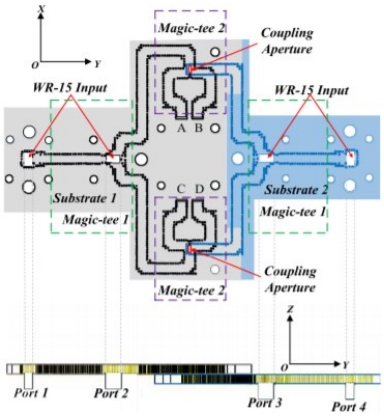

(a) RF part of the example of comparator reported in [71]

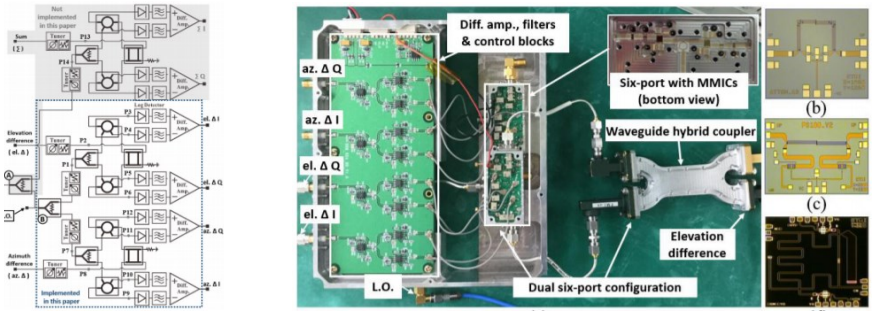

(b) Overall view of the example of comparator reported in [71]

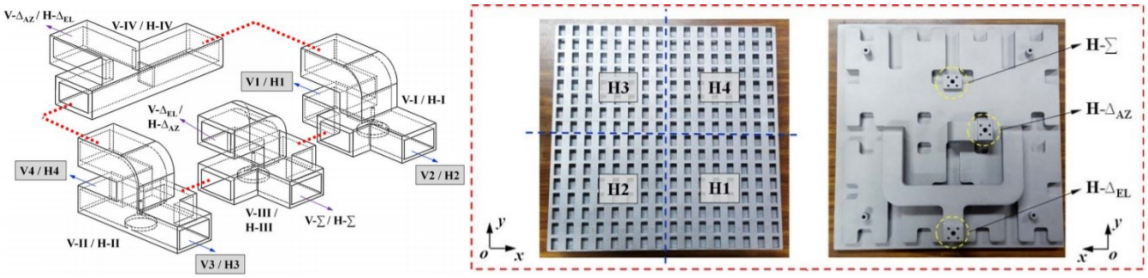

(c) Example of comparator reported in [75]

Figure 2-16. Examples of comparators for 2-D beam and/or dual-polarized monopulse array.

However, in some complicated and versatile tracking systems, the monopulse arrays with two-dimension and/or dual-polarized features are required, which demand more intricate comparators

[70] - [75]. Some of the examples are demonstrated in Figure 2-16 with schematic diagrams or photos.

It can be found that the 2-D and/or dual polarized comparators generally are built by the combination of several conventional couplers or magic-tees, and have relatively complex configurations, in terms of either its structural composition or functional blocks. Besides, they usually occupy a considerable area, which makes it difficult to integrate the comparators with the entire feeding network into the same planar circuit.

On another hand, in addition to the commonly employed four-port couplers [76], [77], which have two input and two output ports, eight-port couplers [59] - [62] could be an alternative competent. Due to the inherent advantages at more ports and lower structural complexity, the eight-port coupler has the potential to build functionally complex feeding networks with a concise configuration [78], [79].

2.4 Beam Number Extension and Structure Simplification

As one of the primary characters of the traditional BMs, the number of beams (or, number of input ports) must be equal to the number of array elements (or, the number of output ports) fed by the BMs. Besides, both numbers must be an integer power of 2, as introduced in Section 1.1. Obviously, this limits the flexibility of applying BMs in many situations where the beam number or element number is not 2^N.

According to the reported work, some researchers have developed many interesting and effective schemes and configurations to break the limitation of BMs order and number of ports and beams

[80] - [85]. As shown in Figure 2-17, the solution to expand the element number by adding some hybrids with specific output phase differences is proposed in [80].

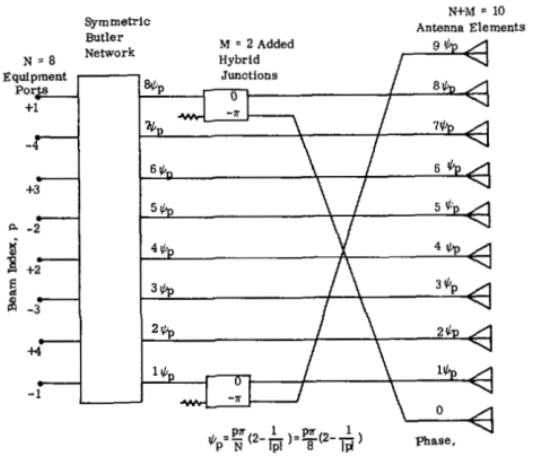

(a) Element number extension by extra power dividers

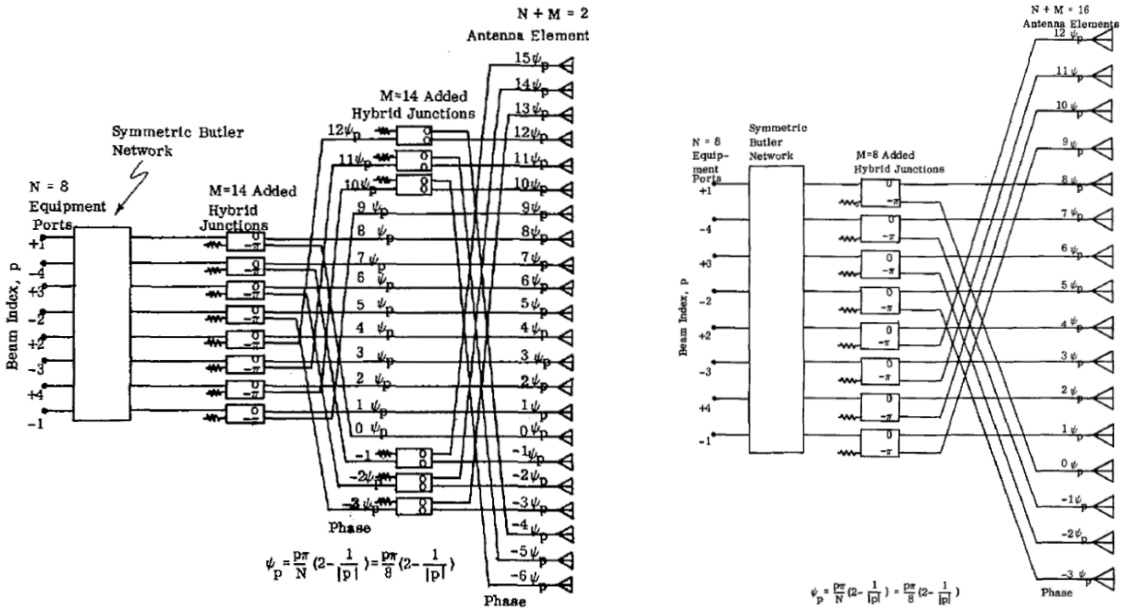

(b) Element number extension by two layers of couplers (c) Element number extended to double

Figure 2-17. Three examples of the scheme proposed by [80] to extend element number.

Theoretically, this scheme provides a comprehensive solution for BMs connected to an arbitrary number of elements. Some examples have been demonstrated in (a), (b), and (c) of Figure 2-17. Based on [80], some improved schemes have been presented in [81] and [82] to decrease the sidelobe levels by changing the ratio of power division among all output ports of BMs. The

schematic diagrams are demonstrated in Figure 2-18 to exhibit the mechanism and configuration, which are exemplified by the extended 4 × 4 Butler matrix. Through (a) and (b) of Figure 2-18, it can be found that some power dividers are inserted between antenna elements and traditional BMs for changing the weights of power distribution on elements. Especially to implement the element number expansion, an extra 180°-phase shift is required in the power dividers. It can also be achieved by rotating some elements by 180° physically.

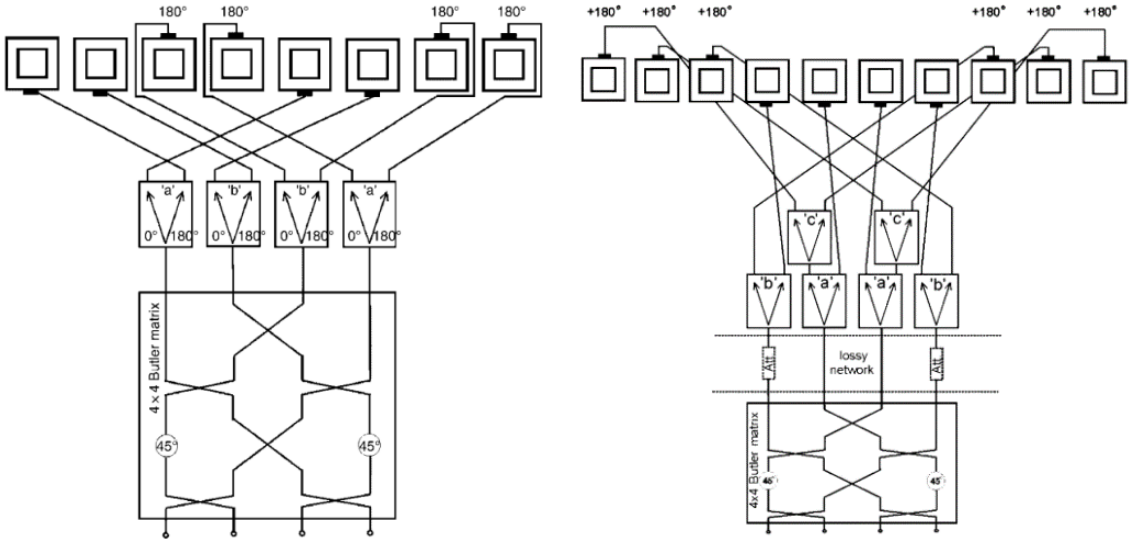

(a) Example of extending the element number [81] (b) Example of extending the element number [82]

Figure 2-18. Two examples of the scheme proposed by [81] and [82] to extend the element number and reduce sidelobe levels.

In addition, some researchers have tried to change the structures inside BMs to involve different properties of the beam and element number, such as [84] and [85]. In the reported work, two different schemes of 3 × 3 Butler matrices were introduced, respectively, as listed in Figure 2-19. The two designs provide similar properties to the conventional BMs, such as equal power distribution, spatially orthogonal beamforming, and theoretically lossless, but they can overcome the rule of beam and element numbers must be an integer power of two.

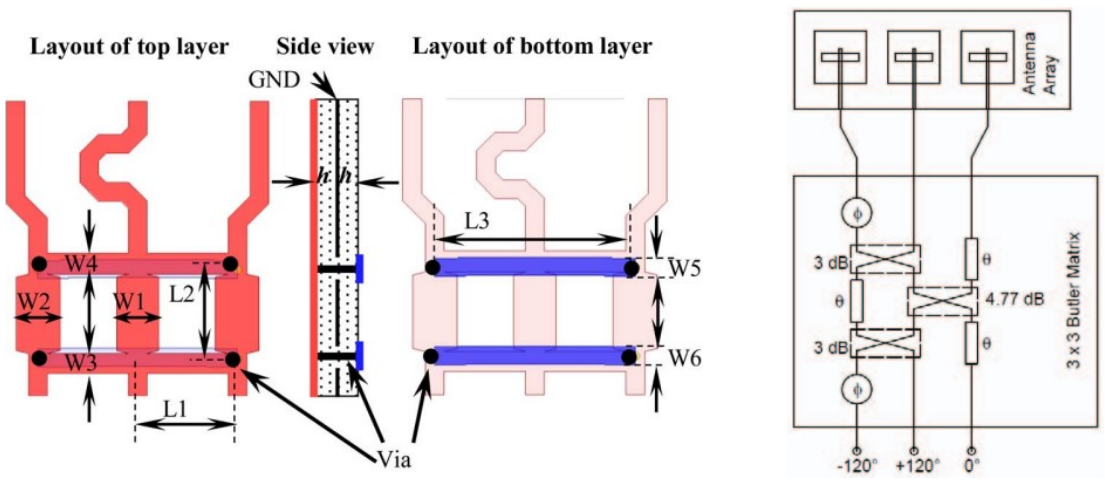

(a) Scheme proposed in [84] (b) Scheme proposed in [85]

Figure 2-19. Two schemes of 3 × 3 Butler matrices proposed by [84] and [85].

Besides the restriction on the beam and element numbers, other potential weakness of BMs is the drastically increasing number of components and structural complexity when the scale is growing. For easy and intuitional understanding of such complexity, one may compare the structures of 4 × 4-, 8 × 8-, and 16 × 16 BMs, as shown in Figure 2-20.

It is easy to image that if the complexity of conventional BMs can be effectively simplified, adopting higher-order BMs can meet the requirements with fewer numbers of beams and/or elements, though some element- and/or beam-ports may be combined or terminated by matching loads. For example, if a 7-element 5-beam MBFN is required, using 8 × 8 BM can meet the needs, but some ports may need to be combined together or terminated by matching loads. Therefore, configuration simplification can also be seen as an alternative solution to expand the adaptability and flexibility of BMs.

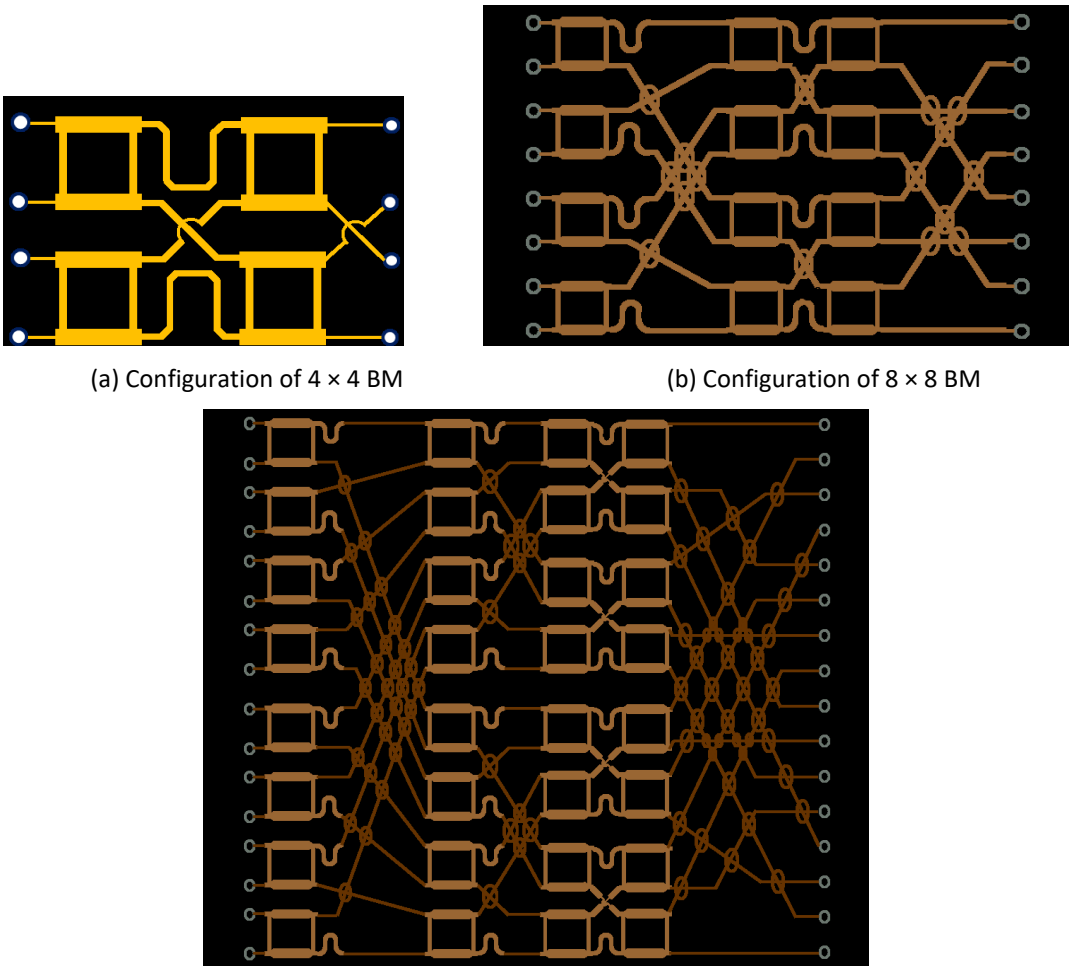

(a) Configuration of 4 × 4 BM

(b) Configuration of 8 × 8 BM

(c) Configuration of 16 × 16 BM

Figure 2-20. Comparison of complexity and numbers of components among 4 × 4- , 8 × 8- , and 16 × 16 BMs.

To achieve a better balance between complexity and capability, some fruitful efforts to simplify or diversify BMs have been reported [86] - [99]. For example, multilayer transmission line technologies [11], [86] - [91] can be applied to avoid using crossovers. In [86], [87], multi-section coupled-line couplers based on multi-layer microstrip lines were introduced and exploited in 4×4- and 8×8 BMs to broaden the bandwidth without using crossovers. The cross-sectional view of the couplers, the configuration of the 8 × 8 BM of [87], is illustrated in Figure 2-21.

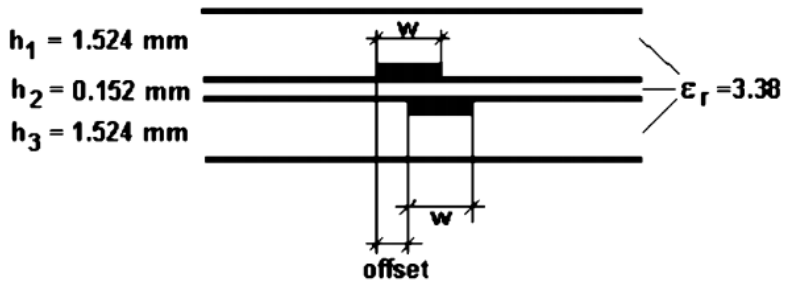

(a) Cross-sectional view of the stripline coupled lines in [87]

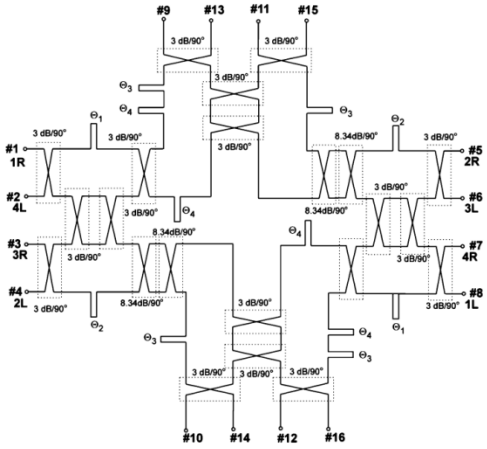

(b) Configuration of the 8 × 8 BM in [87]

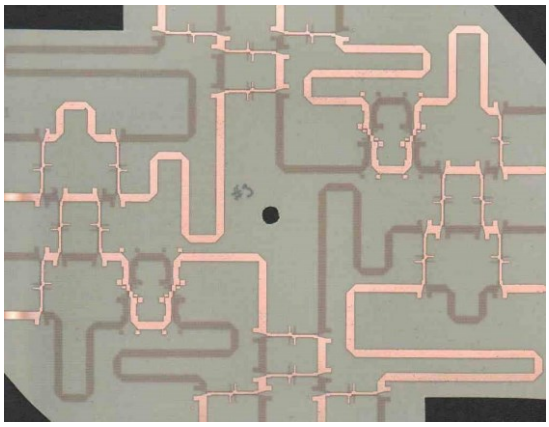

(c) Circuit in [87]

Figure 2-21. The stripline coupled lines, configuration of the 8 × 8 BM, and the example of [87].

For a similar intention, multilayer CPW technology [11], [89], was utilized in a 4×4 BM. Back-to-back microstrip line structure [11], [89], was also employed in 8×8 BMs, as shown in Figure 2-22.

Moreover, by applying the couplers with quasi-arbitrary phase differences [92] - [94], phase shifters can be removed in terms of appearance [95]. Based on this work, the progressive phase differences of BMs could be more flexible than the conventional ones by applying the coupler with phase difference different than 90° [96]. The two examples have been demonstrated in Figure 2-23. In Figure 2-23 (a), there are no 45° phase shifters in the 4 × 4 BM, but the features of the BM is the same as the conventional BMs. By contrast, the BM shown in Figure 2-23 (b) has a conventional structure, but the beam directions (progressive phase differences) are different than conventional BMs. Though the research in [92] - [96] can neither alter nor increase the numbers

of beams and elements, they effectively develop the diversity and flexibility of BMs and provide more possibility and potential for further improvement.

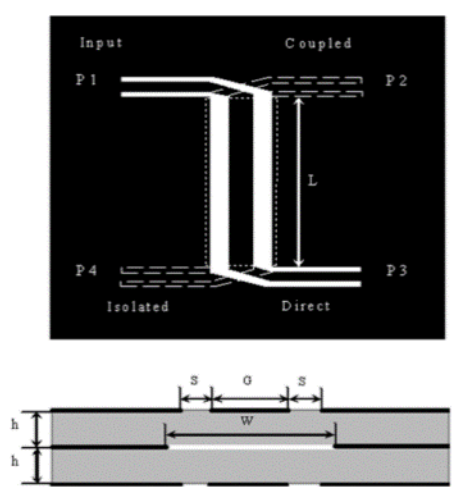

(a) Structure of CPW coupler in [11] and [89]

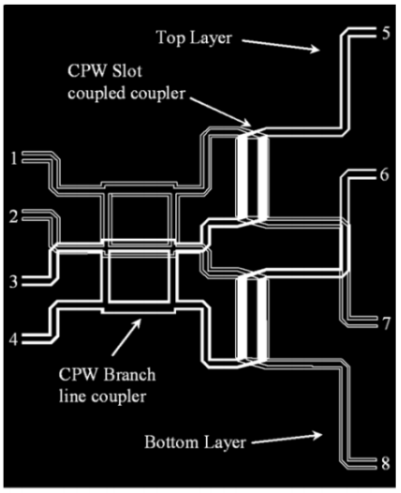

(b) Structure of CPW BM in [11] and [89]

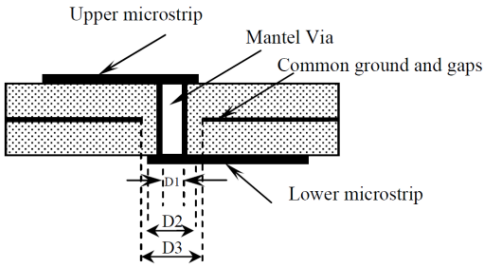

(c) Structure of vias proposed by [90]

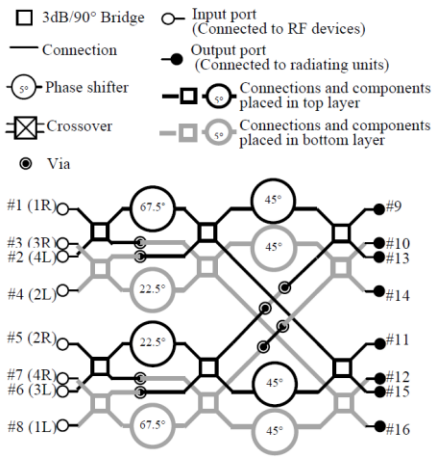

(d) Structure of BM proposed by [90]

Figure 2-22. Structures of CPW coupler and the BMs proposed by [11], [89], and structures of vias and the BMs proposed by [90].

In addition, combining additional phase-shifting devices with the traditional BM [98], [99] could be beneficial to extend the beam-steering ability, although it would not improve the intrinsic characteristics inside BMs.

The schematic diagram of the method proposed in [99] is shown in Figure 2-24. This scheme is the combination of phased arrays and BMs, and therefore have the advantages of relatively lower cost than phased arrays and higher resolution than BMs.

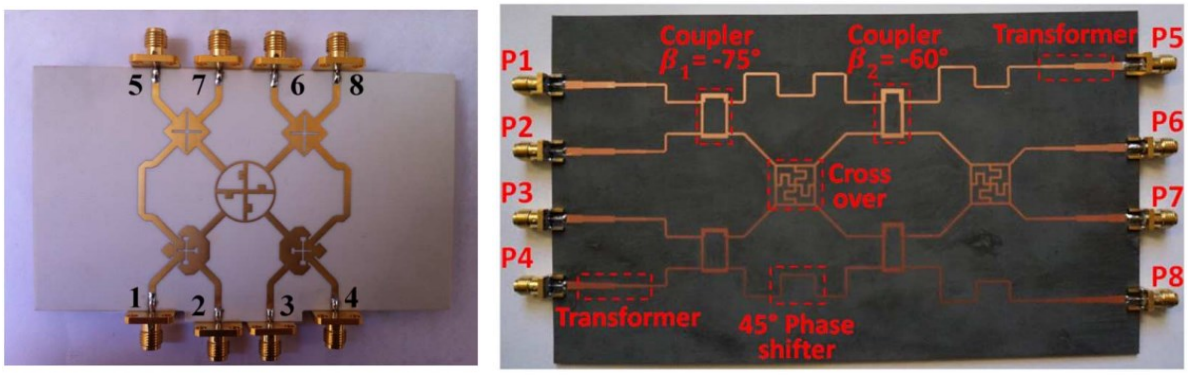

(a) Example of the BM without phase shifter [95] (b) BM with flexible, progressive phase differences [96]

Figure 2-23. Examples of the BM without phase shifter and the BM with flexible, progressive phase differences.

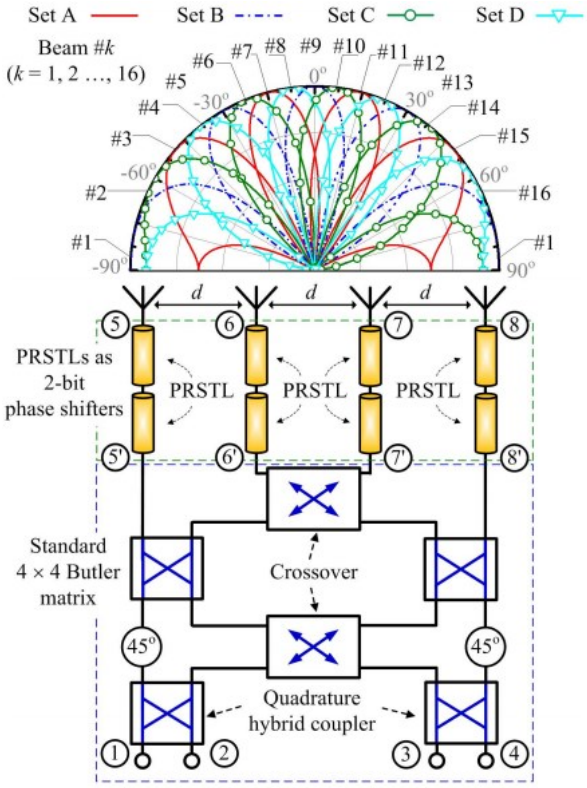

Figure 2-24. Scheme to extend beam based on 4 × 4 Butler matrix proposed by [99].

Chapter 3

Investigations about Effects of Components on Feed Networks

In this chapter, the effects of some components, such as T-junctions and crossovers, on the performance of the feeding network and BMs are discussed, analyzed, and experimentally verified. Consequently, the scheme to build a wideband feeding network is suggested.

Concretely, there are two parts presented in this chapter. First, the impacts of the distances of T-junctions on the matching bandwidth of uniform parallel feeding networks are investigated. Therefore, a scheme to build corporate feeding networks with several-octave fractional bandwidth is proposed with analytical explanation and experimental verification. Secondly, the effect of imperfect isolation of crossovers on the power divisions and phase differences of BMs is demonstrated by mathematical explanation and calculated results. Besides, it has been theoretically proved that the effort to offset the impacts by adopting asymmetrical couplers is insufficient. The conclusion is tested by a comparison of measurements of three BMs adopting different crossovers.

Some of the related work has been published in journal articles [100], [101] and conference paper [34].

3.1 Effect of Distances Between T-junctions on Parallel Feed Network

A feeding network is a necessary part of most antenna arrays to transfer and distribute the energy from the feed port to every element with the required power division and phase distribution. Especially, the parallel feed networks, or, corporate feed networks, have been extensively applied in many situations for broadband arrays and uniform amplitude distribution arrays due to some advantages than series-feeding structures, as described in Section 2.1.1.

Generally, the parallel-feeding networks are built based on the T-junctions as the fundamental and functional components. Consequently, the bandwidth of the networks is supposed to depend on the performance of T-junctions. Besides, it can usually be observed that the bandwidth of the antenna array is apparently narrower than the element. It is commonly ascribed to the mutual coupling between the nearby elements and the limited bandwidth of T-junctions.

However, according to our research, there is still another reason beyond the effect of individual T-junctions. To clarify the reason and reveal the sources of the effect, the impact of distances between T-junctions on the bandwidth is discussed and analyzed based on a simplified and ideal circuit model in this section. A set of recursive expressions is obtained to illustrate the reflection coefficient of the feeding network, which depends on some lengths of the transmission lines between the adjacent T-junctions. Through the numerical calculation, some rules can be revealed regulating these lengths, which distinctly change the bandwidth. Some concise rules are summarized for convenient to use, and one microstrip T-junction structure with flexible directions of branches is proposed for practical implementation.

3.1.1 Methodology

Without loss of generality, a sample of a typical 4×4 parallel fed array and its simplified circuit model are illustrated in Figure 3-1 to elaborate on the proposed principle.

Here, it is assumed that the feeding network and the elements are located at different layers. Besides, all the input impedance of the antenna elements, Z_{cell}, are 50 Ω at all frequencies, and, without the mutual coupling effect. All the transmission lines denoted by TL_T are $\lambda_g/4$ matching sections with 35.35 Ω characteristic impedance to achieve the impedance transformation from 25 Ω to 50 Ω. All the rest of the transmission lines that are denoted by TL_i are 50 Ω lines with various electrical lengths φ_i (at the central frequency, f_0). The node in the middle of each T-junction is numbered as N_i according to its stage from element to feed point, as shown in Figure 3-1 (b).

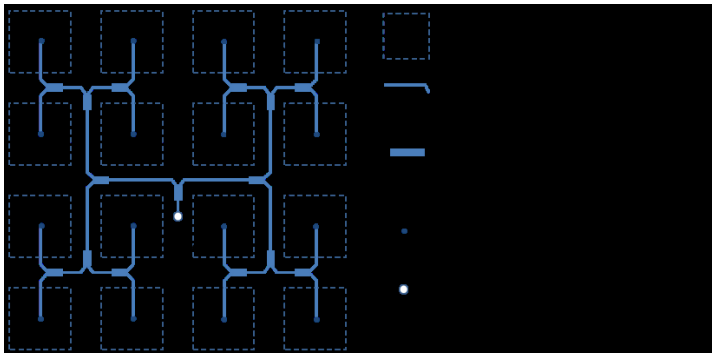

(a) 4×4 array with parallel-fed network

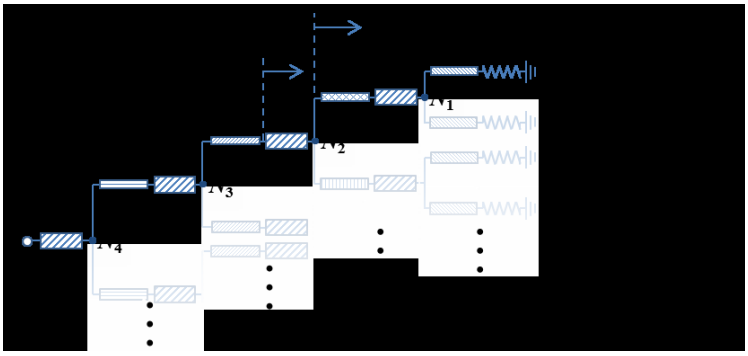

(b) Simplified ideal circuit model with related definitions

Figure 3-1. Example of a 4×4 array with parallel feed network and simplified ideal circuit model.

Due to the symmetry of the parallel feeding network, each branch from an element to the feed point must be identical to each other, which means that the definitions of Z_{cell}, TL_{T}, TL_i, φ_i, and N_i can be applied in each branch. Besides, if we define two input impedances, Z_{Li} and Z_{Ti}, at N_i and after the T-junction, respectively, as the instances of Z_{L2} and Z_{T2} shown in Figure 3-1 (b), we can obtain the recursive expressions (3-1) and (3-2) based on the *transmission line impedance equation*.

$$Z_{Li} = Z_{00}\frac{Z_{T(i-1)} + jZ_{00}\tan(\varphi_i f_r)}{Z_{00} + jZ_{T(i-1)}\tan(\varphi_i f_r)} \quad i = 1,2,3 \ldots \tag{3-1}$$

$$Z_{Ti} = \begin{cases} Z_{cell} & i = 0 \\ Z_{01}\dfrac{\frac{Z_{Li}}{2} + jZ_{01}\tan\frac{\pi f_r}{2}}{Z_{01} + j\frac{Z_{Li}}{2}\tan\frac{\pi f_r}{2}} & i = 1,2,3 \ldots \end{cases} \tag{3-2}$$

Here, Z_{00} is the characteristic impedance of T_{Li}, and usually, it is 50 Ω; Z_{01} is the characteristic impedance of T_{LT}, which is $\sqrt{2}T_{Li}/2$, and usually, it is 35.35Ω; f_r is the ratio of the given frequency to the f_0. In (3-2), the expression of $Z_{Li}/2$ comes from the parallel connection at the node of T-junction, which can produce half of the original impedance. We can find that the output impedance of the network, Z_{feed}, is equal to the Z_{Ti} when i is the maximum value, and the Z_{feed} depends on all φ_i. Through (3-1) and (3-2), the reflection coefficient of the network can be obtained at any frequency for any maximum value of i.

3.1.2 Calculated Results

Some reflection coefficients that are obtained from the numerical calculation are depicted in Figure 3-2 for exemplification and contradistinction. Here, the maximum value of i is 4, or it is a 4×4 parallel feeding network. We can see that when selecting the values of φ_{01} - φ_{04} without any rule, the reflection coefficient could be asymmetric in the frequency domain with respect to f_0. Moreover, the feed network has a limited bandwidth even though all elements have perfectly matching throughout all frequency bands.

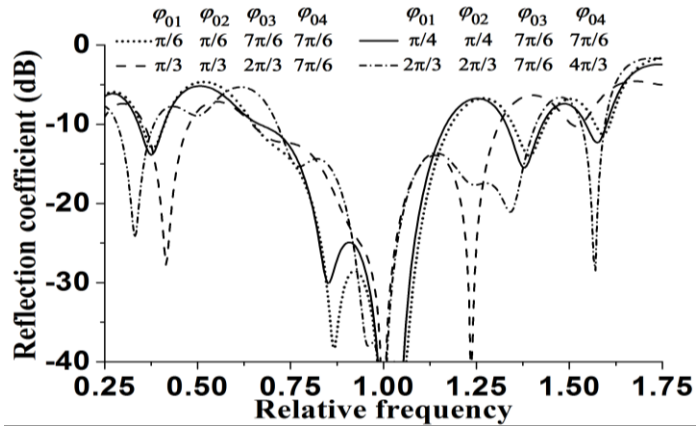

(a) Results without regulating the lengths

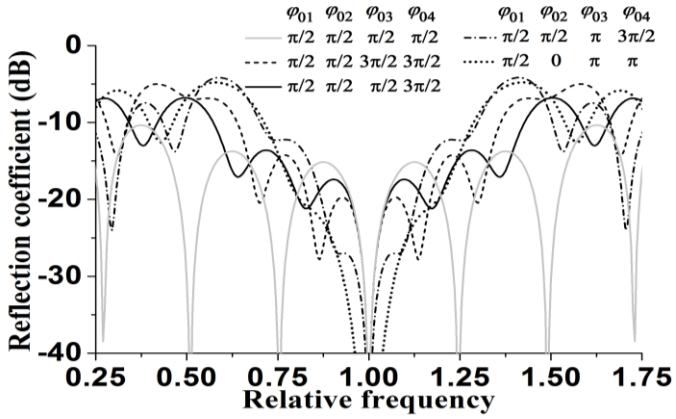

(b) Results with regulating the lengths

Figure 3-2. Reflection coefficient with / without regulating lengths.

In contrast, if we regulate the lengths of φ_{01} - φ_{04} as an integral multiple of $\pi/2$ at f_0, the reflection coefficient will behave in a symmetric fashion; and a satisfied bandwidth can be obtained as well. Especially, when the lengths of φ_i are odd multiples of $\pi/2$, at least a 50% relative wideband is expected, as shown in Figure 3-2 (b).

To implement the proposed regulation to transmission lines, the configuration of the parallel feed network needs to be rearranged, and the T-junction with flexible directions of branches could be required. The possible solutions for the feeding network and T-junctions are proposed and listed in Figure 3-3, which show that the lengths of φ_{01} - φ_{04} can be adjusted as shown.

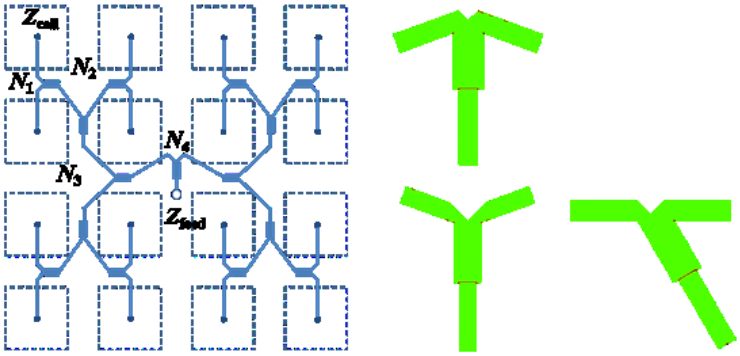

Figure 3-3. Possible configuration of parallel feeding network (left) and required T-junctions with flexible directions of branches (right).

3.2 Multi-Octave Bandwidth of Parallel-Feeding Network Based on Impedance Transformer Concept

Though the method to enhance the bandwidth of a parallel feed work by regulating the distances between T-junctions has been presented in Section 3.1, it may not easy to apply on some applications due to the limited space to arrange the network. However, more importantly, this research has revealed the potential feasibility to extend the matching bandwidth by treating the network as a whole rather than part by part.

As the further study, a procedure to obtain the parallel-feed network with octaves matching bandwidth for a uniform amplitude array is proposed in this section. The entire network is considered as a whole entity between the feed port and all elements to implement the impedance transformation. Furthermore, the concept of a multi-section impedance transformer is applied onto the whole to determine the structural parameters for specific bandwidth and reflection coefficient. For verification and demonstration, three examples based on the binomial, Chebyshev polynomial, and exponential taper transformers for 4 × 4 arrays are designed, and a better than 5:1 fractional bandwidth can be observed in the simulation results of all designs. Besides, the experimental

sample with tapered transmission lines is fabricated and measured. The satisfying agreement between simulations and measurements can be found. Theoretically, the method is expected to perform better with a large-scale network due to the long distance from the feed port to the element port on each path.

3.2.1 Methodology

3.2.1.1 Circuit Model of Parallel-Feeding Network

Here, we only concentrate on the feeding network itself without the impacts of the antenna element's characteristics. Thus, all elements are replaced by the ideal frequency independent load of real resistors. Further, all the effects of mutual coupling between branches of the feeding network, and all the discontinuities due to bends, steps, or junctions are ignored for the simplicity to introduce an ideal circuit model.

Based on the premises mentioned above, all branches in a parallel-feeding network, which start from the feed point and end at each element, will have entirely identical transmission properties to each other. Therefore, the network can be described as a circuit model with an exponentially increasing number of branches, as shown in Figure 3-4 (a) and (b). Without loss of generality, the feeding network and the circuit model are exemplified by a 4 × 4 square array in Figure 3-4.

Here, Z_{cell} is the resistance value of ideal resistors to substitute the antenna elements. It could be any real number value and not necessarily a 50 Ω; Z_{feed} is the required input impedance at the feed port, which is usually supposed to be 50 Ω. The numbers of N_i represent the ranking of each junction. A greater subscript means closer to the feed port of the network. Besides, the total number of elements is not necessary to be an integer power of two; just need to keep the uniformity on each branch.

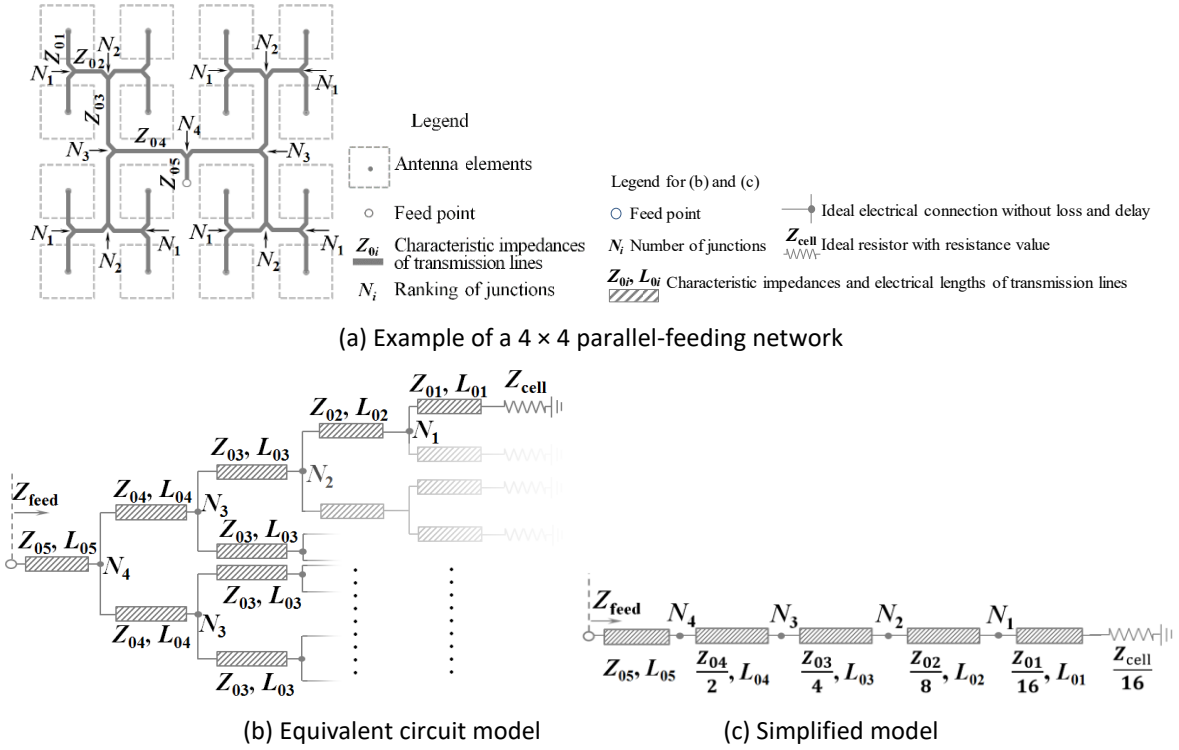

Figure 3-4. Demonstrations of traditional parallel-feeding network with equivalent circuit models.

If the concern is focused only on the impedance matching at the feed port, the circuit model can be simplified further as a single transmission line composed of several segments with respective characteristic impedances, as shown in Figure 3-4 (c). Concretely, each segment of the single transmission line has the same electrical length as the lines have the same two ranks of junctions in the network. The characteristic impedance of each segment needs to be divided by the number of branches between the same two ranks of junctions. The terminating resistor also needs to be divided by the number of elements.

The equivalent circuit model in Figure 3-4 (c) reveals the corresponding relations between the feeding network and the single transmission lines in terms of characteristic impedance and electrical lengths. It can consequently be adopted for network design through a reverse process. Moreover, the circuit model indicates that the network can be seen as an impedance transformer between the feed port and all elements.

3.2.1.2 Wideband Feeding Network Design based on Impedance Transformer

Assume that a parallel-feeding network is required for an *N*-elements uniform array (in-phase and uniform power distribution). Each of the elements has the same input impedance Z_{ele}; and, the input impedance Z_{in} is desired at the feed port of the network. Based on the discussion on the last section, the network can be acquired based on the equivalent impedance transformer between Z_{in} and Z_{ele}/N. The complete procedure to construct the proposed network will be introduced below.

We begin by estimating the total length of the equivalent impedance transformer to ensure it is longer than the distance of the path from one element to the feeding port. If we always route all branches along with the vertical and horizontal directions and placing the feeding port close to the central area of the array, the length should be the sum of the vertical and horizontal distances between a corner element and the feeding port of the network. A surplus length is acceptable because the position of feeding port can be moved on demand as the segment between N_4 and feeding port shown in Figure 3-5 (b).

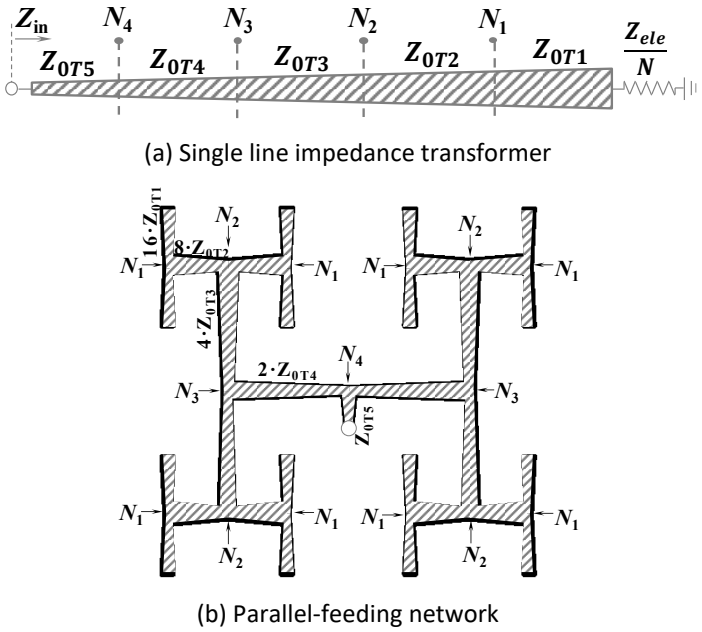

Figure 3-5. Design process from single line impedance transformer to parallel-feeding network.

Secondly, design the impedance transformer based on some design theories, such as binomial bandpass response, Chebyshev bandpass response, and exponential taper line [102]. Theoretically, an arbitrary relative bandwidth can be achieved in which the reflection is lower than any given value if choosing an adequate length. In other words, a large-scale feed network has the best potential to gain a wideband performance based on this scheme.

Finally, the network can be constructed through the reverse process mentioned in the last section, as illustrated in Figure 3-5 (b). To be specific, the transformer needs to be separated into many segments according to the series of lengths between two ranks of junctions in the network. Further, the characteristic impedance of each segment needs to be multiplied by the number of branches between the same two ranks of junctions. This design procedure is exemplified by a 4 × 4 square array in Figure 3-5.

Though the configuration of the proposed network in Figure 3-5 looks highly similar to the traditional one shown in Figure 3-4 (a), they have a definitely distinct bandwidth performance in terms of impedance matching. As the traditional networks just rely on a limited number of T-junctions independently and discretely located at the joining points to perform impedance transformation, the proposed network exploits a multi-section transformer composed of many more sections, or, sub-transformers, distributed everywhere on the whole network along each branch.

3.2.2 Examples and Results

3.2.2.1 Design Procedure

Three examples based on the impedance transformers with varied reflection responses will be designed for a 4 × 4 square array to demonstrate the procedure and illustrate the properties. The

three network types are based on binomial (maximally flat), Chebyshev (equal-ripple), and exponentially tapered line responses, respectively.

Suppose that both input impedances of the elements and the required at the feeding port are 50 Ω. The microstrip line structure will be applied in these examples as the transmission lines based on the laminate of thickness h = 0.524 mm and relative permittivity ε_r = 3.55. Besides, the distance between the antenna elements is a half wavelength in free space at the central frequency. Theoretically, the particular operating frequency, f_0, would not make an effect on the design process if the influence of discontinuities is ignored. It will be discussed in the next section.

It is easy to know that the minimum length from a corner element to the center of the 4 × 4 square array is about 1.5 λ_0 (free space wavelength) along the orthogonal directions, which is approximately 2.8 λ_g (guided wavelength). Hence, 3.0 λ_g is chosen in this case, or, 12 segments of quarter-wave sections.

According to the methods in [102], three multi-section impedance transformers between 50 Ω and 3.125 Ω (50Ω/16) can be realized with the binomial response, Chebyshev response, and exponential taper lines. For the Chebyshev transformer, the maximum ripple level of -25 dB in the passband is expected. The characteristic impedance of each section for the first two kinds of transformers are listed in Table I. For the tapered line transformer; the characteristic impedance is varying with positions, L, can be calculated by

$$Z_{0E}(L) = 3.125 \cdot e^{\frac{L \cdot \ln 4}{3\lambda_g}} \ (\Omega) \tag{3-3}$$

Here, $0 \leq L \leq 3\lambda_g$ and the end at $L = 0$ are connected to the elements and at $L = 3\lambda_g$ connected to the feed port of the network.

It should be explained that although some considerably low characteristic impedances can be found in Table I and expression (3-3) when L is close to 0, they would never appear in the real network. As these low characteristic impedances always are located near the end connected to the elements, they will be multiplied by a relatively higher number to build the parallel feeding network, as shown in Figure 3-5. In fact, at both ends close to the elements and the feed port, the characteristic impedances are generally approximated to 50Ω.

Table I Multi-section transformers characteristic impedances for binomial and Chebyshev responses

No. of sections	Characteristic impedance (Ω)	
	Binomial	Chebyshev
01	3.13	3.24
02	3.15	3.51
03	3.30	4.09
04	3.87	5.18
05	5.35	7.09
06	9.14	10.27
07	17.09	15.21
08	29.21	22.04
09	40.84	30.18
10	47.40	38.17
11	49.56	44.45
12	49.97	48.25

3.2.2.2 Results based on ideal transmission lines

The numerical calculation results of the reflection coefficient at the feed port of the networks based on the three distinct transformers are illustrated in Figure 3-6. In addition, the results from the traditional parallel network based on the quarter-wave transformer and T-junctions are exhibited together for comparison. In the traditional case, all T-junctions consist of two branches with 35.35Ω characteristic impedance and one branch with 50Ω.

The results obtained by the numerical calculation based on an ideal transmission line model, and without consideration of discontinuity between steps, bends, and junctions. As in the last section, all elements are substituted by ideal resistors with 50Ω resistance at all frequencies.

The series of curves in Figure 3-6 manifestly clarify the difference of the intrinsic matching properties from various networks, in terms of relative bandwidth. It should be remarked that the reflection of the traditional network will vary with the distances between T-junctions, as reported in [34]. In other words, any change of the network configuration would lead to a bandwidth alteration. By contrast, the other three networks based on impedance transformers have a relatively stable performance, which relies only on the conformity among all branches, regardless of the positions of elements and the shapes of routes.

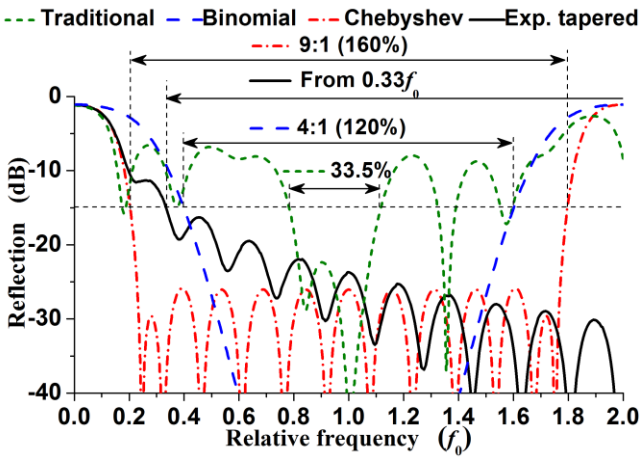

Figure 3-6. Numerical results of reflection performances from the parallel feeding network based on three distinct transformers and one traditional design.

Besides, a small disaccord of ripple levels can be found in the reflection of the network based on a Chebyshev response transformer in Figure 3-6. Because, the precondition to the analyses and design multi-section transformers is the theory of small reflections [102], which assumes that the discontinuity between adjacent sections can be ignored [(5.41) and (5.42) in 108]. In this case, some discontinuities may be greater than the limit value and therefore cause the error. However,

this deviation has limited influence, and it can be discovered and compensated by tuning the expected ripple level in practice.

3.2.2.3 Impact and Solution for the Discontinuity of Steps and Junctions

Heretofore, the discussion is limited to the ideal transmission line model for the generalized properties of the proposed network. It is also supposed to work well in low-frequency situations where the discontinuities between steps, junctions, and bends, can be approximately ignored [103], [104].

However, when the frequency is relatively high, the physical lengths of some sections may have comparable dimensions as the widths, and the parasitic effects from steps, bends, and junctions may notably affect the impedance matching. Two examples of the proposed network based on Chebyshev and binomial transformers are shown in Figure 3-7 to illustrate the configurations and dimensions. All the characteristic impedance of each section in the two networks is entirely the same as the data listed in Table I. The laminate of RO4350 with a thickness of 0.524 mm is used, and the operating frequency is 10 GHz.

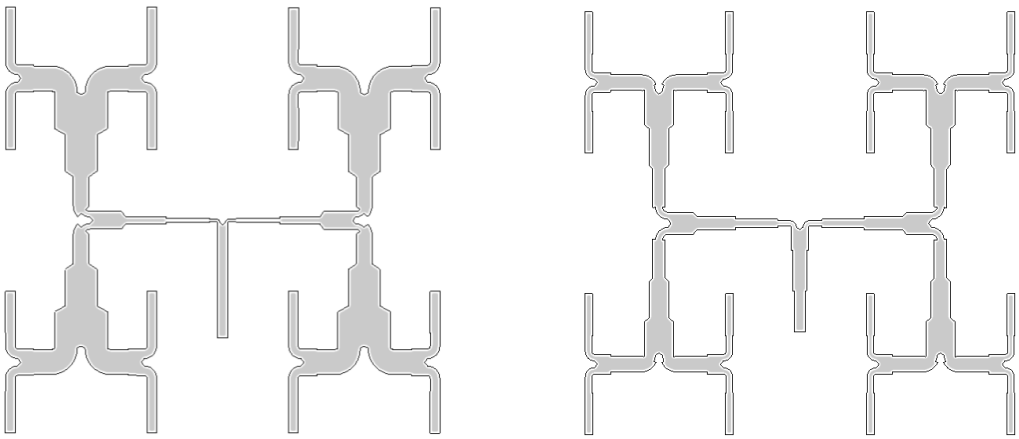

(a) Binomial (b) Chebyshev

Figure 3-7. Microstrip layouts of parallel feeding network based on binomial and Chebyshev properties.

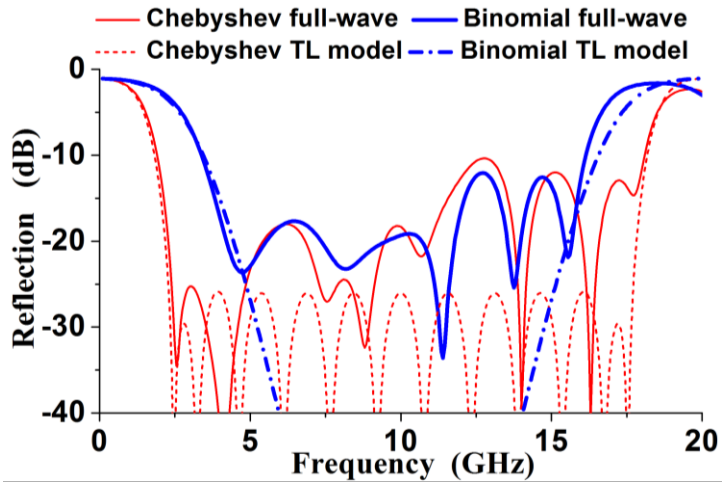

Figure 3-8. Reflection Coefficients from full-wave analysis and ideal transmission line model for the networks based on Chebyshev response and binomial response.

The full-wave analyses for both networks are with ANSYS HFSS in which the 16 terminals connect with ideal 50-Ω lumped resistors. In addition, the simulated results based on the ideal transmission line model are presented in Figure 3-8. Manifestly, when the frequency is lower than 5 GHz, the full-wave results agree well with the transmission line model. However, the effects of the discontinuities appear in high frequency. Though they may conduct better than traditional networks shown in Figure 3-7, a suggested solution could be necessary to apply this scheme to more extensive situations.

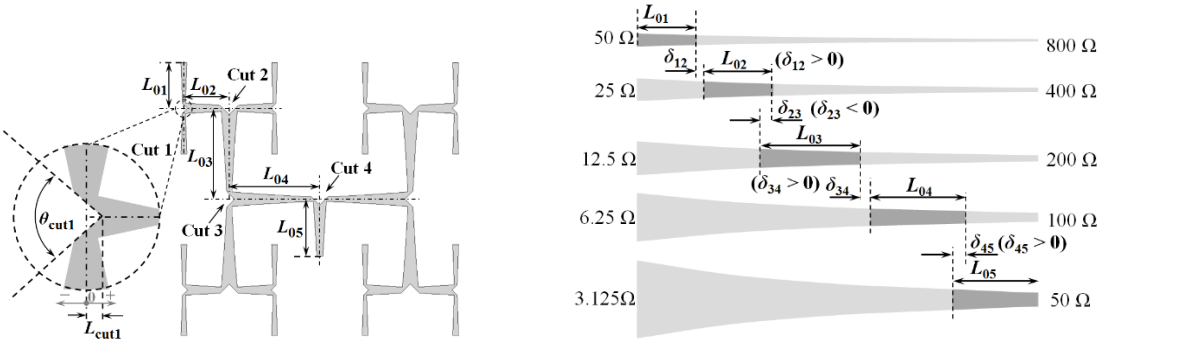

(a) Definitions for corner cut (b) Principle and definitions for changing characteristic impedances

Figure 3-9. Method to compensate for the effect of discontinuity from junctions.

To reduce the effect of the steps, an apparent solution is adopting exponential taper lines. Instead of steps, the gradually varying width would be useful in diminishing the parasitic impacts. Further, to decrease the influence of junctions, two methods for tuning are suggested, as shown in Figure 3-9. The first is a corner cut in the middle of each junction, as demonstrated in the locally enlarged view of Figure 3-9 (a); the two parameters, angle, and depth can be utilized to adjust the reflections. Secondly, changing the characteristic impedances at the starting points of each tapered branch can provide the freedom to compensate for the ambiguity of the electrical length of each branch, as demonstrated in Figure 3-9 (b).

Concretely, according to Figure 3-5 (b), each branch of the proposed network has an individual multiple characteristic impedance than the prototype of the transformer. It can be seen as several transformers, and each branch needs to pick a segment with the required length from each transformer, as shown in Figure 3-9 (b). Consequently, changing the starting point can equivalently be seen as a movement of the segment. We can use $\delta_{n\ n+1}$ to represent the relative movement between two adjacent branches and define relatively moving left as positive. In the ideal situation, all movements should be zero, which means no ambiguity of the electrical length is produced by the junctions and needs to be compensated.

Table II Design results after optimization

Variables	Values	Variables	Values
L_{cut1}	0.8 mm	δ_{12}	-1.1 mm
L_{cut2}	1.0 mm	δ_{23}	-1.1 mm
L_{cut3}	0.9 mm	δ_{34}	-1.1 mm
L_{cut4}	1.0 mm	δ_{45}	-1.1 mm
θ_{cut1}-θ_{cut4}	90°	-	-

The optimized parameters are listed in Table II, and the full-wave simulation results are displayed in Figure 3-10, with the results based on a transmission line model for comparison. It can be found

that a better than -15 dB reflections can be achieved in the frequency band higher than 2.8 GHz and covering more than 6:1 relative bandwidth. The transmission from the feed port to the elements is also exhibited in Figure 3-10. Due to the symmetry, the transmission to four elements in the corners represents the whole transmission property. Satisfying conformity among the transmission can be observed, and the maximum imbalance is lower than 0.8 dB. In addition, the loss due to the dielectric and radiation losses can be found to be not more than 2.0 dB through the bandwidth.

It should be noticed that although the exponentially tapered network has the theoretically infinite bandwidth when the frequency becomes higher, the effect of leakage from the microstrip line will inevitably rise, increase the loss, and exacerbate the matching. Thus, it is necessary to make sure that the thickness of the microstrip line can work properly at the highest required frequency.

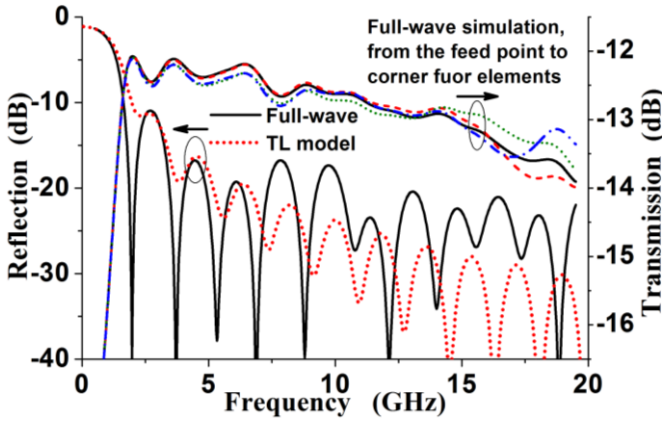

Figure 3-10. Full-wave simulation results of network after optimization with the result from ideal transmission line model.

3.2.2.4 Experimental Measurement Results

An experimental sample of the proposed parallel feeding network based on the design data list in Table II is fabricated and measured. The laminate of RO4350B with 0.254 mm thickness is utilized.

It should be noted that there is a significant difference between the circuit and the model in the previous simulation regarding the implementation of matching loads. In the previous simulation,

the ideal lumped resistors were used without the phase delay and other parasitic effects. However, in the real sample, some 50-Ω surface-mount chip resistors with 0402 package (1.0 mm × 0.5 mm) are adopted and connected between the network and ground plane through a pad with three metalized vias. All these physical structures can produce individual influences on the circuit in terms of the electromagnetic effects, especially at higher frequencies. In other words, the actual load on each end of the network is not an ideal 50-Ω resistance but a frequency-dependent complex impedance.

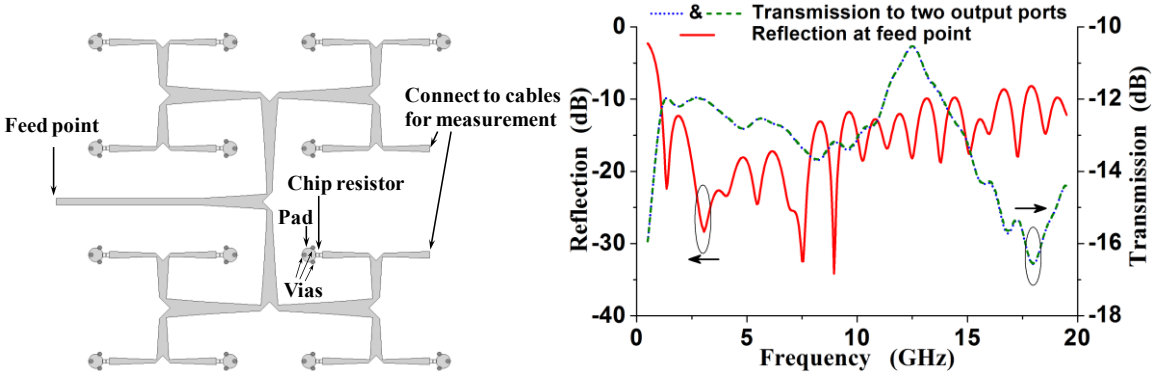

(a) Circuit layout of the network (b) Simulation results

Figure 3-11. Simulation results of reflection and transmission based on the loads with parasitic effect.

To evaluate the impact of parasitic effects of the components, pads, and vias, a model with these considerations is built for full-wave analysis by ANSYS HFSS, as shown in Figure 3-11 (a). It has entirely the same structure as the network shown in Figure 3-9 (a), but only a different form of loads. Concretely, the 14 terminals of the entire 16 ends are connected to the chip resistors, and the other two ends are joined to ports for monitoring the transmission, as indicated in Figure 3-11 (a).

The simulated results are shown in Figure 3-11 (b). Compared with the results in Figure 3-10, an obvious deterioration of the reflection can be perceived, especially when the frequency exceeds 10.0 GHz. Notably, in the band between 12 and 15 GHz, the transmission to the two ports is higher than the theoretical power division level, -12 dB. That means a critical mismatching occurred on

each of 14 ends, and then the equal power division has been destroyed; therefore, more energy transmitted to the two ports with the perfect matching. The mismatching can also lead to a resonance over the whole network and therefore exacerbates the radiation from microstrip lines. This result indicates that the chip resistor with a pad and vias can only provide acceptable performance when operating frequency is lower than 12.0 GHz, although there is still some parasitic effect.

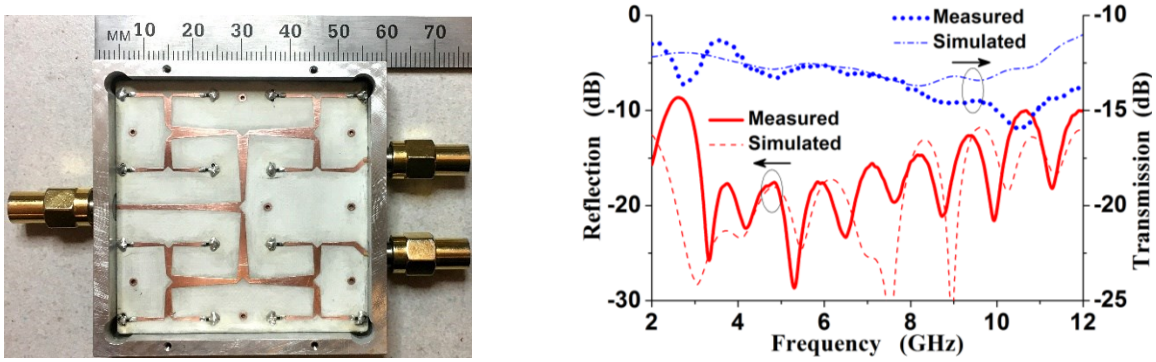

(a) Sample of the proposed network (b) Measured results

Figure 3-12. Sample of the proposed network and measured results of reflection and transmission.

The experimental circuit and the measurement results are exhibited in Figure 3-12 (a) and (b), respectively, and the simulated results shown in Figure 3-11 (b) are plotted with the measured for comparison. The test frequency bandwidth is from 2 GHz to 12 GHz according to the simulation results. A satisfying agreement between measured and simulated curves can be observed. Better than 3:1 fractional bandwidth can be achieved with reflection better than -15 dB. The loss is lower than 2.5 dB. It should be emphasized that the relative bandwidth of the sample is mainly restrained by the parasitic effect of the chip resistors, pads, and vias, as revealed by the comparison between simulations shown in Figure 3-10 and Figure 3-11.

3.3 Effects of Imperfect Isolation of Crossovers on Performance of Butler Matrices

As discussed in Section 2.1.2, generally, and intuitionally, the main properties of BMs, such as equal power distribution and progressive phase differences, are supposed to be related to the couplers and phase shifters. In contrast to this, crossovers are usually treated as structural devices rather than functional devices. For example, the perfect crossovers are expected to behave as two ideal transmission lines with an exchange of the route between the input and output ends.

However, according to the survey and analysis of some reported work, it has been found that there is still some critical influence beyond hybrid couplers and phase shifters on BMs. In other words, crossovers might play a more critical role in BMs than just the structural components, and it has not been discussed and analyzed thoroughly.

In this section, the effect on the power distribution and phase responses of BMs due to the imperfect isolation of crossovers is discussed and demonstrated by analytical expressions with numerical results. The expressions are derived through a forward-transmission circuit model, which is based on the scattering matrices of each component. Notably, the quantitative impacts resulting in the imbalanced power division and phase difference errors are illustrated by sets of curves with respect to the isolation between the branches of crossovers for the case of traditional 4 × 4- and 8 × 8- BMs. Besides, the investigation also indicates that the impact cannot be mitigated or compensated by adjusting the coupling coefficients or phase differences of couplers in the BMs. Three samples of 4 × 4 BMs with different isolations of crossovers were fabricated and tested for the verification. Satisfying agreement with the theoretical results can be observed.

3.3.1 Methodology

3.3.1.1 Circuit Models

To clarify the impact on the performance of a BM and differentiate the contribution of each component from others, a forward transmission circuit model is built and exploited to derive analytical expressions based on S-parameter matrices of the components. Here, the words, forward transmission, means that the focus is concentrated on the power division and phase differences on all output ports rather than the matching and isolation. In short, the emphasis will be on the forward transmission, which is the base to obtain the analytical expressions from the scattering matrices of the components.

Classical BMs are comprised of couplers, phase shifters, and crossovers, as shown in Figure 3-13, exemplified by 4×4- and 8×8 BMs with the individual components. The antenna ports of BMs start with "A"; the input ports start with "B." The round spot close to the coupler is used to signify the line between Port 1 and Port 2.

In this section, the framework of an 8×8 BM is the entire configuration with the sequential order at the antenna ports, and quantities of each kind of component can be calculated by [101, (1) and (2)]. The properties of each component are represented by S-parameters matrices $\mathbf{S}_{CP}$, $\mathbf{S}_{CR}$, $\mathbf{S}_{PH}$ for the coupler, crossover, and phase shifter, respectively. The last number on the subscript is employed to differentiate the distinct components of the same kind, such as $\mathbf{S}_{CP1}$ and $\mathbf{S}_{CP2}$.

The scattering matrix of the entire network is composed of several subnetworks in parallel, series, or cascade, which cannot directly be characterized by the scattering matrices of subnetworks, due to the complex internal reflections among subnetworks. However, if the amplitudes of backward transmission of subnetworks are much less than the forward transmission, the influence on the

forward transmission of the whole network would be negligible. Since part of the forward transmission is driven from the backward transmission, it will have about the square amplitude of the original backward transmission or higher. The principle is highly similar to the theory of small reflections but takes the backward isolation into account as well.

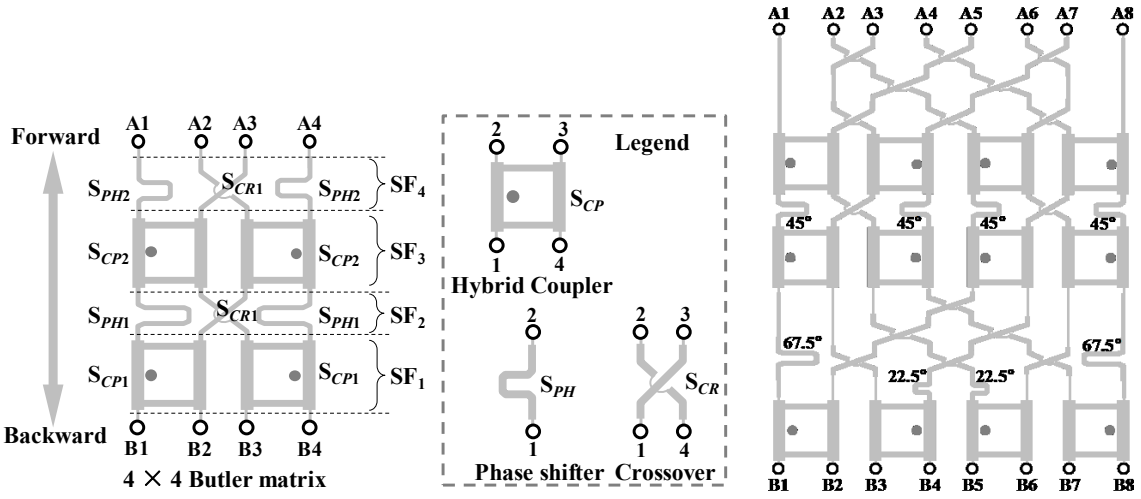

(a) 4 × 4 BM with components (b) 8 × 8 BM with the definitions of port numbers

Figure 3-13. Circuit models of BMs and components.

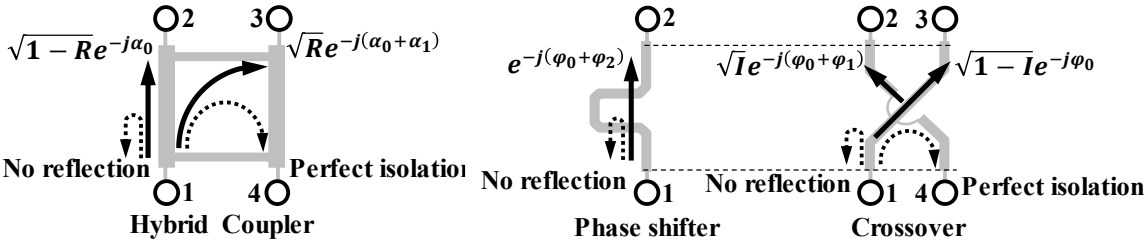

(a) coupler (b) phase shifter, and crossover

Figure 3-14. Partly simplified models to characterize the scattering matrices of coupler, phase shifter, and crossover.

As shown on the left side of Figure 3-13, two opposite directions, forward and backward, are defined according to the transmission from the RF circuits to the antenna arrays. In general, the components constructing BMs have more than the 15-dB difference between the magnitudes of the forward- and backward-transmission. Besides, the concern here is concentrated on the forward-transmission, as clarified earlier. Therefore, the backward transmissions of all components, such

as the reflections of the coupler, phase shifter, and crossover, and the backward coupling of the coupler and crossover, will be simplified as naught, as illustrated in Figure 3-14 (a) and (b) by dotted lines with an arrow. Here, the power transmission directions are exemplified by the cases of excitations at Port 1, and the solid lines with an arrow represent nonzero forward transmission; the dotted lines with arrow signify the zero-amplitude backward transmission.

Based on the premise and postulation, all components are lossless and reciprocal, $\mathbf{S}_{CP}$, $\mathbf{S}_{CR}$, and $\mathbf{S}_{PH}$ can be defined as below.

For the coupler, it is defined as (3-4).

$$\mathbf{S}_{CP} = \begin{bmatrix} 0 & \sqrt{1-R}e^{-j\alpha_0} & \sqrt{R}e^{-j(\alpha_0+\alpha_1)} & 0 \\ \sqrt{1-R}e^{-j\alpha_0} & 0 & 0 & \sqrt{R}e^{-j(\alpha_0+\alpha_1)} \\ \sqrt{R}e^{-j(\alpha_0+\alpha_1)} & 0 & 0 & \sqrt{1-R}e^{-j\alpha_0} \\ 0 & \sqrt{R}e^{-j(\alpha_0+\alpha_1)} & \sqrt{1-R}e^{-j\alpha_0} & 0 \end{bmatrix} \tag{3-4}$$

Here, R is the reciprocal of the coupling coefficient, which is less than 1; α_0 is the phase delay on through path; α_1 is the phase difference between through port and coupled port. For example, a typical 3-dB branch-line hybrid coupler has the properties that $R = 0.707$, $\alpha_0 = 90°$, and $\alpha_1 = 90°$.

For the phase shifter, it is defined as (3-5).

$$\mathrm{S}_{PH} = \begin{bmatrix} 0 & e^{-j(\varphi_0+\varphi_2)} \\ e^{-j(\varphi_0+\varphi_2)} & 0 \end{bmatrix} \tag{3-5}$$

Here, φ_0 is the reference phase delay on all other paths between the two reference planes, as the two dashed lines shown in Figure 3-14 (b); φ_2 is the expected phase shift value. For example, a typical 45° phase shifter can be described as $\varphi_1 = 45°$.

For the crossover, it is defined as (3-6)

$$\mathrm{S}_{CR} = \begin{bmatrix} 0 & \sqrt{I}e^{-j(\varphi_0+\varphi_1)} & \sqrt{1-I}e^{-j\varphi_0} & 0 \\ \sqrt{I}e^{-j(\varphi_0+\varphi_1)} & 0 & 0 & \sqrt{1-I}e^{-j\varphi_0} \\ \sqrt{1-I}e^{-j\varphi_0} & 0 & 0 & \sqrt{I}e^{-j(\varphi_0+\varphi_1)} \\ 0 & \sqrt{1-I}e^{-j\varphi_0} & \sqrt{I}e^{-j(\varphi_0+\varphi_1)} & 0 \end{bmatrix}. \tag{3-6}$$

Here, I is the reciprocal of the coupling coefficient to the unwanted path; φ_0 is the same as mentioned before; φ_1 is the relative phase shift on the unwanted path than the main path. For example, an ideal crossover should be $I = 0$ and $\varphi_1 = 0°$. For the same kind but distinct components, another new number will be added on the last of the subscript.

Then, the forward-transmission scattering matrix of the BM, $\mathbf{SF}_{\boldsymbol{BM}}$, can be defined as (3-7).

$$\begin{bmatrix} b_{A1} \\ b_{A1} \\ b_{A1} \\ b_{A1} \end{bmatrix} = \begin{bmatrix} SF_{BM}(1,1) & SF_{BM}(1,2) & SF_{BM}(1,3) & SF_{BM}(1,4) \\ SF_{BM}(2,1) & SF_{BM}(2,2) & SF_{BM}(2,3) & SF_{BM}(2,4) \\ SF_{BM}(3,1) & SF_{BM}(3,2) & SF_{BM}(3,3) & SF_{BM}(3,4) \\ SF_{BM}(4,1) & SF_{BM}(4,2) & SF_{BM}(4,3) & SF_{BM}(4,4) \end{bmatrix} \cdot \begin{bmatrix} a_{B1} \\ a_{B2} \\ a_{B3} \\ a_{B4} \end{bmatrix} \tag{3-7}$$

Here, a_{B1} - a_{B4} express the incident signals at the corresponding B1 - B4 ports; b_{A1} - b_{A4} express the output signals at the corresponding A1 - A4 ports. Due to the structural symmetry, we can obtain (3-8).

$$SF_{BM}(i,j) = SF_{BM}(5-i, 5-j) \quad (i,j = 1,2,3,4) \tag{3-8}$$

It is clear that (3-9)

$$\mathbf{SF}_{\boldsymbol{BM}} = \mathbf{SF_4} \cdot \mathbf{SF_3} \cdot \mathbf{SF_2} \cdot \mathbf{SF_1} \tag{3-9}$$

Here, $\mathbf{SF}_1$ - $\mathbf{SF}_4$ are the forward-transmission scattering matrices of each section in the BM, as illustrated in the left of Figure 3-13. They have similar port definitions and sequences as $\mathbf{SF}_{\boldsymbol{BM}}$.

According to the expressions of S-parameters of each component, they can be found as (3-10) - (3-13).

$$\mathbf{SF_1} = \begin{bmatrix} S_{CP1}(2,1) & S_{CP1}(2,4) & 0 & 0 \\ S_{CP1}(3,1) & S_{CP1}(3,4) & 0 & 0 \\ 0 & 0 & S_{CP1}(3,4) & S_{CP1}(3,1) \\ 0 & 0 & S_{CP1}(2,4) & S_{CP1}(2,1) \end{bmatrix} \tag{3-10}$$

$$\mathbf{SF_2} = \begin{bmatrix} S_{PH1}(2,1) & 0 & 0 & 0 \\ 0 & S_{CR1}(2,1) & S_{CR1}(2,4) & 0 \\ 0 & S_{CR1}(3,1) & S_{CR1}(3,4) & 0 \\ 0 & 0 & 0 & S_{PH1}(2,1) \end{bmatrix} \tag{3-11}$$

$$\mathbf{SF_3} = \begin{bmatrix} S_{CP2}(2,1) & S_{CP2}(2,4) & 0 & 0 \\ S_{CP2}(3,1) & S_{CP2}(3,4) & 0 & 0 \\ 0 & 0 & S_{CP2}(3,4) & S_{CP2}(3,1) \\ 0 & 0 & S_{CP2}(2,4) & S_{CP2}(2,1) \end{bmatrix} \tag{3-12}$$

$$\mathbf{SF_4} = \begin{bmatrix} S_{PH2}(2,1) & 0 & 0 & 0 \\ 0 & S_{CR1}(2,1) & S_{CR1}(2,4) & 0 \\ 0 & S_{CR1}(3,1) & S_{CR1}(3,4) & 0 \\ 0 & 0 & 0 & S_{PH2}(2,1) \end{bmatrix} \tag{3-13}$$

Substituting (3-9) - (3-13) into (3-8), the expressions for half of all elements of $\mathbf{SF}_{BM}$ can be obtained, as listed below.

$$\begin{aligned} BM(1,1) = {} & S_{CP1}(2,1) \cdot S_{PH2}(2,1) \cdot S_{CP2}(2,1) \cdot S_{PH2}(2,1) \\ & + S_{CP1}(3,1) \cdot S_{CR}(2,1) \cdot S_{CP2}(2,4) \cdot S_{PH2}(2,1) \end{aligned} \tag{3-14}$$

$$\begin{aligned} BM(2,1) = {} & S_{CP1}(3,1) \cdot S_{CR}(3,1) \cdot S_{CP2}(3,4) \cdot S_{CR}(2,4) \\ & + S_{CP1}(3,1) \cdot S_{CR}(2,1) \cdot S_{CP2}(3,4) \cdot S_{CR}(2,1) \\ & + S_{CP1}(2,1) \cdot S_{PH1}(2,1) \cdot S_{CP2}(3,1) \cdot S_{CR}(2,1) \end{aligned} \tag{3-15}$$

$$\begin{aligned} BM(3,1) = {} & S_{CP1}(2,1) \cdot S_{PH1}(2,1) \cdot S_{CP2}(3,1) \cdot S_{CR}(3,1) \\ & + S_{CP1}(3,1) \cdot S_{CR}(2,1) \cdot S_{CP2}(3,4) \cdot S_{CR}(3,1) \\ & + S_{CP1}(3,1) \cdot S_{CR}(3,1) \cdot S_{CP2}(3,4) \cdot S_{CR}(3,4) \end{aligned} \tag{3-16}$$

$$BM(4,1) = S_{CP1}(3,1) \cdot S_{CR}(3,1) \cdot S_{CP2}(2,4) \cdot S_{PH2}(2,1) \tag{3-17}$$

$$\begin{aligned} BM(1,2) = {} & S_{CP1}(2,4) \cdot S_{PH2}(2,1) \cdot S_{CP2}(2,1) \cdot S_{PH2}(2,1) \\ & + S_{CP1}(3,4) \cdot S_{CR}(2,1) \cdot S_{CP2}(2,4) \cdot S_{PH2}(2,1) \end{aligned} \tag{3-18}$$

$$\begin{aligned} BM(2,2) = {} & S_{CP1}(3,4) \cdot S_{CR}(3,1) \cdot S_{CP2}(3,4) \cdot S_{CR}(2,4) \\ & + S_{CP1}(3,4) \cdot S_{CR}(2,1) \cdot S_{CP2}(3,4) \cdot S_{CR}(2,1) \\ & + S_{CP1}(2,4) \cdot S_{PH1}(2,1) \cdot S_{CP2}(3,1) \cdot S_{CR}(2,1) \end{aligned} \tag{3-19}$$

$$\begin{aligned} BM(3,2) = {} & S_{CP1}(2,4) \cdot S_{PH1}(2,1) \cdot S_{CP2}(3,1) \cdot S_{CR}(3,1) \\ & + S_{CP1}(3,4) \cdot S_{CR}(2,1) \cdot S_{CP2}(3,4) \cdot S_{CR}(3,1) \\ & + S_{CP1}(3,4) \cdot S_{CR}(3,1) \cdot S_{CP2}(3,4) \cdot S_{CR}(3,4) \end{aligned} \tag{3-20}$$

$$BM(4,2) = S_{CP1}(3,4) \cdot S_{CR}(3,1) \cdot S_{CP2}(2,4) \cdot S_{PH2}(2,1) \tag{3-21}$$

Another half of the elements can be acquired from (3-14) - (3-21) through (3-8).

3.3.2 Examples and Results

3.3.2.1 Numerical Results

Based on the analytical expressions, the effects of each element on BMs performance, especially crossover, can be quantitatively investigated. To survey the influences only from the forward coupling of the crossover, it is assumed that all couplers and all phase shifters in a BM have the ideal performances. Concretely, in the 4×4 BM, for the coupler of $\mathbf{S}_{CP1}$, $R_1 = 0.707$, $\alpha_{01} = 90°$, α_{11}

= 90°; for the coupler of $\mathbf{S}_{CP2}$, $R_2 = 0.707$, $\alpha_{02} = 90°$, and $\alpha_{12} = 90°$; for the phase shifters of $\mathbf{S}_{PH1}$ and $\mathbf{S}_{PH2}$, $\varphi_{21} = 45°$, $\varphi_{22} = 0°$. Besides, the two crossovers are supposed to have identical properties, and $\varphi_1 = 0$; in the 8×8 BM, all couplers have the same features as $\mathbf{S}_{CP1}$; all phase shifters have the delays as indicated in Figure 3-12 (b).

The effects on power divisions and phase differences of 4×4- and 8×8 BMs due to the limited isolation of crossovers are listed in (g) Power division when B2 is excited in 8×8 BM (h) Phase differences when B2 is excited in 8×8 BM

Figure 3-15. Here, the cases when 4×4 BM's B1 is excited are shown (a) and (b); the cases when B2 is excited are shown (c) and (d); the cases when 8×8 BM's B1 is excited are shown (e) and (f); the cases when B2 is excited are shown (g) and (h); the isolation is defined as the ratio between the amplitudes of the output on the unwanted path and the total incident signal, which is the reciprocal of I used in (3-6). The phase difference between adjacent ports, Ai and A(i+1), for example, is represented as $\Delta\varphi i$.

Overall, if the isolation increases to a high enough value, such as 50 dB, the BMs will achieve the perfect theoretical performance, just like what is indicated in the right ends of all graphs of (g) Power division when B2 is excited in 8×8 BM (h) Phase differences when B2 is excited in 8×8 BM

Figure 3-15. Concretely, in (g) Power division when B2 is excited in 8×8 BM (h) Phase differences when B2 is excited in 8×8 BM

Figure 3-15 (a) and (c), the power divisions of the 4×4 BM will be close to -6 dB when either B1 or B2 is excited; in (g) Power division when B2 is excited in 8×8 BM (h) Phase differences when B2 is excited in 8×8 BM

Figure 3-15 (b) and (d), the consecutive phase differences will be -45° or 135°, respectively; in 8×8 BM, the power division will be -9 dB, and the phase differences will be -22.5° or 157.5°. However, the effects on BM will be considerably apparent when the isolation is limited, even though the value is acceptable in terms of usual criteria, such as 20 dB.

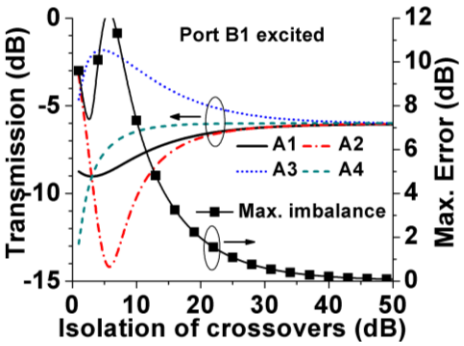

(a) Power division when B1 is excited in 4×4 BM

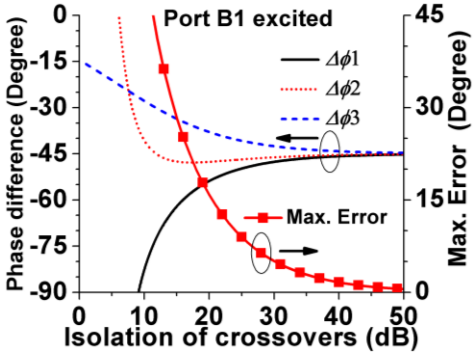

(b) Phase differences when B1 is excited in 4×4 BM

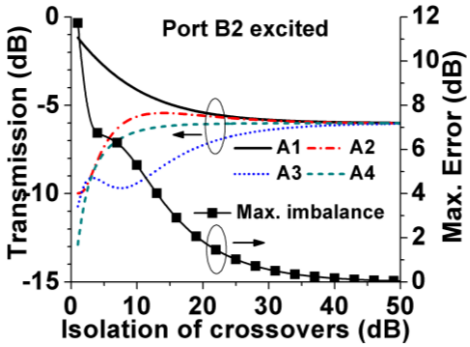

(a) Power division when B2 is excited in 4×4 BM

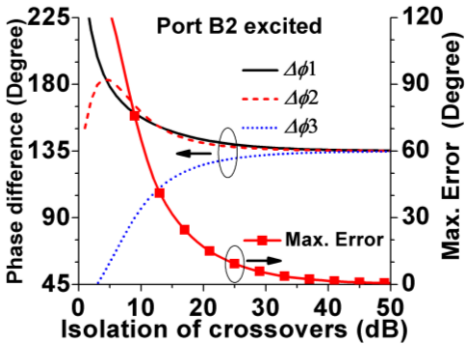

(b) Phase differences when B2 is excited in 4×4 BM

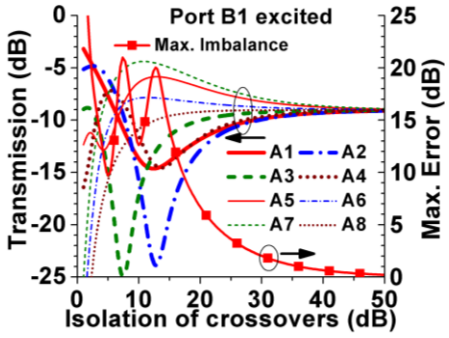

(e) Power division when B1 is excited in 8×8 BM

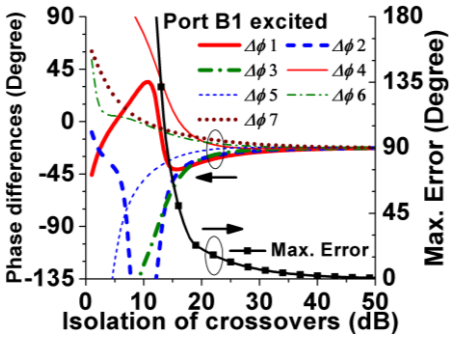

(f) Phase differences when B1 is excited in 8×8 BM

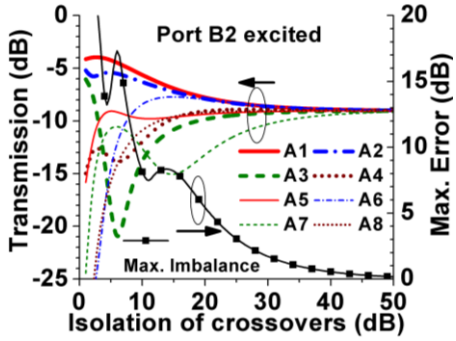

(g) Power division when B2 is excited in 8×8 BM

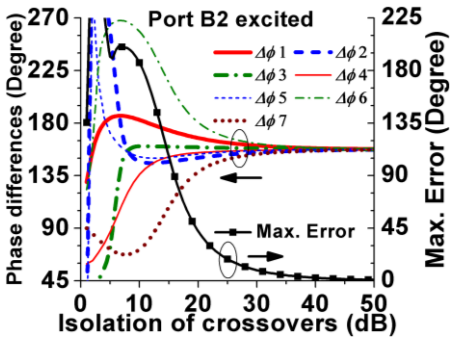

(h) Phase differences when B2 is excited in 8×8 BM

Figure 3-15. Effects on the power division and phase differences of the BM due to limited isolation of crossover.

Assuming the two crossovers in a 4×4 BM having 20-dB isolation and port B1 is excited, the ratio between the maximum and the minimum power distributions among A1 - A4 ports is 1.8 dB, which is referred as the maximum error in (g) Power division when B2 is excited in 8×8 BM (h) Phase differences when B2 is excited in 8×8 BM

Figure 3-15 (a); the progressive phase differences are demonstrated in (g) Power division when B2 is excited in 8×8 BM (h) Phase differences when B2 is excited in 8×8 BM

Figure 3-15 (b); the maximum error between these phase differences and the expected value, -45°, is depicted together as well, which is 10.8 degree. When port B2 is excited, the maximum error of power division is also 1.8 dB; the maximum error of phase difference is 13.7 degrees, as illustrated in (g) Power division when B2 is excited in 8×8 BM (h) Phase differences when B2 is excited in 8×8 BM

Figure 3-15 (c) and (d).

Since many more crossovers are employed in the 8×8 BM than the 4×4, the effects are also much more apparent. According to (g) Power division when B2 is excited in 8×8 BM (h) Phase differences when B2 is excited in 8×8 BM Figure 3-15 (e) and (f), if applying the crossover with 20-dB isolation, whenever B1 or B2 is excited, the maximum imbalance power division is higher than 5.0dB; and the error of phase differences are higher than 20°.

By observing (g) Power division when B2 is excited in 8×8 BM (h) Phase differences when B2 is excited in 8×8 BM Figure 3-15, though these couplers and phase shifters have entirely perfect properties, as well as the crossovers, with matching, and 20-dB isolation, the performance of the two BMs is still not outstanding in terms of either response of amplitude or phase. This is an indication of the influence of the limited isolation of the crossovers. Instead, to achieve a 4 × 4 BM with less than 1-dB power division error and less than 8° phase differences error, a better than 25-dB isolation is required at the crossover. For the 8 × 8 BM case, for the same aim, the crossover with approximate 40-dB isolation is necessary.

It should be clarified that all BMs not smaller than 4 × 4 configuration can have different arrangements but with the same order and the same numbers of each kind of components, as demonstrated in Figure 3-16 by 8 × 8 BMs, and the Figure 3-16 (a) has been analyzed in this section. Here, in Figure 3-16, they have the same numbers of each kind of component and the theoretically same performance. If one ignores the effects of crossovers and the losses on the

transmission lines, all the arrangements with the same order are supposed to have the theoretically same performance with each other. However, when taking the effects into account, there are small differences between the different arrangements.

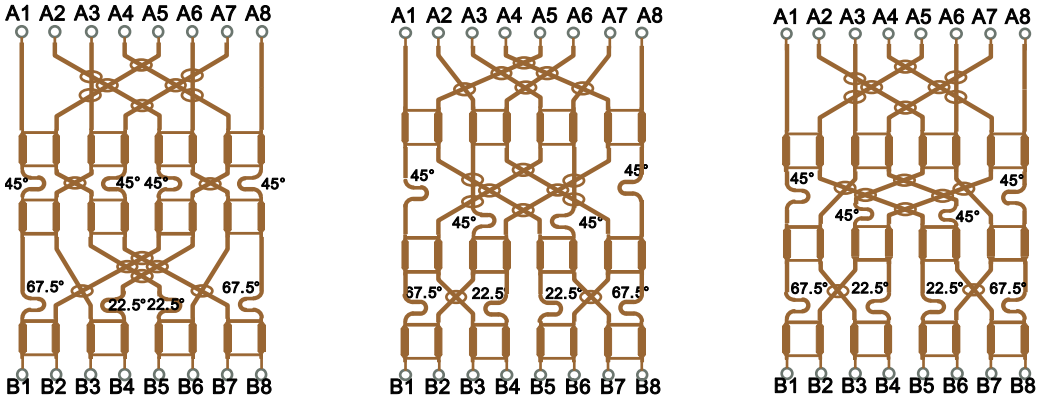

(a) Example1 (b) Example2 (c) Example3

Figure 3-16. Three different arrangements of 8 × 8 BM.

In addition, the analytical expressions and the results are irrelevant to frequency. In other words, the method can be applied at any operating frequency point within the bandwidth. That could also be the explanation for why the bandwidth of a BM is usually narrower than the couplers and phase shifters.

3.3.2.2 Possibility to Offset the Effects by Other Components

In the preceding analysis, all couplers are supposed to have the 3-dB / 90-degree feature, and all phase shifters have the 45-degree performance. A consequent hypothesis would be that whether the detrimental impacts from crossovers can be offset by using the couplers with asymmetry performance and/or the phase shifters with other phase delays. The attempts and corresponding results will be discussed in this section, but only for the 4 × 4 BM case.

It is assumed that the two crossovers in the 4 × 4 BM have fixed 25-dB isolation; the two couplers represented by $\mathbf{S}_{CP1}$ will be adjusted, and all rest of the parameters keep the same values as the last

section. The errors at power division and phase differences will be inspected when tuning the coupling coefficient and the phase differences of the two couplers.

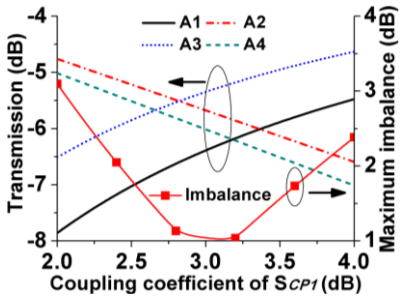

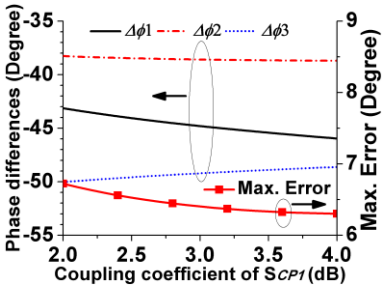

(a) Attempt to correct power division in 4 × 4 BM for B1 (b) Attempt to correct phase differences in 4 × 4 BM for B1

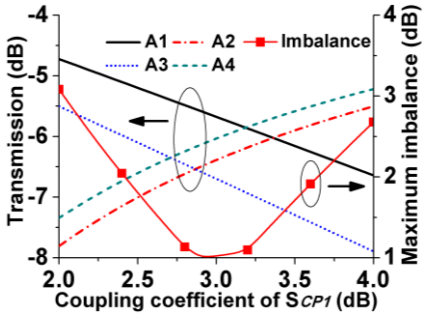

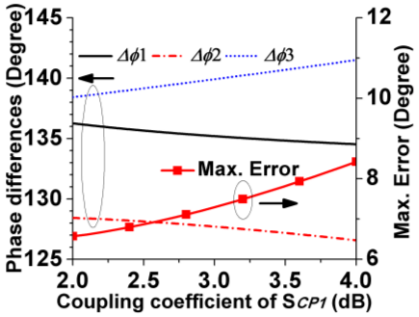

(c) Attempt to correct power division in 4 × 4 BM for B2 (d) Attempt to correct phase differences in 4 × 4 BM for B2

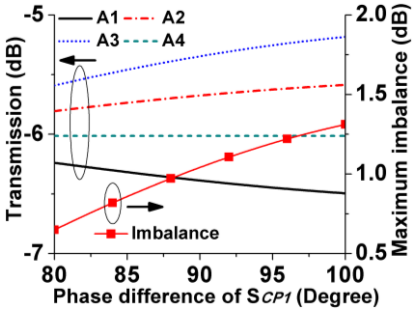

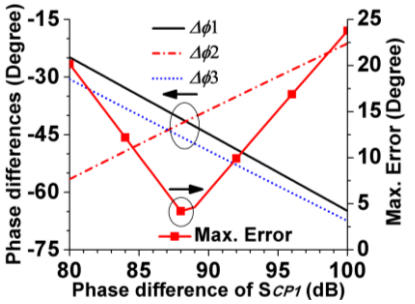

(e) Attempt to correct power division in 4 × 4 BM for B1 (f) Attempt to correct phase differences in 4 × 4 BM for B1

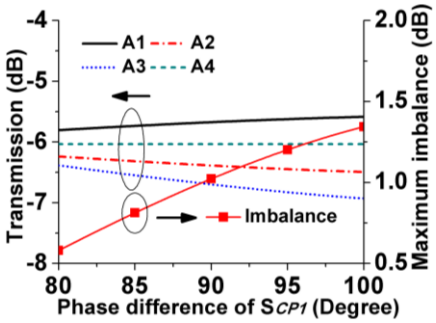

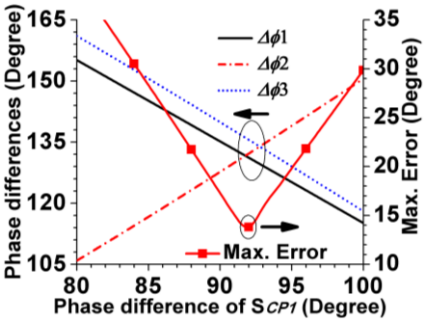

(g) Attempt to correct power division in 4 × 4 BM for B2 (h) Attempt to correct phase differences in 4 × 4 BM for B2

Figure 3-17. Results of the attempts to offset the detrimental impacts by using couplers with coupling coefficients other than 3 dB and/or phase differences other than 90degree.

Here, the phase difference of the couplers is defined as Arg(S31) - Arg(S21). The number of ports is the same, as shown in Figure 3-14 (a). Besides, the feasible and practical way to change the phase differences has been investigated and discussed by several researchers [92] - [94].

Based on the expressions of (3-14) - (3-21), several results can be obtained, and some trends can be revealed. In Figure 3-17 (a) - (d), the coupling coefficient of couplers was continuously tuned from 2.0 dB to 4.0 dB, and the effects on power division and phase differences of 4 × 4 BM have been demonstrated. It can be found that in terms of power distribution, increasing or decreasing the coupling coefficient will deteriorate the performance. By contrast, in terms of phase differences, the increment or reduction of the coupling coefficient will lead to converse impacts on the phase differences of BM when B1 or B2 excited, respectively. In short, the 3-dB coupling coefficient is almost the best compromise choice and tuning this parameter will not be helpful to offset the effects of imperfect isolation of crossovers.

In Figure 3-17 (e) - (h), the phase difference between two output ports of the coupler are continuously tuned. By observing Figure 3-17 (e) and (g), the unbalanced power division of BM can be relieved by raising the phase difference. However, the phase differences of the BM will degrade whenever the parameters are raised or reduced. Obviously, changing the phase difference of the coupler will alleviate these effects.

In addition, the results of modifying the phase delay of phase shifters are not shown here, because it has theoretically the same influence of tuning the phase difference of couplers.

According to the results and the corresponding analysis, the detrimental effects on BMs from crossovers cannot be eliminated by adjusting the parameters of other components in the BM.

3.3.2.3 Experimental Verification

To verify and assure the theoretical analysis, three 4 × 4 BMs using different crossovers with various values of imperfect isolation are designed, simulated, and tested at the center frequency of 5.8 GHz. One of the critical points in this design is to achieve several crossovers with the precisely controlled isolation (mutual coupling) between the two paths.

The structure of the back-to-back double-layer microstrip line is adopted in this design because the nearly perfect isolation can be implemented by placing two paths on the two layers insulated by the middle conducting layer of the ground plane. The cross-section of the structure is illustrated in Figure 3-18. The laminate is Rogers RO4350B, and RO4450F prepregs is used to bond the two layers together.

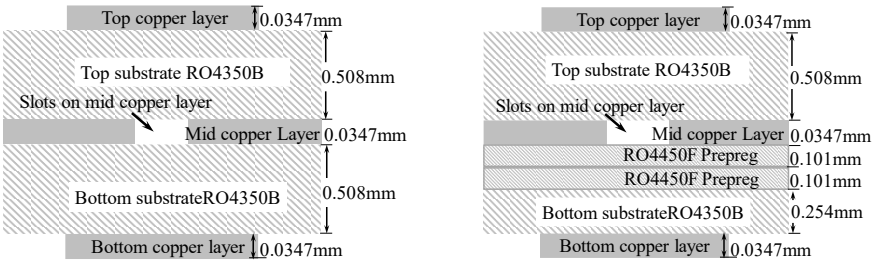

Figure 3-18. Cross-sections of the circuit structure.

The layouts and simulated results of three crossovers with 10-dB and 20-dB mutual coupling and perfect isolation are demonstrated in (e) Layout coupler with theoretically infinite isolation (f)Simulation results

Figure 3-19. In general, the crossovers have two paths placed on both sides of the circuits, and two slots on the middle layer used to alter the mutual coupling (isolation) in between. Obviously, for perfect isolation, there is no slot on the middle layer in the crossover. The red, blue, and yellow colors represent the copper layer shapes on top, bottom, and middle layers, respectively. The detailed structural parameters are described below.

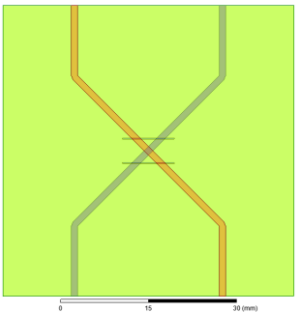

(a) Layout coupler with 10 dB coupling coefficient

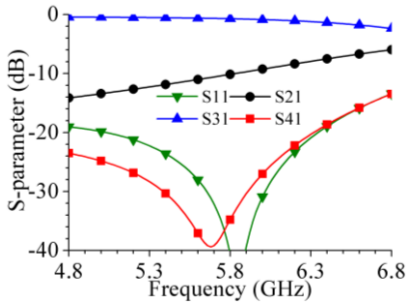

(b)Simulation results

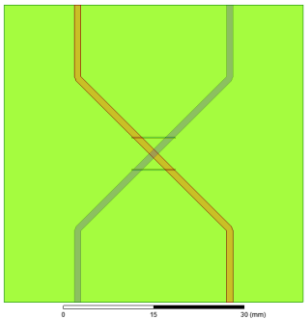

(c) Layout coupler with 20 dB coupling coefficient

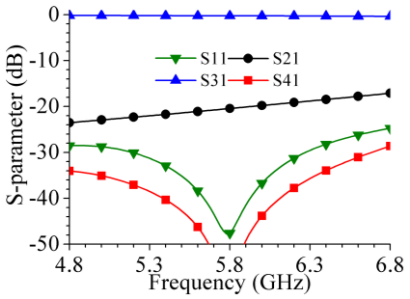

(d)Simulation results

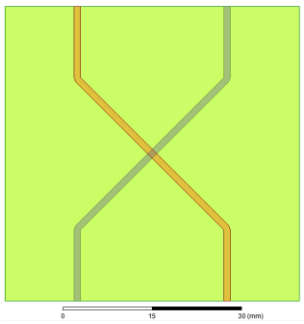

(e) Layout coupler with theoretically infinite isolation

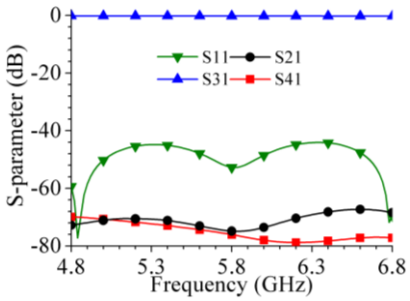

(f)Simulation results

Figure 3-19. Layouts and simulated results of crossovers with various isolation.

Here, (a) is the crossover with 10 dB mutual coupling; the two slots have 0.2-mm width, 10.2-mm length, and 7.2-mm spacing. (c) is the crossover with 20 dB mutual coupling; the two slots have 0.2-mm width, 8.2-mm length, and 8.2-mm spacing. (e) is the crossover with perfect isolation. (b), (d), and (f) are the simulated results of (a), (c), and (e) by ANSYS HFSS.

The required various mutual coupling coefficients can be found in (e) Layout coupler with theoretically infinite isolation (f)Simulation results

Figure 3-19 (b), (d), and (f), which will be used inside 4 × 4 BMs in the next step to confirm the effects. Concretely, S21 will be -10 dB and -20 dB at the center frequency in (e) Layout coupler with theoretically infinite isolation (f)Simulation results

Figure 3-19 (b) and (d).

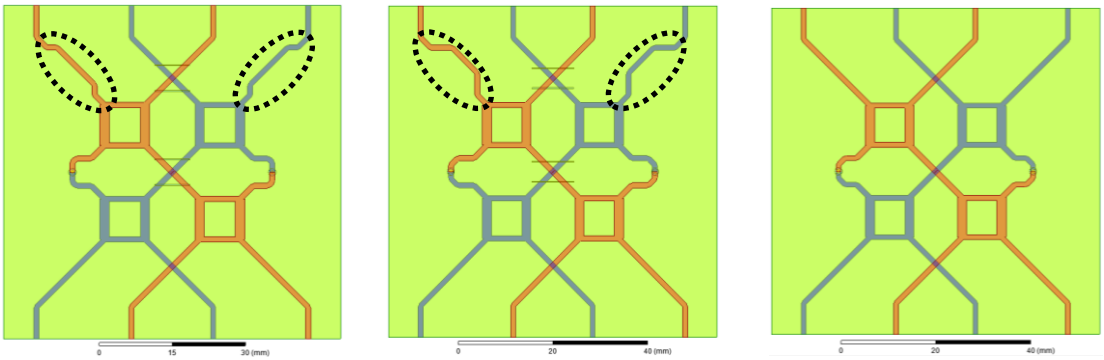

(a) BM with 10-dB-isolation crossovers (b) BM with 20-dB-isolation crossover (c) BM with crossovers

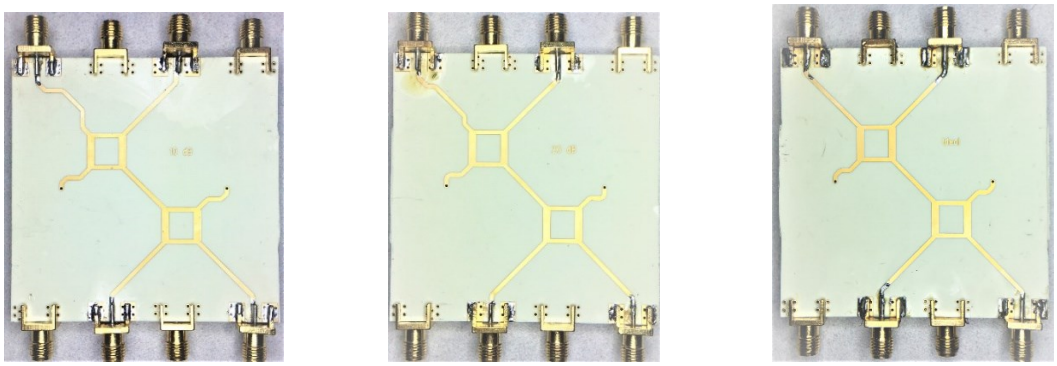

(d) Example with 10-dB-isolation crossovers (e) Example with 20-dB-isolation crossover (f) Example with crossovers

Figure 3-20. Layouts in (a), (b), and (c), are corresponding to the photos in (d), (e), and (f) of the three crossovers with 10 dB and 20 dB coupling and the nearly perfect isolation, respectively.

Three 4 × 4 BMs have been designed, simulated, and fabricated using the three kinds of crossovers described above. The layouts and pictures of the circuits are exhibited in (d) Example with 10-dB-isolation crossovers (e) Example with 20-dB-isolation crossover (f) Example with crossovers

Figure 3-20.

It should be noted that the three crossovers had different phase delays for the signal passed through them because the slots on the middle layer have some effects on the transmission. To compensate for the impact, some bends with different lengths have been applied on each of the 4 × 4 BMs, as indicated by the dotted cylinders in (d) Example with 10-dB-isolation crossovers (e) Example with 20-dB-isolation crossover (f) Example with crossovers

Figure 3-20 (a) and (b). The crossover with nearly perfect isolation does not have slots on the ground plane. Therefore, it is used as a reference. Consequently, there are no extra bends in the layout shown in (d) Example with 10-dB-isolation crossovers (e) Example with 20-dB-isolation crossover (f) Example with crossovers

Figure 3-20 (c). The photos of experimental circuits based on the cross-section shown in Figure 3-18 (b) are demonstrated in (d) Example with 10-dB-isolation crossovers (e) Example with 20-dB-isolation crossover (f) Example with crossovers

Figure 3-20 (d), (e), and (f).

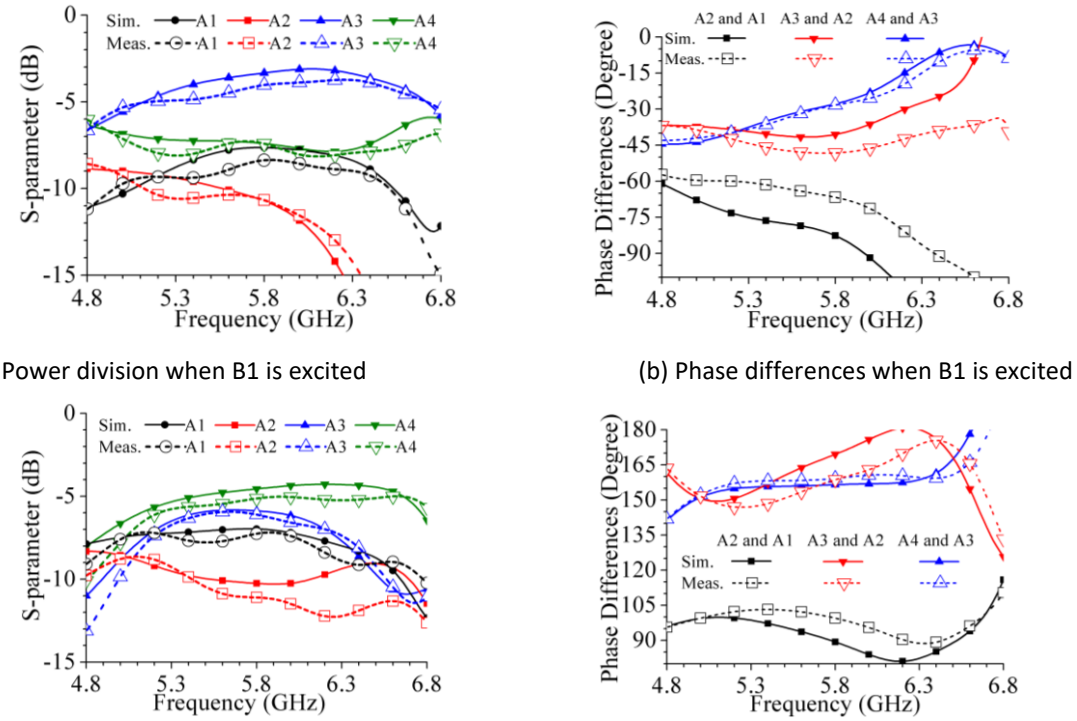

(a) Power division when B1 is excited

(b) Phase differences when B1 is excited

(c) Power division when B2 is excited

(d) Phase differences when B2 is excited

Figure 3-21. Simulated and measured results of the 4 × 4 BM using 10-dB crossover.

The comparisons of simulated and measured results among the three 4 × 4 BMs are listed in Figure 3-21 - Figure 3-23. In the figures, the power division (a) and (c) and phase difference (b) and (d) are with B1 and B2 excited, respectively. First, it should be pointed out that the imbalanced power distributions and deviations of phase differences in the three charts are very close to the numerically calculated results shown in (g) Power division when B2 is excited in 8×8 BM (h) Phase differences when B2 is excited in 8×8 BM

Figure 3-15 at the central frequency of 5.8 GHz. For example, the simulated results in Figure 3-21 (a), the outputs on A1 - A4 ports are -7.9dB, -10.9dB, -3.7dB, and -7.6dB when B1 is activated. Almost the same results can be obtained from (g) Power division when B2 is excited in 8×8 BM (h) Phase differences when B2 is excited in 8×8 BM

Figure 3-15 (a) when the mutual coupling (isolation) equals to 10 dB. The similar coincidences can be observed from the power division and phase differences of all three cases. The satisfying agreement between the numerical calculation and simulation indicates that the forward transmission circuit model has an adequate accuracy in predicting the performance of BMs.

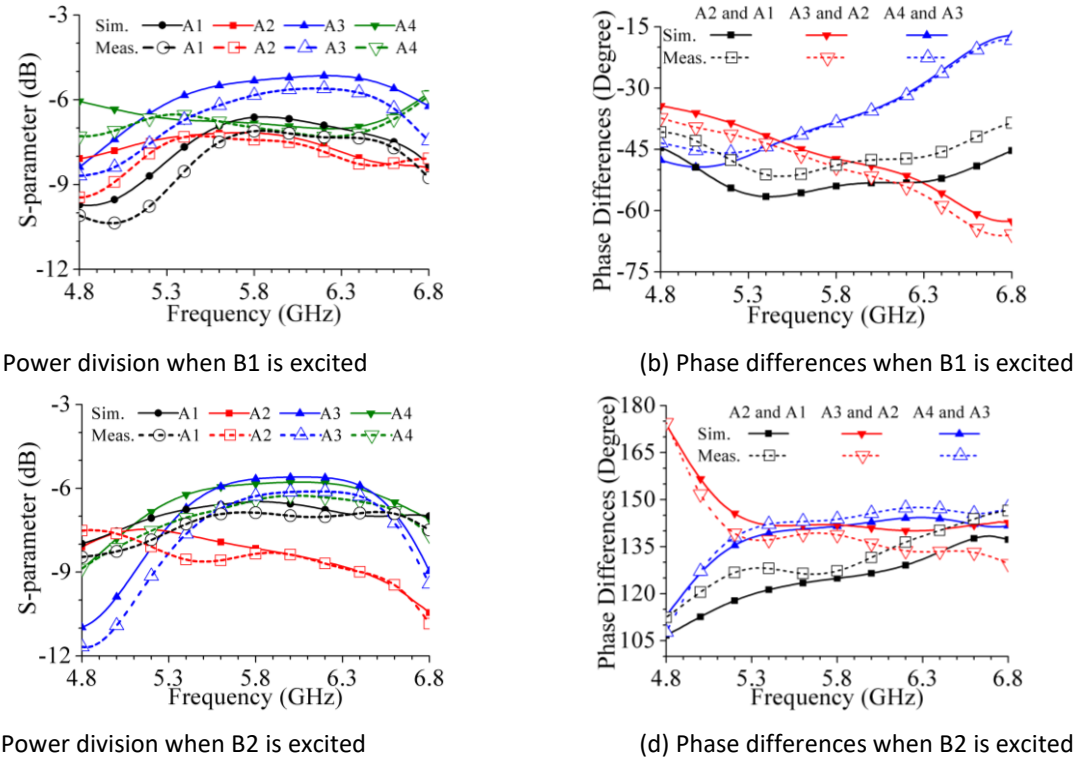

(a) Power division when B1 is excited

(b) Phase differences when B1 is excited

(c) Power division when B2 is excited

(d) Phase differences when B2 is excited

Figure 3-22. Simulated and measured results of the 4 × 4 BM with 20-dB crossover.

Secondly, the consistency between simulated and measured results is reasonable and acceptable in terms of the trend and derivation. Due to the discrepancy of the cross-sections shown in Figure 3-18 (a) and (b), there will be differences at the characteristic impedance and propagation constant. Moreover, the further losses can be introduced by the connectors soldered on the circuits' board. It can be clearly observed through the comparisons that the effects of crossovers on BMs might be very apparent if there is non-negligible mutual coupling between the two paths inside crossovers.

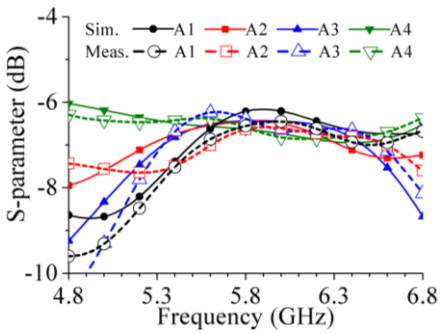

(a) Power division when B1 is excited

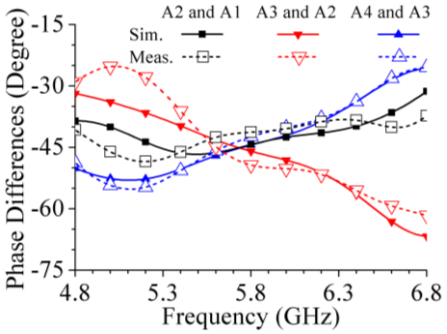

(b) Phase differences when B1 is excited

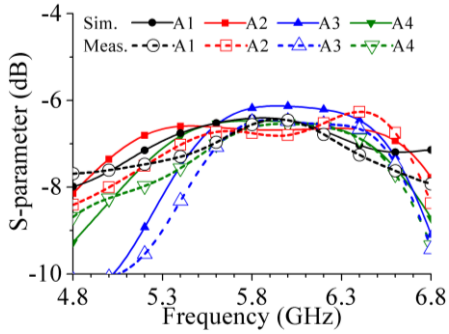

(c) Power division when B2 is excited

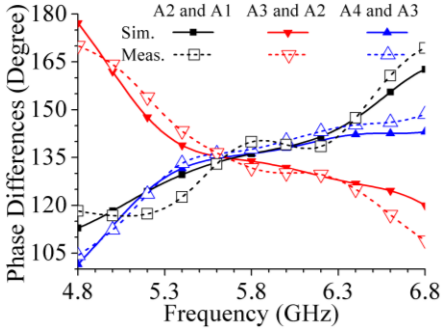

(d) Phase differences when B2 is excited

Figure 3-23. Simulated and measured results of the 4 × 4 BM with nearly ideal crossover.

Chapter 4

Two-Dimensional Butler Matrices

In this chapter, a generalized method to build 2D-BMs with $2^{M+N} \times 2^{M+N}$ configurations based on conventional $2^M \times 2^M$- and a $2^N \times 2^N$ BMs is introduced. The fundamental principles, design process, crucial components, and the consideration for uniplanar layouts of 2D-BMs are discussed in detail with diagram illustrations. Another novel component, the phase shifter, which is necessary to the proposed 2D-BMs, is introduced with the characteristic, suggested circuit model, and the analytical solution. For the verification and demonstration, an experimental example of 2D-BM with 16 × 16 configurations based on a back-to-back double layer structure for 2.4 GHz is fabricated and measured. Satisfying performance can be observed at matching, isolation, equal power division, and progressive phase differences among all output ports covering a 17% relative bandwidth. In terms of structural features, all the output ports are placed on a plane and straight fit in a rectangular array. Moreover, it still has the freedom to rearrange for other configurations of planar arrays.

Some of the related work has been published in the journal article [57] and conference paper [58].

4.1 Two-Dimensional Butler Matrices

4.1.1 Major Properties

Before starting the discussion about 2D-BMs, it is necessary to clarify the feature of 2D-BMs compared to traditional BMs. The most significant improvement of the proposed 2D-BMs over the traditional BMs is extending the arrangement of the output ports from a linear configuration

into a planar one. Therefore, the distribution of the progressive phase differences is developed from along a line to cover a plane. Meanwhile, all other crucial performances as traditional BMs can be entirely preserved. In short, the proposed 2D-BM is highly suitable to feed a 2-D antenna array for 2-D beam scanning.

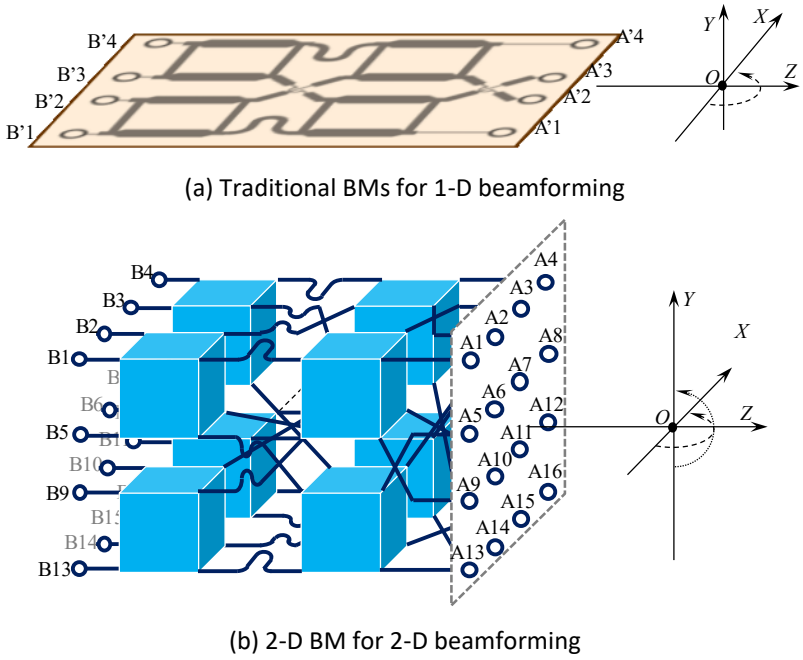

Figure 4-1. Comparison between traditional a BM and a 2D-BM.

As an example, the comparison between a traditional 4 × 4 BM and a 16 × 16 2D-BM is shown in Figure 4-1. In Figure 4-1 (a), four output ports, A'1 - A'4, are arranged along the *OX* axis, and the consecutive series of the phase difference, -135°, -45°, +45°, and +135°, are produced along the *OX* direction. In contrast, in Figure 4-1 (b), the 16 output ports, A1 - A16, of the proposed 2D-BM are placed in the *XOY* plane and organized into a parallelogram shape. The progressive phase differences between adjacent rows and columns can be -135°, -45°, +45°, and +135° separately and independently. Thereby, any combination of phase differences along rows and columns can be achieved depending on which input port is excited. Notably, the *OX* and *OY* directions are not necessary to perpendicular to each other.

Compared to the conventional configurations, the proposed 2D-BMs have a fewer number of phase shifters because some phase shifters that are utilized initially for each row or column can be merged in the 2D-BMs. Therefore, the performance in terms of insertion loss, and accuracy of the phase shift could be improved further.

4.1.2 Methodology

4.1.2.1 Principle and Design Method

The proposed 2D-BM can be implemented in any $2^{M+N} \times 2^{M+N}$ configurations by following several rules (M and N are integer number not less than 1). In terms of construction, the method to build a 2D-BM can be concisely summarized as a spatial intersection from two traditional BMs placed on two orthogonal planes. Concretely, it is a spatial multiplication from a $2^{M} \times 2^{M}$ BM and a $2^{N} \times 2^{N}$ BM to obtain a $2^{M+N} \times 2^{M+N}$ 2D-BM according to some specific regulations. The rules contain two steps: aligning and spatially multiplying.

For easier understanding, two instances of building 2D-BMs are illustrated in Figure 4-2 for demonstrating the principle of alignment and spatial multiplication. The two examples are the cases of $M = 1$, $N = 2$ and $M = 2$, $N = 2$, respectively. The legend of Figure 4-2 for symbols is shown in the lower right corner of (b). The ports named starting with A' and A'' are input ports of traditional BM; the ports named starting with B' and B'' are output ports of traditional BM; ports named starting with A and B are the input- and output- ports of 2D-BM. The number of *C1* - *C8* on eight-port hybrids will be used in Section 4.1.2.2.

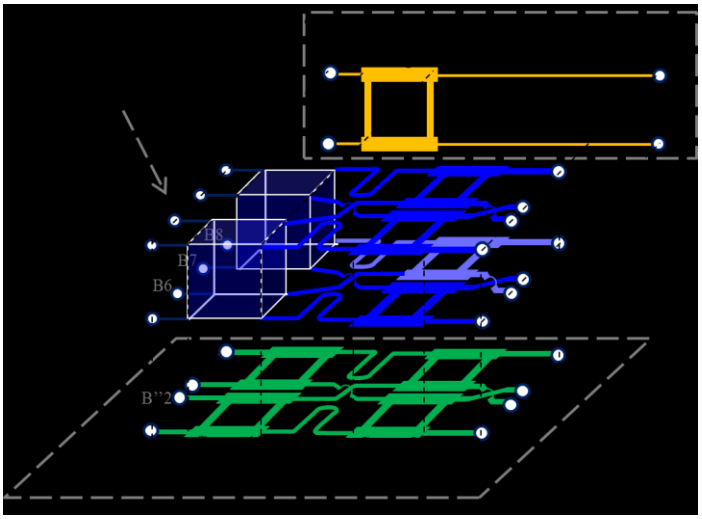

(a) 8 × 8 2D-BM achieved based on a 2 × 2 BM and a 4 × 4 BM

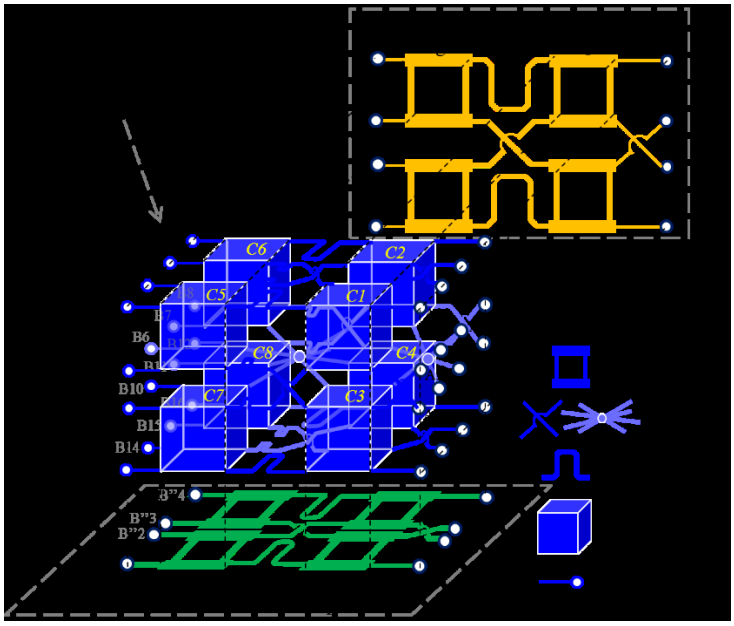

(b) 16 × 16 2D-BM obtained based on two 4 × 4 BMs

Figure 4-2. Two instances of constructing a 2D-BMs based on two traditional BMs.

In the step of alignment, the two traditional BMs should be placed onto two orthogonal planes, for example, vertical and horizontal planes, respectively. Then, each of the BMs should be separated into several layers according to the functions of the components inside BMs. Concretely, all couplers with the same distance from input ports will be assigned to the same layer, and this layer will be named and numbered as Stage1, Stage2, until the last one. A higher number means far from

input ports. Similarly, all transmission lines, phase shifters, and crossovers between adjacent stage-layers will be allocated to the same layer, which will be named and numbered as Link1, Link2, and so on. These layers have been exemplified in Figure 4-2 (a) and (b) by a series of parallel dash lines. Based on the separation, all layers of both traditional BMs should be aligned with the same name and number. If one BM has a lower rank than another, it should be extended to the same length as another by adding transmission lines after the last layer, as shown in the vertical plane of Figure 4-2 (a).

For spatial multiplication or intersection, all components of the two BMs should be extruded along the respective normal directions until two components intersect with each other. At each position of the intersection, one component of 2D-BM should be generated based on the set of rules illustrated in Figure 4-3. The purpose of these rules is to obtain the behaviors of each component on two orthogonal projections independently.

In Figure 4-3, (a) - (c) illustrate the cases based on two couplers, or one coupler and one transmission line; (d) - (f) illustrate the cases of two crossovers, or one crossover and one transmission line; (g) - (i) illustrate the cases of two phase shifters, or one phase shifter and one transmission line The values in (g) - (i), such as 0, α, β, and $\alpha+\beta$, represent the phase shifting values.

A brief explanation of the mechanism of the rules is described below. For the power distribution of 2D-BMs, the eight-port couplers can behave as couplers on two orthogonal planes. In addition, it isolates the mutual influence between the orthogonal planes. For the phase shift, increasing an identical value of phase shift on all paths in the same plane will not produce relative phase differences among the paths. Further, assigning different values as the identical values for respective planes will not change the phase differences between the paths in the same plane but

can generate the differences among the planes. If applying this method on vertical and horizontal planes, respectively, then the rules of summation can be obtained.

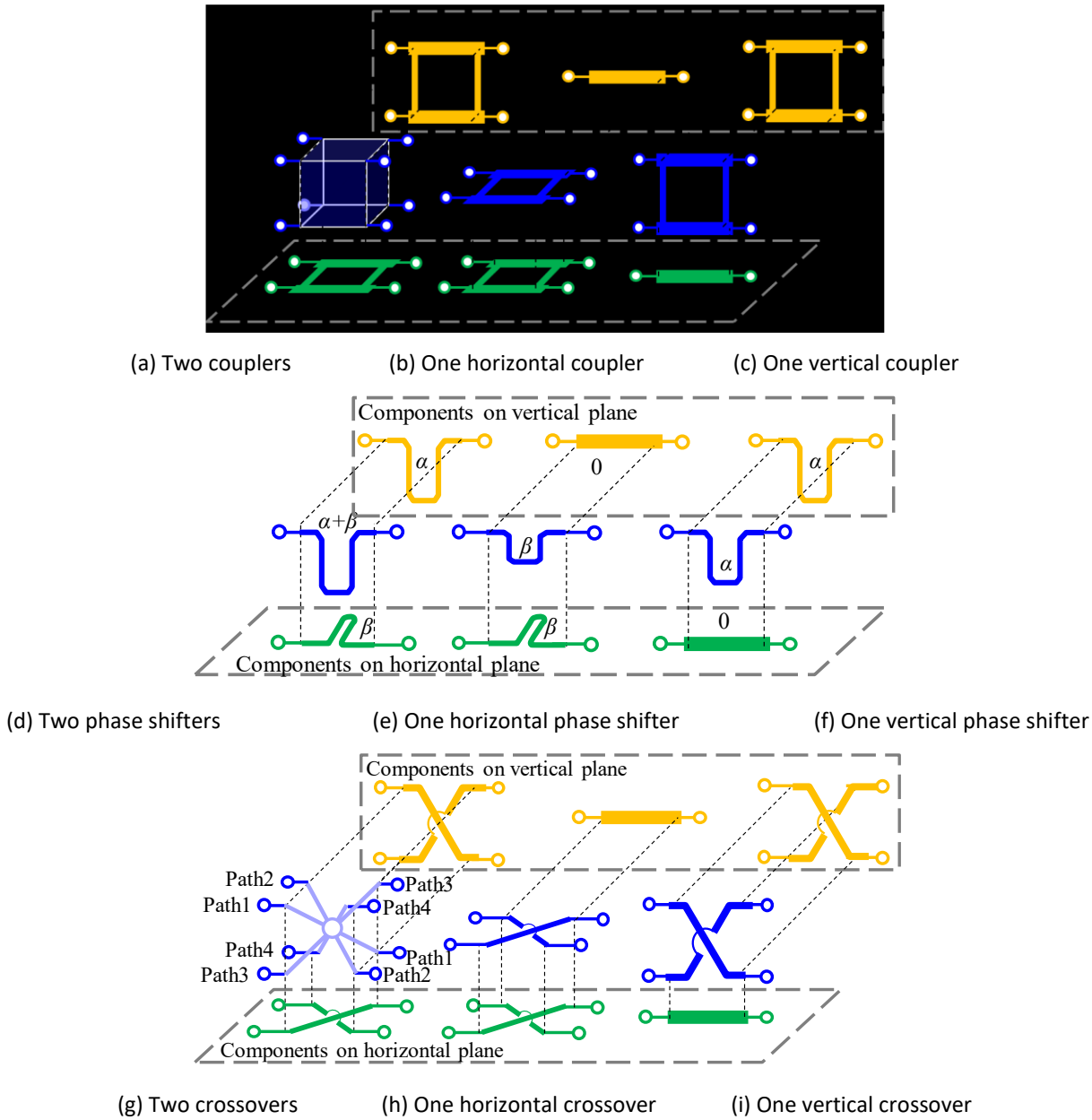

Figure 4-3. Basic rules to generate components for 2-D BM from two components in traditional BMs on two orthogonal planes.

Based on these rules, the proposed 2D-BM can be easily achieved by two traditional BMs, as the two examples in Figure 4-2. Moreover, the significant merits from traditional BMs, such as perfect

matching, lossless transmission, spatially orthogonal beams, and equal power division, can be entirely inherited.

By applying the two steps, any 2D-BM with $2^{M+N} \times 2^{M+N}$ configuration can be accomplished based on a $2^{M} \times 2^{M}$- and a $2^{N} \times 2^{N}$ BMs. Notably, the 8 × 8- and 16 × 16- 2D-BMs have different structures than traditional 8 × 8- and 16 × 16-BMs though they have the same numbers of input- and output- ports. Even two 2D-BMs with the same numbers of ports, they may have different structures and thereby various performances due to a distinct combination of *M* and *N*. For example, 16 × 16 2D-BMs can be obtained based on 2 × 2- and 8 × 8- BMs, or, two 4 × 4 BMs.

Besides, due to the orthogonality between the two planar BMs, some technologies with flexible beam configurations of planar BMs, such as some proposed in Chapter 6, can be applied to the one or two planar BMs to build a 2D-BM for comprehensive and diverse performance.

4.1.2.2 Key Components and Important Factors

In addition to the components that are usually used in the traditional BMs, such as couplers, phase shifters, and crossovers, there are two distinct components that are needed in the proposed 2D-BMs. The two components are the eight-port hybrid and the phase-shifter group. They are essential to 2D-BMs in terms of functionality and property.

For the eight-port hybrid, it can be found in Figure 4-2 (a) and (b) presented as a cube. The eight-port hybrid can be seen as a form of a 2-D quadrature coupler, which was proposed in 1991 by T. Kawai et al. [61]. A block view with numbered ports, a functional view composed of traditional quadrature couplers, and an example circuit based on microstrip line is illustrated in Figure 4-4 for exhibiting the function and implementation of a typical eight-port hybrid.

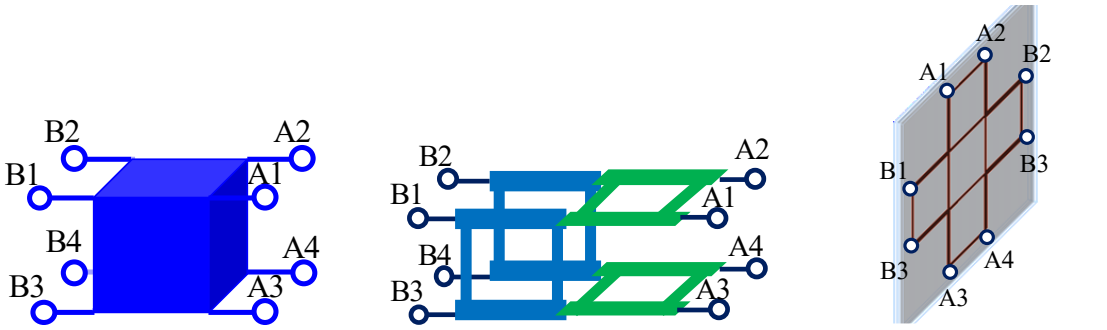

Figure 4-4. Schematic of eight-port hybrid.

It is highly recommended to apply wideband eight-port hybrids for a high-rank 2D-BMs, such as higher than 8 × 8 configurations. A traditional eight-port hybrid composed of quadrature couplers is expected to work correctly at the design frequency. When many eight-port hybrids are approximately cascaded together in a 2D-BM, the effective bandwidth of the whole 2D-BM will be drastically diminished due to the accumulation of reflections from each eight-port hybrid. A simple and effective way to broaden bandwidth has been discussed and analyzed in [55].

Another pivotal device required for 2D-BMs is a phase-shifter group, which is a new concept and is not apparently obvious to be found in 2D-BMs. In Figure 4-2 (b), there are 16 paths in the layer Link1 of the 16 × 16 2D-BM. They have three different phases shifting values among these paths, which are 0°, 45°, and 90°, respectively. Or, in other words, we simultaneously need two phase differences, which are 45° and 90°, on some paths relative to other paths. Traditional differential phase shifters need one particular reference line for each specific phase shifting value [54] - [56]. Hence, it is difficult to be achieved in a compact size.

Unlike traditional differential phase shifters, the proposed phase-shifter groups may contain three paths or more, but no particular reference line among them. More clearly, two or more phase differences can be obtained by a phase-shifter group, rather than only one in the traditional phase

shifter. A comparison of using the traditional one and the new one to realize the four-way phase shift is shown in Figure 4-5.

In the Figure 4-5, (a) is a traditional differential phase shifter; (b) is the scheme of traditional phase shifters to obtain three successive phase differences, α, β, and γ; (c) is the scheme of phase-shifter group to obtain three successive phase differences, α, β, and γ. It is clear that the phase-shifter group has a remarkable advantage of compactness and simplicity, especially when the number of paths increases.

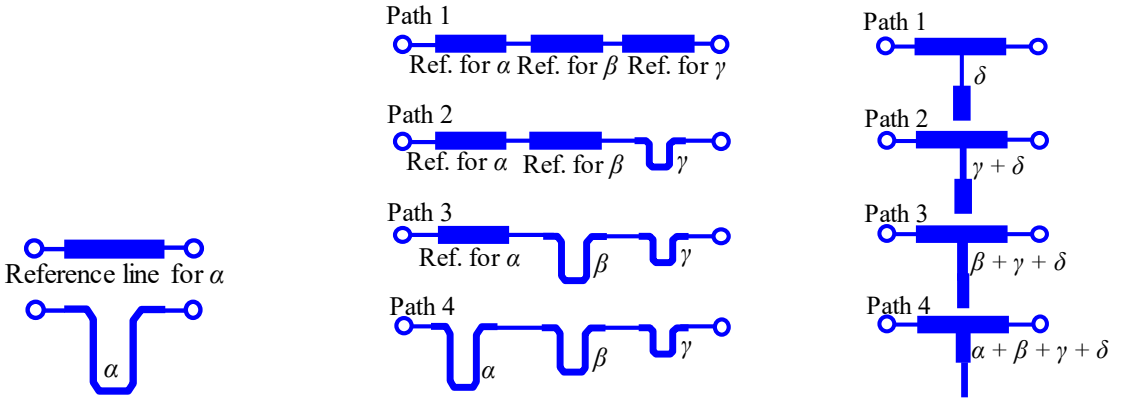

(a) Traditional phase shifter (b) Phase-shifter group based on the traditional way (c) Propose scheme

Figure 4-5. Schematic diagrams of four paths phase shift.

A more detailed principle and design method about the phase-shifter group will be discussed in Section 4.2. A particular design based on a microstrip line for 16 × 16 BM will be presented with an analytical solution as well.

4.1.2.3 Consideration of Layout for Planar Circuits

According to Figure 4-2 2 (a) and (b), it can be found that the proposed 2D-BMs have a three-dimensional block diagram. Consequently, it could become a crucial concern about how to implement a 2D-BM by planar circuits in a practical and economical way. Here, planar circuits

mean microstrip line, stripline, coplanar waveguide, and other printed circuit forms. Microstrip line circuits will be exemplified in section as an example for others.

First, the planar 2D-BM circuit will be established on the plane where all output ports are distributed to facilitate the connection with a planar array. Moreover, multi-layer structures are recommended for most 2D-BMs when M or N is greater than one because at least four crossovers are needed, and a single-layer structure has little space to arrange them.

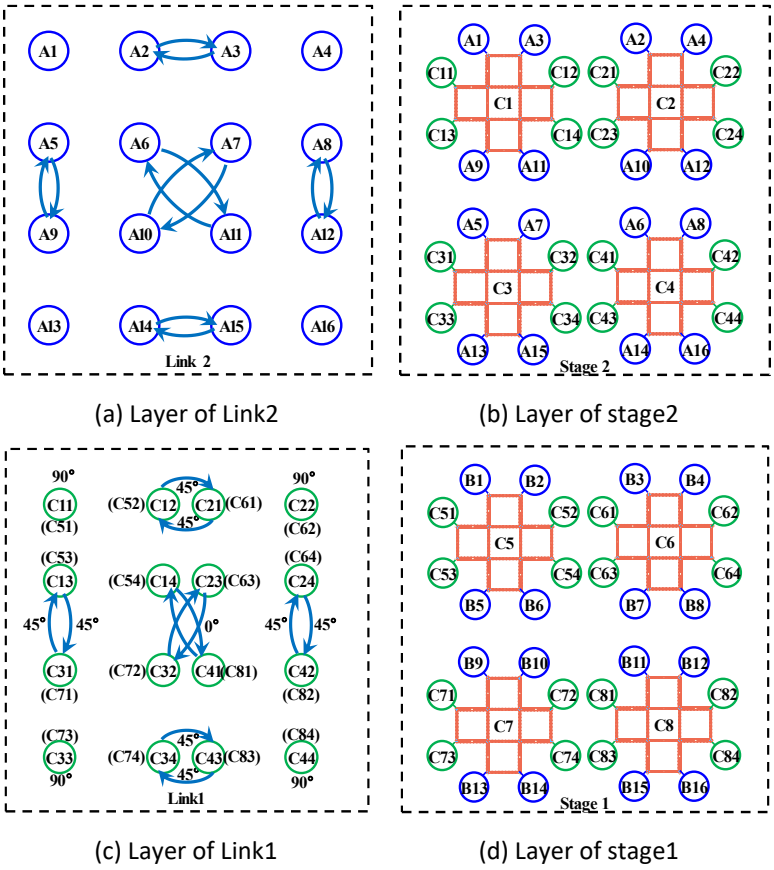

Figure 4-6. Plane graphs of functional layers of 16 × 16 2D-BM. This series of functional layers are listed in order from the output ports to the input ports.

Based on the definition of the functional layers mentioned in Section 4.1.2.1, a preliminary planar circuit layout can generally be obtained. For example, in Figure 4-2 (b), four functional layers of the 16 × 16 2D-BM can be redrawn into four plane graphs, as shown in Figure 4-6. The names of

eight-port hybrids, C1-C8 are the same as in Figure 4-2 (b). The curves with an arrow in Link1 and Link2 demonstrate crossovers in this layer; the phase shift values represent the phase delays on each path.

It can be expected to place Stage1 and Stage2 on two layers separately and use the double layer structure to deal with the crosses and the connections in Link1 and Link2. Therefore, a back-to-back double layer microstrip structure with a common ground layer in the middle can be exploited for the implementation of the planar 2D-BM.

For sure, there could be many techniques of layout and routing required for fitting an array or reducing sizes in a specific and practical case. However, the preliminary layout shown in Figure 4-6 can still be referenced as an initial design.

4.2 Phase-shifter Group

4.2.1 Definition and Major Properties

The phase-shifter group is a component that contains *N*-way paths (*N* is an integer not less than three) and provides specific *N*-1 relative phase differences among the *N*-way paths covering a specific bandwidth centered at a given frequency. Perfect matching and lossless transmission can be achieved in the same bandwidth at each path.

The phase-shifter group can generate more phase differences within a smaller space compared with the traditional phase shifters, as discussed in Section 4.1.2.2 and shown in Figure 4-5. The proposed phase-shifter group has the advantage of the wider bandwidth compared to a set of transmission lines that have the same phase differences among them, as demonstrated in Figure

4-7. The proposed phase-shifter group can realize zero derivatives in each phase difference at the center frequency.

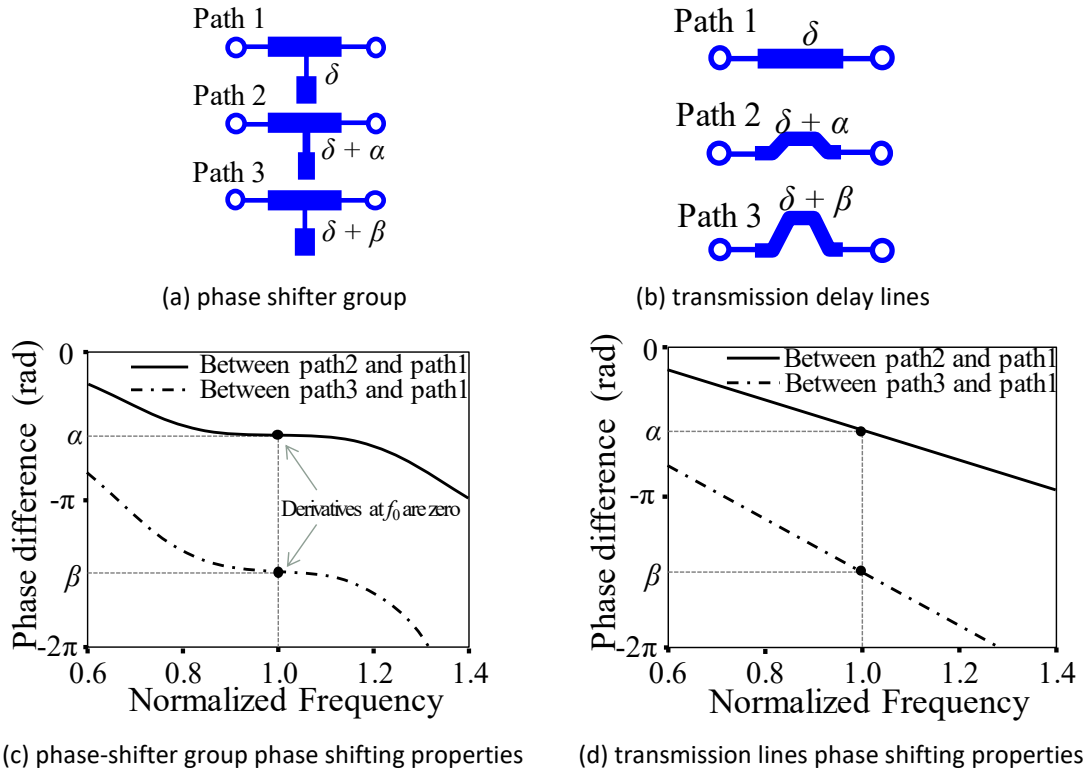

Figure 4-7. Comparison of phase-shift performances between transmission lines and phase-shifter group versus the normalized frequency.

It should be clear that there is more than one form of the paths of the phase-shifter group, such as [54] - [56]. Also, the broadband phase shifters based on the all-pass network [105], [106]. The phase shifter based on the all-pass network has a remarkable independent design and performance at the matching and phase shift bandwidth. In addition, the phase shifter structure is compact due to the use of lumped components. However, when using a conventional phase shifter inside the phase-shifter group, the derivative of the phase delay with frequency is not necessary to compensate precisely the delay of a specific reference line. All derivatives on each path need to be coordinated together to compensate for the differences among the paths (probably with a constant delay on each path if it is needed).

4.2.2 Methodology

A feasible and practical scheme to implement a phase-shifter group is proposed in this section. The general circuit model for one of these paths to construct the phase-shifter group is clarified in Figure 4-8. Here, each of the strips filled with patterns represents a transmission line, and the same pattern means the same transmission line characteristics. The characteristic impedance and the electrical length at the center frequency of each segment of lines are listed. The ABCD-parameters of each block outlined by dashed lines named A_1, A_2, and A_r. The same circuit model can represent all paths but with different parameters. The circuit is composed of six segments of transmission lines and has a symmetrical configuration centered at the middle two lines.

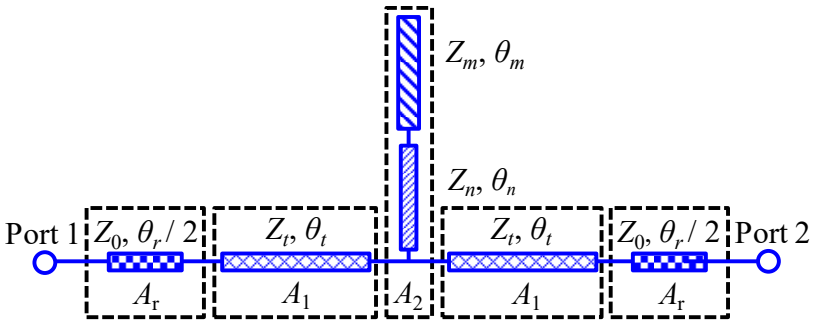

Figure 4-8. Circuit model of a single path in the proposed phase-shifter group.

The two lines on both outer sides have the same characteristic impedance as the input impedance of two ports, Z_0. They will be utilized to adjust the phase delays at the central frequency of each individual path by changing their total electrical length, θ_r, and without impacts on the matching and transmission. They are not necessarily the same length, but the sum of their lengths, θ_r, needs to be fixed.

The central four lines are supposed to have an adjustable derivative of phase delay at the center frequency to offset the effect of the two outer lines compared with the reference path. Meanwhile, they should produce the same phase delay with respect to each other on all paths. The perfect

matching and transmission are assured, as well. Such a property for the central four lines can be expressed by the S-parameter matrix of [S_C]:

$$[S_C] = \begin{bmatrix} S_{C11} & S_{C12} \\ S_{C12} & S_{C22} \end{bmatrix} \quad (4\text{-}1)$$

$$S_{C11} = S_{C22} = 0 \quad (4\text{-}2)$$

$$|S_{C21}| = |S_{C12}| = 1 \quad (4\text{-}3)$$

$$\mathrm{Arg}(S_{C21}) = C \quad (4\text{-}4)$$

$$\frac{d[\mathrm{Arg}(S_{C21})]}{df} = -\frac{(\theta_r - \theta_{r0})}{f_0} \quad (4\text{-}5)$$

Here, f_0 is the center frequency; C is an identical phase delay among all paths; θ_{r0} is the total length of the two outer lines on the path reference. The requirements of (4-2) - (4-5) should be met at f_0 among all paths.

As a possible solution, when $\theta_m = \pi/2$, $\theta_n = \pi/2$, and $\theta_t = \pi/2$, the requirements of (4-2) - (4-4) can be satisfied regardless of the values of Z_m, Z_n, and Z_t, and, C is zero constant in this case. We will apply this solution for simplicity, though it may not be optimal in terms of compactness.

It becomes clear that the gist of implementing phase shifter groups is to find the relations among Z_m, Z_n, and Z_t to meet the requirement (4-5). The question can be simplified further by assuming $Z_m = Z_t = a\ Z_0$, $Z_n = b\ Z_0$, and normalizing them as a, and b, respectively. The values of θ_m, θ_n, and θ_t will be replaced by a frequency-dependent function, θ_q, in a subsequent derivation.

$$(f) = \frac{\pi f}{2f_0} \quad (4\text{-}6)$$

According to the definition of the transmission matrix and transmission line impedance equation [102], we can obtain the normalized ABCD-matrices of $[a_1]$ and $[a_2]$ to represent the properties of the circuit parts A_1 and A_2 shown in Figure 4-8.

$$[a_1] = \begin{bmatrix} \cos\theta_q & j\,a\sin\theta_q \\ \frac{j}{a}\sin\theta_q & \cos\theta_q \end{bmatrix} \tag{4-7}$$

$$[a_2] = \begin{bmatrix} 1 & 0 \\ \frac{a+b}{-j\,ab\cot\theta_q + j\,b^2\tan\theta_q} & 1 \end{bmatrix} \tag{4-8}$$

If the product of the cascaded three matrices can be presented as:

$$[a_1][a_2][a_1] = \begin{bmatrix} a_C & b_C \\ c_C & d_C \end{bmatrix} \tag{4-9}$$

Then, the results are

$$\begin{cases} a_C &= \cos^2\theta_q - \sin^2\theta_q + \dfrac{j\,a(a+b)\sin\theta_q\cos\theta_q}{-jab\cot\theta_q + j\,b^2\tan\theta_q} \\ b_C &= 2j\,\mathrm{a}\sin\theta_q\cos\theta_q - \dfrac{a^2(a+b)\sin^2\theta_\mathrm{q}}{-j\,ab\cot\theta_q + j\,b^2\tan\theta_q} \\ c_C &= \dfrac{2j}{a}\sin\theta_q\cos\theta_q + \dfrac{(a+b)\cos^2\theta_q}{-j\,ab\cot\theta_q + j\,b^2\tan\theta_q} \\ d_C &= \mathrm{A_C} \end{cases} \tag{4-10}$$

Converting the normalized ABCD-matrix to S-parameters through

$$S_{C21} = \frac{2}{2a_C + b_C + c_C} \tag{4-11}$$

Then, the phase shift can be obtained as

$$\begin{aligned} \mathrm{Arg}(S_{C21}) &= \tan^{-1}\frac{\mathrm{Im}(S_{C21})}{\mathrm{Re}(S_{C21})} \\ &= \tan^{-1}\frac{E1}{E2} \end{aligned} \tag{4-12}$$

Therefore, the derivative of the phase shift can be obtained from

$$\frac{d[\mathrm{Arg}(S_{C21})]}{df} = \frac{E1' \cdot E2 - E1 \cdot E2'}{E2^2 + E1^2} \tag{4-13}$$

In (4-12) and (4-13), the expressions of E1 and E2 are listed below.

$$E1 = \left(2ab^2 + \frac{2b^2}{a} + a^2 + a^2 b\right)\tan^3\theta_q - (2ab^2 + 3b + a)\tan\theta_q \tag{4-14}$$

$$E2 = 2b^2\tan^4\theta_q - 2(a+b)^2\tan^2\theta_q + 2ab \tag{4-15}$$

However, the result of (4-13) is still a complicated fractional expression that contains polynomials of $\tan\theta_q$ on both numerator and denominator with the highest-order terms of $\tan^6\theta_q \cdot \sec^2\theta_q$ and $\tan^8\theta_q$, respectively.

According to the limits of the functions,

$$\lim_{\theta q \to \frac{\pi}{2}} \sin\theta_q = 1 \; and \; \lim_{\theta q \to \frac{\pi}{2}} \cos\theta_q = 0 \tag{4-16}$$

And then,

$$\lim_{\theta q \to \frac{\pi}{2}} \tan\theta_q = \sec\theta_q = \infty \tag{4-17}$$

So that, $\tan^6\theta_q \cdot \sec^2\theta_q$ and $\tan^8\theta_q$ have the same-order infinity, and, we can only take the coefficients of the highest terms into account to calculate the ratio. Finally, we can obtain

$$\frac{d[\mathrm{Arg}(S_{C21})]}{df} = -\left(a + \frac{1}{a} + \frac{a^2}{2b^2} + \frac{a^2}{2b}\right)\frac{\pi}{2f_0} \tag{4-18}$$

It is clear that the derivative of each path phase shift can be independently adjusted by manipulating the values of *a* and *b* in an individual path. More detailed characters of the phase-shifter group can

be revealed by defining a new function of D(a,b) as below and depicting their performance in Figure 4-9.

$$\mathrm{D}(a,b)=\frac{d[\mathrm{Arg}(S_{C21})]}{df}\cdot f_0=-\left(a+\frac{1}{a}+\frac{a^2}{2b^2}+\frac{a^2}{2b}\right)\frac{\pi}{2} \tag{4-19}$$

The set of curves in Figure 4-9 exhibits the adjustable range of D(a, b), or precisely, the derivative of the phase shift at f_0 by changing a and b. It is the ability to counterbalance the effect of the phase shift derivative from the two outer sidelines to implement the zero-derivative phase shift. There is an adequate margin to select appropriate a and b to cover a phase shift greater than 2π.

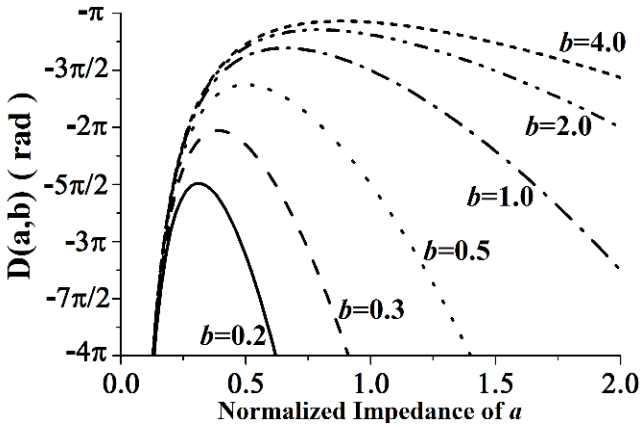

Figure 4-9. Curves of D(a,b) versus a for different values of b.

4.3 Examples and Results

A phase-shifter group with three delays, 0°, 45°, and 90°, are required in the Link1 layer of a 16 × 16 2D-BM. Using the function D(a,b) or Figure 4-9, the design parameters of this example can be found as listed in Table III. In this case, the value of a is kept the same among the three paths, but the values of b are varied.

Table III Design Parameters for the Phase-shifter Group Based on D(a,b)

Number of paths	a	b	D(a , b)[a]	θ_r^a
Path1	0.80	1.35	-1.23π	0.50π
Path2	0.80	0.79	-1.48π	0.25π
Path3	0.80	0.60	-1.74π	0.00π

[a] The unit for electrical length is radian

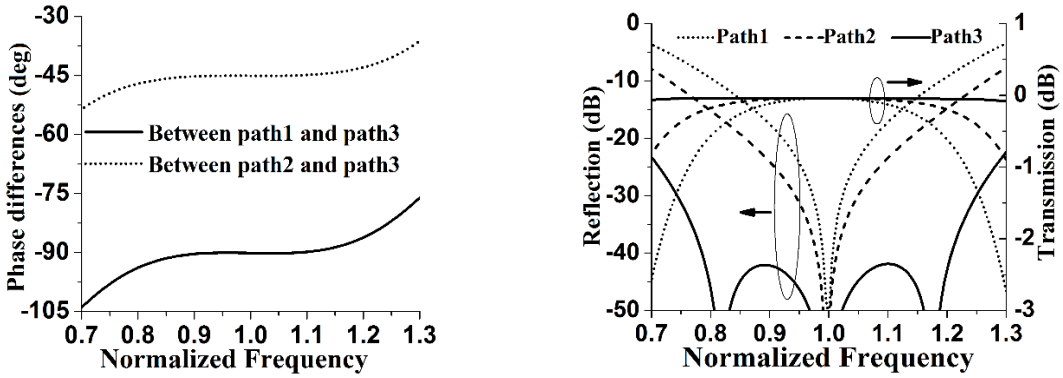

(a) Phase shifting (b) Reflection and transmission

Figure 4-10. Results of the phase-shifter group calculated by the transmission line model using the parameters in Table III.

The numerical results calculated by the transmission line model are demonstrated in Figure 4-10. All the requirements of (4-2) - (4-5) can be adequately satisfied at the central frequency. Besides, it is not difficult to imagine that more paths with various phase shifts can be achieved by duplicating the same procedure.

The proposed structure of the phase-shifter group has more potential to match broader bandwidth if the constraint conditions among Z_m, Z_n, and Z_t are released, as mentioned in the premise. However, the analytical solution for this case will be more difficult to be obtained and applied due to the increased number of variables.

Table IV Improved Design Parameters Improved for Better Bandwidth

Number of paths	Z_m	Z_n	Z_t	θ_r
Path1	0.84	1.35	0.80	0.50π
Path2	0.84	0.79	0.70	0.25π
Path3	0.84	0.60	0.64	0.00π

All the characteristic impedances are normalized by Z0; the unit for electrical length is radian

An example of distinct values of Z_m, Z_n, and Z_t for the same requirement is demonstrated in Table IV and Figure 4-11 for comparison. It can be found that by applying different values to Z_m, Z_n, and Z_t, the matching bandwidth can be remarkably expanded. Though there are some derivations of phase shift near the center frequency, the phase variation is less than ±7°, which could be acceptable for most of the cases.

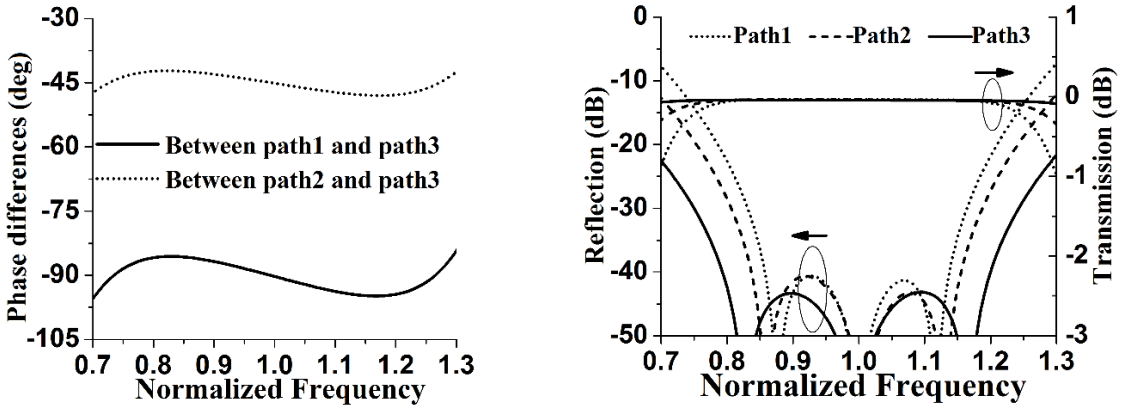

(a) Phase shift results (b) Reflection and transmission results

Figure 4-11. Results based on the parameter in Table IV.

An experimental example of 16 × 16 2D-BM based on two traditional 4 × 4 BMs working at 2.4 GHz is designed, fabricated, and measured for verification and illustration. The back-to-back double layer microstrip line is employed, and RO4350B laminate with 20 mil thickness is exploited for each layer. For saving space, MMCX- type connectors are utilized in this design.

As shown in Figure 4-12, all output ports are placed on the same side surface and arranged in a square grid with 61 mm intervals along with both vertical and horizontal directions for the convenience to feed the array. The dotted rectangles with a phase value indicate the paths of a phase-shifter group and its individual phase shift. The two dotted circles on both views indicate two signs that identify the same position and the same direction on both sides of the board. All input- and output- ports are labeled with port numbers corresponding to the positions and connections in Figure 4-2 (b). The two triangular signs on the top of both views marked by dotted circles are intended to indicate the same position and same direction of the board on both sides.

Though the layout of the example is generally obtained from the scheme illustrated in Figure 4-6, some improvements are applied. Firstly, each of the eight-port hybrids is separately placed onto two sides, more clearly, two opposite quadratic couplers in an eight-port hybrid are arranged on the same side. Then, all phase-shifter groups are routed into meandering lines to save space. Besides, an open-end transmission line with approximately half-wavelength is shunted to each input port for broader matching bandwidth by adjusting the impedance matching to compensate for the mismatching at some frequency points within the bandwidth.

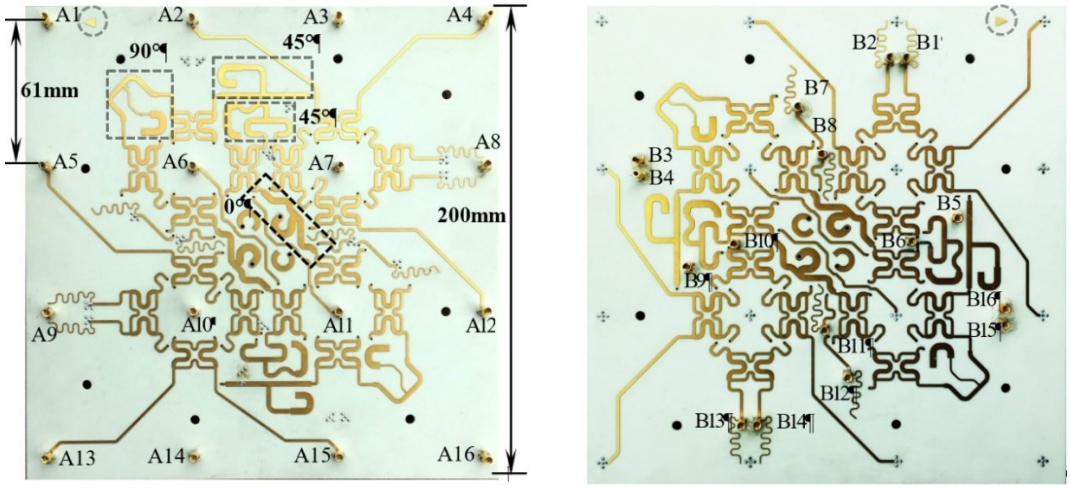

(a) Front view (b) Rear view

Figure 4-12. Photos of the prototype of the 2D-BM.

The measurement results of matching, power division, isolation, and phase differences are displayed in Figure 4-13 and Figure 4-14. Due to the symmetrical configuration, and to save space, only some representative results are selected and demonstrated here. In Figure 4-13, acceptable matching performance with less than -10 dB reflection covering 2.2 GHz to 2.6 GHz is observed. The unbalance of power division is less than ±1.2 dB and approximately -1.8 dB average insertion loss is observed within the bandwidth.

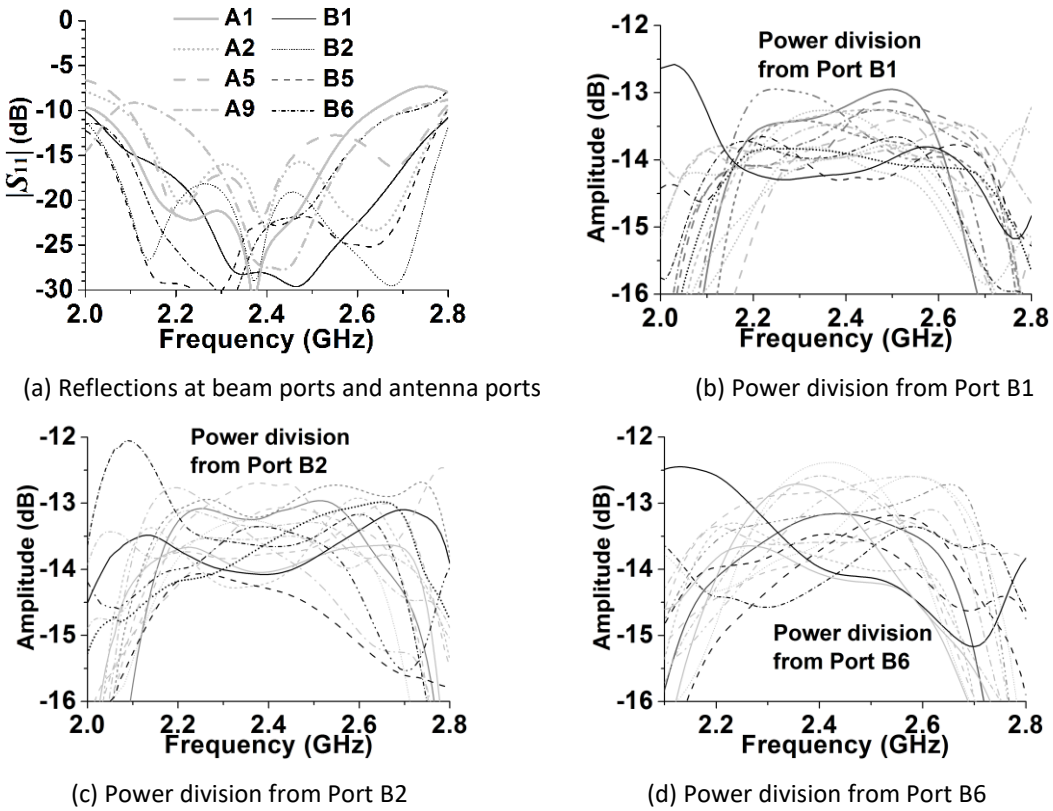

(a) Reflections at beam ports and antenna ports

(b) Power division from Port B1

(c) Power division from Port B2

(d) Power division from Port B6

Figure 4-13. Measure results of return loss (a) and power division (b) - (d).

Figure 4-14 indicates that the isolations among the input ports exhibit reasonable isolation better than -10 dB over 2.2 to 2.6 GHz. Moreover, the relatively inferior isolations come from the same quadratic coupler, the same eight-port hybrid, and the symmetrical input port according to the center of the layer of Stage1 shown in Figure 4-6 (d). The progressive phase differences between adjacent rows and adjacent columns excited by B2 port are shown in Figure 4-14 (c) and (d). The

variations of the phase differences are approximately less than ±7° within the bandwidth of 2.2 GHz to 2.6 GHz.

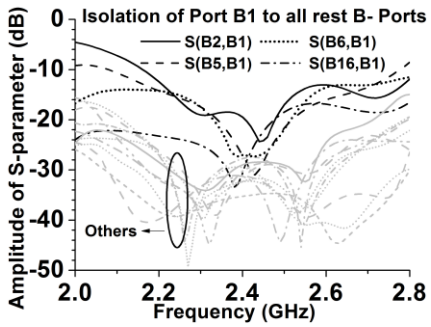

(a) Measured results of isolation from B1

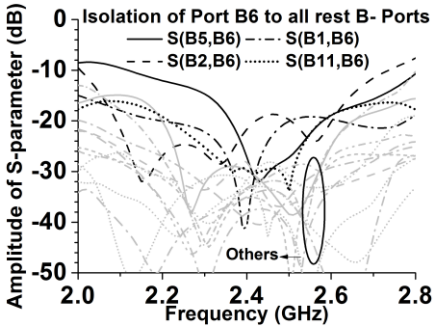

(b) Measured results of isolation from B6

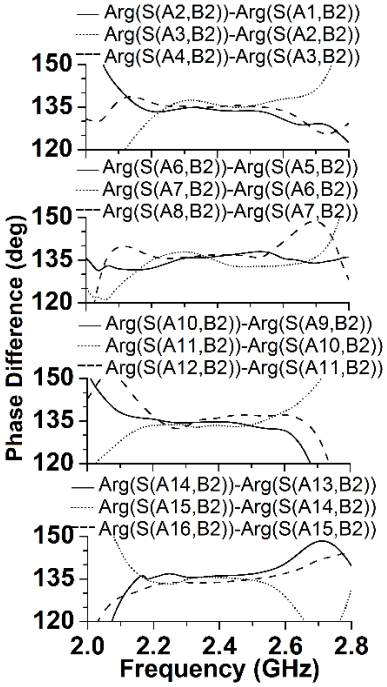

(c) Measured phase differences between columns

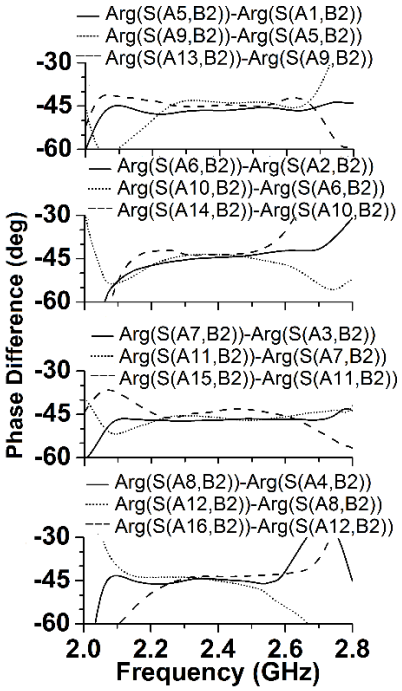

(d) Measured phase differences between rows

Figure 4-14. Measured results of isolation, (a) and (b), and phase differences (c) and (d).

The series of calculated array factors based on the measured results is shown in Figure 4-15 to show the 2-D beam-forming capability. Here, the spacing between the elements is a half wavelength. The definition of a coordinate system is the same as Figure 4-1 (b). The 16 beams with spatially orthogonal directions can be realized. Therefore, the two-dimensional beam

distribution can be seen as the spatial multiplication of two independent planar beam distributions. That means some technologies with flexible beam configurations discussed in Chapter 6 can be applied in 2D-BM for various two-dimensional beam distributions.

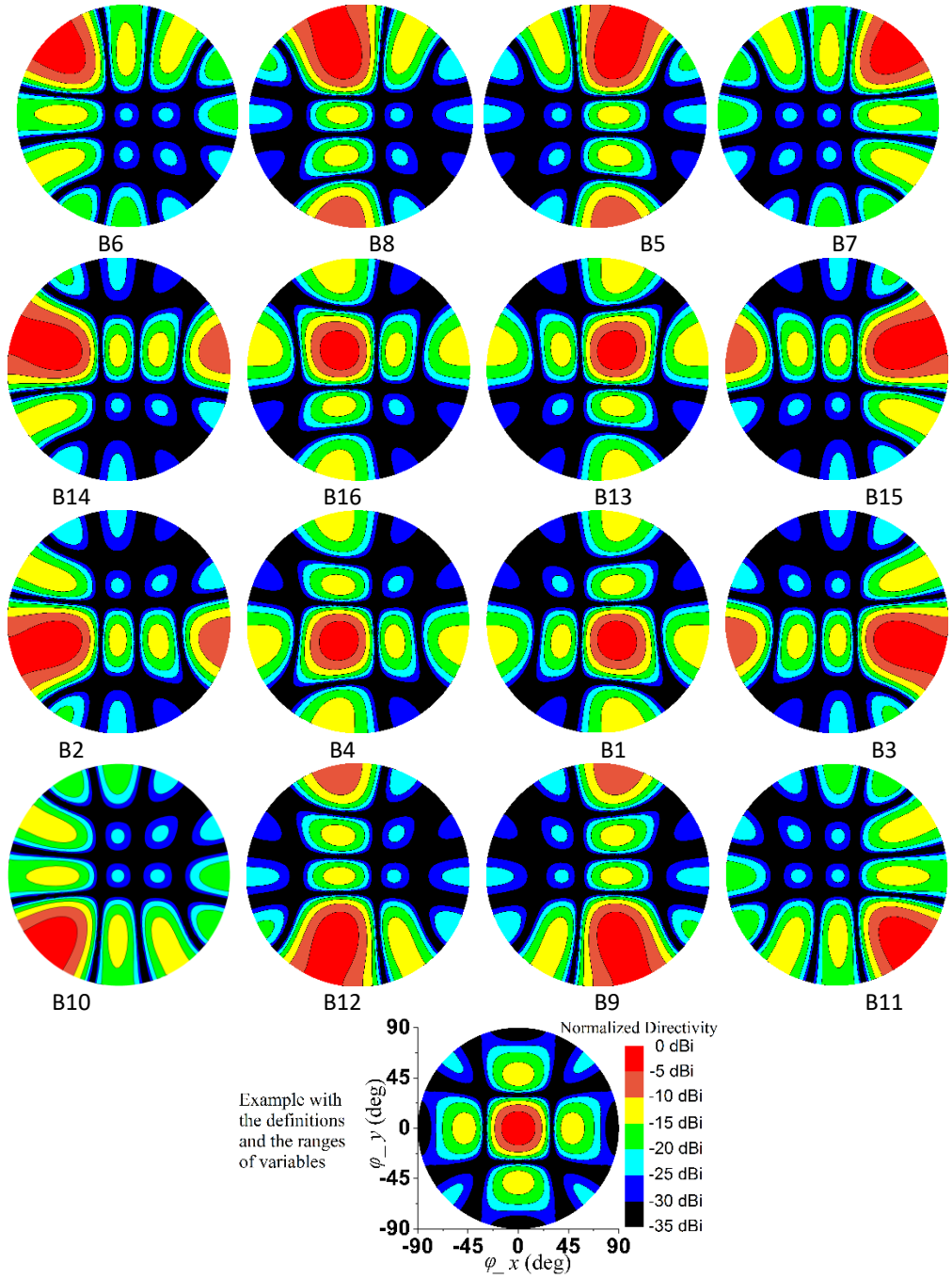

Figure 4-15. Calculated array factors with the excited port numbers expressed as normalized directivity. Here, $\varphi\_x = \theta \cos \varphi$, $\varphi\_y = \theta \sin \varphi$. The definitions and the ranges of variables for all figures are illustrated in the bottom.

Chapter 5

Eight-Port Coupler and Applications

A compact planar eight-port coupler without bends, junctions, vias, and steps is proposed in this chapter, as well as two application examples on monopulse antenna arrays as two-dimensional (2-D) and dual-polarized comparators respectively.

The coupler is based on a back-to-back double layer microstrip configuration with a common ground in between, and the entire structure is only composed of two half-wavelength microstrips on both layers with two half-wavelength slots in the ground. Remarkably, the property of the coupler at the central frequency is barely sensitive to the widths of either the strips or the slots according to the principle of operation. The analytical expressions of the characteristics are deduced by the symmetry and equivalent circuit model, as well as verified by measured results. Satisfying performance for matching, power division, and isolation can be achieved in fractional bandwidth of more than 24% centered at 5.8 GHz. Two examples of a compact comparator based on the coupler for monopulse arrays with 2-D and dual-polarized sum-difference beams are designed and demonstrated respectively, the concise configuration with reasonable performance can be achieved.

Some of the related work has been published on conference papers [78], [79], and [107].

5.1 Structural Configuration

The three-dimensional perspective diagram of the proposed eight-port coupler is illustrated in Figure 5-1 (a) to show the back-to-back microstrip configuration. Further, the layouts for the three

metal layers are depicted in Figure 5-1 (b) to elaborate on the relative positions of the strips, slots, and the eight ports with numbers.

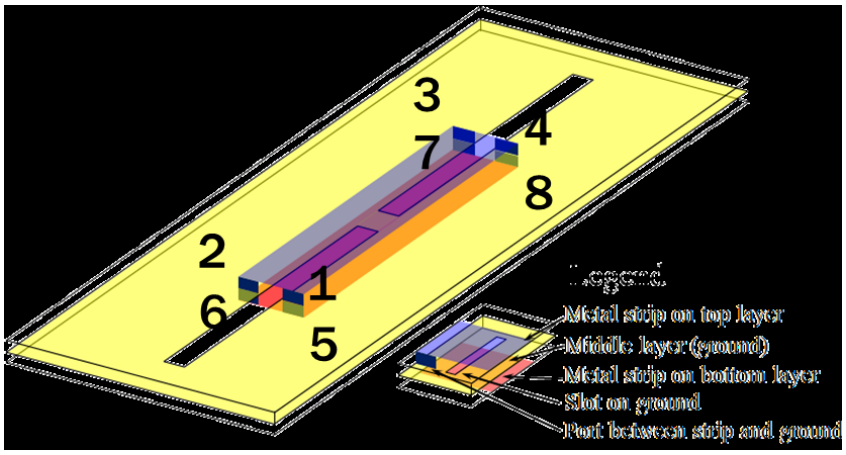

(a) Three-dimensional perspective with numbers of port

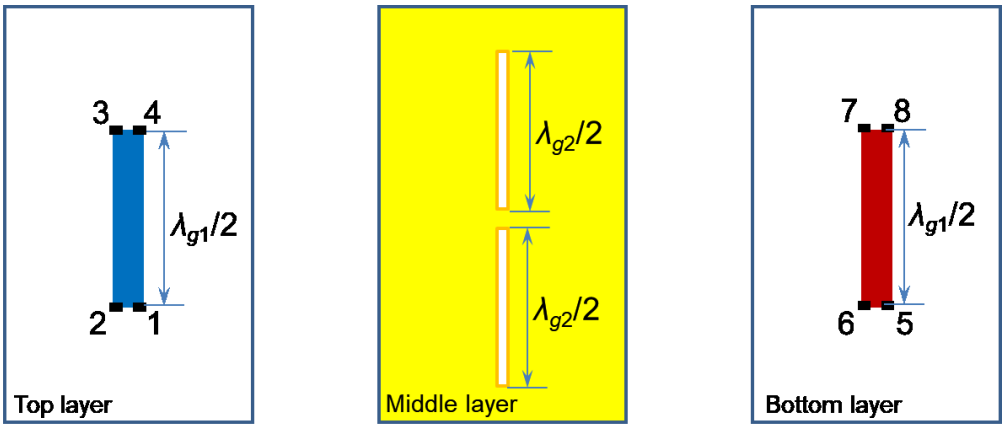

(b) Layouts for each of the three layers

Figure 5-1. Diagrams of the proposed eight-port coupler.

It can be found that the two strips on both layers with two slots on the common ground plane are the complete structures. Concretely, both strips are aligned with each other about the normal direction of the circuit plane. Then, the two slots in the ground are arranged in parallel to the strips, successively aligned with each other, and centered in the middle of the strips. The eight ports are located at all corners of both strips.

In terms of the characteristics of the directional coupler, the four ports on both layers at two opposite sides can be utilized as one set of input/isolation ports; another four ports are the output ports with equal output amplitudes. For example, when any one of Port 1, 2, 7 and 8 being used as an input port, the other three ports are isolated ports, and Port 3, 4, 5 and 6 are output ports.

5.2 Methodology

5.2.1 Analysis Method Based on Complete Symmetry

It is evident that the proposed coupler is a highly symmetrical structure about three planes, which are Plane 1, Plane 2, and Plane 3, respectively, and they are spatially orthogonal to each other, as shown in Figure 5-2 (a). The symmetry with three reference planes refers to the 'complete symmetry' [108] and can consequently be utilized to obtain the properties of the coupler based on a much simpler circuit model.

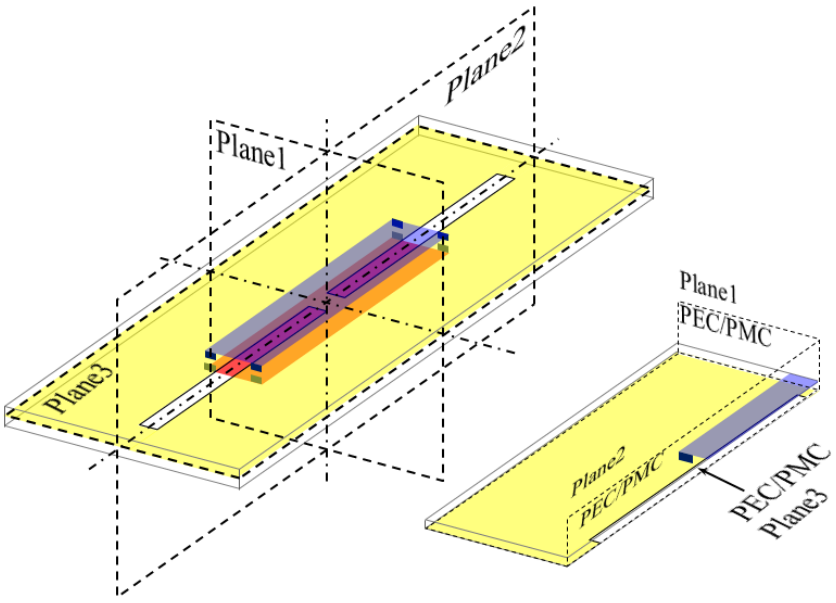

(a) Complete symmetry with three reference planes (b) One-eighth circuit

Figure 5-2. Complete symmetry of the eight-port coupler with three reference planes and the one-eighth circuit of the coupler with three reference planes.

It has been known that the properties of the symmetrical circuit with a reference plane can be expressed by the combinations of the properties of the even and odd modes, which have the half circuit structure with a perfect electrical conductor (PEC) or perfect magneto conductor (PMC) boundaries on the reference planes. Similarly, the performance of a complete symmetrical circuit with three reference planes can be characterized by the combinations of several modes, which are derived from the one-eighth of the circuit with PEC or PMC on the reference plane, as shown in Figure 5-2 (b). More clearly, there are entirely (2^3) eight different one-eighth circuits, or modes, because each of the three reference planes could be PEC or PMC. Besides, each of the one-eighth circuits has only one port, and therefore the scattering property can be characterized by S_{11}.

To describe and differentiate the eight different S_{11} of the modes, letter '*S*' with three subscripts is utilized to indicate the particular mode, which also indicates PEC or PMC boundaries applied to each one of the three reference planes in sequence. For example, S_{eoe} means S_{11} of 'even-odd-even' mode, which is derived from the one-eighth circuit with PMC, PEC, and PMC boundaries on Plane 1, Plane 2, and Plane 3, respectively.

Based on the complete symmetry feature and the reciprocity of the passive lossless network, the scattering parameters of Port 1 of the eight-port coupler, S_{EP11}, S_{EP12} … S_{EP18} can be expressed by (5-1) - (5-8).

$$S_{EP\,11} = \frac{1}{8}(S_{eee} + S_{oee} + S_{eoe} + S_{ooe} + S_{eeo} + S_{oeo} + S_{eoo} + S_{ooo}) \tag{5-1}$$

$$S_{EP\,12} = \frac{1}{8}(S_{eee} + S_{oee} - S_{eoe} - S_{ooe} + S_{eeo} + S_{oeo} - S_{eoo} - S_{ooo}) \tag{5-2}$$

$$S_{EP\,13} = \frac{1}{8}(S_{eee} - S_{oee} - S_{eoe} + S_{ooe} + S_{eeo} - S_{oeo} - S_{eoo} + S_{ooo}) \tag{5-3}$$

$$S_{EP\,14} = \frac{1}{8}(S_{eee} - S_{oee} + S_{eoe} - S_{ooe} + S_{eeo} - S_{oeo} + S_{eoo} + S_{ooo}) \tag{5-4}$$

$$S_{EP\ 15} = \frac{1}{8}(S_{eee} + S_{oee} + S_{eoe} + S_{ooe} - S_{eeo} - S_{oeo} - S_{eoo} - S_{ooo}) \quad (5\text{-}5)$$

$$S_{EP\ 16} = \frac{1}{8}(S_{eee} + S_{oee} - S_{eoe} - S_{ooe} - S_{eeo} - S_{oeo} + S_{eoo} + S_{ooo}) \quad (5\text{-}6)$$

$$S_{EP\ 17} = \frac{1}{8}(S_{eee} - S_{oee} - S_{eoe} + S_{ooe} - S_{eeo} + S_{oeo} + S_{eoo} - S_{ooo}) \quad (5\text{-}7)$$

$$S_{EP\ 18} = \frac{1}{8}(S_{eee} - S_{oee} + S_{eoe} - S_{ooe} - S_{eeo} + S_{oeo} - S_{eoo} + S_{ooo}) \quad (5\text{-}8)$$

Due to the complete symmetry, all other seven ports have entirely identical performance as Port 1, but only the various correspondences with the respectively coupled ports and isolated ports. More concretely, the whole scattering matrix of the eight-port coupler, [S_{EP}], is given by (5-9) [108].

$$[S_{EP}] = [A] \cdot [S_d] \cdot [A] \quad (5\text{-}9)$$

Here, [A] is a symmetrical matrix to represent the symmetrical structural property, as defined in (5-10). It also depends on the sequence of the port number.

$$[A] = \frac{\sqrt{2}}{4}\begin{bmatrix} 1 & 1 & 1 & 1 & 1 & 1 & 1 & 1 \\ 1 & 1 & -1 & -1 & 1 & 1 & -1 & -1 \\ 1 & -1 & -1 & 1 & 1 & -1 & -1 & 1 \\ 1 & -1 & 1 & -1 & 1 & -1 & 1 & -1 \\ 1 & 1 & 1 & 1 & -1 & -1 & -1 & -1 \\ 1 & 1 & -1 & -1 & -1 & -1 & 1 & 1 \\ 1 & -1 & -1 & 1 & -1 & 1 & 1 & -1 \\ 1 & -1 & 1 & -1 & -1 & 1 & -1 & 1 \end{bmatrix} \quad (5\text{-}10)$$

Another matrix, [S_d], is a diagonal matrix consisting of the eight S_{11} of the one-eighth circuits with different boundaries, S_{eee} - S_{ooo}, which are also the eigenvalues of [S_{EP}] [108], as defined in (5-11). For a lossless device such as the proposed coupler, these eigenvalues must have unit amplitude.

$$[S_d] = \begin{bmatrix} S_{eee} & 0 & 0 & 0 & 0 & 0 & 0 & 0 \\ 0 & S_{oee} & 0 & 0 & 0 & 0 & 0 & 0 \\ 0 & 0 & S_{eoe} & 0 & 0 & 0 & 0 & 0 \\ 0 & 0 & 0 & S_{ooe} & 0 & 0 & 0 & 0 \\ 0 & 0 & 0 & 0 & S_{eeo} & 0 & 0 & 0 \\ 0 & 0 & 0 & 0 & 0 & S_{oeo} & 0 & 0 \\ 0 & 0 & 0 & 0 & 0 & 0 & S_{eoo} & 0 \\ 0 & 0 & 0 & 0 & 0 & 0 & 0 & S_{ooo} \end{bmatrix} \quad (5\text{-}11)$$

It is evident that the characteristics of the eight-port coupler can be derived from the eight eigenvalues through (5-1) - (5-8) or (5-9) - (5-11). Conversely, these eigenvalues can be acquired from a given performance of the coupler, and therefore to design the coupler.

5.2.2 Design of Eight-Port Coupler

To work as a typical coupler, the fundamental features should include impedance matching, isolation, and equal-amplitude directional coupling. As a particular instance and exemplified by the Port 1 of the eight-port coupler, the features can be characterized by conditions (5-12) - (5-14), respectively.

$$S_{EP\,11} = 0 \tag{5-12}$$

$$S_{EP\,12} = 0, \quad S_{EP\,17} = 0, \quad S_{EP\,18} = 0 \tag{5-13}$$

$$S_{EP\,13} = -\frac{1}{2},\ S_{EP\,14} = -\frac{1}{2},\ S_{EP\,15} = \frac{1}{2},\ S_{EP\,16} = -\frac{1}{2}\ . \tag{5-14}$$

Here, (5-12) represents the characteristics of the ideal matching at Port 1; (5-13) characterizes the isolation of Port 2, Port 7, and Port 8; (5-14) indicates the coupling to Port 3, Port 4, Port 5, and Port 6. These properties (5-12) - (5-14) are the same as described at the end of Section 5.1. The solution of the eigenvalues can consequently be obtained

$$\begin{aligned} &S_{eee} = -1, \quad S_{oee} = 1, \quad S_{eoe} = 1, \quad S_{ooe} = 1 \\ &S_{eeo} = -1, \quad S_{oeo} = 1, \quad S_{eoo} = -1, \quad S_{ooo} = -1\ . \end{aligned} \tag{5-15}$$

The series of S_{11} with the values of 1 or -1 means the electrically equivalent open or short at the port. In other words, the one-eighth circuit should behave as open or short circuit alternatively, according to which PEC or PMC boundary is applied to the reference plane.

On the other hand, in terms of the structure, the one-eighth circuit can be generally seen as a microstrip line above a slot (deformed ground plane) with one boundary at the end and two

boundaries parallel to the microstrip line and the slot. It is not difficult to image that alternatively by applying a PEC or PMC at the end of a segment of the strip, which results in the change between short or open. Besides, changing the length of this segment of the transmission line by a quarter wavelength, either microstrip or slot, can also lead to the change between short and open. Thus, the structure composed of microstrip lines and slots with several quarter-wavelength segments can be finally obtained, as shown in Figure 5-2 (b). For sure, any odd integer multiple of quarter wavelength can theoretically also work, but with longer physical length and narrower bandwidth. For simplicity and miniaturization, only the case with one-quarter wavelength is discussed in this chapter.

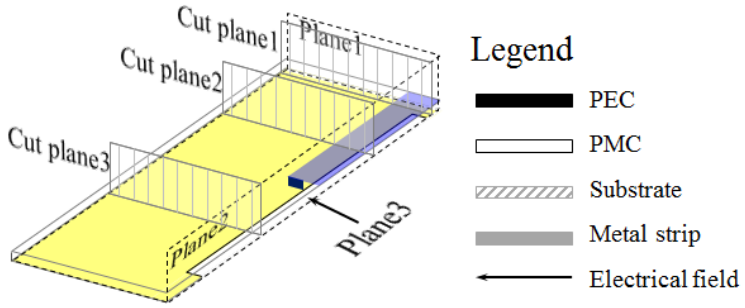

(a) Positions of three cut planes

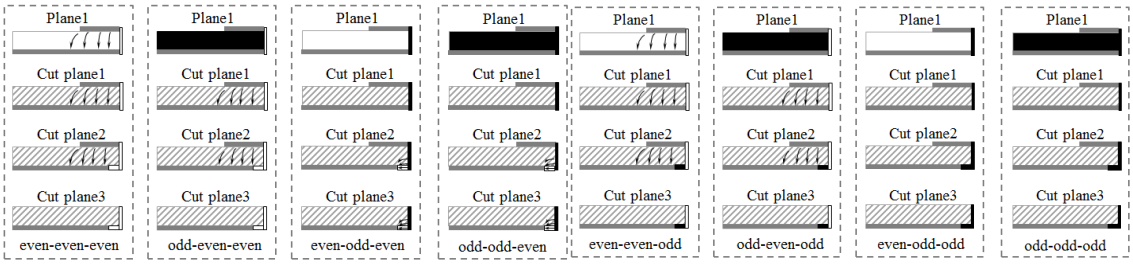

(b) Legend for electrical field distribution

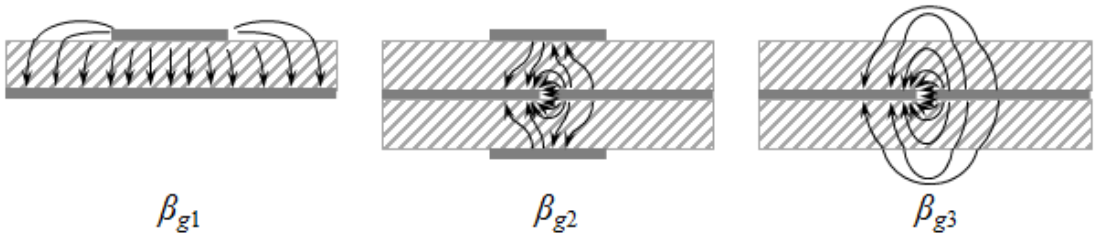

(c) Electrical field distributions on each cut plane for eight different modes

Figure 5-3 Positions of three cut planes located on the one-eighth circuits.

Two notable points of this design should be pointed out for a more elaborate description. Firstly, the characteristic impedance of the microstrip and slot will theoretically not affect the property of the coupler, because the impedance transition between the open and short by the quarter-wavelength conversion is irrelevant to the characteristic impedance. Furthermore, the characteristic impedance of the microstrip and slot are not necessary to be constant along the line. For sure, all widths of the microstrip and slot are supposed to be much smaller than the wavelength and without suffering from leakage (radiation). Secondly, the microstrips and slots with an electrical quarter wavelength, for example, may have different physical lengths due to the different propagation coefficients, as $\lambda_{g1}/4$, $\lambda_{g2}/4$, and $\lambda_{g3}/4$ shown in Figure 5-2 (b).

To clarify the electrical field distributions and therefore to determine the propagation coefficients, the distributions at different plane cuts for all eight modes are illustrated in Figure 5-3. Notably, there is a gap between Plane 1 and the internal end of the slot to prevent the joining the two slots with each other, and, the Plane 1 cut is located at the middle of this gap. The reason for the existence of this gap is the difference in propagation coefficients between the microstrip and the slots. The properties of eight modes will be demonstrated, respectively.

Even-even-even mode: It behaves as a microstrip line between Port 1 and Plane 1. The field distributions can be seen as a typical microstrip line even with the presence of the slot in the ground beneath the microstrip, the slot parallel to the microstrip will barely make an impact on the field distribution, especially when the width of the slot is much narrower than the microstrip. When a PMC is applied on Plane 1, and the length of the strip is a quarter wavelength, $\lambda_{g1}/4$, $S_{eee} = -1$.

Odd-even-even mode: It has the same transmission line as the even-even-even mode, but the PEC is applied at the end. Therefore, $S_{oee} = 1$.

Even-odd-even mode: It behaves as a slot line. Concretely, the slot line is separated into two segments by the port. One segment is partially covered by the strips, but another segment is

not, as Plane 1 and Plane 2 shown in the mode of Figure 5-3. When the lengths of the two segments have a quarter wavelength, $\lambda_{g2}/4$ and $\lambda_{g3}/4$, respectively, $S_{eoe} = 1$.

Odd-odd-even mode: It is the same as the even-odd-even mode, in terms of the property of S_{11}. Since the change on Plane 2 will not affect the matching at Port 1. Thus, $S_{ooe} = 1$.

Even-even-odd mode: It behaves as a standard microstrip line between Port 1 and Plane 1. When PMC is applied on Plane 1 and λ_{g1} is a quarter wavelength, $S_{eeo} = -1$.

Odd-even-odd mode: It has the same transmission line as the even-even-odd mode, but PMC is applied at the end. Thus, $S_{oeo} = -1$.

Even-odd-odd and odd-odd-odd modes: The port is equivalently shorted to the ground by the PEC on Plane 2 and Plane 3. Therefore, $S_{eoo} = -1$, and $S_{ooo} = -1$.

Based on the above analysis, the required eigenvalues listed in (5-15) can be realized, and the expected properties of the coupler listed in (5-12) - (5-14) can consequently be achieved, when the lengths of the microstrips and the slots are $\lambda_{g1}/4$, $\lambda_{g2}/4$, and $\lambda_{g3}/4$, respectively, as indicated in Figure 5-2 (b). Besides, the propagation coefficients, β_{g1}, β_{g2}, and β_{g3}, which are corresponding to $\lambda_{g1}/4$, $\lambda_{g2}/4$, and $\lambda_{g3}/4$, respectively, can be calculated according to the cross-sections shown in Figure 5-3 (c) by numerical or analytical methods.

Notably, by numerical simulation and comparison, it can be found that β_{g2} is slightly greater than β_{g1}. Based on the electrical field distribution on the traverse cut plane inside the substrate, as the diagrammatic sketches shown in Figure 5-3 (c), β_{g2} has more proportionality to the electric field inside the substrate more than β_{g1}. That means the effective permittivity of β_{g2} is greater than β_{g1}. In other words, $\lambda_{g2}/4$ has a shorter physical length than$\lambda_{g1}/4$.

Besides, the transverse propagation across the microstrip is ignored in the previous discussion because it is assumed that the widths of microstrip and slots are much smaller than the wavelength. If the widths of microstrip or slots are not negligible, the effective electrical lengths between the

port and Plane1 and between the port and Plane 2 will be evidently affected. That means narrower widths of microstrip and slots would be helpful to approach the ideal performance, though the characteristic impedances, apparently, will not affect the performance. Similarly, the thickness of the two-layer substrate can have the same effect on the performance due to the complete symmetry.

5.2.3 Properties of Eight-Port Coupler

According to the equivalent circuit of each mode described in the last subsection, the eight S_{11} for each one-eighth circuit, or, S_{eee} - S_{ooo}, can be obtained by the transmission line equation [102]. Therefore, the ideal properties of the proposed eight-port coupler based on ideal transmission lines can be calculated through (5-1) - (5-8). Here, the ideal transmission lines mean that the microstrips or slots are lossless and have the characteristic impedances independent from the changing of frequency. Besides, their electrical lengths are precisely a quarter wavelength at the center frequency. All the delays, discontinuities due to the traverse propagation and junctions are ignored.

The amplitude and phase features of the coupler for three cases with different characteristic impedances of microstrips and slots are shown in Figure 5-4. Here, the S_{11} - S_{81} express the same properties of S_{EP11} - S_{EP81} mentioned in (5-12) - (5-14). It is assumed that the characteristic impedance of microstrip is Z_{0ms}, and the two segments of the slot, either with or without covering by the strips, have the same characteristic impedance, Z_{0sl}.

First, all expected features listed in (5-12) - (5-14) can be achieved at the center frequency for various characteristic impedances. Especially, the S_{71} and S_{81} have the amplitude close to -∞ dB during the entire calculated bandwidth. Secondly, the Z_{0ms} will affect the consistency of S_{11} and S_{21}. Concretely, when Z_{0ms} = 50 Ω, S_{11} and S_{21} will coincide with each other; when Z_{0ms} is

increasing, the bandwidth of S_{21} will become narrower than S_{11}, conversely, the opposite. Moreover, a higher value of Z_{0sl} will be helpful to expand the bandwidth of matching and isolation.

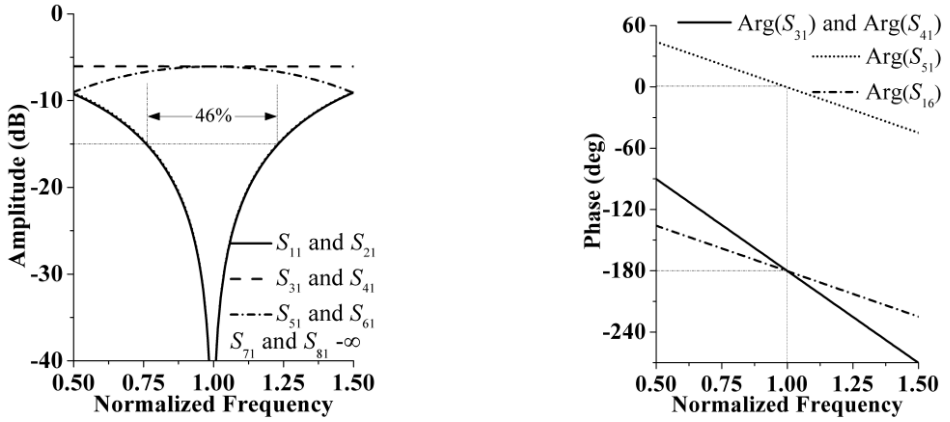

(a) Z_{0ms} = 50 Ω and Z_{0sl} =100 Ω;

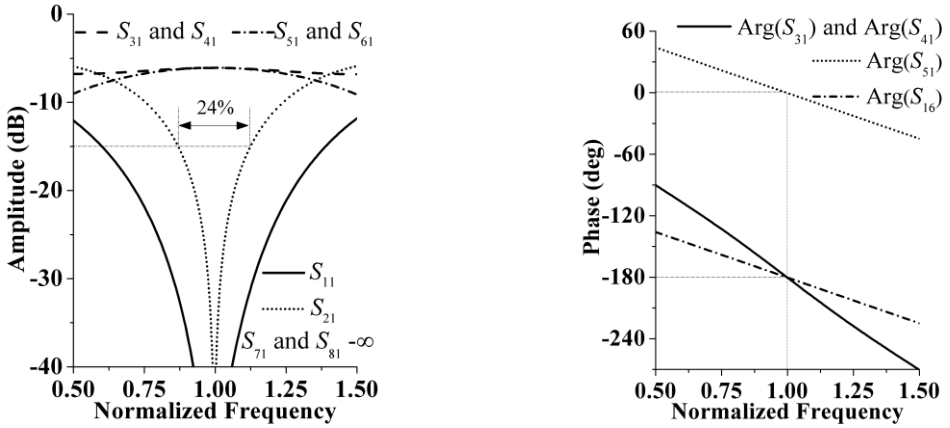

(b) Z_{0ms} = 75 Ω and Z_{0sl} =100 Ω;

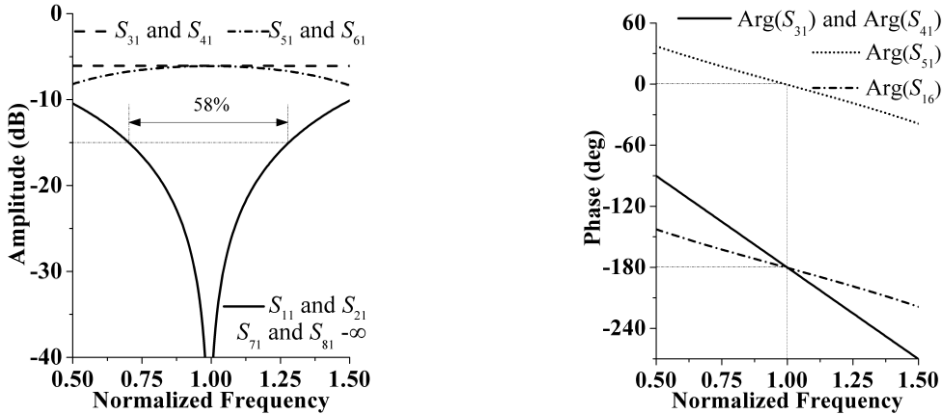

(c) Z_{0ms} = 50 Ω and Z_{0sl} =125 Ω.

Figure 5-4. Properties of the proposed eight-port coupler calculated by transmission line equation for different characteristic impedances of microstrips and slots, or Z_{0ms} and Z_{0sl}.

In terms of the phase responses at the four coupled ports, S_{31} and S_{41} have the exact same phase delay, while S_{51} and S_{61} have a constant 180° difference in between. Moreover, S_{31} and S_{41} have a greater increment of phase delay than S_{51} and S_{61} when the frequency is rising. Besides, all the phase responses are not sensitive to the varying of Z_{0ms} and Z_{0sl}.

5.2.4 2-D add/or Dual-Polarized Comparators Based on Eight-Port Coupler

As mentioned above, the feature of the coupler at a central frequency can be represented by (5-16):

$$[S_{EP}] = \frac{1}{2}\begin{bmatrix} 0 & 0 & -1 & -1 & 1 & -1 & 0 & 0 \\ 0 & 0 & -1 & -1 & -1 & 1 & 0 & 0 \\ -1 & -1 & 0 & 0 & 0 & 0 & 1 & -1 \\ -1 & -1 & 0 & 0 & 0 & 0 & -1 & 1 \\ 1 & -1 & 0 & 0 & 0 & 0 & -1 & -1 \\ -1 & 1 & 0 & 0 & 0 & 0 & -1 & -1 \\ 0 & 0 & 1 & -1 & -1 & -1 & 0 & 0 \\ 0 & 0 & -1 & 1 & -1 & -1 & 0 & 0 \end{bmatrix} \tag{5-16}$$

If using Port 3, 4, 5, and 6 as the output ports to connect with the array elements and increasing a 180-degree phase shift on port 6, the partial scattering matrix of (5-16) can be obtained as (5-17):

$$\begin{bmatrix} S_{31} & S_{41} & S_{51} & S_{61} \\ S_{32} & S_{42} & S_{52} & S_{62} \\ S_{37} & S_{47} & S_{57} & S_{67} \\ S_{38} & S_{48} & S_{58} & S_{68} \end{bmatrix} = \frac{1}{2}\begin{bmatrix} -1 & -1 & 1 & 1 \\ -1 & -1 & -1 & -1 \\ 1 & -1 & -1 & 1 \\ -1 & 1 & -1 & 1 \end{bmatrix} \tag{5-17}$$

It is clear that if Port 2 is an input port, the in-phase distribution, or the sum radiation pattern, can be achieved. Similarly, Port 1 and 7 can generate two differential radiation patterns in two orthogonal planes. Besides, Port 8 can create the product of two differential beams from Port 1 and 7. That is the principle of building a 2-D comparator based on the eight-port coupler.

For the dual-polarized case, based on the same expression (17), if connecting Port 3 and Port 4 to the two ports of one element, and Port 5 and 6 to another, the dually-polarized monopulse array can be achieved. Concretely, when Port 1 is excited, the two ports of each element are in-phase, but the two elements are out-phase to each other. When Port 2 is excited, the two ports of one element are in-phase, as well as the two elements. If the element can generate the horizontal

polarization when two ports being in-phase, the horizontally polarized difference- and sum- beams can be implemented. Consequently, Port 1 and 2 can be referred to as Port HD (horizontal difference) and Port HS (horizontal sum), respectively. Similarly, Port 3 and 4 are referred to as Port VD and Port VS.

5.3 Examples and Results

5.3.1 Eight-Port Coupler for 5.8 GHz Applications

To verify the characteristics of the proposed coupler, an example is designed for 5.8-GHz applications. The laminate of Rogers RO4003 with a 5-mil thickness and $\varepsilon_r = 3.0$ is utilized for each of the double-layer substrates. The numbers of parts and the structural parameters of the example are indicated in the schematic layout, as shown in Figure 5-5 (a) - (b). Notably, the shape of slots on the middle layer has been modified from a straight line into a “T” shape for a smaller size. The measured results of amplitude and phase responses of the example are listed in Figure 5-6. Here, Port 1 is assumed to be the input port, and therefore, the S11 represents the reflection; S31, S41, S51, and S61 characterize the power division; S21, S71, and S81 depict the isolation.

It can be found that at the central frequency, 5.8 GHz, the matching, isolation, and equal power division can be achieved with remarkably satisfying performance. Besides, the phase differences among the output ports are 0° and 180°, which agree with the analytical results. If considering -15 dB as the acceptable value for the reflection and isolation (15 dB, exactly), the fractional bandwidth is about 24% (5.15 - 6.55 GHz). The experimental example is fabricated and measured for further verification. A good agreement between simulated and measured results can be found in terms of bandwidth and general performance.

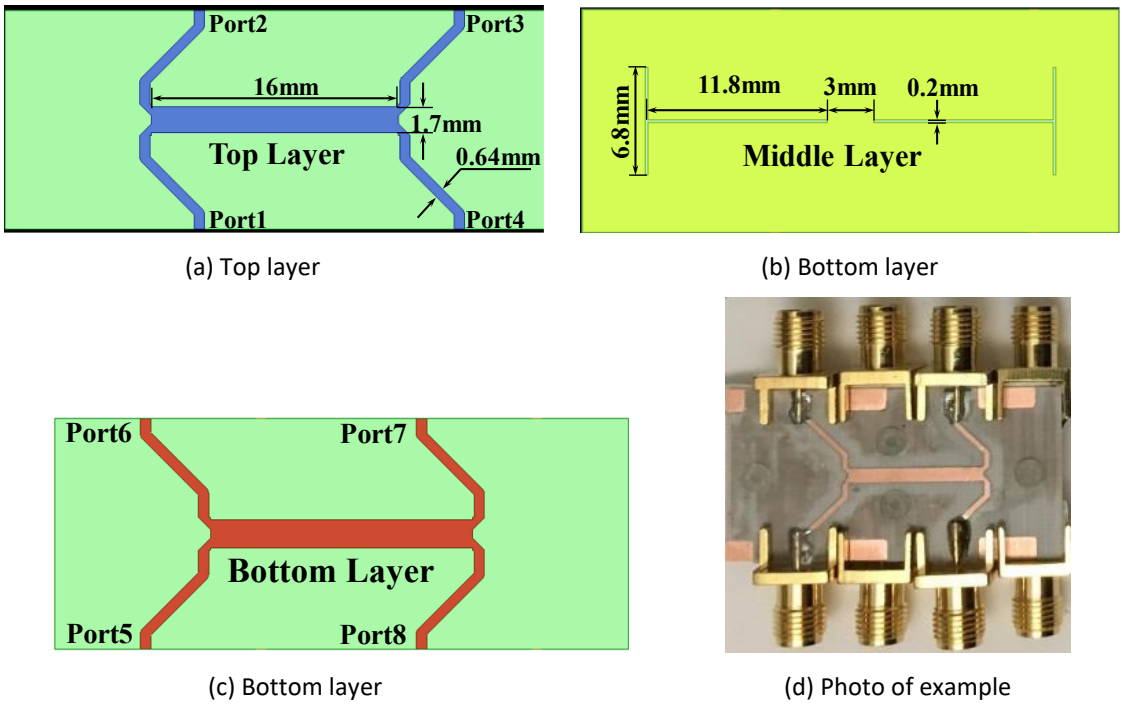

(a) Top layer

(b) Bottom layer

(c) Bottom layer

(d) Photo of example

Figure 5-5. Layouts and photo of the example for 5.8-GHz application.

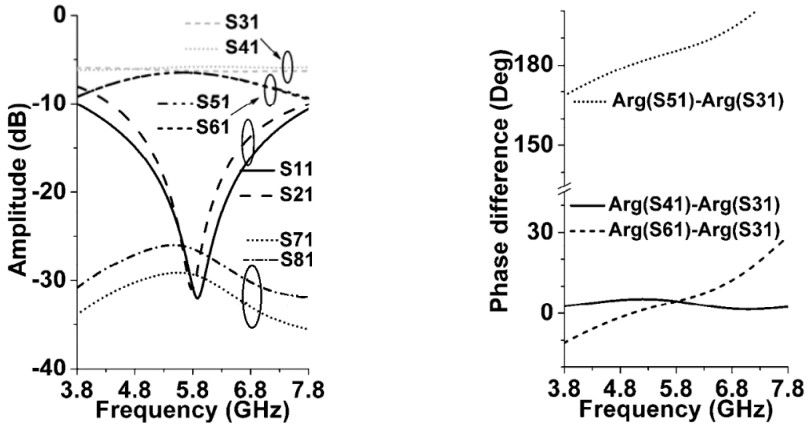

(a)amplitude

(b)phase responses

Figure 5-6. Measurement results of the eight-port coupler.

5.3.2 Comparator for 2-D Monopulse Array

A 2-D monopulse antenna array with 2×2 elements for 5.8-GHz applications is designed and simulated the 2-D comparator based on the novel eight-port coupler is demonstrated in Figure 5-7. The overall configuration, layouts of each layer, substrates parameters, and the main dimensions

of the antenna elements and feeding network are elaborated in Figure 5-7 (a) - (f). Here, the port to generate the sum radiation pattern is referred to as Port S1; the other three ports are referred to as Port D1, Port D2, and Port D3.

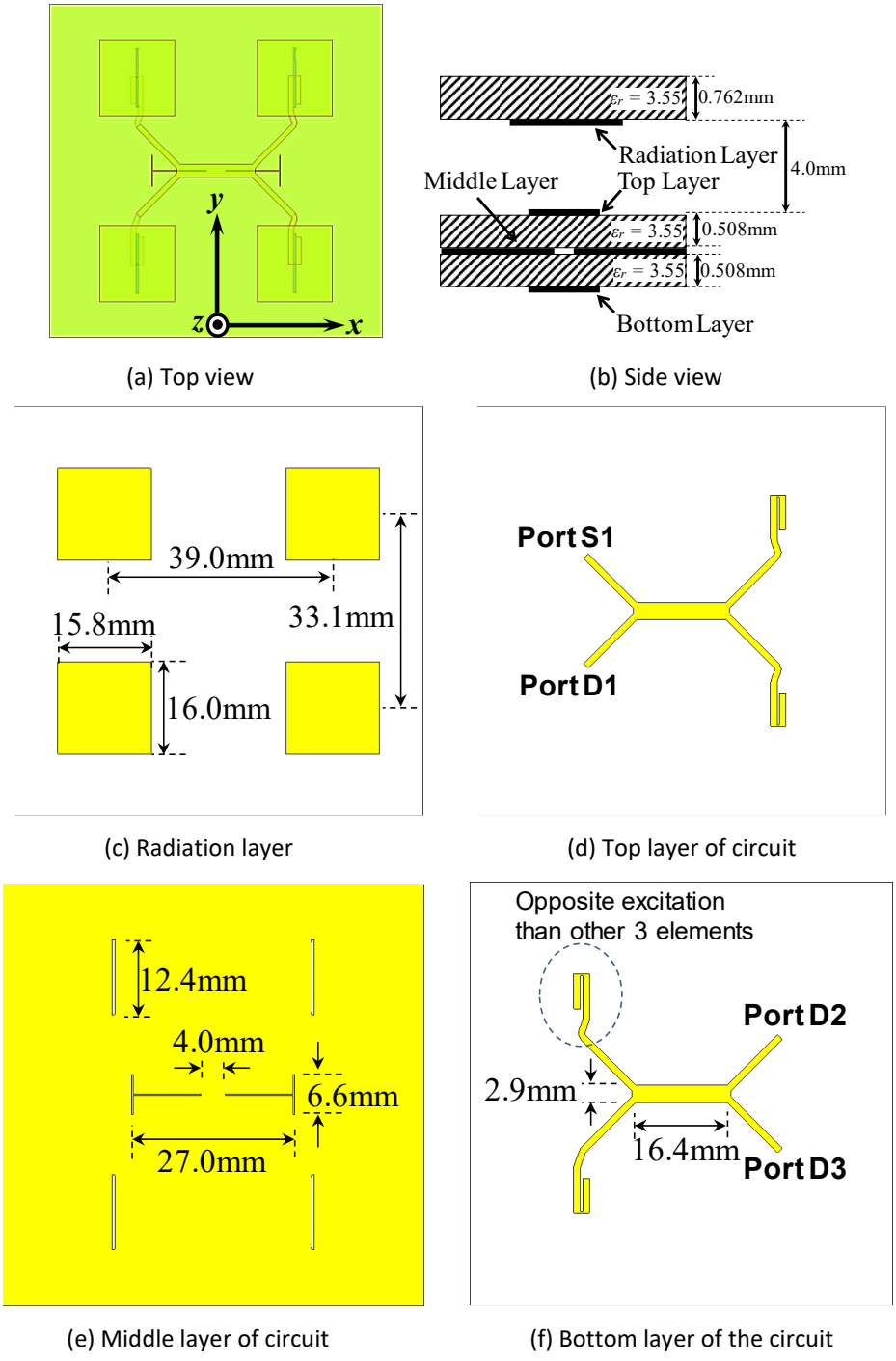

Figure 5-7. Structure of 2-D monopulse 2 × 2 array.

The remarkably compact size of the comparator can be observed by the comparison with the spacing between elements of the antenna array. Especially, only one extra component, a 180-degree phase shifter, is required to build the comparator besides the coupler, as explained in Section 5.2.4. Here, the phase shifter is replaced by an opposite excitation, which can provide a wideband phase response than phase delay lines.

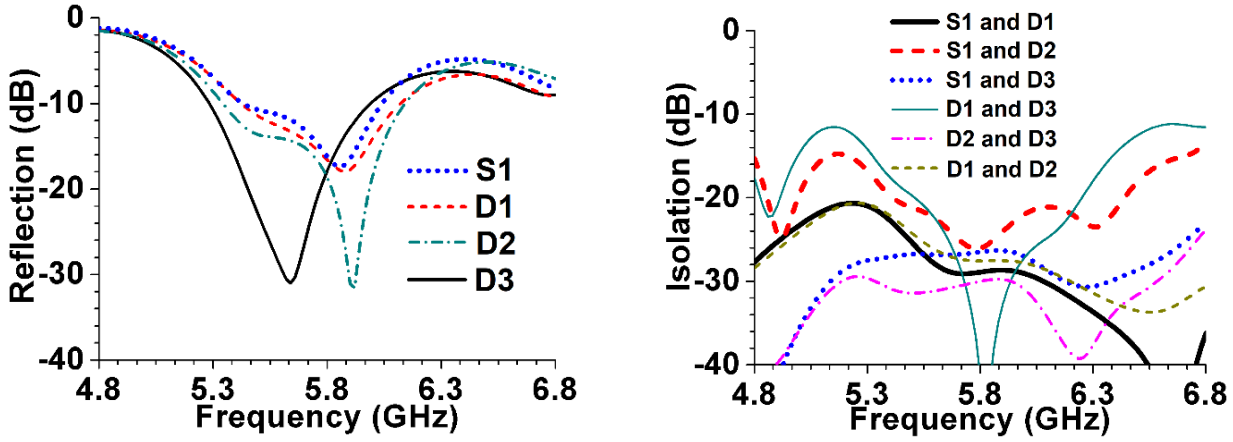

(a) Simulated results of matching

(b) Simulated results of isolation

Figure 5-8. Simulated results of the 2-D monopulse array.

The simulated results of matching, isolation, and radiation patterns are demonstrated in Figure 5-8 and Figure 5-9 to exhibit the performance of the comparator. ANSYS HFSS was utilized during modeling and simulation. The sum- and three difference- radiation patterns can be apparently observed in Figure 5-9. Besides, the reflection less than -10 dB and isolation better than 20 dB can be achieved in 5.5 - 6.1 GHz. It should be indicated that the bandwidth is mainly limited by the antenna elements rather than the comparator.

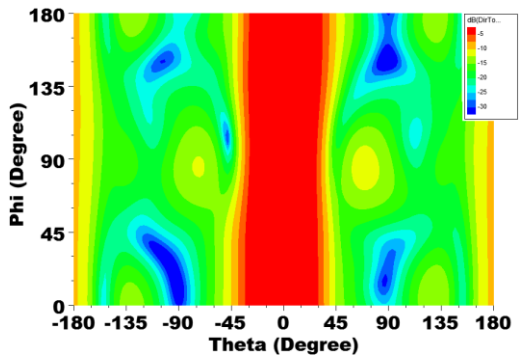

(a) Sum beam (beam S1) contour

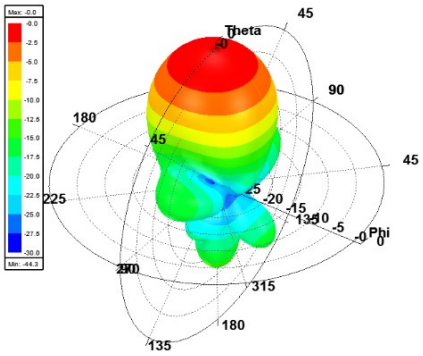

(b) Sum beam (beams S1) 3-D polar

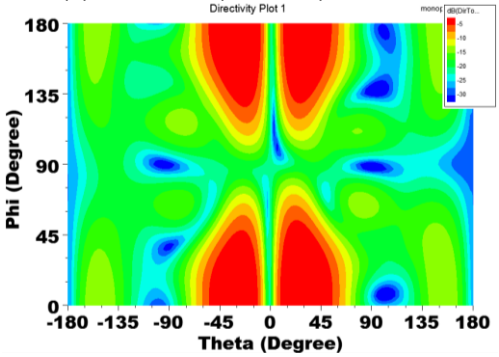

(c) Differential beam 1 (beam D1) contour

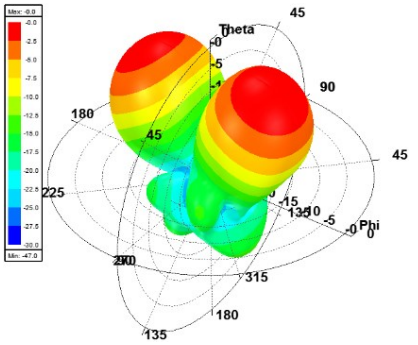

(d) Differential beam 1 (beam D1) 3-D polar

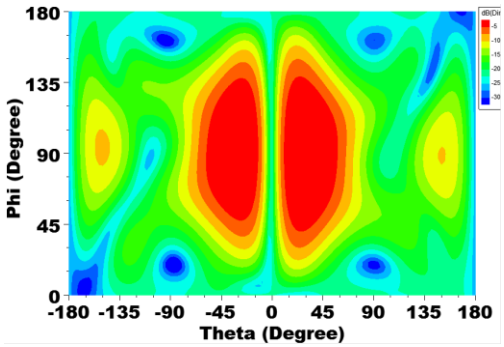

(e) Differential beam 2 (beam D2) contour

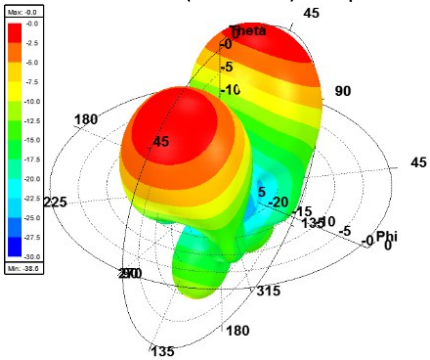

(f) Differential beam 2 (beam D2) 3-D polar

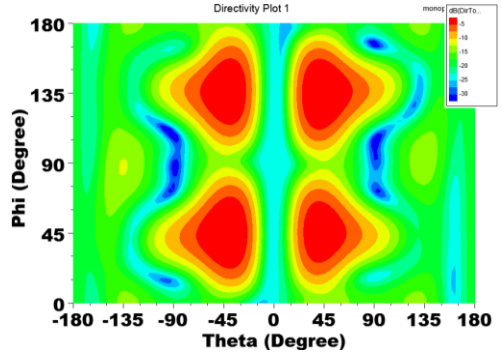

(e) Differential beam 3 (beam D3) contour

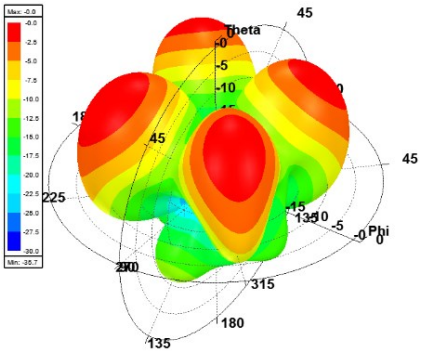

(f) Differential beam 3 (beam D3) 3-D polar

Figure 5-9. Simulated radiation patterns for sum- and differential beams of 2-D monopulse array.

5.3.3 Comparator for Dual-Polarized Monopulse Array

Another comparator for dual linearly-polarized monopulse array working at 5.8-GHz applications is devised to demonstrate the potential of the eight-port coupler further. The overall configuration, layouts of each layer, substrate parameters, and the main dimensions are elaborated in Figure 5-10.

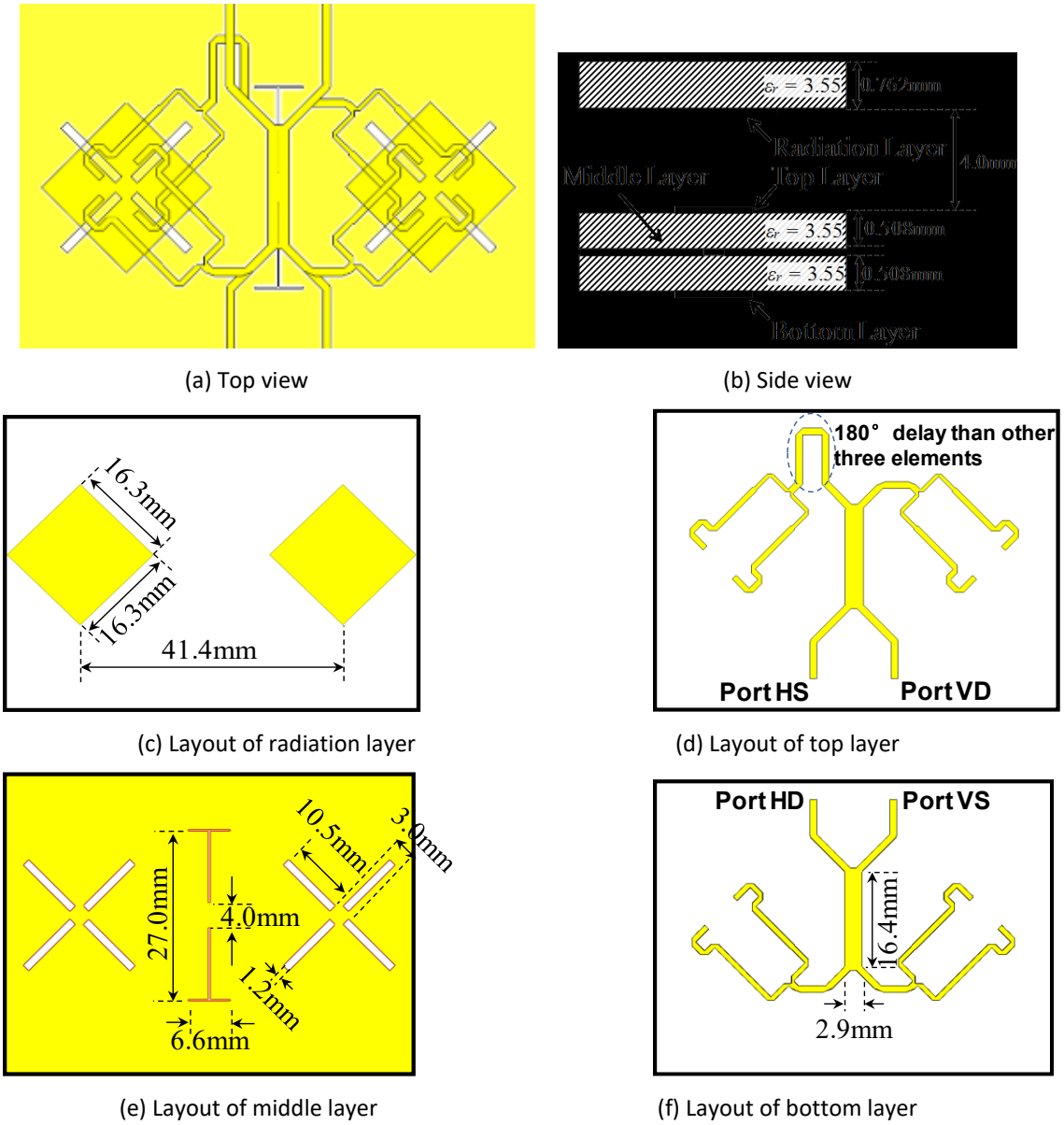

Figure 5-10. Structure of two-element dual-polarized monopulse array with the comparator based on the eight-port coupler.

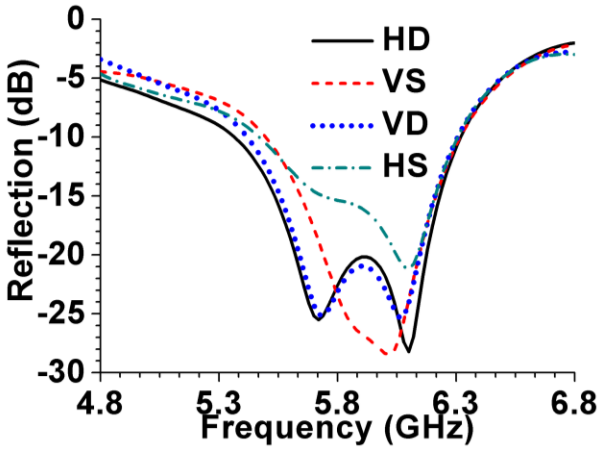

(a) Simulated results of matching

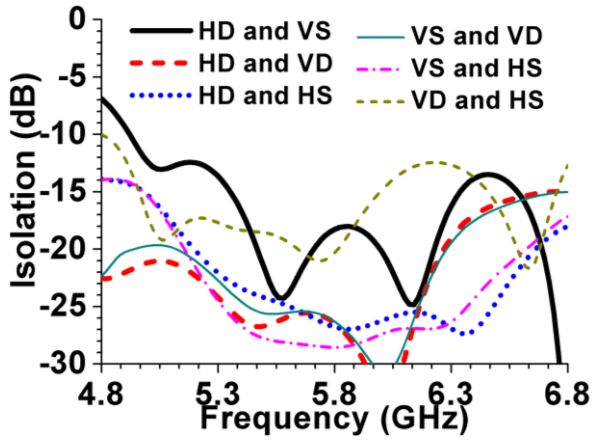

(b) Simulated results of isolation

Figure 5-11. Simulated results of matching (a) and isolation (b) of the dual-polarized monopulse array.

Here, a dual-linearly polarized patch antenna [109] is adopted as the element, and a segment of the transmission line is employed to obtain a 180-degree phase delay. All detailed dimensions of the structure have been given in Figure 5-10.

The simulated results of matching and isolation are demonstrated in Figure 5-11. The performance shows a reflection lower than -10 dB and isolation better than 12 dB can be achieved within 5.5 - 6.3 GHz. Besides, the distributions of surface current on the patches with corresponding radiation patterns for each of the four modes are listed in Figure 5-12.The features of sum- and difference-beams with two orthogonal polarizations can be apparently observed through Figure 5-2 (a) - (h).

It should be indicated that the bandwidth is mainly limited by the phase shifter and antenna elements.

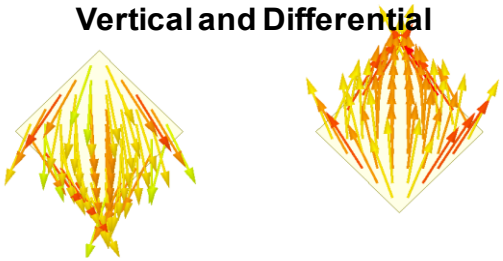

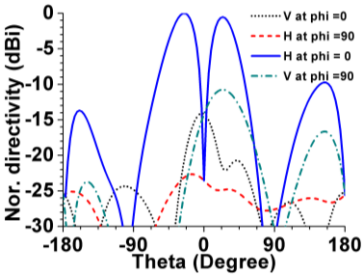

(a) Current distribution on the antenna for VD mode (b) Radiation patterns for VD model

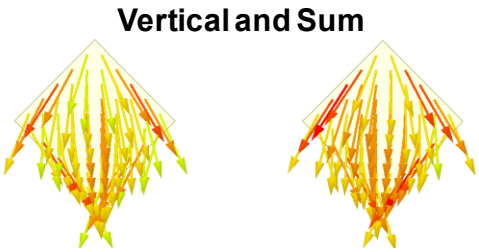

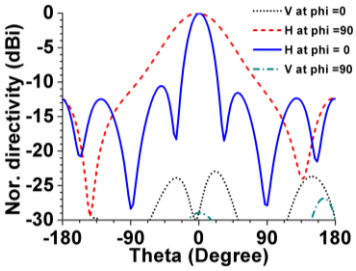

(c) Current distribution on the antenna for VS mode (d) Radiation patterns for VS model

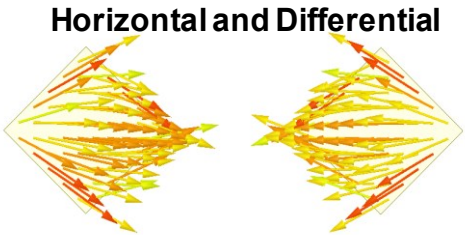

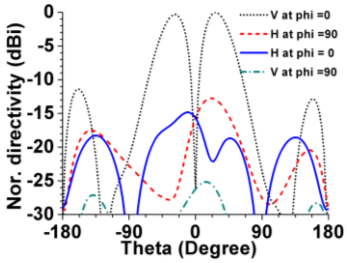

(e) Current distribution on the antenna for HD mode (f) Radiation patterns for the HD model

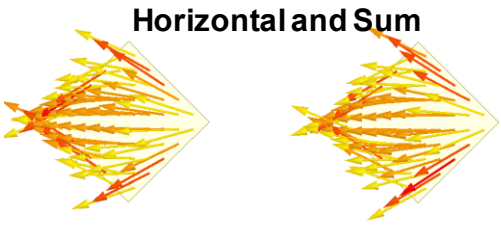

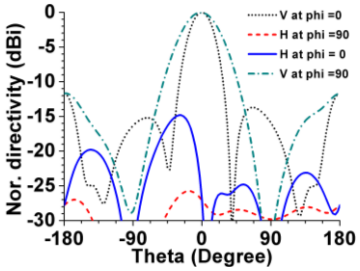

(g) Current distribution on the antenna for HS mode (h) Radiation patterns for HS model

Figure 5-12. Simulated current distributions and the corresponding radiation patterns for each of four modes.

Chapter 6

Extension of Butler Matrices Beam Number

In this chapter, the topologic configuration of BMs for more flexible numbers of beams and elements over the traditional BMs are introduced. Two approaches are proposed and demonstrated, which are using three-way couplers and adopting electrically reconfigurable couplers to replace the traditional quadrature couplers. Two parts are described in this chapter, which are based on the traditional passive circuit and electrically reconfigurable approaches. Based on the method of passive circuits, three-way directional couplers are utilized to diversify the topologic configuration and extend beam numbers from 2^N to $3 \cdot 2^N$. Two prototypes are constructed and demonstrated with different topologies, and then, a quasi 6 × 6 BM and a real 6 × 6 BM are achieved in succession. For the scheme based reconfigurable structure, an electrically controllable wideband coupler is adopted for the switchable multiple sets of beams of BMs, for example, generating $M \cdot 2^N$ beams in a time-sharing form based on traditional $2^N \times 2^N$ BM configuration. The advantage of the reconfigurable scheme is clarified through comparison to the combination of electrically controllable phase shifters and BMs.

Some of the related work has been published in the journal articles [84], [110], [111] and conference paper [97].

6.1 6 × 6 Quasi-Butler Matrices

To enhance the functional flexibility of BMs by improving the structural configuration, a novel 6×6 beam-forming network with the topology structure and the properties like Butler matrices is represented. Two 3 × 3 hybrid couplers are adopted as the substitution of traditional 3dB - 90° hybrids to introduce the factor of 3 into in this network for changing the numbers of ports and beams from conventional 2^N to 6. Moreover, one kind of 2 × 2 hybrid couplers with quasi-arbitrary phase-difference is utilized as well to eliminate using fixed phase shifters in this design for a smaller size and a lower loss. As an example, one proposed 6×6 network working at 5.8 GHz has been designed, simulated, fabricated and measured. Good performance in matching, isolations, equal power divisions, coherent phase differences at all ports have been achieved. The possibility of improving the structural flexibility of BMs by employing 3 × 3 hybrids is demonstrated.

6.1.1 Methodology

The fundamental principle and structural layout for the mentioned 6 × 6 beamforming network (BFN) are demonstrated in Figure 6-1. The most apparent distinction of proposed BM than the conventional is the introduction of the 3 × 3 hybrid couplers.

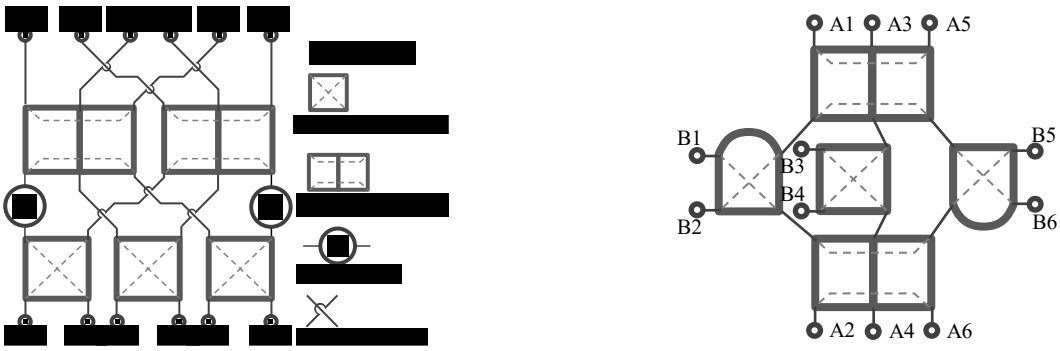

(a) Schematic framework of 6 × 6 quasi-BM in [35] (b) Modified configuration in [35]

Figure 6-1. Schematic framework of 6 × 6 quasi-BM based three-way coupler (a) and modified BM without using crossovers (b) [35].

The 3 × 3 couplers [84] can provide +120°, 0°, -120° phase differences between adjacent ports respectively respecting to which port has been activated, shown in Figure 6-2. In addition, ideal matching, isolation and equal power division can be acquired at each excitation port simultaneously. Based on the properties of 3 × 3 couplers, and using the concept of BM, one 6 × 6 BFN can be constructed with six independent beams and theoretically perfect isolation, matching, and equal power division.

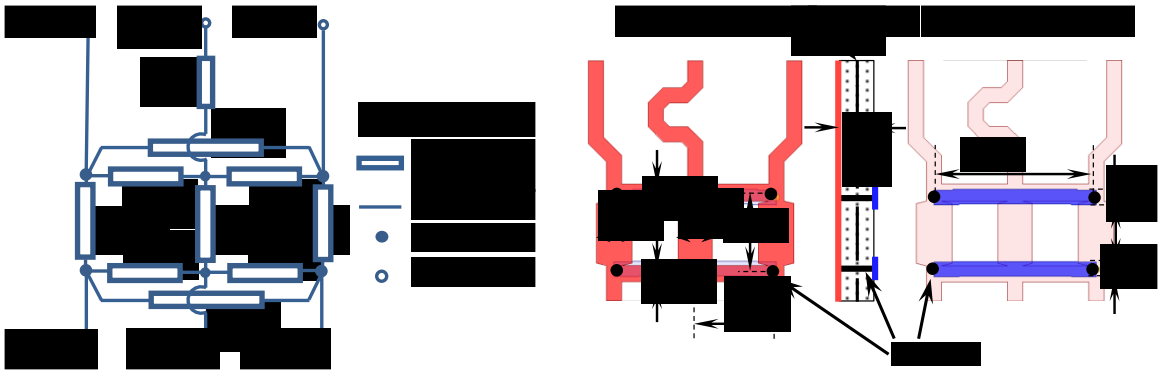

(a) Structure of three-way directional coupler (b) Layout of the three-way directional coupler

Figure 6-2. Structure and layout of the three-way directional coupler.

The properties of quasi-coherent output phase differences between adjacent ports are listed in Table V. Due to the restriction from the symmetry of the 3 × 3 couplers when port B3 or B4 is excited. The perfect consecutive phase differences cannot be realized. Instead of that, an alternate phase difference of -90° or +90° can be achieved. In both cases, the adjoining two elements, such as A1 and A2, A3 and A4, A5 and A6, can be seen as a sub-array with a declining beam. In this way, beam steering can be obtained by changing the subarray's direction.

Table V Output phase differences with different input ports

Excited Port	Output phase status on each port						Phase Differences
	A1	A2	A3	A4	A5	A6	
B1	0°	-60°	-120°	-180°	-240°	0°	-60°
B2	0°	+120°	+240°	0°	+120°	+240°	120°
B3	0°	-90°	0°	-90°	0°	-90°	-90° *
B4	0°	+90°	0°	+90°	0°	+90°	+90° *
B5	0°	-120°	-240°	0°	-120°	-240°	-120°
B6	0°	+60°	+120°	+180°	+240°	0°	60°

6.1.2 Examples and Results

An example serving 5.8 GHz applications was designed, simulated, and manufactured. The AD260A laminate ($\varepsilon_r = 2.60$) with thickness h=30mil was selected as the substrate.

Since the 3 × 3 couplers have a double-layer structure, this 6 × 6 BFN is designed in a double-layer structure consequently. ANSYS HFSS was exploited to design, simulate and optimize. The structures of each layout on various layers have been illustrated in Figure 6-3.

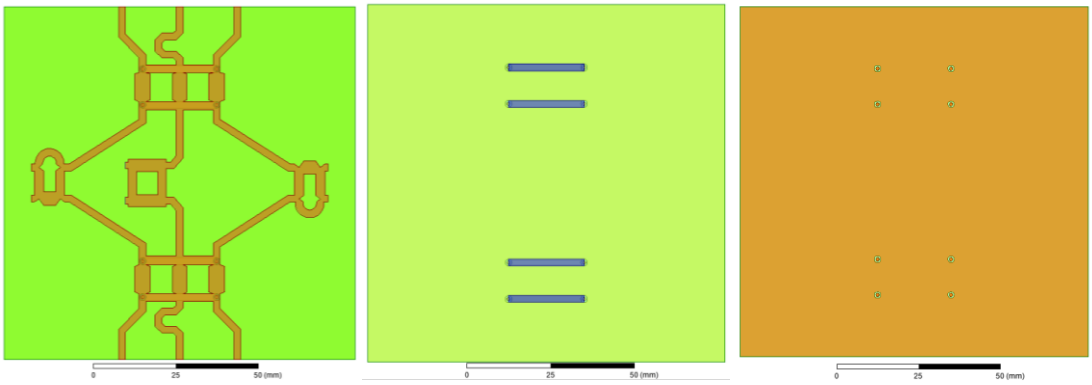

(a) Top layer (b) Bottom layer (c)Middle layer

Figure 6-3. Layouts of the top , bottom, and middle layers.

The major simulation results, including matching, isolation, power division, and output phase difference, have been demonstrated in Figure 6-4 and Figure 6-5.

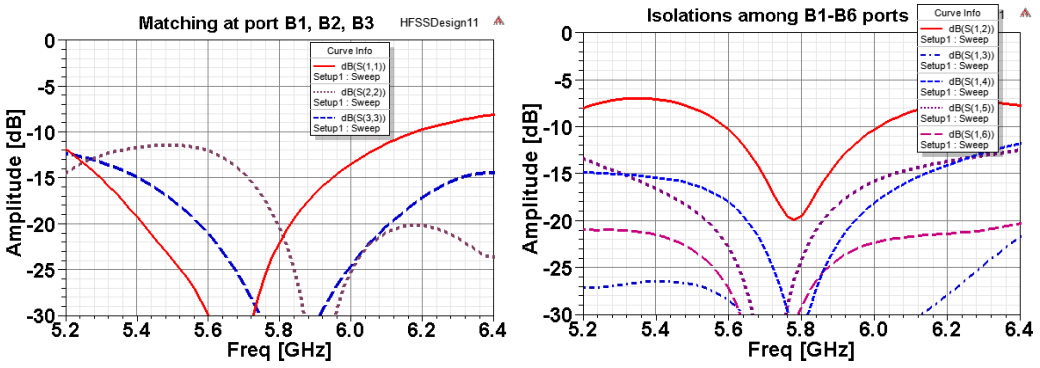

(a) Matching (b) Isolation

Figure 6-4. Simulated results of matching at B1, B2, and B3 ports and isolations between B1 and other B- ports.

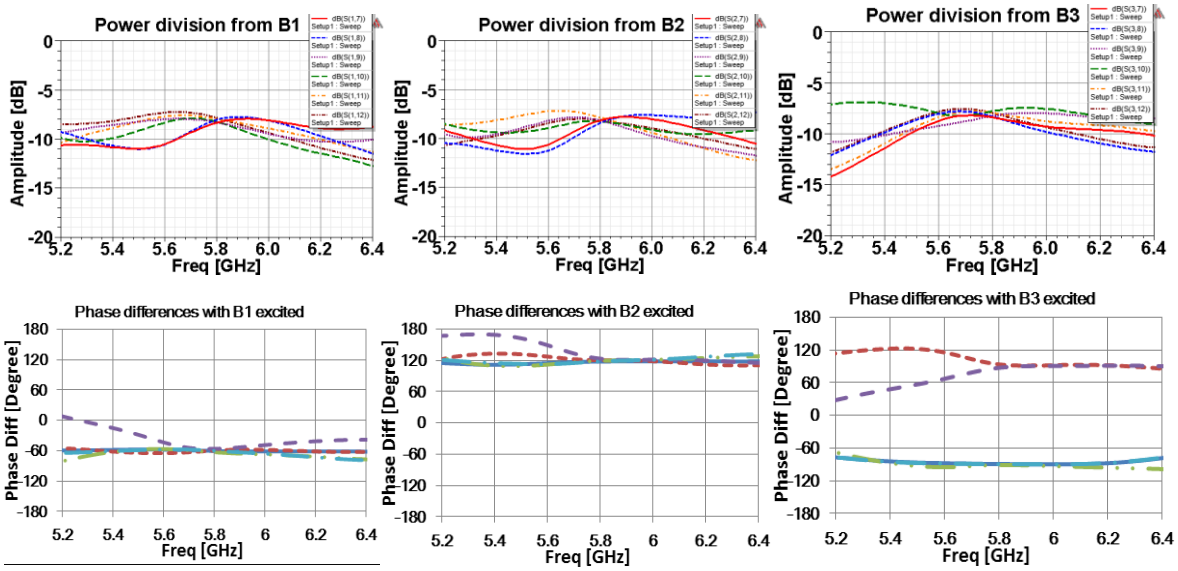

(a) B1 excited (b) B2 excited (c) B3 excited

Figure 6-5. Power divisions and phase differences when port B1, B2, or B3 excited.

We can see that the performance of matching is less than -10 dB reflection, and the isolation is higher than 10dB in the range of 5.6 GHz – 6.0 GHz. At 5.8 GHz, the center frequency point, the unbalance of power division is less than ± 0.3 dB, and the error of the output phase difference is less than ±4 degrees.

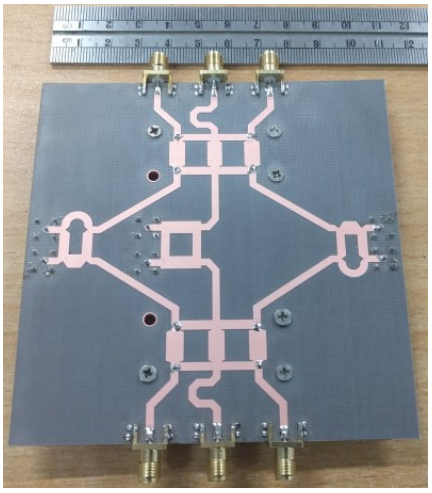

(a) Top view

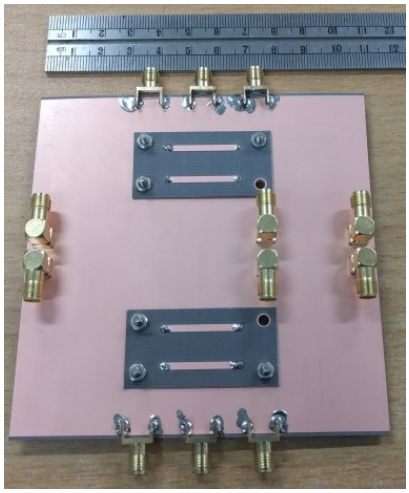

(b) Bottom view

Figure 6-6. Top view and bottom view of the example of the quasi-6×6 BFN.

One example has been fabricated for the experimental test, shown in Figure 6-6. The Keysight PNA-L 5230C was used to measure the example. The results are shown in Figure 6-7. We can see that some significant performance parameters, such as matching, isolation, and phase differences, are reasonable at 5.8 GHz and agreed well with simulation results.

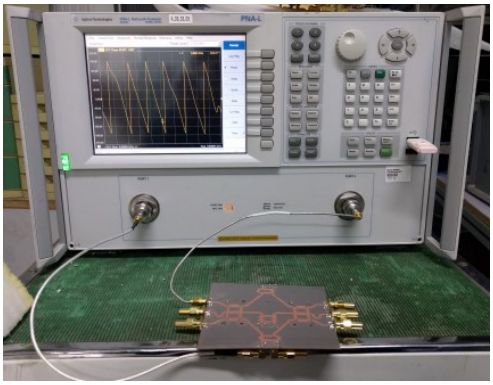

(a) Measurement

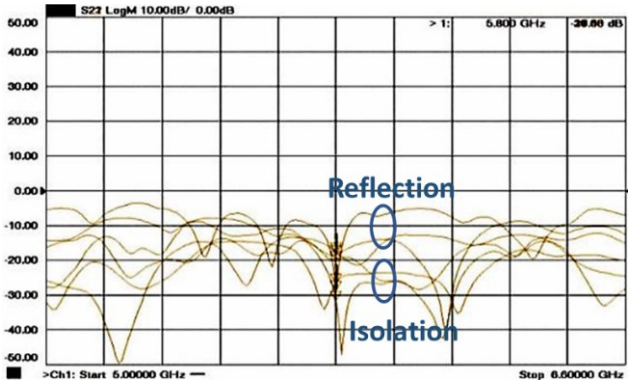

(b) Measured results of matching and isolation

Figure 6-7. Measurement results of matching and isolation.

6.2 Wideband 6 × 6 Butler Matrices

Though the three-way coupler has been involved in BMs for more flexible beam numbers, the proposed quasi- 6 × 6 BM is not real BMs because some of the phase differences are not in the progressive sequence. Besides, the three-way coupler proposed in [84] has a limited bandwidth, which restricts the performance of 6 × 6 BM.

To solve the problems, a real- 6 × 6 BM with 35% fractional bandwidth and the features of typical BMs, such as progressive phase differences and spatially orthogonal beams, will be proposed in this section.

6.2.1 Methodology

The primary reason we cannot obtain the ideal progressive phase difference for each beam is that the three-way coupler has a 0° phase difference among output ports when someone input port is excited.

Concretely, when extending three beams into six beams, it is supposed that each of the phase differences from a three-way coupler can be divided into a smaller value, which is half of the original phase difference. However, obviously, 0° / 2= 0°. That means any coupler with 0°-phase difference will break the rule and cannot generate more beams.

To solve this problem, phase shifters outside couplers can be adopted to shift all the phase differences from the three-way coupler. The scheme is shown in Figure 6-8.

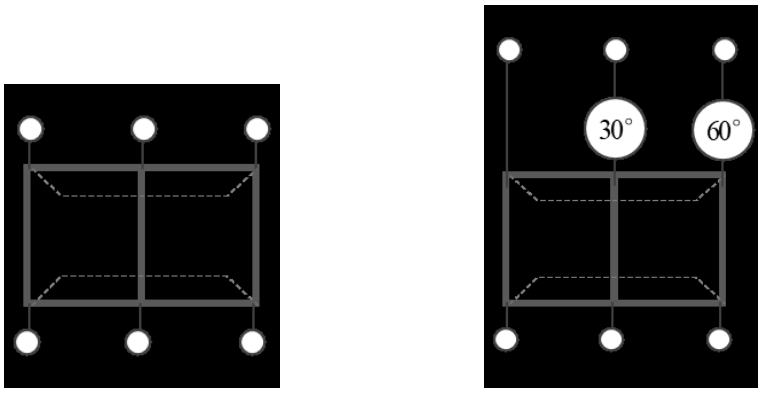

(a)Original three-way coupler (b) Modified three-way coupler

Figure 6-8. Scheme to shift all phase differences of three-coupler by increasing 30°.

Therefore, the phase differences will be changed from -120°, 0°, and 120° into -150°, -30°, and 90°. There is no 0° phase difference anymore.

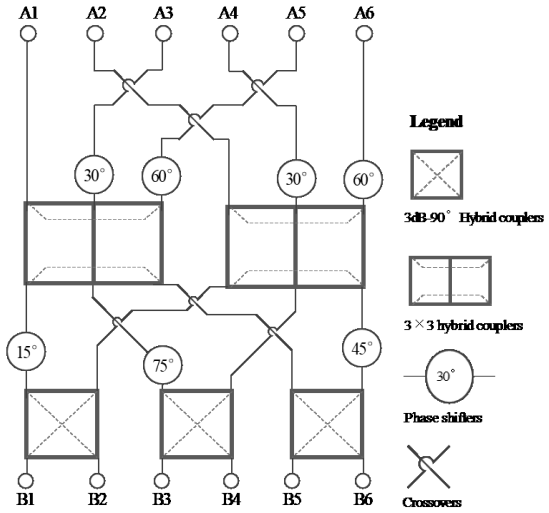

Figure 6-9. Scheme of 6 × 6 Butler matrix based on the three-way coupler.

Based on the modified three-way coupler, a real - 6 × 6 Butler matrix can be realized; the scheme is shown in Figure 6-9. It can be found that by combining three-way coupler and quadrature coupler together, a 6 × 6 Butler matrix can be achieved. The typical features of BMs, such as equal power division, progressive phase differences, ideal matching and isolation, and spatially

orthogonal beams, can be reserved in this BM. The phase differences for each of beam-ports are listed in Table VI, and the performance can be seen clearly.

Table VI Output phase differences of 6 × 6 Butler matrix

Excited Port	Output phase status on each port						Phase Differences
	A1	A2	A3	A4	A5	A6	
B1	0°	-75°	-150°	-225°	-300°	15°	-75°
B2	0°	105°	210°	315°	-60°	-165°	105°
B3	0°	-15°	-30°	-45°	-60°	-75°	-15°
B4	0°	165°	330°	-135°	-300°	105°	165° *
B5	0°	-135°	-270°	45°	180°	315°	-135°
B6	0°	45°	90°	135°	180°	225°	45°

6.2.2 Examples and Results

To verify the scheme of a 6 × 6 Butler matrix, a wideband beamforming network working at 1.695 GHz - 2.69 GHz is constructed. In the network, a three-way coupler proposed in [112] is adopted. The configuration of the coupler is shown in Figure 6-10. One of the advantages of this coupler is that wideband 3dB - 90-degree coupler can be used in this three-way coupler to extend the bandwidth.

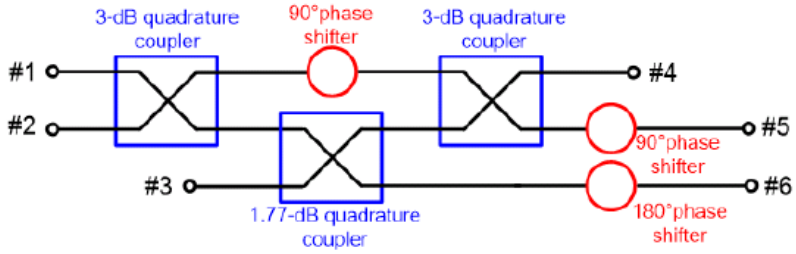

Figure 6-10. Three-way directional coupler (3×3 BM) proposed in [112].

According to the framework [112], a wideband three-way coupler is built, as shown in Figure 6-11. Here, the coupler is based on a back-to-back double layer microstrip line. The shape with red color

is located on the top layer; the shape with blue color is on the bottom layer; the yellow color represents the shape of the common ground layer.

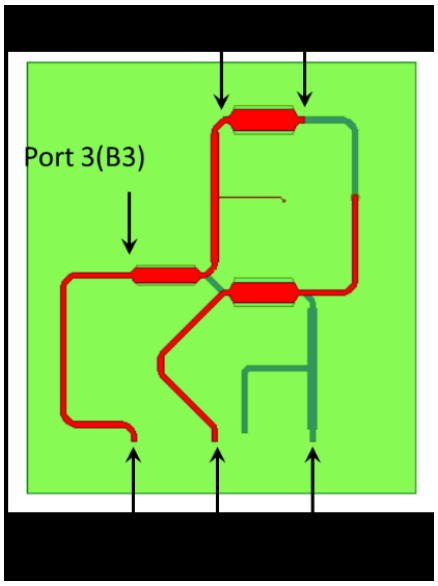

Figure 6-11. Layout and configuration of ports of the wideband three-way directional coupler.

The simulated results through full-wave analysis by ANSYS HFSS of the three-way coupler performance are shown in Figure 6-12. Satisfying characteristics can be found through the simulated results over 1.695 GHz - 2.69 GHz. The error of power division is less than ±0.5 dB; the error of phase differences is less than ± 5°. The performance of phase differences agrees with the expected value (but a negative sign due to the definition) shown in Figure 6-8 (b).

Based on the wideband three-way coupler, a wideband 6 × 6 Butler matrix is constructed, as shown in Figure 6-13. Here, the BM is based on a back-to-back double layer microstrip line. The shape with red color is located on the top layer; the shape with blue color is on the bottom layer; the yellow color represents the shape of the common ground layer.

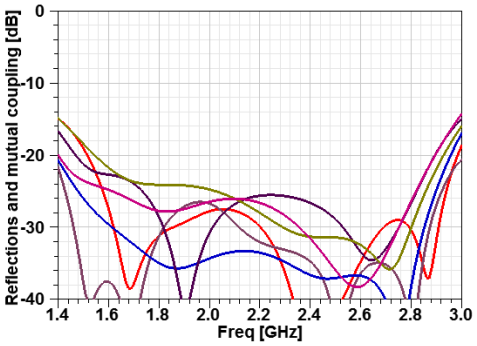

(a) Reflections at beam-ports and isolations among beam-ports

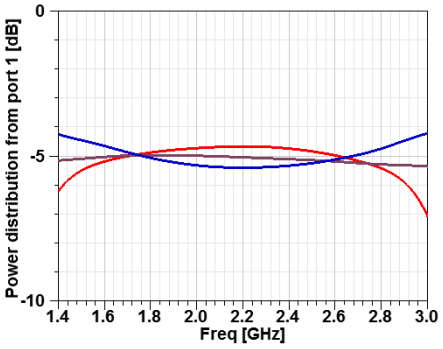

(b)Power division from B1

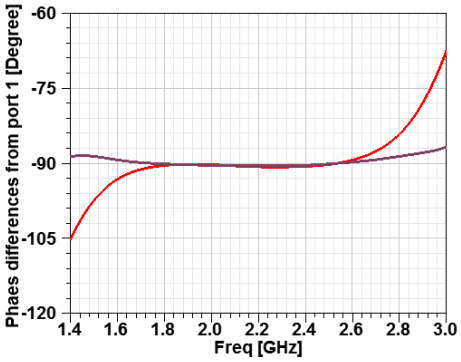

(c)Phase differences from B1

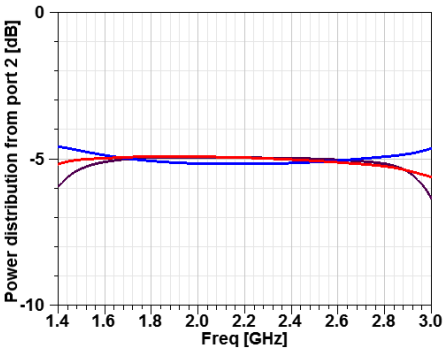

(d)Power division from B2

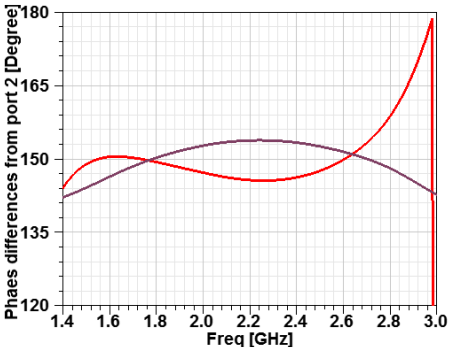

(e)Phase differences from B2

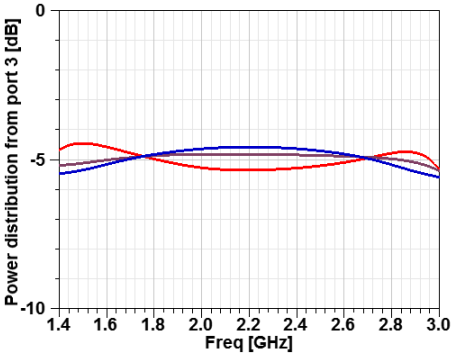

(f)Power division from B3

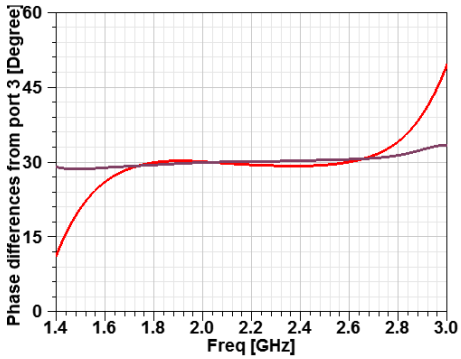

(g)Phase differences from B3

Figure 6-12. Simulated performances of matching, isolations, power divisions, and phase differences of the three-way coupler.

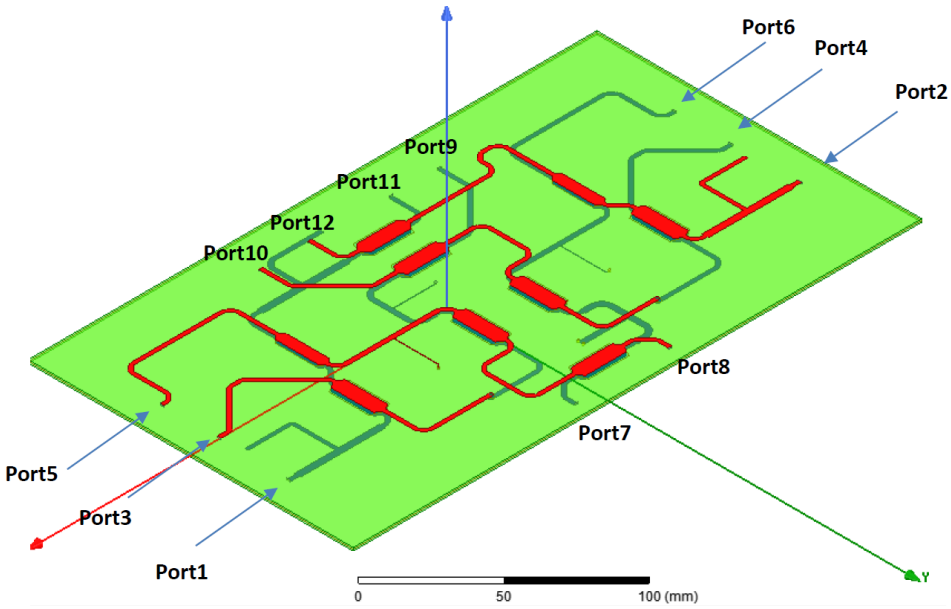

(a) 3-D view

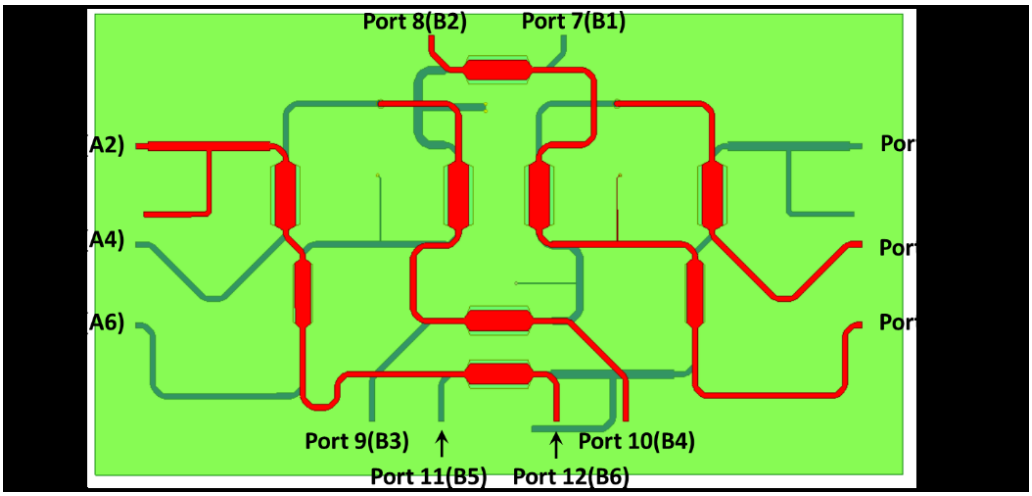

(b) Top view

Figure 6-13. Layout and configuration of ports of the wideband 6 × 6 Butler matrix.

The simulated results through full-wave analysis by ANSYS HFSS of the 6 × 6 BM performance are shown in Figure 6-14. Due to the similarity of power divisions from each of beam-port, only the results of power division from B1 and B2 are shown in Figure 6-14.

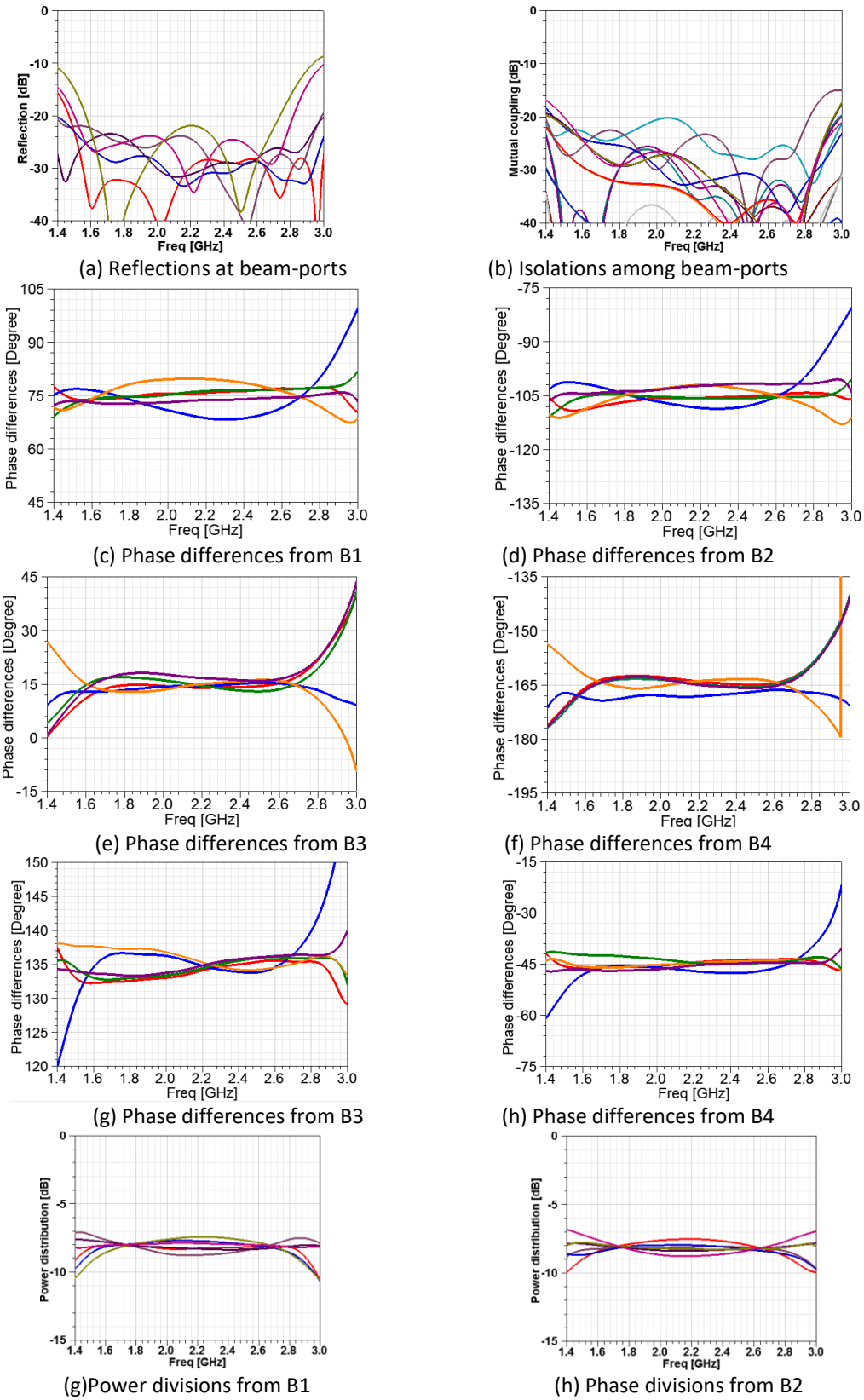

Figure 6-14. Simulated performances of matching, isolations, power divisions, and phase differences of the 6 × 6 Butler matrix.

Satisfying characteristics can be found through the simulated results over 1.695 - 2.69 GHz. The error of power division is less than ±0.8 dB; the error of phase differences is less than ± 5°. The performance of phase differences agrees with the expected value (but a negative sign due to the definition) shown in Table VI. The array factor is calculated and shown in Figure 6-15. The six-beam forming property is clear and reasonable.

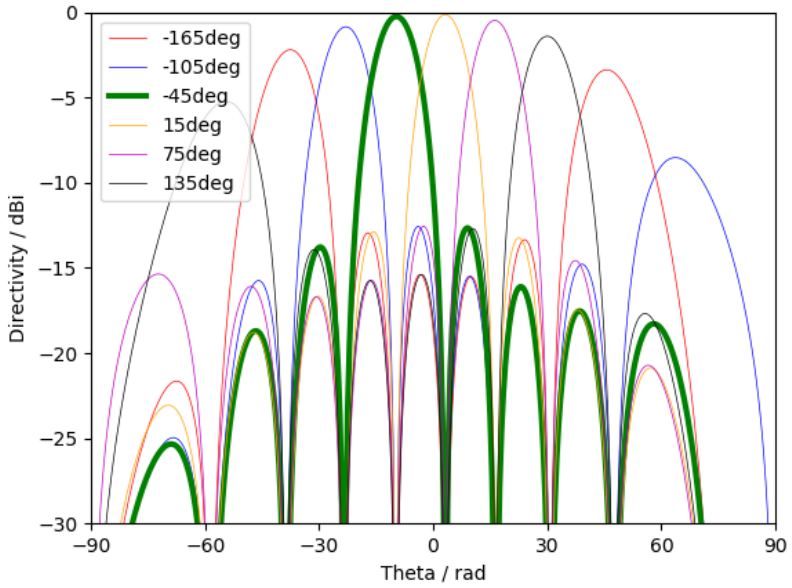

Figure 6-15. Calculated array factor according to the results of 6 × 6 Butler matrix

6.3 Wideband Electrically Switchable Coupler

In this section, we will present a hybrid coupler with three electrically switchable output phase differences, 90° and 90 ± a°, and equal power division with 30% relative bandwidth. This coupler can be used to build switchable BMs for a more flexible beam number.

6.3.1 Methodology

Structurally, this design is based on two-section quadrature hybrids and referring to the structure proposed in [92] - [94]; the asymmetrical configuration is adopted for distinct phase differences

rather than the conventional 90°. Moreover, a compact, low loss, and low-cost scheme of reconfigurable transmission lines is introduced and applied for the capability of electrical switching. The effective circuits for radio frequency (RF) - circuit and direct current (DC) - circuit are shown in Figure 6-16.

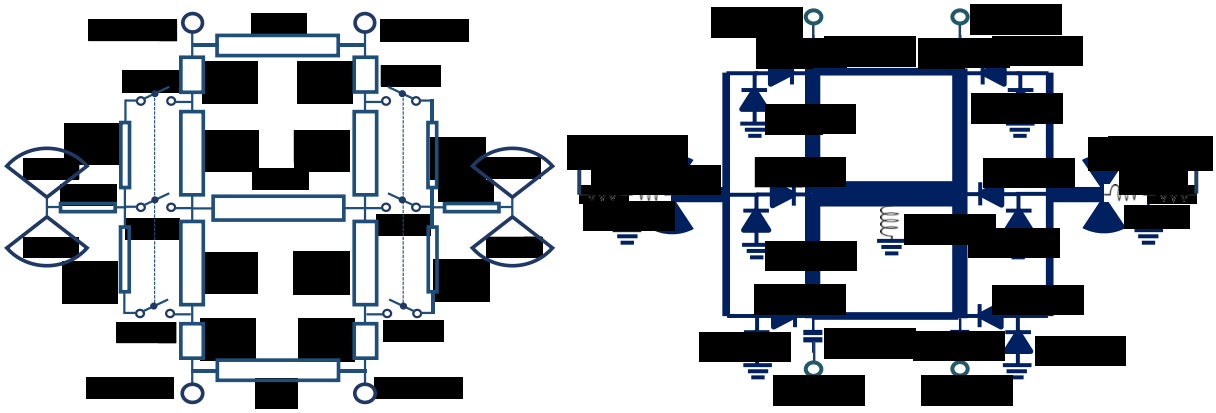

(a) Equivalent RF-circuit (b) Equivalent DC-circuit

Figure 6-16. Schematic diagrams of equivalent RF-circuit and DC- circuit .

The proposed hybrid coupler can be designed and implemented through three major steps:

I) obtaining the preliminary theoretical parameters of the asymmetrical two-section hybrid with 90 + a° phase difference from the derived design equations from [94];

II) acquiring the parameters of the reconfigurable transmission lines based on the results of I) and the design curves, and replacing the four transmission lines in I) for the switchable phase differences 90° and 90 ± a°;

III) substituting switches by PIN diodes and bias circuits and using open sectors to improve bandwidth, then optimizing and balancing the overall performance for the final results.

The design process is shown in Figure 6-17.

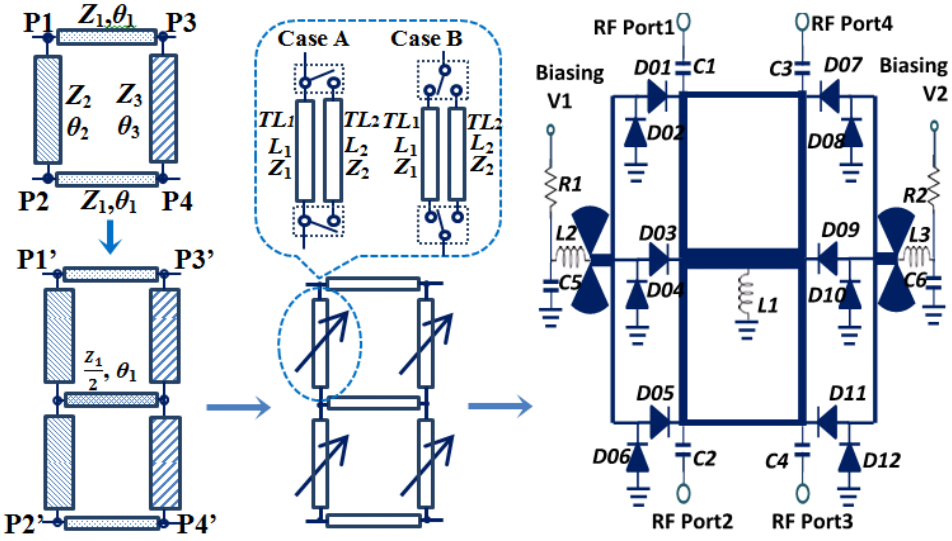

(a) Step I (b) Step II (c) Step III

Figure 6-17. Sketch of the design process of each step with the definitions of principal parameters.

This design procedure begins by solving the parameters of the two-section hybrid coupler, which have a given phase difference and equal power division. We can assume that the required hybrid, or second-order one, is composed of cascading two identical couplers, or first-order ones, closely together. The first-order coupler has been presented in [92] - [94]. This assumption is sufficient but not necessary. However, based on this, we can reuse all results in [92] - [94] and obtain feasible solutions more easily with perfect matching and isolation. Therefore, all transmission lines in the second-order one are identical as in the first-order one, but the horizontal-directed line at the center, which has a half characteristic impedance of the original, as shown in Figure 6-17 (a). The transmission properties of the second-order coupler can be represented by

$$S_{2'1'} = S_{21}^2 + S_{41}^2 \text{ and } S_{4'1'} = S_{21}\,S_{41} + S_{41}S_{43}\,. \tag{6-1}$$

Here, the prime represents properties for the second-order case and the unprimed means they are defined for the first-order case, and the definitions are the same as in [92].

Letting $|S_{2'1'}|=|S_{4'1'}|$ and substituting [92, Eqs (9) - (11)] into, we can obtain the equal power division condition:

$$C^2 = \frac{1}{2} \pm \frac{\sqrt{-\cos 2\psi}}{2\sqrt{2}\sin\psi}. \tag{6-2}$$

Here, $\psi \in (\pi/4, 3\pi/4)$. Then, defining the output phase difference as ψ' = Arg ($S_{2'1'}$) - Arg ($S_{4'1'}$) and substituting [32, Eqs (9) - (11)] into, we can attain that

$$\psi' = \operatorname{atan}\frac{(1-C^2)\sin 2\psi}{(1-C^2)\cos 2\psi + C^2} - \frac{\pi}{2}. \tag{6-3}$$

All other parameters can be obtained from ψ and C through [32, Eqs (23)-(28)]. (6-2) and (6-3) mean that we can always find an adequate ψ and corresponding C for the required ψ' and equal power division to build the required two-section coupler.

It should be clear that this solution is just the one with the best matching and isolation at the center frequency of infinite solutions, because of the limitation from the assumption at the beginning. However, it is helpful to be used as the initial value of the optimization for a wider bandwidth in this design. Besides, both solutions from (6-2) are valid, but the one from '+' will cause very low characteristic impedances that are scarcely feasible in practice.

Furthermore, reconfigurable transmission lines are needed to integrate various options of phase difference into one coupler, as shown in Figure 6-17 (b). A solution is introduced, which consists of two transmission lines and two SPST switches, different than the conventional way that uses SPDTs, as *case A* and *case B*, shown respectively in Figure 6-17 (b). Here, Figure 6-17 (a) is the equivalent electric length and characteristic impedance of virtual TL_3 varying with Z_1, Z_2 and L_2. Here, postulating Z_1 equals toZ_0, a given value, Z_2 and Z_3 are represented in terms of Z_0 for universalism. Figure 6-17 (b) is the comparison of losses in *case A* and *case B* respect to changing

of L_1, L_2 and Z_2. Assume that in *case A*, switches are turned on, in *case B*, TL_2 is selected. All switches are considered as having 2Ω resistance and 0 delay when they are passed through.

When the switches are turned off, *case A* behaves as just TL_1 with length L_1 and characteristic impedance Z_1; when the switches are turned on, it acts as TL_1 in shunt with TL_2 with the equivalent L_3 and Z_3, as a virtual transmission line TL_3. Obviously, using *case A* can reduce the electrical control components by half those of *case B*. Consequently, it leads to lower cost and complexity.

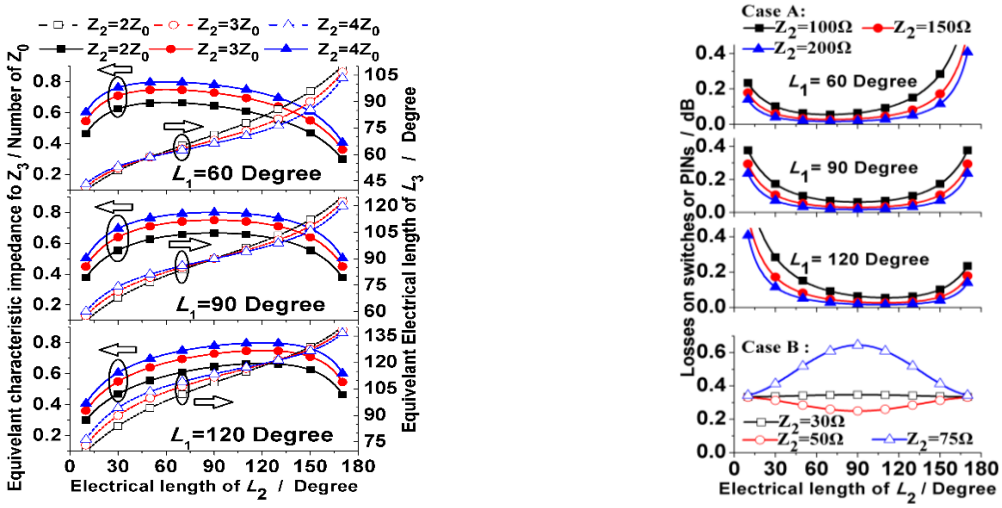

(a) Equivalent length based on L_1 and L_2 (b) Comparison of insertion loss between CaseA and CaseB

Figure 6-18. Properties of the proposed reconfigurable transmission line.

Through fundamental transforming operations among ABCD-, Y-, Z- matrices and S- parameters, the numerical solution of functions of Z_3 and L_3 in terms of L_1, Z_2, and L_2 can be obtained, as illustrated in Figure 6-18 (a). Here, the electrical length of TL_3 is defined as $L_3 = \text{Arg}\,(S^{TL3}{}_{21})$; the characteristic impedance is defined as $Z_3 = (Z^{TL3}{}_{11} / Y^{TL3}{}_{11})^{1/2}$. Choosing adequate L_2 and Z_2 can achieve the required characters of TL_3.

However, there are two limitations: I) Z_3 should always be less than Z_1; II) the deviation between L_1 and L_3 should be less than a specific value, for example, 15°, for a reasonable wideband property of the virtual TL_3. For the limitation I, by employing a greater value of Z_2, Z_3 can be close to Z_1 to

an acceptable level. However, limitation II will restrict the limit of ψ'; therefore, $\psi' \in [\pi/3, 2\pi/3]$ is the recommended value in this design.

In addition, *case A* can also provide remarkably lower losses than *case B*, and the comparison is shown in Figure 6-18 (b). In *case A*, when turning switches off, there is almost no loss theoretically; even when turning on, only part of current passes through switches, rather than *case B* in which all the current always flows through switches.

As mentioned before, two reconfigurable transmission lines on the same side (right or left) of the two-section hybrid will be switched synchronously to meet the symmetry with respect to the horizontal. Thus, the middle switches on each side can be shared, which requires six switches. Moreover, each two PIN diodes in series are exploited as one switch for better isolation. Therefore, a total of 12 PINs are needed with two biasing points and auxiliary bias circuits, as the schematic shows in Figure 6-17 (c).

Overall, the hybrid coupler has a perfectly symmetrical configuration with respect to both vertical and horizontal. However, biasing voltages at V1 and V2 can be set in symmetry or not. Concretely, when V1 is high level, and V2 is low, we can obtain the phase difference ψ', or 90-a°; interchanging the biasing state can gain π-ψ', or 90+a°; when both V1 and V2 are high level, 90° can be achieved. For sure, theoretically, these three states cannot be accomplished in one structure exactly. Nevertheless, by adding some components, such as open-end sectors, referring to [49], and optimizing all parameters, the reasonable results with good balance can be performed.

6.3.2 Examples and Results

Two switchable couplers have been designed and optimized as examples with output phase differences of 75°/90°/105° and 60°/90°/120°, or a = 15° and a = 30°, respectively. The substrate

is Rogers RT/Duroid 5880 with $\varepsilon_r = 2.2$, $h = 0.787$ mm, and the PIN diode type is Infineon BAR63-02V.

The optimized parameters by using *Advanced Design System* are listed in Table VII; the corresponding definitions of each parameter are demonstrated in Figure 6-16 (a). Here, the delay due to PIN diodes has to be considered in the optimization. Performance from the simulation is shown in Figure 6-19.

Table VII Structural parameters of two couplers

Name	$a = 15°$	$a = 30°$
TL01, TL03	106Ω/82°	104Ω/91°
TL02	51Ω/103°	64Ω/112°
TL04 - TL07	45Ω/87°	52Ω/85°
TL08 - TL11	138Ω/56°	135Ω/32°
TL12, TL13	87Ω/50°	127Ω/21°
TL14 - TL17	45Ω/3°	50Ω/8°
SC01-SC04	20mm/70°	

The characters of both couplers provide satisfactory performance in the band of 2.0 - 2.8 GHz. The unbalances of power division are less than ±1dB; the reflections are less than -15 dB; the isolations are higher than 14 dB for the two couplers in all states throughout the whole band. Each output phase difference is carried out stably with an error less than ±6°.

The examples of two switchable couplers are shown in Figure 6-20 with $a = 15°$ and $a = 30°$, respectively. The measurement results of both couplers are exhibited in Figure 6-21. Generally, the results agree well with the simulated features over 2.0 - 2.8 GHz.

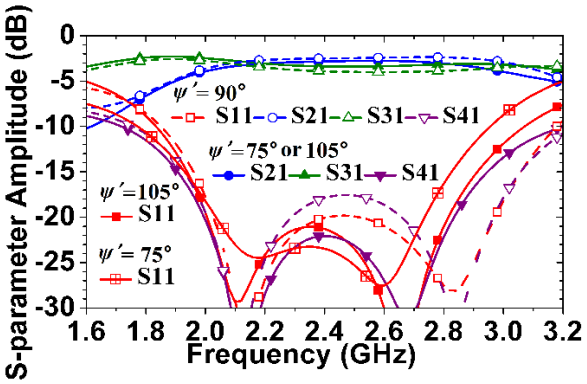

(a) S-parameters of coupler *a* = 15°

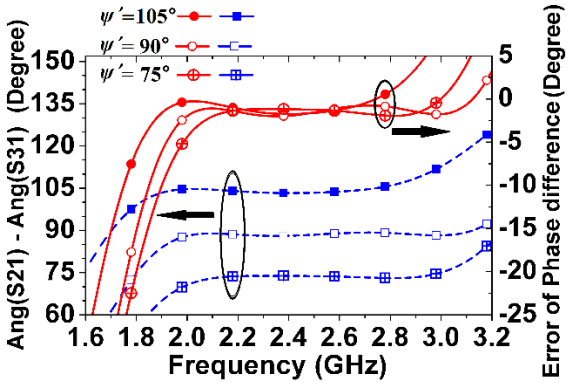

(b) Phase difference of coupler *a* = 15°

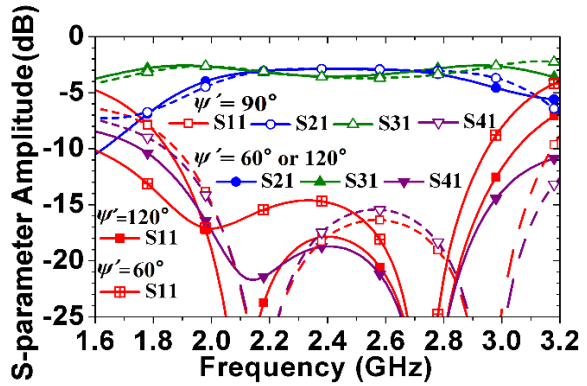

(c) S-parameters of coupler a = 30°

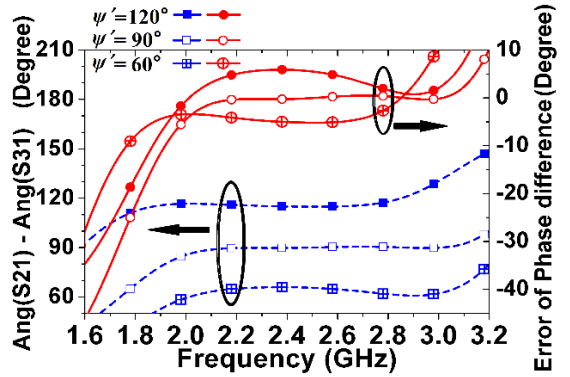

(d) Phase difference of coupler a = 30°

Figure 6-19. Simulating results after optimization. Due to the symmetry, some reduplicated results have been shown in incorporate in (a) and (c).

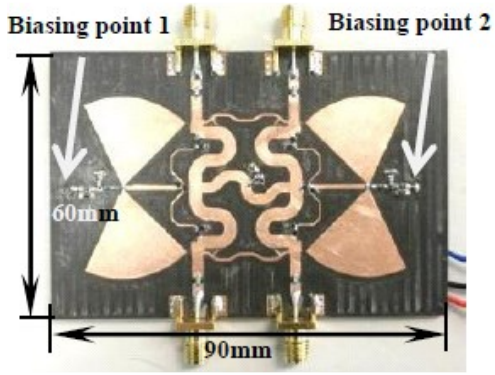

(a) Coupler with *a* = 15°

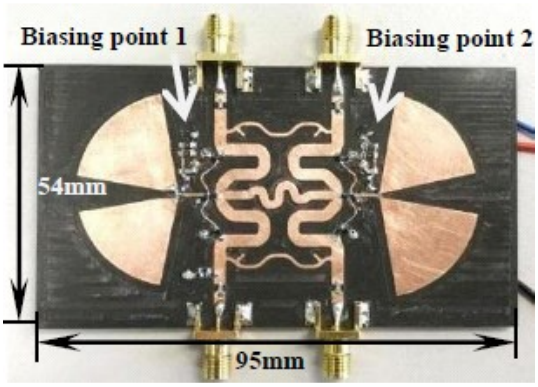

(b) Coupler with *a* = 30°

Figure 6-20. Two fabricated couplers for measurement. Two biasing points in each coupler have been connected to back through drills for lower effects on RF.

Power division, phase differences, matching, and isolation can be achieved reasonably in overall. However, some deviations can be observed compared with the simulation results. The reflections

and isolations of both couplers degrade by about 4 dB approximately. And, in Figure 6-21 (a), a visible deterioration of power division near 2.8 GHz can be seen. The reason can be the errors from machining, soldering or discontinuity between components or connectors.

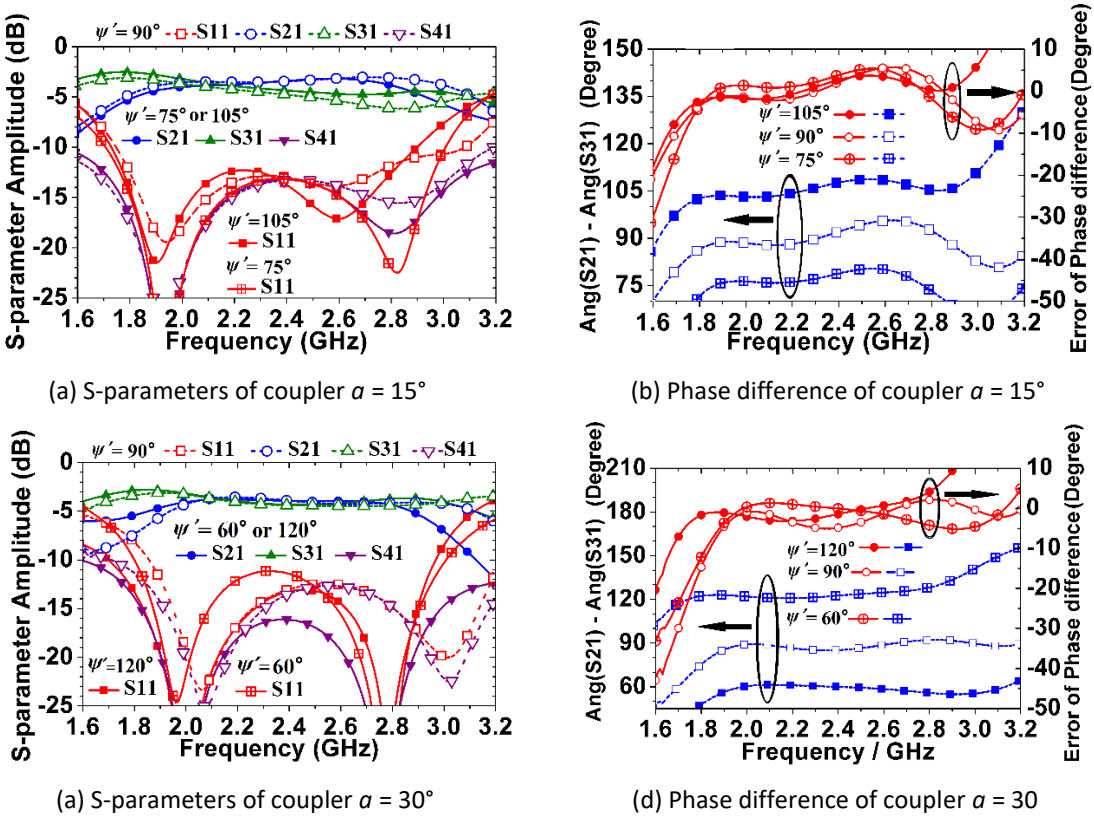

(a) S-parameters of coupler a = 15°

(b) Phase difference of coupler a = 15°

(a) S-parameters of coupler a = 30°

(d) Phase difference of coupler a = 30

Figure 6-21. Measurement results. There are little differences when different ports are excited in (a) and (c). but only one result is shown due to the limited space.

6.4 Beam Number Extension based on Switchable Coupler

A scheme to extend the beam number of Butler matrices in time-sharing form by utilizing reconfigurable couplers is presented and illustrated in this chapter with experimental verification. The beam number of a traditional $2^N \times 2^N$ Butler matrix can be increased to $3 \cdot 2^N$ by substituting reconfigurable couplers for all hybrids while maintaining the structure and other components as the original.

Moreover, only N sets of different parameters are required for these couplers. The principle, properties, and the generalized expressions for the N sets of parameters will be discussed and exhibited. The properties of the extended beams are illustrated in terms of beams directions and crossover levels. As an example, a switchable 12 beam forming network extended from a 4 × 4 Butler matrix for 2.4 GHz applications is fabricated and tested. Over a 30% relative bandwidth is achieved with phase errors less than ±12°, amplitude unbalances lower than ±1.7 dB, isolations better than -15.5 dB, and a return loss better than 11.5 dB.

6.4.1 Methodology

6.4.1.1 Efficiency of Beamforming per Component

As N increases, the number of couplers and crossovers will drastically increase, exceeding the exponential increment, as discussed in [113], [114], and the appendix of [111]. Quantitatively, for a traditional $2^N \times 2^N$ BM, the required number of couplers and crossovers, C and X, respectively, can be obtained by:

$$C(N) = N2^{N-1} \tag{6-4}$$

$$X(N) = \begin{cases} 0 & (N = 1) \\ 2X_{N-1} + 2^{N-1}(2^{N-1} - 1) & (N \geq 2) \end{cases}. \tag{6-5}$$

As described in the introduction, the number of crossovers can effectively be restrained in many ways. Hence, we can only be concerned about the number of couplers as the measure of the complexity of a BM. Further, we can define a function, B, which is the average number of beams formed by one coupler.

$$B(N) = 2^N / C_N = 2/N\ . \tag{6-6}$$

Therefore, B represents the efficiency of each coupler to produce beams. Expression (6-6) clearly reveals that the coupler in a higher order BM will have less efficiency in producing beams. For example, each coupler in a traditional 4 × 4 BM can produce one beam on average; but only 0.67 beams in an 8 × 8 BM. In other words, increasing the order of BM to produce a larger number of beams complicates the circuit and increases its size. In addition, it makes unnecessary expensive, especially when the number of elements associated with the array is not required for needed gain.

More importantly, the monotonically decreasing character in (6-6) implies a potential solution for balancing the complexity and the beam number, which is duplicating lower-order BMs for a more significant number of beams. It is easy to imagine utilizing two 4 × 4 BMs with their respective four beams reclined from each other into an alternating pattern to produce eight beams. Only 8 couplers are needed in this case, rather than 12 couplers in an 8 × 8 BMs. Therefore, combining two lower-order BMs in an appropriate way to produce more beams is more economical and more straightforward.

6.4.1.2 BM with Reclined Beams by Asymmetrical Couplers

in this section, the solution will be generalized for any $2^N \times 2^N$ BM in a more concise and practical form, by using three variables, α, β, and γ. These variables are defined to characterize the phase response properties of the asymmetrical coupler, phase shifter, and BM.

For the asymmetrical coupler with a particular output phase difference and with the configuration shown in the left of Figure 6-22 (a). We can define α as a real number with the dot sign to sketch the phase responses as shown in the right of Figure 6-22 (a) through

$$\angle\big(S(2,1)\big) - \angle\big(S(2,3)\big) = \pi/2 - \alpha \tag{6-7}$$

$$\angle\big(S(4,3)\big) - \angle\big(S(4,1)\big) = \pi/2 + \alpha \tag{6-8}$$

Physically, α represents the extent of the asymmetry of the coupler in terms of the phase response; and, the dot indicates which side is the reference. For example, a 3-dB / 90° hybrid coupler can be represented as $\alpha = 0$, which means it is symmetric.

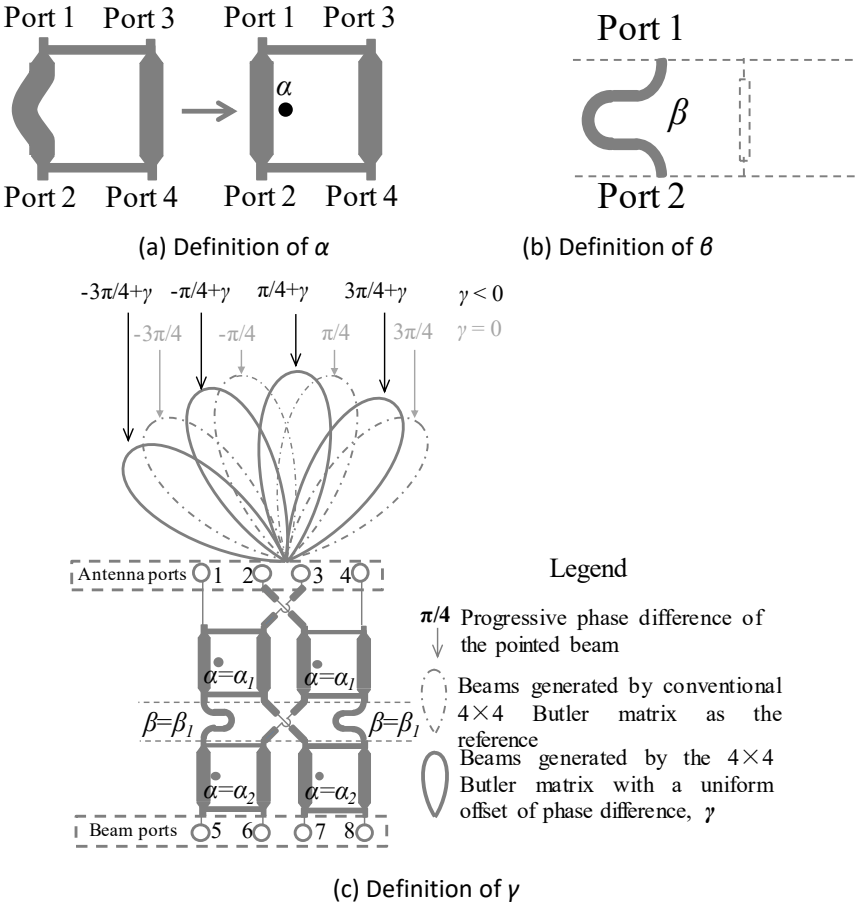

Figure 6-22. Schematic for the definitions of α, β, and γ.

For phase shifters, we define β as a non-negative real number to represent a phase delay longer than the reference lines, as shown in Figure 6-22 (b). Then, we can define γ as a real number, to depict the property of the progressive phase difference of BM with reclined beams. Thus, γ presents the dissimilarity of the progressive phase difference of BM with scanned beams.

An instance is shown in Figure 6-22 (c) that exemplifies a 4 × 4 BM with scanned beams. The four beams produced by 4 × 4 traditional BM have the consecutive phase differences of -3π/4, -π/4, π/4, and 3π/4, respectively. To recline the beams, the phase differences become -3π/4 + γ, -π/4 + γ, π/4 + γ, and 3π/4 + γ.

We can obtain a very concise expression of the relationship between BM and couplers in terms of phase responses by using α and β. For the configuration shown in Figure 6-22 (c), it is listed below:

$$\alpha_1 = -2\gamma; \quad \alpha_2 = -\gamma; \quad (\text{when } \beta_1 = \pi/4)\,. \tag{6-9}$$

If we keep all phase shifters same as in the traditional BMs, a generalized solution for all symmetrical couplers in any $2^N \times 2^N$ BM with a specific γ can be acquired in a more concise form:

$$\alpha_n = -2^{N-n}\gamma \ (\text{when } n = 1, 2, .. N)\,. \tag{6-10}$$

Here, αn expresses the phase responses of the asymmetrical couplers with the same distance from the antenna ports. A larger value of n means a farther distance from antenna ports, as shown in Figure 6-22 (c) and exemplified by the case of $N = 2$. Expression (6-9) also indicates that only N sets of asymmetrical couplers are required for a $2^N \times 2^N$ BM with the reclined beam.

6.4.1.3 Reconfigurable Couplers for Modified BFN

A reconfigurable directional coupler with three electrically switchable output phase differences is reported in [110]. In terms of the performance of phase response, this coupler can be seen as the combination of two asymmetrical couplers and symmetrical ones in a time-sharing form, as shown in Figure 6-23. Moreover, the three equivalent couplers can be characterized as $\alpha = \alpha_S$, 0, and $-\alpha_S$, respectively. Here, α_S is a positive real number, and it can be used to distinguish the reconfigurable coupler from others uniquely.

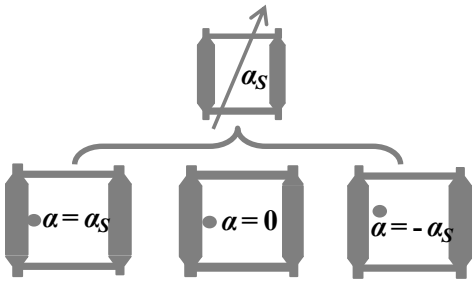

Figure 6-23. Schematic of the reconfigurable coupler with three switchable phase differences.

Based on equation (6-10), it is not difficult to find that an electrically switchable beamforming network (BFN) with treble beams can be built by substituting all traditional hybrids of the conventional BM by the reconfigurable couplers. The three sets of beams consist of two sets of scanned symmetrically to each other, and one set with no scanned. The symmetrically scanned two sets of beams can be characterized by $\gamma = \pm \gamma_S$. Thereby, the non-negative real value γ_S and the order N can uniquely distinguish the switchable BFN. Specifically, the BFN with $3 \cdot 2^N$ switchable beams can be implemented based on a traditional $2^N \times 2^N$ BM structure. A total of $N \cdot 2^{N-1}$ reconfigurable couplers are required to replace all traditional hybrids. These reconfigurable couplers only need N configurations. Each configuration will be applied to 2^{N-1} couplers. Concretely, the couplers with the same distance from antenna ports have the same configuration, as shown in Figure 6-24 and exemplified by the case of $N = 3$.

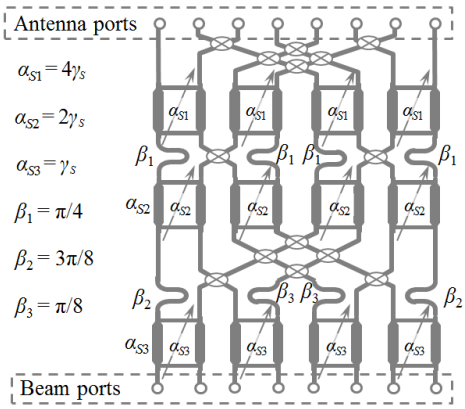

Figure 6-24. Example of switchable BM of $N = 3$. This 24-beam BFN is extended from traditional 8 × 8 BM by using 12 reconfigurable couplers with 3 different configurations, α_{S1}, $\alpha_{S2}$and α_{S3}.

Using α_{S1}, α_{S2}... α_{SN} to characterize the N configurations, and using γ_s to represent the switchable BM, the solution can be represented as

$$\alpha_{Sn} = 2^{N-n}\gamma_s \quad (n = 1, 2, .. N). \tag{6-11}$$

Here, α_{Sn} with a larger value of n means a farther distance from antenna ports.

Based on Expression (6-11) and the procedure mentioned above, any traditional BM can be extended to the BFN with a treble number of switchable beams by applying the reconfigurable couplers.

A case with $\gamma_S = \pi/2^{N+1}$ is interesting because the two scanned sets of beams have precisely the same progressive phase difference as the higher-order BM. For example, when $N = 2$ and $\gamma_S = \pi/8$, a switchable BFN can be built based on 4 × 4 BM by (6-11), and the two scanned sets of beams have the phase differences -7π/8, -3π/8, π/8, 5π/8, and -5π/8, -π/8, 3π/8, 7π/8, respectively. They are entirely the same as the phase differences of the eight beams generated by a traditional 8 × 8 BM. In this case, the 12 switchable beams generated by the BFN can entirely cover the beam directions of 4 × 4 BM and 8 × 8 BM.

However, the same progressive phase differences of the switchable BFN and the higher-order BM does not mean the same property of the two sets of beams due to the different number of elements. Concretely, there are two important differences between the proposed BFN and the higher-order BM. Firstly, the beams from the BFN can only be operated by a time-sharing form. Only half of the total beams in other distribution are available at the same time. By contrast, all the beams of the higher-order BM can be manipulated at the same time. Secondly, each of the proposed BFN beams has a lower directivity and wider beam width than the corresponding beam from BM because of the smaller number of elements.

6.4.1.4 Properties of Extended Beams

It could be better to clarify the situation of the extended beams before the discussion regarding the property of the beams. One of the advantages of BMs is that the multiple beams can be simultaneously and physically linked to different ports. However, it is impossible to keep this advantage in the proposed BFN, because it means achieving more beams with the same number of ports. As a compromise between BMs and single-beam phased array, the extended beams of the proposed scheme will be operated in a time-sharing form to share the ports.

If ignoring the effect of time-sharing work, and considering all switchable beams to be the same as fixed beams, the extended BFN has a remarkably improved beam coverage compared with the traditional BM. The dominant factor to determine the beam properties is the value of γ_S, though many other factors, such as the space between array elements, the directivity of elements, and mutual coupling, may also have an impact on the properties.

The relation between beam characters and γ_S will be discussed and demonstrated below by sets of design curves. For a generalized consideration, the space between elements is a half wavelength in free space, all elements are perfectly isotropic, and the effect of mutual coupling is ignored.

In addition, some definitions are utilized to represent the switchable beam properties, such as beam directions and the levels of beam crossover, as illustrated and explained in Figure 6-25. Here, the variables beginning with 'P' express the directions of beam peak; the number after 'P' signifies the sequence close to the direction of $\theta = 0°$ in the set of beams working simultaneously; the suffixes of 'L' and 'R' are applicable to the sets of $\gamma = -\gamma_S$ and $\gamma = +\gamma_S$, respectively. The variables beginning with 'C' indicate the levels of beam crossovers; the number following expresses the sequence close to the direction of $\theta = 0°$. Due to the symmetry, we concentrate on the region of $\theta \geq 0$.

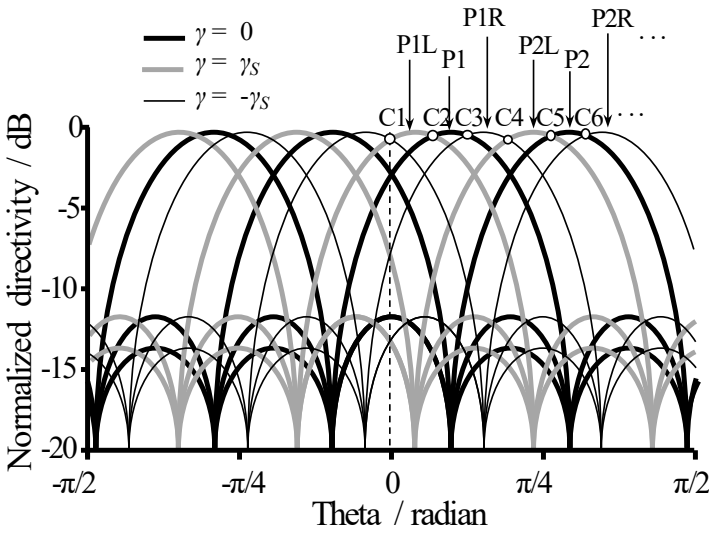

Figure 6-25. Schematic of some definitions to illustrate the beam properties of the extended beamforming network. The switchable 12 beams extended from a 4×4 BM is exemplified to demonstrate the names and numbers of the beam directions with the positions of beam crossovers.

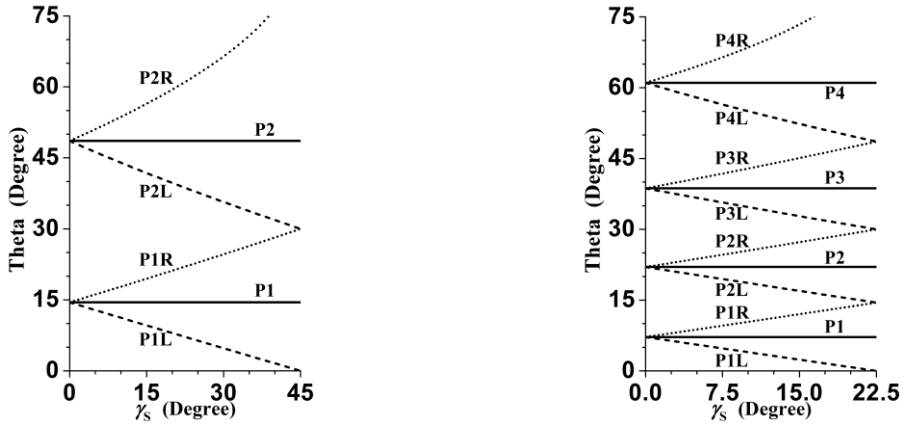

(a) BFNs are extended from 4 × 4 BM

(b) BFNs are extended from 8 × 8 BM

Figure 6-26. Relation between beam directions and γ_S for the switchable BFNs. The BFNs are extended from 4 × 4 BM and 8 × 8 BM.

The design curves to illustrate the relation between beam directions and γ_S are shown in Figure 6-26. We can find that the values of γ_S are not necessarily greater than $\pi/2^N$ for any N. As a higher value of γ_S means that the two scanned sets of beams will be close to each other, even might overlap with each other, which is not helpful in providing adequate beam coverage. Approximately, $\gamma_S = \pi/2^{N+1}$ is recommended to achieve the balance between the distribution of beam directions and the

design of switchable couplers. In that case, we can obtain $\alpha_{S1} = \pi/4$ for any N based on equation (6-11).

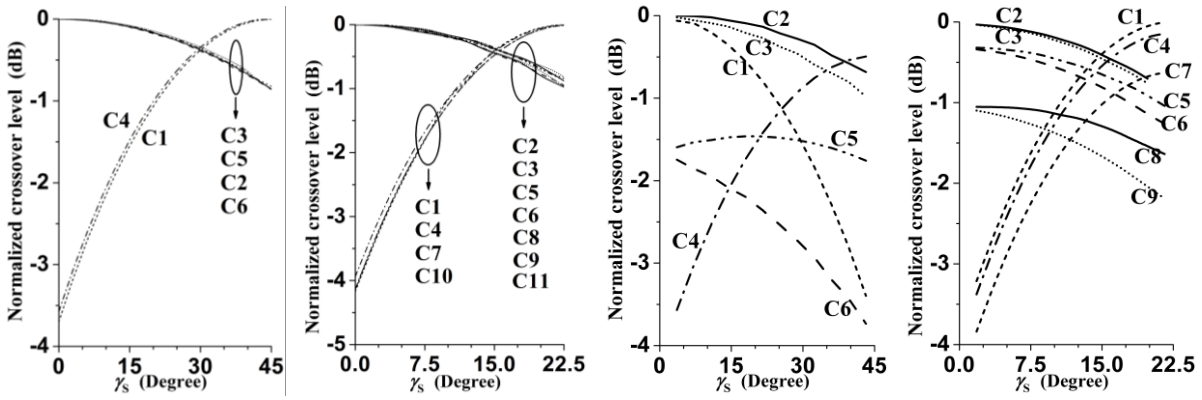

(a)* (b)** (c)*** (d)****

* The BFNs are extended from 4 × 4 BM without the loss of directivity; ** Extended 8 × 8 BM without the loss of directivity; ***Extended from 4 × 4 BM with the loss of directivity; ****Extended from 8 × 8 BM with the loss of directivity.

Figure 6-27. Relation between crossover levels and γ_S for the switchable BFNs.

The design curves to illustrate the relationship between the beams crossover levels and γ_S are shown in Figure 6-27. In Figure 6-27 (a) and (b), the effect of directivity loss with respect to the broadside is not taken into account. It clearly exhibits the contribution by changing γ_S to improve the crossover level. The crossovers at the intersections of two scanned sets of beams have approximately the same property. Similarly, the crossovers at the intersections of one scanned and one non-scanned set of beams have another property.

Especially when $\gamma_S \approx \pi/(3 \cdot 2^{N-1})$, we can obtain the maximum crossover level for all crossovers, which is about 0.4 dB lower than the maximum directivities. In that case, α_{S1} is approximately $\pi/3$ for any N, and more than 3-dB improvements can be achieved compared with traditional BMs.

In Figure 6-27 (c) and (d), the effect of the directivity loss is taken into account to illustrate its impact. It can be found that the crossover levels will decrease when they move further away from the normal direction, and the directivity drops at the crossovers and becomes more severe. Besides,

it should be noted that when some beams move too close to the edges, the directivity will drastically decrease. This effect can be found by comparing Fig. 7 (b) and (d). In Fig. 7 (b), the maximum number of crossovers is C11, but in Fig. 7 (d), it is only C9. Another two crossovers cannot be shown in this curve due to the severe directivity drop. This situation could happen when the order of BM is higher than 8.

6.4.2 Examples and Results

An example of a circuit with $N = 2$ and $\gamma_S = \pi/12$ operating at 2.4 GHz is designed, fabricated and measured for verification and demonstration. The layout with instructions for components is shown in Figure 6-28 (a). Rogers Duriod 5880 with $\varepsilon_r = 2.20$ and $h = 31$mil is utilized. The photo, dimensions, and port numbers of the circuits are shown in Figure 6-28 (b).

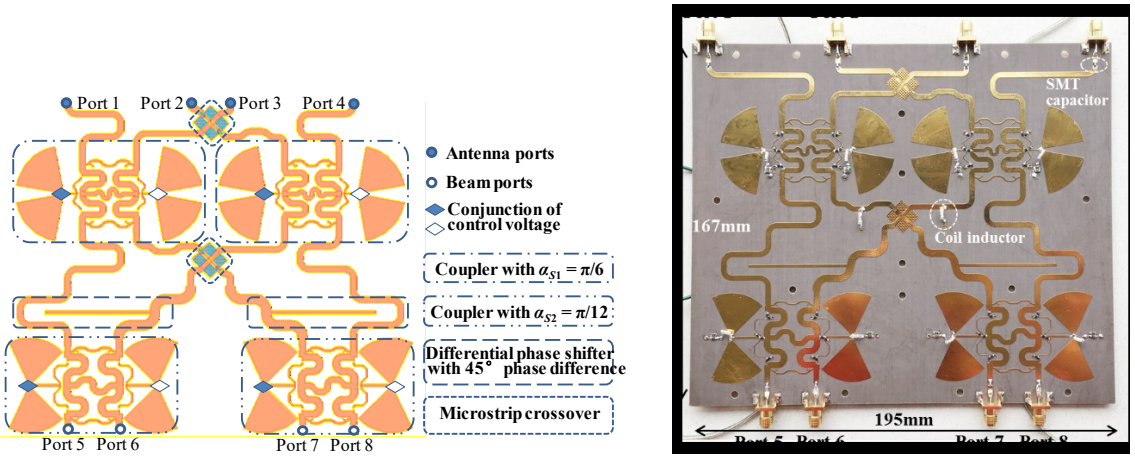

(a) Circuit layout, (b) Circuit photo

Figure 6-28. Switchable beamforming network extended from 4 × 4 BM for 2.4GHz application.

In terms of the circuit structure, a notable advantage of this design is the simplicity of controlling the biasing voltages. Though there are eight nodes that need biasing voltages, every four nodes on the same side of four couplers can be operated synchronously, as illustrated in Figure 6-29,

according to the mechanism presented in Expression (6-11). More clearly, only two wires are required to manipulate this network, and each wire only needs two voltages, ±3.0 V.

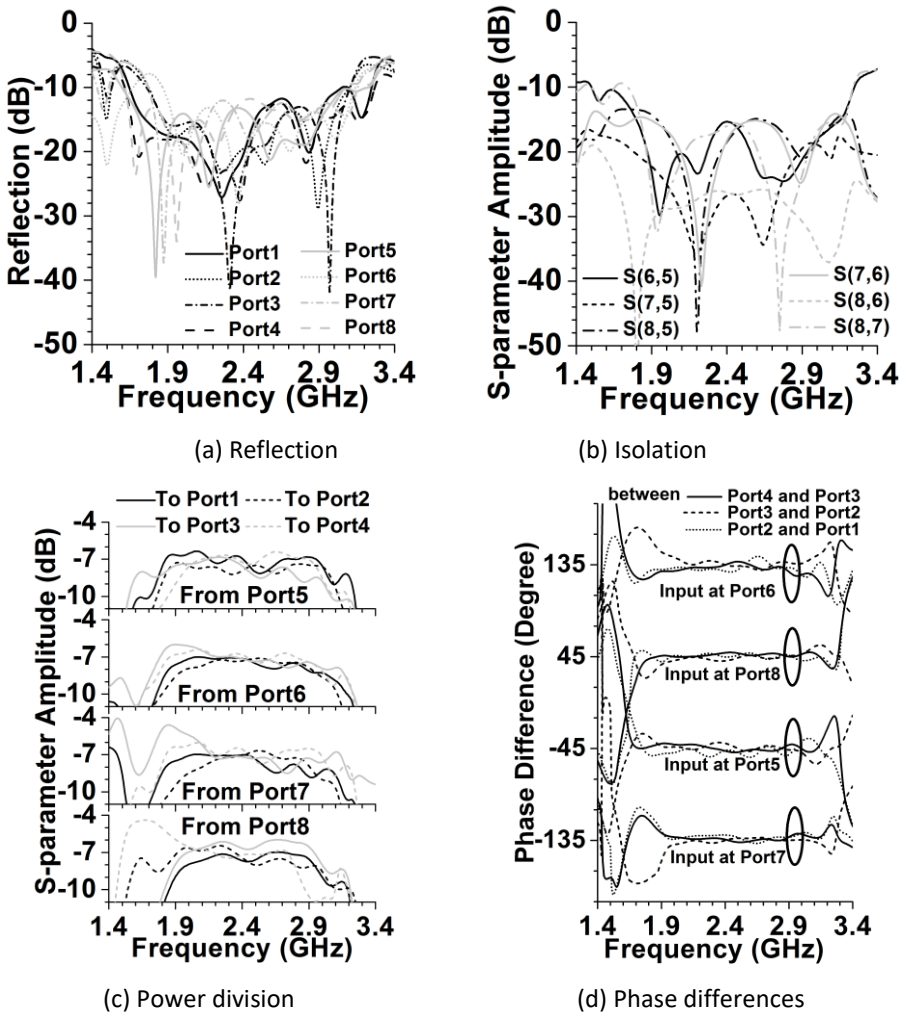

Figure 6-29. Measurement results of the non-scanned set of beams. The reflection, isolation , power division , and phase differences are illustrated, respectively.

Besides the couplers, a compact microstrip crossover [115] and a wideband differential phase shifter with a fixed phase shift [55] is employed as integral parts. Both components deliver satisfying performance with the bandwidth. The measured results are plotted in Figure 6-29 and Figure 6-30. Due to the structural symmetry, only one set of scanned beams is demonstrated here.

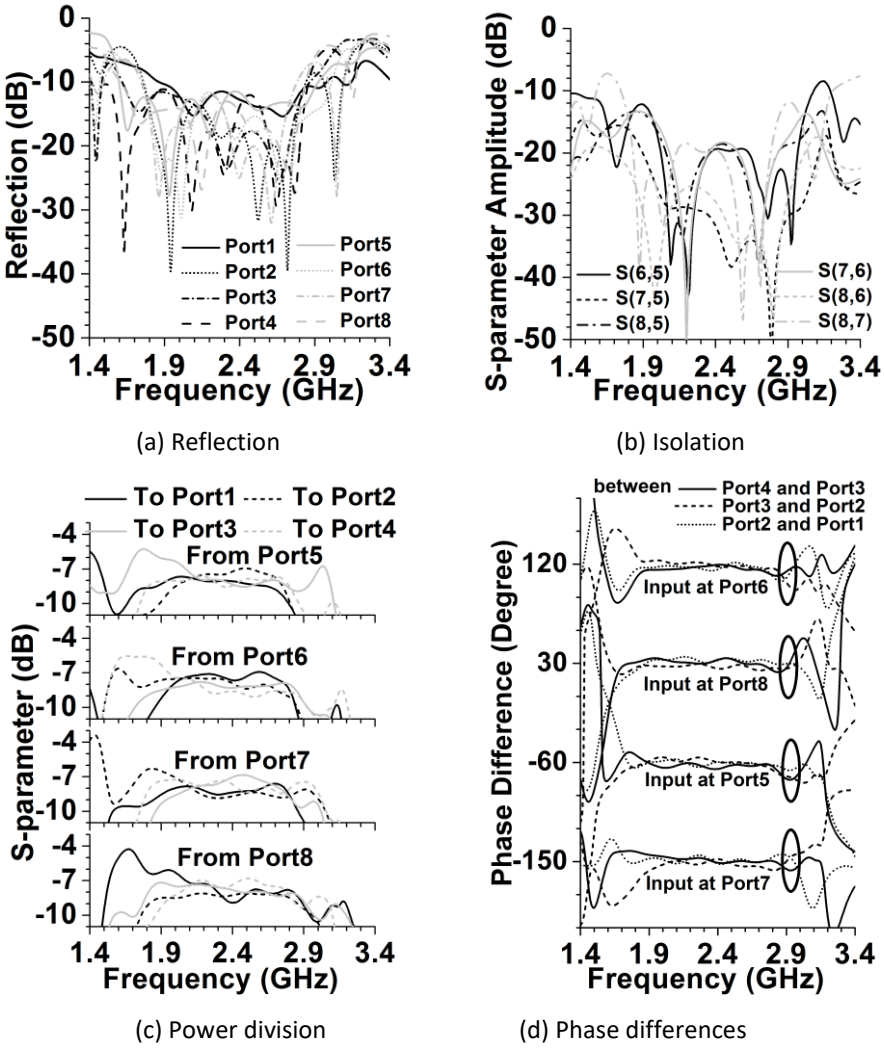

Figure 6-30. Measurement results of the scanned set of beams. The reflection, isolation, power division, and phase differences are illustrated, respectively.

Through both sets of curves, we can see that the three sequences of the progressive phase differences, -3π/4, -π/4, +π/4, +3π/4, and -5π/6, -π/3, π/6, 2π/3, and -2π/3, -π/6, π/3, 5π/6, can be achieved. The equal power division with unbalance less than ±1.7 dB, the coherent phase differences with the error lower than ±12°, the reflection under -11.5 dB at all ports, and the isolation better than -15.5 dB among all beam ports can be obtained over 2.0 GHz to 2.8 GHz. The insertion loss is about 1.8 dB.

The remarkable flatness on phase response can be observed in Figure 6-29 (d) and Figure 6-30 (d), which reveals the prospective potential of a wideband steerable antenna array based on the proposed BFN. To verify the capability of beamforming and coverage, the radiation patterns of an array factor are calculated based on the measured transmission properties at 2.0 GHz, 2.4 GHz, and 2.8 GHz, and displayed in Figure 6-31. Here, the space between elements is 60 mm, which is about 0.48 λ_0 at 2.4 GHz. A minimum -1.7 dBi crossover level can be found at 2.4 GHz and theta = 0, which shows a good agreement with the results shown in Figure 6-27 (a). At 2.0 GHz and 2.8 GHz, the minimum crossover levels are -1.8 dBi and -1.6 dBi, respectively. In terms of beam coverage, approximately 2.0 dB improvement of the crossover level can be obtained by using this scheme.

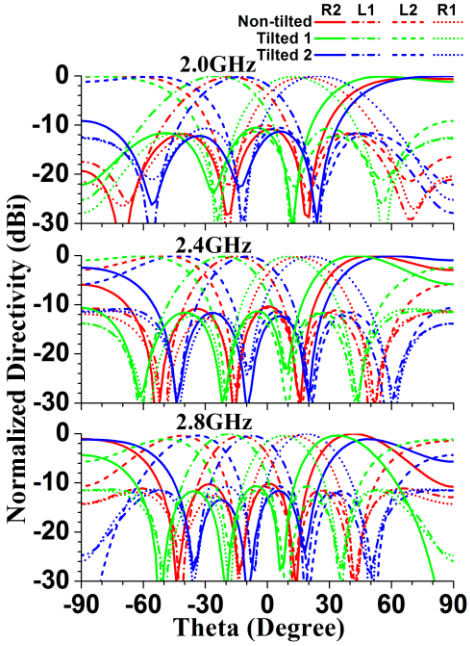

Figure 6-31. Calculated radiation patterns of array factor based on measured transmission properties at different frequencies.

Through the experimental circuit and the measurement results, some unique advantages of this scheme can be found compared with other solutions, such as using tunable phase shifters outside

Butler matrices. Firstly, a wideband and switchable phase response can be achieved due to applying the switchable mechanism inside the second-order hybrid coupler. Moreover, each option of the switchable couplers can exactly provide one set of beams without the phase errors that are usually occurred on digital phase shifter. Besides, in terms of the number of switchable components, it will increase in logarithmic with the beam number, rather than in linear.

6.4.3 Advantages Over Traditional Phased Arrays

The proposed scheme promises to be an alternative low-cost array because it provides more beams with flexible beam directions than the traditional BMs. Some works in [38], [39] combine traditional BMs with some phase shifters outside BMs for a similar purpose. The combination of BMs and phased arrays, in terms of the structural mechanism for such intention, can probably confuse the difference between both. Therefore, it could be helpful to clarify the distinct points.

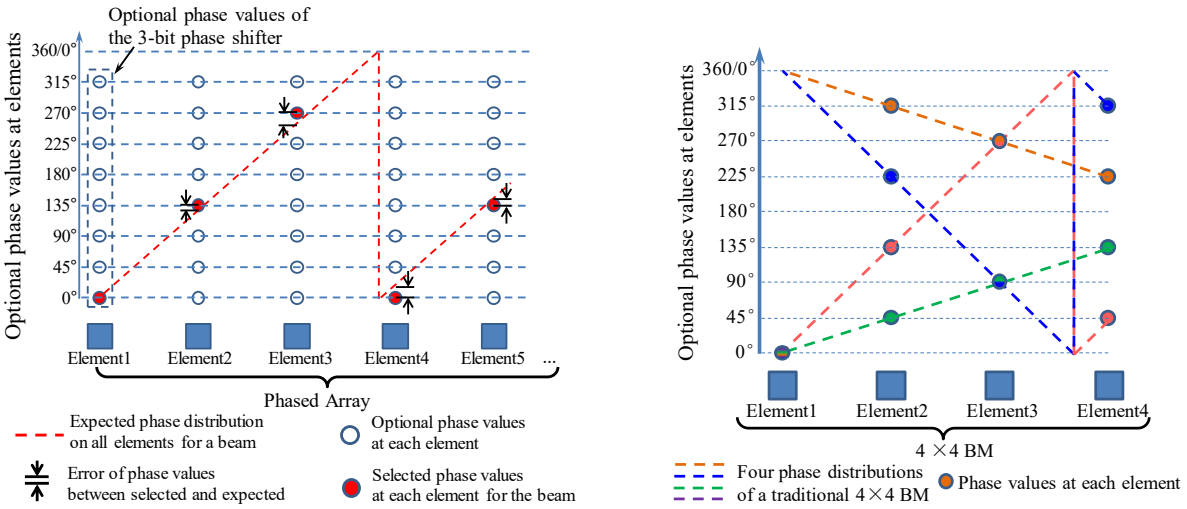

Figure 6-32. Comparison of phase distributions to form beams.

For a typical phased array, the phase distribution at each element is designed independently without any consideration for beams, or, the relationship with other elements. As exemplified in Figure 6-32 (a), for anyone of specific beams, the available optional phases from the phase shifter

may not be precisely equal to the required phase at elements. Even if enhancing the resolution of phase shifters by using higher-order phase shifters, it can only reduce the maximum possible error, but cannot theoretically eliminate the possible deviation from the needed phase at any element for a specific beam direction. It is quite clear that the traditional scheme of phased arrays is only aimed to diversify the phase values on each individual element, and without any consideration to coordinate values on different elements together. Therefore, the scheme of phased arrays can be referred to as Element- Based (EB).

By contrast, BMs are aimed to generate beams, or, progressive phase differences among elements, rather than the phases on each of the individual elements. Every input port of BMs is designed to produce a set of progressive phase differences on all output ports. Theoretically, there is no phase error for each of these beams, as the example demonstrated in Figure 6-32 (b). Consequently, this scheme can be referred to as Beam-Based (BB).

The scheme of EB is generally more versatile, but not as efficient as BB, in terms of beamforming. For example, in all phased arrays, it is easy to be implemented that increase an identical phase value on all elements synchronously. Obviously, this operation will not change the beam because it does not alter the relative phase differences of two adjacent elements. In other words, these optional statues in all the phased arrays are redundant for beamforming. However, the redundancy occupies the reconfigurable options, expends the interconnections of layout, and consumes the resource of control logic. On the contrary, the scheme of BB has a much better efficiency because each of the valid statuses is corresponding to a unique beam.

It is easy to see that the proposed idea is a BB scheme, and all the valid statuses are corresponding to particular beams different than each other. The switchable couplers in this proposed scheme can

be seen as ‘beam shifters’ to change the beams than the traditional BMs, compared to the ‘phase shifters’ utilized in other work to enhance the beam coverage.

Chapter 7

Compact Butler Matrices for 2-D Beamforming at Millimeter-wave

The design of a 2-D beamforming antenna array operated at mm-wave frequencies based on the eight-port coupler is discussed in this chapter. To reduce the leakage of traditional microstrip lines at a higher frequency, the microstrip packaged by artificial magnetic conductor (AMC) is adopted. Mainly, a back-to-back double-layer microstrip line with two layers of AMC covering the top and bottom surfaces is utilized.

Concretely, the antenna elements with two different feed configurations, the AMC layer with essential features, the eight-port coupler based PMSL, and the entire 2 × 2 array with 2-D beam-steer performance are introduced respectively. According to the structural characters of the eight-port coupler discussed in Chapter 5, the ports connected to array elements are located on the top and bottom layers separately, and therefore, two different designs for the antenna element are required to adapt the two configurations of feeding but have the same radiation patterns and matching property. The effect of an AMC layer on the eight-port couplers is simulated and illustrated. To achieve the performance of 2-D beam steering, two 90° phase delay lines are added in between the eight-port couplers and the antenna elements. Simulation results exhibit promising performances of the 2-D beam steerable array at matching, isolation, and radiation pattern.

7.1 Slot Antenna Based on Double-Layer Microstrip Lines

It can be found in Chapter 5 that the output ports of the eight-port coupler could be on either the top layer or bottom layer. Consequently, there are two different configurations of the slot antennas based on double-layer PMSL to suit to the outputs of the coupler.

The side views of the two configurations are shown in Figure 7-1 (a) and (b). It can be found that there are two AMC layers covering to the top and bottom of the back-to-back microstrip structure, respectively. However, the window on the AMC layer to produce radiation is constantly on the top AMC layer. This configuration can generate the directional radiation pointing to up-direction regardless of which layers the excitation located on.

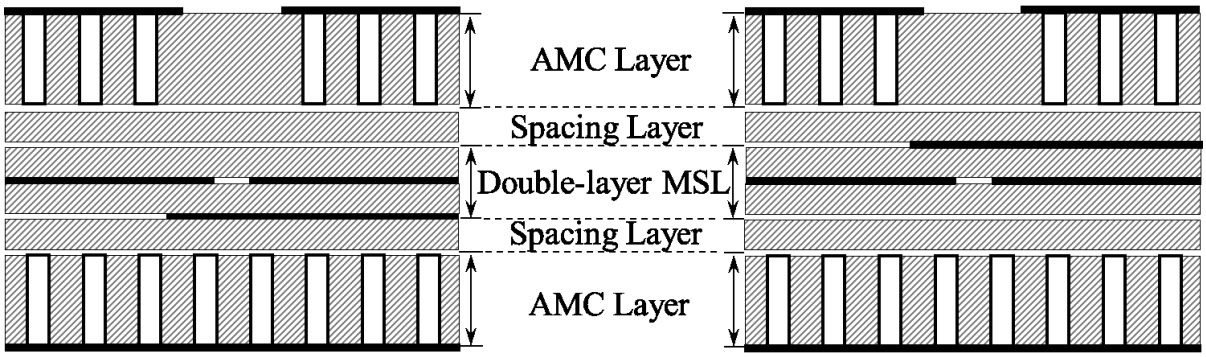

(a) The excited microstrip on the bottom layer (b) The excited microstrip on the top layer

Figure 7-1. Side views of two slot antennas based double-layer PMSL.

The layouts of each layer for the two slots antennas are demonstrated in Figure 7-2 (a) and (b), respectively. Especially when the driven microstrip on the bottom layer, there is a parasitic element required on the top layer for impedance matching.

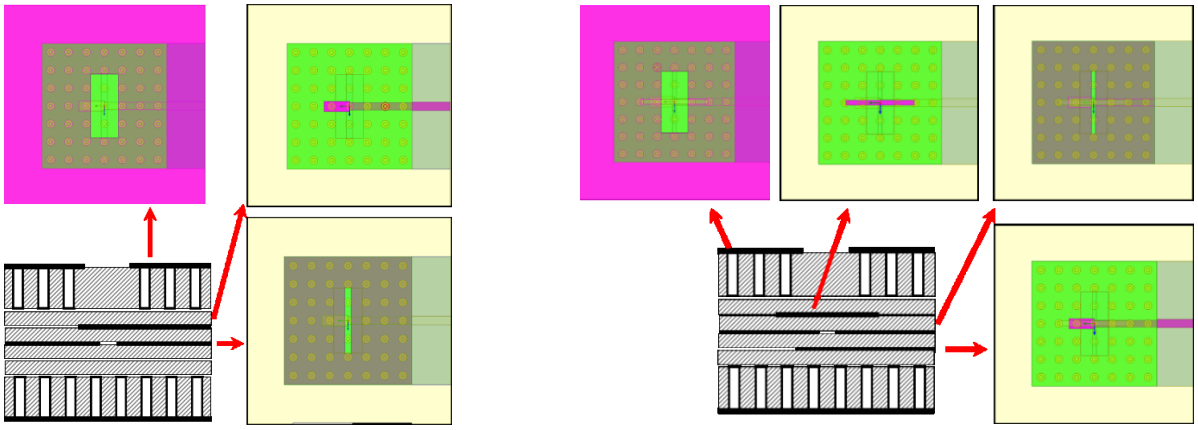

(a) The excited microstrip on the top layer (b) The excited microstrip on the bottom layer

Figure 7-2. Layouts of each layer of two slot antennas based on double-layer PMSL.

The simulated results of matching and radiation for the two slot antennas by ANSYS HFSS are illustrated in Figure 7-4 and Figure 7-3. Here, in the (c) of both figures, red lines are the E-plane; blue lines are the H-plane; solid lines are the co-pol.; dotted lines are the x-pol.

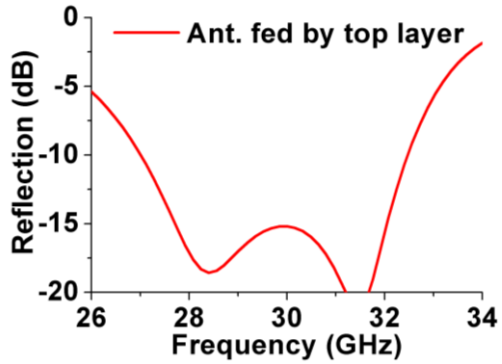

(a) VSWR

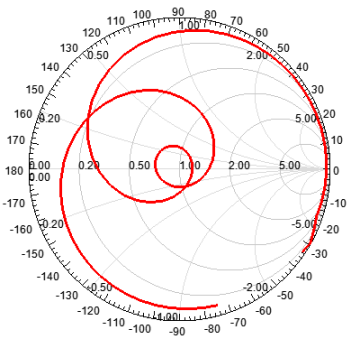

(b) Smith chart

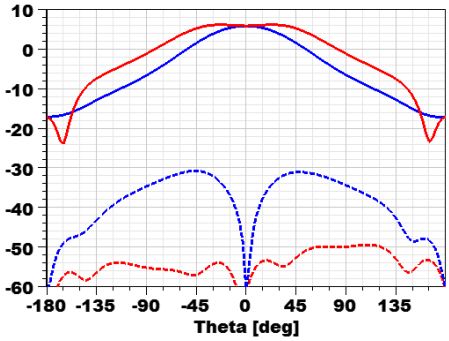

(c) Radiation pattern

Figure 7-3. Simulated results of matching and radiation for the slot antenna fed by the microstrip on the top layer.

Concretely, the simulated results for the slot antenna fed by the microstrip on the top layer are shown in; Figure 7-3,the simulated results for the slot antenna fed by the microstrip on the bottom layer are shown in Figure 7-4. Both results have the almost same matching bandwidth and radiation patterns, but only the reflection coefficients inside working bandwidth have a small difference between each other.

Here, to ensure the two antennas have the same radiation patterns, the windows on the top AMC layer for both antennas have the same dimensions, as well as the slots on the common ground are the same size and position. To compensate for the effects of different feeding structures on the matching performance, a parasitic strip on the top layer is adopted for the antenna fed by the bottom layer, as shown in Figure 7-2 (b).

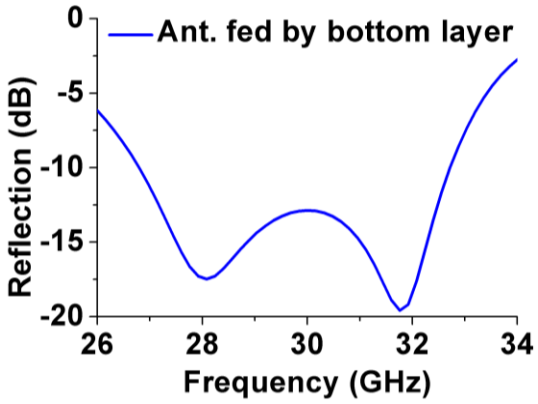

(a) VSWR

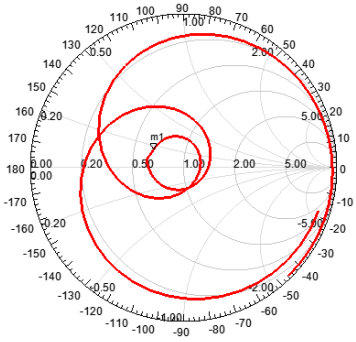

(b) Smith chart

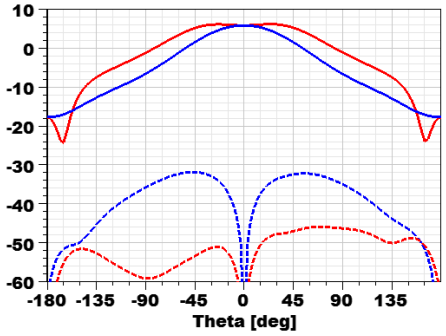

(c) Radiation pattern

Figure 7-4. Simulated results of matching and radiation for the slot antenna fed by the microstrip on the bottom layer.

7.2 AMC Package Layer

To suppress the high-order propagation modes when microstrip lines operated at mm-wave frequencies, an AMC packaging layer is required to cover on the surface of the microstrip line. Due to the structural properties of the eight-port couple, the back-to-back double layer microstrip line is amended, and therefore, two layers of AMC are needed to cover both surfaces of the double layer microstrip line.

The unicell of the pin for the AMC layer is demonstrated in Figure 7-5 (a). It is a standard cylinder pin with about λ/4 length, which can provide about 2:1 fractional bandwidth for quasi-TEM propagation. To be convenient to manufacture, the pin has been separated into three layers, which can be implemented by multi-layer printed circuit board technology.

The thickness of the pins is 60mil (1.524mm); the length of side is 1.4mm; the diameter of the pins is 12mil (0.3048mm) the diameter of the pad on the bottom of the pins is 24mil (0.6096mm); the thickness of spacing layer is 20mil (0.508mm); the thickness of microstrip is 20mil (0.508mm).

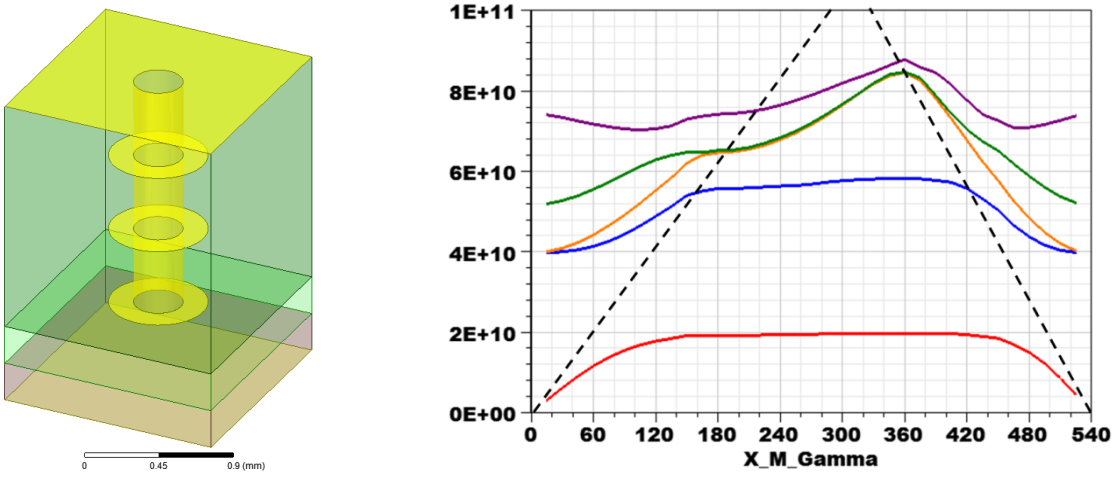

(a) Structure of unicell of the pin (b) Dispersion diagram

Figure 7-5. Structure of unicell of the pin for the AMC layer and the dispersion diagram.

The dispersion diagram based on the eigenmode simulation with 2-D periodic boundary conditions is illustrated in Figure 7-5 (b). The bandgap for quasi-TEM mode propagation is between 20 GHz to 40 GHz approximately, though the bandwidths of antenna elements and eight-port coupler are narrower than this.

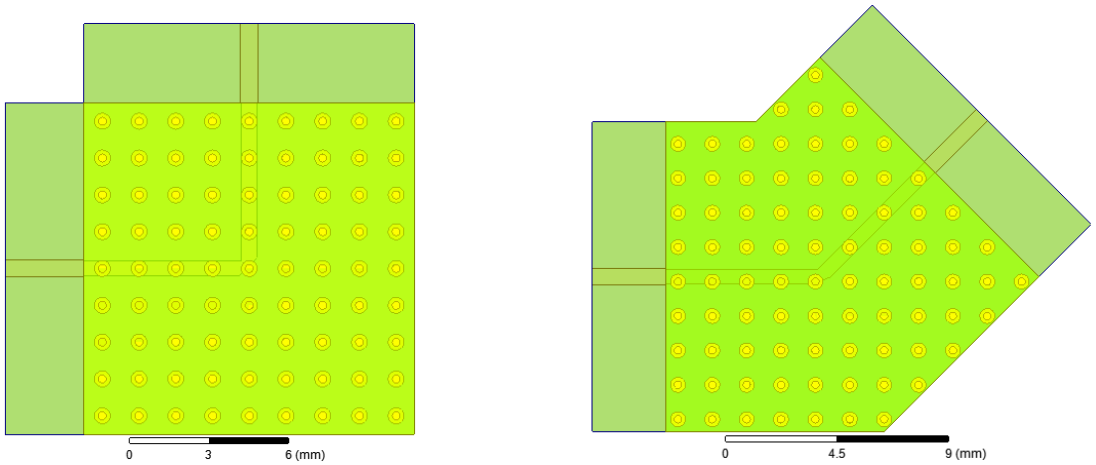

(a) 90°bend (b) 45° bend

Figure 7-6. Structures of 90°bend and 45° bend based on the PMSL for full-wave simulation.

Based on the AMC layer structure, two circuits of 45° bend and 90° bend based on PMSL are built for full-wave analysis to evaluate the effects of the discontinuity from bends, as shown in Figure 7-7. By the simulation of the two bends, the transmission properties of the PMSL can be preliminarily verified. Here, the simulation for the transmission line based on the 1-D periodic structure will not be conducted because the eight-port coupler and the feed network are very small, which do not have long uniform transmission structures. Instead, there will be some bends in the network.

The simulated results of transmission and reflection of the two bends by ANSYS HFSS are illustrated in Figure 7-8. It can be found that from 22 GHz to 38 GHz, the matching is pretty good and stable with reflections lower than -25 dB for both models. There are not spurs or leakage due to other models propagating. Here, the effect of the transition between PMSL and traditional

microstrip lines has been considered through the full-wave simulation. The difference between the widths of PMSL and traditional microstrip lines can be found at the borders between them.

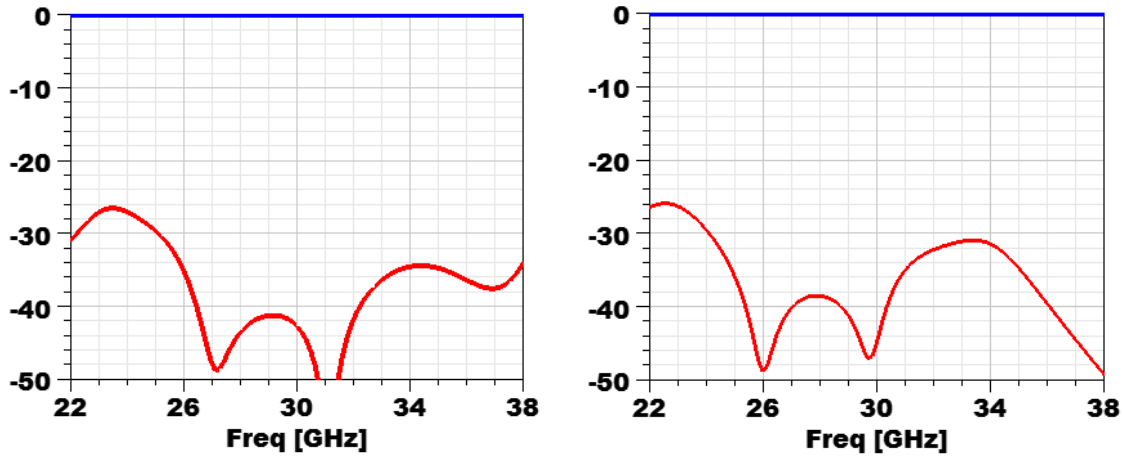

(a) 90°bend (b) 45° bend

Figure 7-8. Simulated results of transmission and reflection for the 90°bend and 45° bend based on the PMSL.

7.3 Eight-Port Coupler Based on Double Layer PMSL

Based on the design of the AMC layer and eight-port coupler proposed in Chapter 5, an eight-port coupler operated at mm-wave frequencies can be achieved, as shown in Figure 7-9.

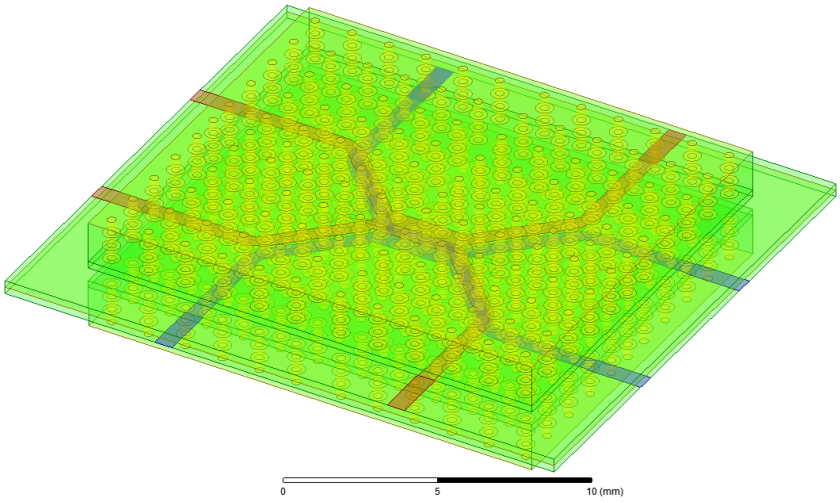

Figure 7-9. Structure of eight-port coupler based on the PMSL for full-wave simulation.

The structure of the eight-port coupler based on the PMSL for full-wave simulation is demonstrated in Figure 7-9, and the layouts for each layer are illustrated in Figure 7-10. The layout with red color represents the shape of the conductor on the top microstrip layer; the layout with blue color represents the shape of the conductor on the bottom microstrip layer.

It can be found that there are no vias needed and only a few bends and steps in the layout. The structure is compact and concise, and very easy to be integrated into antenna array.

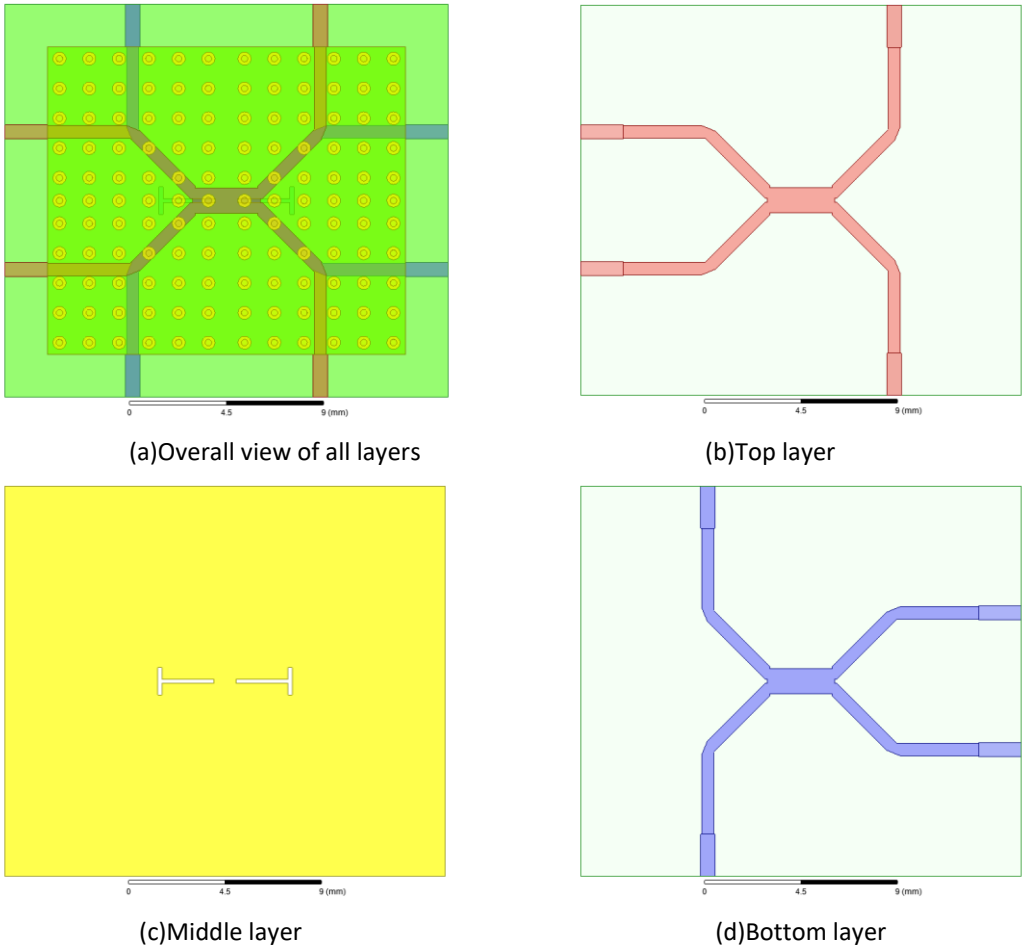

Figure 7-10. Layouts of each layer for the eight-port coupler.

The full-wave simulation results of matching, power divisions, and isolations are listed in Figure 7-11. It can be found that in about 13% fractional bandwidth, the satisfying performances can be

achieved, for example, the matching better than 20 dB, isolation higher than 15 dB, and equal power division with unbalance loss than ±0.5 dB.

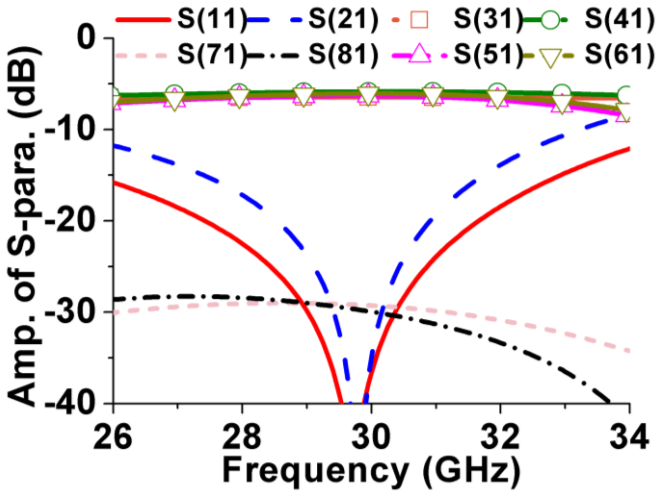

Figure 7-11. Full-wave simulation results of transmission and reflection for the coupler.

Concretely, the matching better than 20 dB can be achieved over 28 GHz - 32 GHz; the isolation between port 1 and 2 is better than 15 dB; the transmissions from port 1 to port 3, 4, 5, and 6 are about -6 dB with good agreement with each other; the isolations between port 1 and port 7 and 8 are better than 30 dB.

7.4 Antenna Array With 2-D Beam Steering

Based on the designs of the mm-wave eight-port coupler and the slot antennas, a 2 × 2 antenna array with 2-D beam steerable capability operated at 30 GHz can be achieved. The structure and the layouts for each layer are shown in Figure 7-12.

Here, the cross-section of the antenna array with the network is the same as shown in Figure 7-1. It is a back-to-back double layer microstrip with two AMC layers covering the top and bottom surfaces. The thickness of the AMC layer is 60mil; the thickness of the spacing layer is 5mil; the

thickness of each layer of microstrip is 10mil, and all laminates are RO 3003 with ε_r = 3.0. The distances of four-element either along the horizontal or vertical directions are 8.6mm, which is about 0.86 λ_0 at the central frequency, 30GHz.

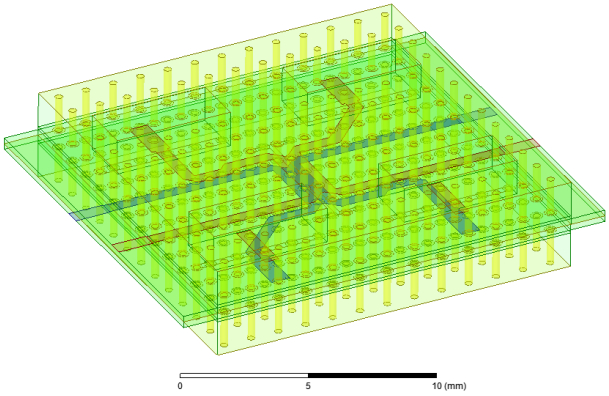

(a) Whole structure of array with feed network

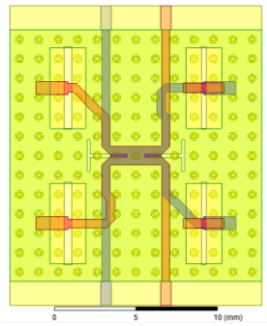

(b) Top view of whole structure

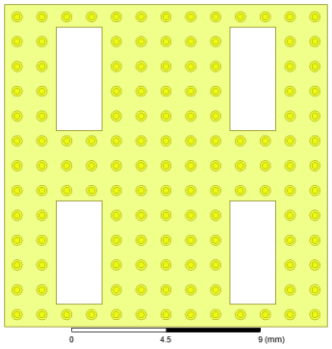

(c) Layout of top AMC layer

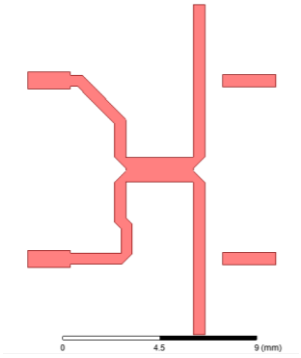

(d) Layout of top microstrip line

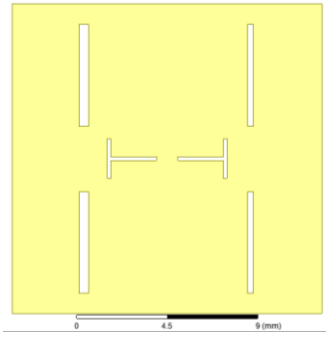

(e) Layout of middle microstrip line

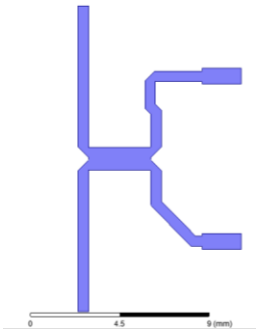

(f) Layout of bottom microstrip line

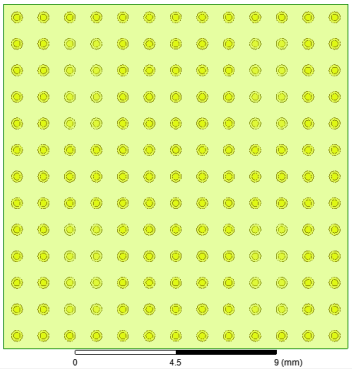

(g) Layout of bottom AMC layer

Figure 7-12. Structure of 2-D beam steerable array based on the eight-port coupler for mm-wave.

The transition between the traditional microstrip line and PMSL has been built into the model for full-wave simulation, and therefore, the effects have been considered. And, two 90-degree phase delay lines are placed on the diagonal two branches of the four branches connected to antenna elements to regulate the beam directions.

The simulated results of matching, isolations, and radiation patterns are demonstrated in Figure 7-13 and Beam4

Figure 7-14. Concretely, from Figure 7-13, it can be found that the matching at the four beam-ports is better than 12dB from 28 GHz to 32 GHz; the isolations are better than 9 dB.

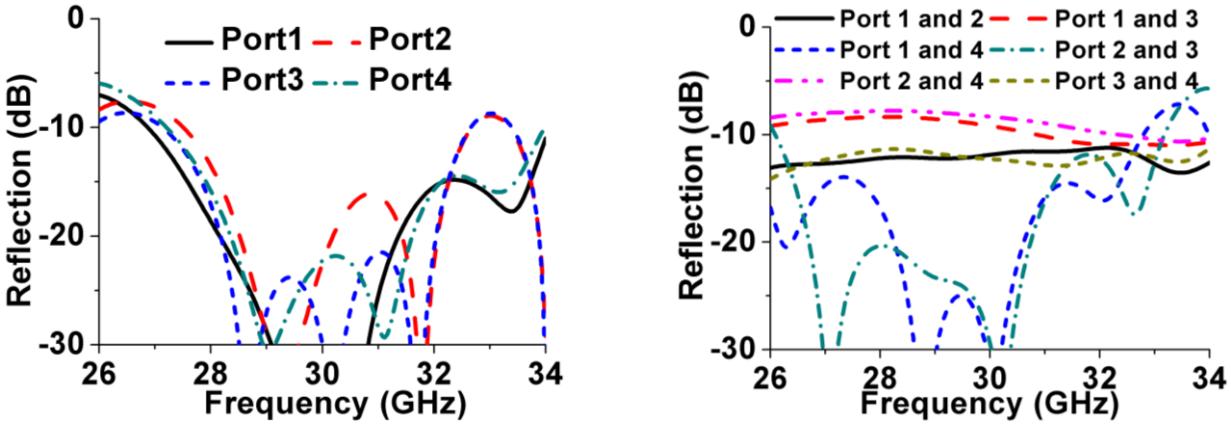

(a) Matching of each port

(b) Isolations among ports

Figure 7-13. Matching and isolations of 2-D beam steerable array.

The isolations may not be good enough for some applications, and the main reason for the lower isolation is the reflections from antenna elements. In other words, the mutual coupling between elements degrades the isolation.

The radiation patterns when each of the four ports is excited are illustrated in

. The multi-beam forming features can be observed clearly. However, the sidelobe levels are relatively high for some applications.

There is still room for further improvements for the reduction of sidelobe levels and an increase of the isolations.

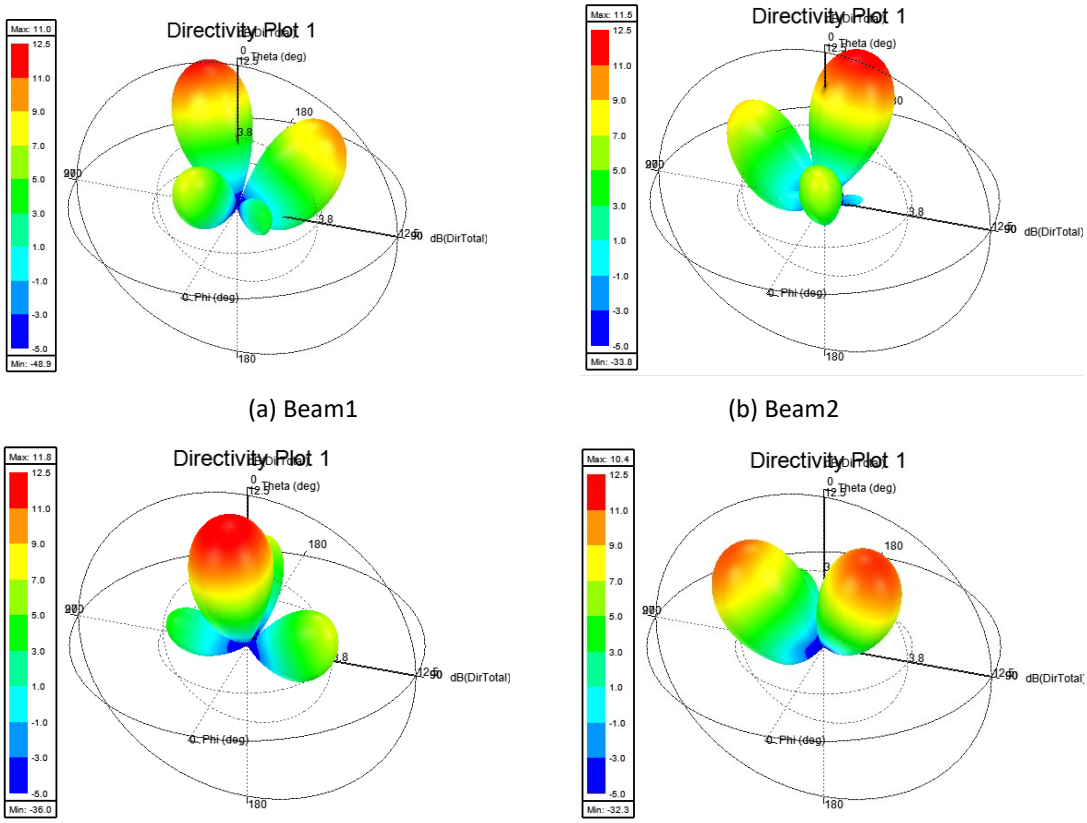

(a) Beam1 (b) Beam2

(c) Beam3 (d) Beam4

Figure 7-14. 3-D radiation patterns when each of the four ports is excited, respectively.

Chapter 8

Conclusions and Future Works

8.1 Conclusions

8.1.1 Beam Number Extension for BMs Based on Switchable Coupler

The concept of extending the beam number of Butler matrices by employing reconfigurable couplers has been presented and illustrated. The beam number can be increased to a triple number of the traditional BM. The principle and generalized design method have been discussed and demonstrated by a series of expressions. Moreover, the design curves have been provided to depict the extended beam coverage. An example of 12-beam switchable BFN extended from a 4 × 4 BM working at 2.4 GHz has been fabricated and tested. Such reconfigurable BFN has provided satisfying performance over a 30% relative bandwidth. This scheme could become an economical alternative to the phased array in some applications.

8.1.2 Two-Dimensional Butler Matrices

A new beam-forming device, 2D-BM, has been presented. The principle of the design method has been generalized, and experimental examples have been presented. As a crucial component of the 2D-BM, a new phase-shifter group has been introduced with its definition, property, circuit model, and analytical solution.

The two innovative devices have the potential to be applied to the beam-forming network, phased array, and a reconfigurable antenna array for the communication systems.

8.1.3 Eight-Port Coupler and Applications

A novel eight-port coupler with a very compact configuration has been thoroughly introduced in terms of the principle, structural framework, analytical features, and the potential for some applications on monopulse arrays. The advantage of building compact feeding networks for 2-D and dual-polarized comparator has been experimentally exhibited by the examples of two antenna arrays. Reasonable performance can be achieved within a quite simple structure and small area.

The proposed eight-port coupler could have further potential to be utilized at millimeter-wave frequencies for automotive radars and imaging systems.

8.1.4 Investigations of Components on Feed Networks

8.1.4.1 Multi-Octave Bandwidth of Parallel-Feeding Network Based on Impedance Transformer Concept

The idea to achieve an octaves-bandwidth parallel-feeding network based on the concept of the impedance transformer has been introduced. The principle, design method, and consideration for discontinuities have been proposed and exemplified by the instances.

The generalized scheme can be extensively applied to the feeding networks for antenna arrays with uniform distribution, and it would not be limited to the particular forms of transmission lines.

8.1.4.2 Effects of Imperfect Isolation of Crossovers on Performance of Butler Matrices

The investigation of the effects of imperfect isolation of crossovers on Butler matrices has been conducted and described. The circuit model of BMs has been built based on forward transmission

S-parameters, and the effects can be numerically calculated by the circuit model. The method has been verified by simulation and experimental measurement. It has been revealed by the investigation that crossovers can produce non-negligible effects on BMs, and it cannot be offset by other components.

8.2 Major Contributions

The main contributions of this thesis are summarized in several topics below. The related publications are listed after the references.

8.2.1 Beam Number Extension for BMs based on Switchable Coupler

A scheme to extend the beam number of BMs by using an electrically switchable coupler is proposed [J-2] and [J-4]. The beam properties, design method and process, are introduced and experimentally verified.

8.2.2 Two-Dimensional Butler Matrices

A generalized method to construct a 2-D BM with required beam number based on traditional BMs is proposed. Besides, as a key component, the phase-shifter group is introduced with the features represented by analytical expressions [J-3], [C-2].

8.2.3 Eight-Port Coupler With Applications

A compact eight-port coupler with a very compact structure is introduced for 2-D beamforming and 2-D / dual-polarized monopulse array. The novel coupler can be implemented by a planar circuit and without vias, steps, junctions, and bends [J-6], [C-1], [C-3], [C-4].

8.2.3.1 Effects of Imperfect Isolation of Crossovers on Performance of Butler Matrices

The effect of imperfect isolation of crossover on the performance of BMs is analyzed by an analytical method with experimental verification [J-5].

A scheme to build a uniform parallel feed network with multi-octave fractional bandwidth is proposed with experimental verification [J-1] [C-5].

8.3 Further Works

The experimental verification of the 2-D beamforming array based on the eight-port coupler with PMSL working at mm-wave has not been completed yet with satisfying performance. This work could be done in the future.

Besides, the high-order 2-D BMs based on eight-port coupler and PMSL would have more potential for the fifth-generation communications due to more beams generated. Furthermore, the combination of high-order 2-D BMs and electrically controllable components will provide much more attractive features with the traditional passive circuits. It has broad prospects for the applications of automotive radars and intelligent devices.

References

[1] J. Butler and R. Lowe, “Beamforming matrix simplify design of electronically scanned antennas,” *Electron. Design*, vol. 9, pp. 170-173, Apr. 1961.

[2] J. Shelton, and K. S. Kelleher, “Multiple beams from linear arrays,” *IRE Trans. Antennas Propag.*, vol. 9, no. 2, pp. 154-161, Mar. 1961.

[3] J. W. Lian, Y. L. Ban, C. Xiao, and Z. F. Yu, “Compact substrate-integrated 4 × 8 Butler matrix with sidelobe suppression for millimeter-wave multibeam application,” *IEEE Antennas Wireless Propag. Lett.*, vol. 17, no. 5, pp. 928-932, May 2018.

[4] J. W. Lian, Y. L. Ban, Q. L. Yang, B. Fu, Z. F. Yu and L. K. Sun, “Planar millimeter-wave 2-D beam-scanning multibeam array antenna fed by compact SIW beam-forming network,” *IEEE Trans. Antennas Propag.*, vol. 66, no. 3, pp. 1299-1310, March 2018.

[5] J. Blass, “The multidirectional antenna: A new approach to stacked beams,” in. *IRE Int. Conv. Rec.*, pp. 48-50, 1960.

[6] J. Nolen, “Synthesis of multiple beam networks for arbitrary illuminations,” Ph.D. dissertation, Baltimore, MD, Apr. 1965, Radio Division, Bendix Corp.

[7] W. Rotman and R. Turner, “Wide-angle microwave lens for line source applications,” *IEEE Trans. Antennas. Propag.*, vol. 11, no. 6, pp. 623-632, Nov. 1963.

[8] P. S. Hall and S. J. Vetterlein, “Review of radio frequency beamforming techniques for scanned and multiple beam antennas,” in *IEE Proc.H - Microw., Antennas Propag.*, vol. 137, no. 5, pp. 293-303, Oct. 1990.

[9] S. Gruszczynski, K. Wincza and K. Sachse, “Reduced sidelobe four-beam N-element antenna arrays fed by 4 × *N* Butler matrices," *IEEE Antennas Wireless Propag. Lett.*, vol. 5, pp. 430-434, 2006.

[10] K. Wincza and S. Gruszczynski, “Broadband integrated 8×8 butler matrix utilizing quadrature couplers and Schiffman phase shifters for multibeam antennas with broadside beam,” *IEEE Trans. Microw. Theory Techn.*, vol. 64, no. 8, pp. 2596–2604, Aug. 2016.

[11] M. Nedil, T. A. Denidni, and L. Talbi, “Novel Butler matrix using CPW multilayer technology,” *IEEE Trans. Microw. Theory Techn.*, vol. 54, no. 1, pp. 499–507, Jan. 2006.

[12] Y. Li, J. Wang and K. Luk, “Millimeter-wave multibeam aperture-coupled magnetoelectric dipole array with planar substrate integrated beamforming network for 5G applications,” *IEEE Trans. Antennas Propag.*, vol. 65, no. 12, pp. 6422-6431, Dec. 2017.

[13] J. Remez and R. Carmon, "Compact Designs of Waveguide Butler Matrices," *IEEE Antennas Wirel. Propag. Lett.*, vol. 5, pp. 27-31, 2006.

[14] M. Kishihara, A. Yamaguchi, Y. Utsumi and I. Ohta, “Fabrication of waveguide butler matrix for short millimeter-wave using X-ray lithography,” in *Proc. IEEE MTT-S, Int. Microw. Symp. (IMS)*, Honolulu, HI, 2017, pp. 568-571.

[15] M. M. M. Ali and A. Sebak, “2-D scanning magnetoelectric dipole antenna array fed by RGW Butler matrix,” *IEEE Trans. Antennas Propag.*, vol. 66, no. 11, pp. 6313-6321, Nov. 2018.

[16] F. Julian, G. Bernal and E. Rajo-Iglesias, “Design of a wide band Butler matrix in groove gap waveguide technology,” In *Proc. Int. Symp. Antennas Propag. (ISAP)*, Phuket, 2017, pp. 1-2.

[17] N. Ashraf, A. A. Kishk and A. Sebak, “AMC packaged - Butler matrix for millimeter wave beamforming,” in *Proc. IEEE/AP-S Int. Symp. Antennas Propag.*, Boston, MA, 2018, pp. 417-418.

[18] C. Liu, S. Xiao, Y. Guo, M., Tang, Y. Bai and B. Wang, "Circularly polarized beam-steering antenna array with Butler matrix network," *IEEE Antennas Wireless Propaga. Lett.*, vol. 10, pp. 1278-1281, 2011.

[19] L. Zhong, Y. Ban, J. Lian, Q. Yang, J. Guo and Z. Yu, "Miniaturized SIW multibeam antenna array fed by dual-layer 8 × 8 Butler matrix," *IEEE Antennas Wireless Propaga. Lett.*, vol. 16, pp. 3018-3021, 2017.

[20] D. M. Pozar and B. Kaufman, "Comparison of three methods for the measurement of printed antenna efficiency," *IEEE Trans. Antennas Propag.*, vol. AP-36, no. 1, pp. 136–139, Jan. 1988.

[21] M. S. Abdallah, Y. Wang, W. M. Abdel-Wahab, and S. Safavi-Naeini, "Design and optimization of SIW center-fed series rectangular dielectric resonator antenna array with 45° linear polarization," *IEEE Trans. Antennas Propag.*, vol. 66, no. 1, pp. 23–31, Jan. 2018.

[22] J. Xu, W. Hong, H. Zhang, G. Wang, Y. Yu, and Z. H. Jiang, "An array antenna for both long–and medium-range 77 GHz automotive radar applications," *IEEE Trans. Antennas Propag.*, vol. 65, no. 12, pp. 7207–7216, Dec. 2017.

[23] R. Mailloux, J. McIlvenna, and N. Kernweis, "Microstrip array technology," *IEEE Trans. Antennas Propag.*, vol. AP-29, no. 1, pp. 25–37, Jan. 1981.

[24] W. Wang, J. Wang, A. Liu, and Y. Tian, "A novel broadband and high-isolation dual-polarized microstrip antenna array based on quasisubstrate integrated waveguide technology," *IEEE Trans. Antennas Propag.*, vol. 66, no. 2, pp. 951–956, Feb. 2018.

[25] K. Ding, X. Fang, A. Chen, and Y. Wang, "A novel parallel-series feeding network based on three-way power divider for microstrip antenna array," IEEE Antennas Wireless Propag. Lett., vol. 12, pp. 757–760, 2013.

[26] E. Levine, G. Malamud, S. Shtrikman, and D. Treves, "A study of microstrip array antennas with the feed network," *IEEE Trans. Antennas Propag.*, vol. 37, no. 4, pp. 426–434, Apr. 1989.

[27] M. Zhang, J. Hirokawa, and M. Ando, "A four-way divider for partially corporate feed in an alternating-phase fed single-layer slotted waveguide array," *IEEE Trans. Antennas Propag.*, vol. 56, no. 6, pp. 1790–1794, Jun. 2008.

[28] Y. Miura, J. Hirokawa, M. Ando, K. Igarashi, and G. Yoshida, "A circularly-polarized aperture array antenna with a corporate-feed hollow-waveguide circuit in the 60 GHz-band," in *Proc. IEEE Int. Symp. Antennas Propag. (APSURSI)*, Jul. 2011, pp. 3029–3032.

[29] H. Irie and J. Hirokawa, "Perpendicular-corporate feed in three-layered parallel-plate radiating-slot array," *IEEE Trans. Antennas Propag.*, vol. 65, no. 11, pp. 5829–5836, Nov. 2017.

[30] M. Sano, J. Hirokawa, and M. Ando, "Single-layer corporate-feed slot array in the 60-GHz band using hollow rectangular coaxial lines," *IEEE Trans. Antennas Propag.*, vol. 62, no. 10, pp. 5068–5076, Oct. 2014.

[31] A. U. Zaman and P.-S. Kildal, "Wide-band slot antenna arrays with single-layer corporate-feed network in ridge gap waveguide technology," *IEEE Trans. Antennas Propag.*, vol. 62, no. 6, pp. 2992–3001, Jun. 2014.

[32] S. G. Zhou, G. L. Huang, T. H. Chio, J. J. Yang, and G. Wei, "Design of a wideband dual-polarization full-corporate waveguide feed antenna array," *IEEE Trans. Antennas Propag.*, vol. 63, no. 11, pp. 4775–4782, Nov. 2015.

[33] Z. Shi-Gang, H. Guan-Long, P. Zhao-Hang, and L.-J. Ying, "A wideband full-corporate-feed waveguide slot planar array," *IEEE Trans. Antennas Propag.*, vol. 64, no. 5, pp. 1974–1978, May 2016.

[34] K. Ding and A. Kishk, "Bandwidth enhancement for parallel feeding networks by regulating transmission line lengths," in *Proc. IEEE Int. Symp. Antennas Propag. (APS/URSI)*, Jul. 2018, pp. 1–2.

[35] J. Shao, H. Ren, B. Arigong, C. Z. Li, and H. L. Zhang, "A fully symmetrical crossover and its dual-frequency application," *IEEE Trans. Microw. Theory Tech.*, vol. 60, no. 8, pp. 2410–2416, Aug. 2012.

[36] N. Ashraf, A. A. Kishk and A. Sebak, "Broadband millimeter-wave beamforming components augmented with AMC packaging," *IEEE Microw. Wireless Compon. Lett.*, vol. 28, no. 10, pp. 879-881, Oct. 2018.

[37] M. M. M. Ali and A. Sebak, "Compact printed ridge gap waveguide crossover for future 5G wireless communication system," *IEEE Microw. Wireless Compon. Lett.,* vol. 28, no. 7, pp. 549-551, July 2018.

[38] Y. Wang, K. Ma and Z. Jian, “A low-loss Butler matrix using patch element and honeycomb concept on SISL platform,” *IEEE Trans. Microw. Theory Techn.*, vol. 66, no. 8, pp. 3622-3631, Aug. 2018.

[39] E. Gandini, M. Ettorre, R. Sauleau and A. Grbic, “A lumped-element unit cell for beam-forming networks and its application to a miniaturized Butler matrix,” *IEEE Trans. on Microw. Theory Techn.*, vol. 61, no. 4, pp. 1477-1487, Apr. 2013.

[40] G. Tian, J. Yang and W. Wu, “A novel compact Butler matrix without phase shifter,” *IEEE Microw. Wireless Compon. Lett.*, vol. 24, no. 5, pp. 306-308, May 2014.

[41] M. M. M. Ali and A. Sebak, “2-D Scanning Magnetoelectric Dipole Antenna Array Fed by RGW Butler Matrix,” *IEEE Trans Antennas Propag.*, vol. 66, no. 11, pp. 6313-6321, Nov. 2018.

[42] H. Ren, B. Arigong, M. Zhou, J. Ding, H. Zhang, “A novel design of 4 × 4 Butler matrix with relatively flexible phase differences,” *IEEE Antennas Wireless Propag. Lett.*, vol. 15, pp. 1277-1280, 2016.

[43] R. D. Cerna and M. A. Yarleque, “A 3D compact wideband 16×16 Butler matrix for 4G/3G applications," in *IEEE/MTT-S Int. Microw. Symp.*, Philadelphia, PA, 2018, pp. 16-19.

[44] A. A. M. Ali, N. J. G. Fonseca, F. Coccetti and H. Aubert, “Design and implementation of two-layer compact wideband Butler matrices in SIW technology for Ku-band applications,” *IEEE Trans. Antennas Propag.*, vol. 59, no. 2, pp. 503-512, Feb. 2011.

[45] A. Moscoso-Mártir, I. Molina-Fernández and A. Ortega-Moñux, "Wideband slot-coupled Butler matrix," *IEEE Microw. Wireless Compon. Lett.*, vol. 24, no. 12, pp. 848-850, Dec. 2014.

[46] Y. Li and K.-M. Luk, “60-GHz dual-polarized two-dimensional switch-beam wideband antenna array of aperture-coupled magneto-electric dipoles,” *IEEE Trans. Antennas Propag.*, vol. 64, no. 2, pp. 554–563, Feb. 2016.

[47] A. B. Guntupalli, T. Djerafi, and K. Wu, “Two-dimensional scanning antenna array driven by integrated waveguide phase shifter,” *IEEE Trans Antennas Propag*., vol. 62, no. 3, pp. 1117-1124, 2014.

[48] W. Chen, Y. Hsieh, C. Tsai, Y. Chen, C. Chang and S. Chang, "A compact two-dimensional phased array using grounded coplanar-waveguides Butler matrices," in *Proc. Eur. Microw. Conf.*, Amsterdam, 2012, pp. 747-750.

[49] J. W. Lian, Y. L. Ban, Q. L. Yang, B. Fu, Z. F. Yu and L. K. Sun, “Planar millimeter-wave 2-D beam-scanning multibeam array antenna fed by compact SIW beam-forming network,” *IEEE Trans. Antennas Propag.*, vol. 66, no. 3, pp. 1299-1310, March 2018.

[50] W. Y. Chen, Ming-Huei Huang, Pei-Yu Lyu, S. F. Chang and C. C. Chang, “A 60-GHz CMOS 16-beam beamformer for two-dimensional array antennas,” in *IEEE MTT-S Int. Microw. Symp. Dig.*, Tampa, FL, 2014, pp. 1-3.

[51] S. I. Orakwue, R. Ngah, and T. A. Rahman, “A two-dimensional beam scanning array antenna for 5G wireless communications,” in *IEEE Wireless Commun. Netw. Conf. Workshop*, Doha, 2016, pp. 1-4.

[52] W. F. Moulder, W. Khalil, and J. L. Volakis, “60-GHz two-dimensionally scanning array employing wideband planar switched beam network,” *IEEE Antennas Wireless Propag. Lett.*, vol. 9, pp. 818-821, 2010.

[53] J. Wang, Y. Li, L. Ge, J. Wang, and K. M. Luk, “A 60 GHz horizontally polarized magnetoelectric dipole antenna array with 2-D multibeam endfire radiation,” *IEEE Trans. Antennas Propag.*, vol. 65, no. 11, pp. 5837-5845, Nov. 2017.

[54] B. M. Schiffman, “A new class of broad-band microwave 90-degree phase shifters,” *IRE Trans. Microw. Theory Techn., vol. MTT-6*, pp. 232-237, Apr. 1958.

[55] S. Y. Zheng, W. S. Chan, and K. F. Man, “Broadband phase shifter using loaded transmission line,” *IEEE Microw. Wireless Compon. Lett.*, vol. 20, no. 9, pp. 498-500, Sept. 2010.

[56] S. Y. Zheng and W. S. Chan, “Differential RF phase shifter with harmonic suppression,” *IEEE Trans. Ind. Electron.*, vol. 61, no. 6, pp. 2891-2899, June 2014.

[57] K. Ding, A. A. Kishk, “Two-dimensional Butler matrix concept for planar array,” in *Proc. IEEE MTT-S, Int. Microw. Symp. Dig.*, Philadelphia, PA, 2018, pp. 1-4.

[58] K. Ding, A. A. Kishk, “Two-dimensional Butler matrix and phase-shifter group,” *IEEE Trans. Microw. Theory Techn.*, vol. 66 December 2018.

[59] G. P. Riblet, “A compact planar microstrip-slot line symmetrical junction comparator circuit,” in *Proc. IEEE MTT-S, Int. Microw. Symp. Dig.*, Long Beach, CA, USA, 1989, pp. 239-242 vol.1.

[60] G. P. Riblet, “A compact ring-style 8-port comparator circuit using coupled lines,” *IEEE Trans. Microw. Theory Techn.,* vol. 41, no. 6, pp. 1224 - 1226, June 1993.

[61] T. Kawai, K. Iio, I. Ohta and T. Kaneko, “A branch-line-type eight-port comparator circuit,” in *Proc. IEEE MTT-S, Int. Microw. Symp. Dig.*, Boston, MA, USA, 1991, pp. 869-872 vol.2.

[62] I. Ohta, T. Kawai, S. Shimahashi and K. Ho, “A transmission-line-type eight-port hybrid,” in *Proc. IEEE MTT-S, Int. Microw. Symp. Dig.*, Albuquerque, NM, USA, 1992, pp. 119-122 vol.1.

[63] H. Ting, S. Hsu and T. Wu, "A novel and compact eight-port forward-wave directional coupler with arbitrary coupling level design using four-mode control technology," *IEEE Trans. Microw. Theory Techn.,* vol. 65, no. 2, pp. 467-475, Feb. 2017.

[64] H. Ting, S. Hsu and T. Wu, "Broadband eight-port forward-wave directional couplers and four-way differential phase shifter," in IEEE Transactions on Microwave Theory and Techniques, vol. 66, no. 5, pp. 2161-2169, May 2018.

[65] J. L. Vazquez-Roy, A. Tamayo-Domínguez, E. Rajo-Iglesias and M. Sierra-Castañer, “Radial line slot antenna design with groove gap waveguide feed for monopulse radar systems,” *IEEE Trans. Antennas Propaga.*, vol. 67, 2019. (Early access)

[66] F. Zhao, Y. J. Cheng, P. F. Kou and S. S. Yao, “A wideband low-profile monopulse feeder based on silicon micromachining technology for W-band high-resolution system,” *IEEE Antennas Wireless Propag. Lett.*, vol. 18, no. 8, pp. 1676-1680, Aug. 2019.

[67] Y. Wang, G. Wang, Z. Yu, J. Liang and X. Gao, “Ultra-wideband E-plane monopulse antenna using Vivaldi antenna,” *IEEE Trans. Antennas Propaga.*, vol. 62, no. 10, pp. 4961-4969, Oct. 2014.

[68] S. Wang and W. Lin, “A 10/24-GHz CMOS/IPD monopulse receiver for angle-discrimination radars,” *IEEE Tran. Circuits Syst. I, Reg. Papers*, vol. 61, no. 10, pp. 2999-3006, Oct. 2014.

[69] K. Tekkouk, M. Ettorre and R. Sauleau, “Multibeam pillbox antenna integrating amplitude-comparison monopulse technique in the 24 GHz band for tracking applications,” *IEEE Trans. Antennas Propag.*, vol. 66, no. 5, pp. 2616-2621, May 2018.

[70] P. F. Kou and Y. J. Cheng, “A dual circular-polarized extremely thin monopulse feeder at W-band for prime focus reflector antenna,” *IEEE Antennas Wireless Propag. Lett.*, vol. 18, no. 2, pp. 231-235, Feb. 2019.

[71] J. Zhu, S. Liao, S. Li and Q. Xue, “60 GHz substrate-integrated waveguide-based monopulse slot antenna arrays,” *IEEE Trans. Antennas Propag.*, vol. 66, no. 9, pp. 4860-4865, Sept. 2018.

[72] S. Moon, I. Yom and H. L. Lee, “K-band phase discriminator using multiport downconversion for monopulse tracker,” *IEEE Microw. Wireless Compon. Lett.*, vol. 27, no. 6, pp. 599-601, June 2017.

[73] A. Vosoogh, A. Haddadi, A. U. Zaman, J. Yang, H. Zirath and A. A. Kishk, “W-band low-profile monopulse slot array antenna based on gap waveguide corporate-feed network,” *IEEE Trans. Antennas Propag.*, vol. 66, no. 12, pp. 6997-7009, Dec. 2018.

[74] P. Zheng, G. Zhao, S. Xu, F. Yang, and H. Sun, “Design of a W-Band full-polarization monopulse Cassegrain antenna,” *IEEE Antennas Wirel. Propag. Lett.*, vol. 16, pp. 99-103, Apr. 2016.

[75] G. Huang, S. Zhou, T. Chio, C. Sim and T. Yeo, "Wideband dual-polarized and dual-monopulse compact array for SAR system integration applications," *IEEE Geosci. Remote Sens. Lett*, vol. 13, no. 8, pp. 1203-1207, Aug. 2016.

[76] J. Reed and G. J. Wheeler, “A method of analysis of symmetrical four-port networks,” *IRE Trans. Microw. Theory Techn.*, vol. 4, no. 4, pp. 246-252, October 1956.

[77] A. M. Abbosh and M. E. Bialkowski, “Design of compact directional couplers for UWB applications,” *IEEE Trans. Microw. Theory Techn.*, vol. 55, no. 2, pp. 189-194, Feb. 2007.

[78] K. Ding and A. A. Kishk, “Compact comparator for dual-polarized monopulse array based on novel eight-port coupler,” in *Proc. IEEE/AP-S Int. Symp. Antennas Propag.*, Atlanta, GA, USA, 2019.

[79] K. Ding and A. A. Kishk, “Compact comparator for 2-D monopulse array based on novel eight-port coupler,” in *Proc. IEEE/AP-S Int. Symp. Antennas Propag.*, Atlanta, GA, USA, 2019.

[80] H. E. Foster and R. E. Hiatt, “Butler network extension to any number of antenna ports,” *IEEE Trans. Antennas Propag.*, vol. AP-18, no. 9, pp. 818–820, Nov. 1970.

[81] S. Gruszczynski, K. Wincza, and K. Sachse, “Reduced sidelobe four beam *N*-element antenna arrays fed by 4 × *N* Butler matrices,” *IEEE Antennas Wireless Propag. Lett.*, vol. 5, pp. 430–434, 2006.

[82] K. Wincza, S. Gruszczynski, K. Sachse, "Reduced sidelobe four-beam antenna array fed by modified Butler matrix," *Electron. Lett.*, vol. 42, no. 9, pp. 508-509, Apr. 2006.

[83] L. G. Sodin, “Method of synthesizing a beam-forming device for the N-beam and N-element array antenna, for any N,” *IEEE Trans. Antennas Propag.*, vol. 60, no. 4, pp. 1771–1776, Apr. 2012.

[84] K. Ding, X. Fang, Y. Wang and A. Chen, “Printed dual-layer three-way directional coupler utilized as 3 × 3 beamforming network for orthogonal three-beam antenna array,” *IEEE Antennas Wireless Propag. Lett.*, vol. 13, pp. 911-914, 2014.

[85] S. Odrobina, K. Staszek, K. Wincza and S. Gruszczynski, “Broadband 3 x 3 butler matrix,” in *Conf. Microw. Tech.* (COMITE), Brno, 2017, pp. 1-5.

[86] S. Gruszczynski and K. Wincza, “Broadband 4 × 4 Butler matrices as a connection of symmetrical multisection coupled-line 3-dB directional couplers and phase correction networks,” *IEEE Trans. Microw. Theory Tech.*, vol. 57, no. 1, pp. 1-9, Jan. 2009.

[87] K. Wincza, S. Gruszczynski, and K. Sachse, “Broadband planar fully integrated 8 × 8 Butler matrix using coupled-line directional couplers,” *IEEE Trans. Microw. Theory Tech.*, vol. 59, no. 10, pp. 2441-2446, Oct. 2011.

[88] K. Wincza, K. Staszek, and S. Gruszczynski, “Broadband multibeam antenna arrays fed by frequency-dependent Butler matrices,” *IEEE Trans. Antennas Propag.*, vol. 65, no. 9, pp. 4539-4547, Sept. 2017.

[89] M. Nedil, T. A. Denidni, and L. Talbi, “Novel Butler matrix using CPW multi-layer technology,” in *IEEE int. Symp. AP-S,* 2005, pp. 299-302, vol. 3A.

[90] K. Ding, F. He, X. Ying, and J. Guan, “A compact 8×8 Butler matrix based on double-layer structure,” in *Proc. IEEE Int. Symp. MAPE, 2013*, Chengdu, 2013, pp. 650-653.

[91] Zhai, Y., Fang, X., Ding, K., and He, F. “Miniaturization design for 8× 8 Butler matrix based on back-to-back bilayer microstrip,” *Int. J Antennas Propag.*, *2014*.

[92] Y. S. Wong, S. Y. Zheng, and W. S. Chan, “Quasi-arbitrary phase-difference hybrid coupler,” *IEEE Trans. Microw. Theory Tech.*, vol. 60, no. 6, pp. 1530-1539, Jun. 2012.

[93] M. J. Park, “Comments on “Quasi-arbitrary phase-difference hybrid coupler,” *IEEE Trans. Microw. Theory Techn.,* vol. 61, no. 3, pp. 1397-1398, March 2013.

[94] Y. Wu, J. Shen, and Y. Liu, “Comments on “quasi-arbitrary phase-difference hybrid coupler,” *IEEE Trans. Microw. Theory Techn.*, vol. 61, no. 4, pp. 1725-1727, April 2013.

[95] G. Tian, J. P. Yang, and W. Wu, “A novel compact Butler matrix without phase shifter,” *IEEE Microw. Wireless Compon. Lett.*, vol. 24, no. 5, pp. 306-308, May 2014.

[96] H. Ren, B. Arigong, M Zhou, J. Ding, and H. Zhang, “A novel design of 4×4 Butler matrix with relatively flexible phase differences”, *IEEE Antennas Wireless Propag. Lett*., vol. 15, pp. 1277-1280, 2016.

[97] K. Ding, J. Bai, and A. Kishk, “A quasi Butler matrix with 6×6 beam-forming capacity using 3×3 hybrid couplers,” in *Proc. 32nd General Assembly Scientific Symp. Int. Union Radio Sci.*, Montreal, QC, 2017, pp. 1-4.

[98] C. C. Chang, R. H. Lee and T. Y. Shih, “Design of a beam switching/steering Butler matrix for phased array system,” *IEEE Trans. Antennas Propag.*, vol. 58, no. 2, pp. 367-374, Feb. 2010.

[99] H. N. Chu and T. G. Ma, “An extended 4 x 4 Butler matrix with enhanced beam controllability and widened spatial coverage,” *IEEE Trans. Microw. Theory Techn.*, vol. 66, no. 3, pp. 1301 - 1311, 2018.

[100] K. Ding and A. A. Kishk, “Multioctave bandwidth of parallel-feeding network based on impedance transformer concept,” *IEEE Trans. Antennas Propag.*, vol. 67, no. 4, pp. 2803-2808, April 2019.

[101] K. Ding and A. A. Kishk, “Investigation of imperfect isolation of crossovers on Butler matrices,” *IEEE Trans. Microw. Theory Techn.*, (Submitted).

[102] D. M. Pozar, *Microwave Engineering*. Hoboken, NJ: Wiley, 2012.

[103] W. Menzel and I. Wolff, “A method for calculating the frequency-dependent properties of microstrip discontinuities,” *IEEE Trans. Microw. Theory Tech.*, vol. 25, no. 2, pp. 107-112, Feb 1977.

[104] N. H. L. Koster and R. H. Jansen, “The microstrip step discontinuity: a revised description,” *IEEE Trans. Microw. Theory Tech.*, vol. 34, no. 2, pp. 213-223, Feb 1986.

[105] X. Tang and K. Mouthaan, "Design of large bandwidth phase shifters using common mode all-pass networks," *IEEE Microw. Wireless Compon. Lett.*, vol. 22, no. 2, pp. 55-57, Feb. 2012.

[106] X. Tang and K. Mouthaan, "Large bandwidth digital phase shifters with all-pass, high-pass, and low-pass networks," *IEEE Trans. Microw. Theory Techn.*, vol. 61, no. 6, pp. 2325-2331, June 2013.

[107] K. Ding, A. A. Kishk, “Very concise eight-port coupler for two-dimensional beamforming application,” in *Proc. IEEE/MTT-S Int. Microw. Symp.*, Boston, MA, USA, June 2019, pp. 1241-1244.

[108] C. G. Montgomery, R. H. Dicke, and E.M. Purcel1, *Microwave Circuits*, New York, USA: McGraw-Hill, 1948.

[109] J. Lu, Z. Kuai, X. Zhu and N. Zhang, "A high-isolation dual-polarization microstrip patch antenna with quasi-cross-shaped coupling slot," *IEEE Trans. Antennas Propag*., vol. 59, no. 7, pp. 2713-2717, July 2011.

[110] K. Ding and A. A. Kishk, “Wideband hybrid coupler with electrically switchable phase-difference performance,” *IEEE Microw. Wireless Compon. Lett.*, vol. 27, no. 11, pp. 992-994, Nov. 2017.

[111] K. Ding and A. A. Kishk, “Extension of Butler matrix number of beams based on reconfigurable couplers,” *IEEE Trans. Antennas Propag.*, vol. 67, no. 6, pp. 3789-3796, June 2019.

[112] H. Zhu, H. Sun, B. Jones, C. Ding and Y. J. Guo, “Wideband dual-polarized multiple beam-forming antenna arrays,” *IEEE Trans. Antennas Propag.*, vol. 67, no. 3, pp. 1590-1604, March 2019.

[113] H. Chaloupka, “Application of high-temperature superconductivity to antenna arrays with analogue signal processing capability,” in *Proc. 24th Eur. Microwave Conf.*, Cannes, France, 1994, pp. 23-35.

[114] A. Corona and M. J. Lancaster, “A High-temperature superconducting Butler matrix,” *IEEE Trans. Appl. Supercond.*, vol. 13, no. 4, pp. 3867-3872, Dec. 2003.

[115] W. Liu, Z. Zhang, Z. Feng and M. F. Iskander, “A compact wideband microstrip crossover,” *IEEE Microw. Wireless Compon. Lett.*, vol. 22, no. 5, pp. 254-256, May 2012.

Publications

Journal Articles

J-1. K. Ding and A. A. Kishk, "Multioctave bandwidth of parallel-feeding network based on impedance transformer concept," *IEEE Trans. Antennas Propag.*, vol. 67, no. 4, pp. 2803-2808, April 2019.

J-2. K. Ding and A. A. Kishk, "Extension of Butler matrix number of beams based on reconfigurable couplers," *IEEE Trans. Antennas Propag.*, vol. 67, no. 6, pp. 3789-3796, June 2019.

J-3. K. Ding and A. A. Kishk, "2-D Butler matrix and phase-shifter group," *IEEE Trans. Microw. Theory Techn.*, vol. 66, no. 12, pp. 5554-5562, Dec. 2018.

J-4. K. Ding and A. A. Kishk, "Wideband hybrid coupler with electrically switchable phase-difference performance," *IEEE Microw. Wireless Compon. Lett.*, vol. 27, no. 11, pp. 992-994, Nov. 2017.

J-5. K. Ding and A. A. Kishk, "Investigation of imperfect isolation of crossovers on Butler matrices," *IEEE Trans. Microw. Theory Techn.*, (Submitted).

J-6. K. Ding and A. A. Kishk, "Eight-port coupler with very concise structure for two-dimensional beamforming application," *IEEE Trans. Antennas Propag.*, (Submitted).

Conference Papers

C-1. K. Ding, A. A. Kishk, "Very concise eight-port coupler for two-dimensional beamforming application," in *Proc. IEEE/MTT-S Int. Microw. Symp.*, Boston, MA, USA, June 2019, pp. 1241-1244.

C-2. K. Ding and A. A. Kishk, "Two-dimensional Butler matrix concept for planar array," in *Proc. IEEE/MTT-S Int. Microw. Symp.*, Philadelphia, PA, 2018, pp. 632-635.

C-3. K. Ding, A. A. Kishk, "Compact comparator for dual-polarized monopulse array based on novel eight-port coupler," in *Proc. IEEE AP-S, Int. Symp. Antennas. Propag.* Atlanta, GA, USA, Jul. 2019.

C-4. K. Ding, A. A. Kishk, "Compact comparator for 2-D monopulse array based on novel eight-port coupler," in *Proc. IEEE AP-S, Int. Symp. Antennas. Propag.* Atlanta, GA, USA, Jul. 2019.

C-5. K. Ding and A. A. Kishk, “Bandwidth enhancement for parallel feeding networks by regulating transmission line lengths,” in *Proc. IEEE AP-S, Int. Symp. Antennas Propag.*, Boston, MA, 2018, pp. 959-960.

C-6. K. Ding, J. Bai and A. A. Kishk, “A quasi Butler matrix with 6×6 beam-forming capacity using 3×3 hybrid couplers,” in *Proc. 32nd General Assem. Sci. Symp. Int. Union Radio Sci. (URSI GASS)*, Montreal, QC, 2017, pp. 1-4.